ANALYSIS OF UNSATURATED HYDRAULIC PROPERTIES FOR LOW IMPACT DEVELOPMENTS AND THEIR PERFORMANCE UNDER CHANGING CLIMATE

Satbir Kaur Guram

A THESIS SUBMITTED TO
THE FACULTY OF GRADUATE STUDIES
IN PARTIAL FULFILLMENT OF THE REQUIREMENTS
FOR THE DEGREE OF
MASTER OF APPLIED SCIENCE

GRADUATE PROGRAM IN CIVIL ENGINEERING
YORK UNIVERSITY
TORONTO, ONTARIO

March 2021

Abstract

Climate change has resulted in an increase in both intensity and frequency of extreme rainfall events leading to a higher probability of flooding. Urbanization has also raised the risk of flooding due to the increase in impervious surfaces. To counter the impacts of climate change and urbanization, engineers have developed ingenious solutions to reduce flooding and capture stormwater contaminants through the use of Low Impact Developments (LIDs). Green roofs and bioretention facilities are examples of LIDs. The soil is generally considered to be completely saturated when designing for the LIDs. However, this may not always be an accurate or realistic approach, as the soil could be variably unsaturated leading to inaccurate designs. To analyze the flow under variably unsaturated conditions, Richards' equation can be used. In order to solve the Richards' equation, two nonlinear hydraulic properties, namely soil water characteristic curve (SWCC) and the unsaturated hydraulic conductivity function are required. Laboratory and field measurements of unsaturated hydraulic properties are cumbersome, expensive and time-consuming. An alternative approach is to estimate unsaturated hydraulic properties using pedotransfer functions. Pedotransfer functions (PTFs) estimate soil hydraulic properties using routinely measured soil properties, such as soil texture, grain size distribution, bulk density, or porosity. This first part of this research presents a comparison between the direct measurement obtained through experimental procedures and the use of pedotransfer functions to estimate soil hydraulic properties for two green roof and three bioretention soil medias. Comparison between the measured and estimated soil hydraulic properties was accomplished using two different approaches. Statistical analyses and visual comparisons were used to compare the measured and estimated soil hydraulic properties. Additionally, numerical modeling to predict the water balance at the ground surface was conducted using the measured and estimated soil hydraulic properties. Results indicate that there is a high level of uncertainty when using PTFs for LID materials.

It is ideal to analyze existing and future LID systems within the context of changing climate. Thus, the second part of this research will assist in the determination of whether the LID system design objectives can be met within the context of changing climate. In order to conduct this analysis, numerical modelling using HYDRUS software was completed. Material properties previously measured in the laboratory for bioretention and green roof substrates were used in the numerical modeling. Long-term and short-term climate data for ten locations in Ontario was used in this examination. Historical climate data was compiled from Environment and Climate Change Canada weather stations. Future long-term climate data from four different general circulation models (GCMs) with four representative concentration pathways (RCP) for the time period of 2011 to 2100 was used in the assessment. Short-term design storms were developed from historical and future intensity-duration-frequency (IDF) curves using the Chicago storm method. The results of this research suggest that LID performance may decrease due to the increased quantity of water projected in the future due to climate change. Results indicate that the percent change in future long-term maximum infiltration values for green roofs can be as much as 100%, whereas for bioretention facilities it can be in the order of 50%. Moreover, a general decrease in both the peak reduction and peak time delay for the green roof facilities can be expected for the future. Some 100-year storms in Ontario can see as much as 50 cm increase in untreated stormwater run-off from bioretention facilities.

Acknowledgments

I would like to express my sincere gratitude to my supervisor, Dr. Bashir, in providing me the opportunity to complete this research. His constant encouragement and mentoring has assisted me in throughout the completion of this research and supported me through the pandemic.

I would also like to thank Kunjan Rupakheti for his advice and positivity while working in the laboratory.

Thank you to Mr. Govers of LiveRoof Ontario, Ms. Argo and Ms. North of Gro-Bark, and Mr. Haig of Earthco Soil Mixtures for generously supplying the substrates used in this study.

Lastly, I am truly thankful in the constant support of my mom and sister.

Table of Contents

List of Figures

List of Tables

Chapter 1: Introduction

With the increase in urbanization, the risk of flooding rises due to the increase in impervious surfaces. Impervious surfaces, such as roads or other infrastructure, reduces the amount of precipitation infiltrating into the ground and increases the stormwater runoff. As the percentage of impervious surfaces increases, the amount of surface water runoff increases and groundwater recharge decreases. This can lead to major flooding in highly dense cities. Climate change has also resulted in an increase in both intensity and frequency of extreme rainfall events leading to a higher probability of flooding. This leads to older stormwater systems being overwhelmed as they are not designed to handle heavy rainfalls within a small time period. Typically, flooding can be attained by snow melting during the spring, rainfall during winter season, severe thunderstorms leading to intense rain bursts, and large precipitation over a long period during the hurricane season (Martin-Downs, 2013). However, due to rising annual temperatures, it is causing an increase in the atmosphere's ability to hold moisture, climate change can assist in causing earlier floods from spring snowmelt, ice jams leading to upstream flooding due to blockage, and rain-on-snow events (O'Malley, 2019). With the combined impact of climate change and impervious surfaces, major flooding can occur leading to major disasters within a community.

With this increase in flooding, engineers and urban planners develop stormwater management practices to assist in reducing the impact of flooding. Previous stormwater practices aimed to block or re-direct water from infrastructure, such as using culverts. These conventional stormwater practices would aim to control peak flow rates, without concern for possible contaminants collected from surface runoff and deposited to nearby water bodies (Credit Valley Conservation; Toronto and Region Conservation Authority, 2010). To counter the impacts of urbanization and climate change, engineers have developed ingenious solutions to reduce flooding and capture contaminants through the use of Low Impact Developments. Low Impact Developments (LIDs) are defined as a stormwater management strategy that aims to mitigate the

impacts of increased runoff and stormwater pollution by managing the runoff as close to the source as possible (U.S. EPA, 2007). With LIDs, stormwater can be treated as a resource in helping to preserve and recreate natural landscapes, rather than as a waste that needs to be re-routed from its source (U.S. EPA, 2018). LIDs assist in developing sustainable cities and include systems such as permeable pavements, green roofs, bioretention cells, and rain barrels.

When designing for LIDs, it is traditionally assumed that the substrate is completely saturated allowing for the use of Darcy's equation. One key reason for assuming saturated conditions is possibly due to the difficulty in obtaining the unsaturated hydraulic properties (Brunetti et al. 2016). However, with the assumption of saturated conditions, the use of Darcy's equation may lead to inaccurate results such as ponding or overflow within the soil media (Liu and Fassman-Beck, 2017). Furthermore, it is more likely that unsaturated flow dominates in both green roof and bioretention systems, rather than a saturated flow. Even though bioretention systems are designed for ponded conditions, it is noted that unsaturated conditions would prevail as most individual rainfall events are generally smaller than the design storm of about 25 mm (Barbu and Ballestero, 2014; Liu and Fassman-Beck, 2017). Green roofs, on the other hand, are not designed for ponded conditions, as this will lead to an additional load to the buildings structure (Liu and Fassman-Beck, 2018; Perelli, 2014). Therefore, green roof substrates are designed to have a saturated hydraulic conductivity larger than peak intensities to avoid ponding, thus decreasing the likeliness of saturated conditions.

Due to the difficulty in measuring the unsaturated hydraulic properties, some LID studies utilize estimated hydraulic properties which can lead to inaccurate results (Li and Babcock, 2015). An alternative approach is the use of pedotransfer functions. Pedotransfer functions estimate soil hydraulic properties using routinely measured soil properties, including: soil texture, grain size distribution, bulk density, or porosity. However, as LIDs are constructed with engineered materials that vary from place to place, the hydraulic properties for each individual design can vary. Factors

such as field compaction, organic content, root growth and age can also impact the hydraulic properties and are crucial for accurate modelling (Li and Babcock, 2015). With improved accuracy, the models can assist in quantifying the impact of climate change on LID design, such as the optimal substrate depth that provides the best retention.

1.1 Thesis Objectives

1. Measure the soil hydraulic properties of various bioretention and green roof substrates;
2. Assess the performance of various pedotransfer functions in predicting the hydraulic properties of low impact development materials;
3. Numerical modelling to highlight the importance of accurate soil hydraulic properties; and
4. Examine the effects of climate change on the design of low impact developments in the province of Ontario

1.2 Thesis Outline

1.2.1 Chapter 2: Literature Review

Chapter 2 begins with a background of the design and benefits of green roof and bioretention systems. The chapter provides a detailed review of the engineered substrates used in both LID systems. Furthermore, soil hydraulic properties are discussed to provide the reader a brief background of the unsaturated soil theory. Additionally, components of the water balance at ground surface such as the net infiltration, potential evaporation, actual evaporation, surface runoff, and transpiration are presented in this chapter. Finally, climate data, particularly climate models and future emission scenarios, are also discussed briefly.

1.2.2 Chapter 3: Measured versus Predicted Soil Hydraulic Properties

This chapter assesses the performance of pedotransfer functions in estimating the soil hydraulic properties of green roof and bioretention media. Regression models, physicoempirical models, and artificial neural network were the three types of pedotransfer functions used to predict the

hydraulic properties for the LID substrates. To compare the measured and predicted SWCC, statistical analysis was carried out by calculating the coefficient of determination, mean square deviation, and mean absolute deviation. To confirm the validity of the statistical analysis, a visual examination was also completed.

This chapter also presents the materials and experimental methods used to examine the LID substrates. In total, two green roof and three bioretention substrates were tested in the laboratory. Laboratory testing included measurement of the organic content (ASTM D2974, 2014), specific gravity (ASTM D854, 2014), particle size distribution using both the sieve test (ASTM D6913, 2017) and hydrometer test (ASTM D7928, 2017), and the saturated hydraulic conductivity using the constant head test (ASTM D5856, 2015). The soil water characteristic curves were also measured using the HYPROP measurement system (UMS, 2015).

1.2.3 Chapter 4: Design and Performance of Low Impact Developments Under Changing Climate

This chapter conducts an examination of green roof and bioretention substrates under changing climate to determine if current and future LID systems are required to be modified. A methodology to analyze the LID designs for changing climate is presented. Various design aspects of the LID systems are examined, including future quantities of water that enters the system, peak intensity delay, peak time delay, run-off, ponding and overflow within the bioretention facilities, residence times, storage capacity, and substrate thickness. Furthermore, both future long-term and extreme precipitation events are examined and compared to historical climate data for the ten locations in Ontario. Numerical modelling was carried out using HYDRUS software (Šimůnek et al. 2008).

1.2.4 Chapter 5: Summary, Conclusions, and Recommendations for Future Research

Chapter 5 presents the summary and conclusions of the research. It also presents recommendations for future research.

Chapter 2: Literature Review

2.1 Design

Low Impact Developments are not simply green spaces that are constructed to reduce flooding. Rather, they are engineered systems comprised of various components in order to meet various social and environmental criteria. Green roofs, as the name suggests, are vegetated zones located on roofs that are able to withstand the additional load. Figure 2.1 demonstrates the various layers found within a green roof system. The top layers include vegetation and growth media that is able to support the plant life and is necessary for water retention. A filter layer is located beneath the growth medium to prevent blockage in the drainage layer (CVC and TRCA, 2011). The drainage layer ensures that a surplus of water is not retained on the roof and allows for sufficient drainage. This assists in allowing for adequate ventilation for roofs, reduces water-logged conditions, and decreases the building load. In addition, this layer provides water storage for plant uptake. As shown in Figure 2.2, the built-in cup design, or cavities, are used to store water during a storm event to be made available during drought conditions. The water evaporates from the cavities and penetrates the filter layer, later reaching the roots by capillarity (Cascone, 2019). Furthermore, a waterproof membrane is required to protect the roof structure (CVC and TRCA, 2010). Overall, each of these layers play an important role in either protecting the roof or supporting the plant life.

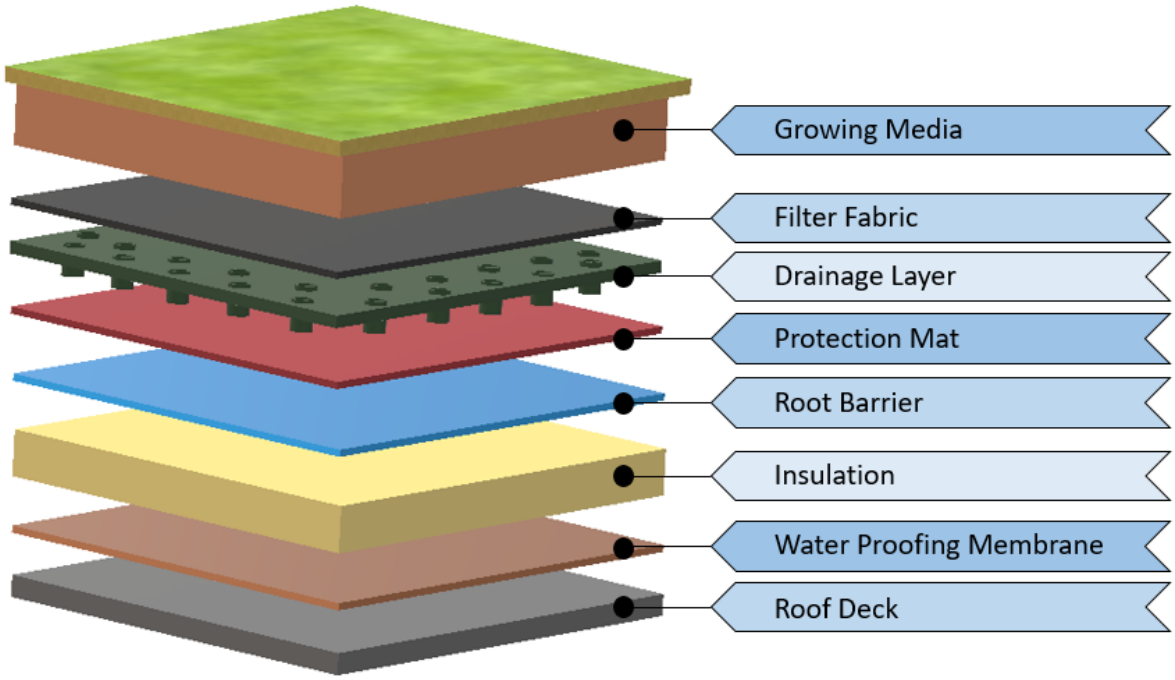

Figure 2.1: Green roof layers (modified from Kelmendi and Aliu, 2013)

Figure 2.2: Green roof drainage layer (retrieved from Cascone, 2019)

Bioretention systems are localized sites that temporarily stores, treats, and infiltrates stormwater runoff (CVC and TRCA, 2010; Khan, 2010). Figure 2.3 illustrates the typical design of a

bioretention system. Major components of the bioretention system include pretreatment, inlet, ponding area, vegetation, mulch, growing media and the optional underdrain (Khan, 2010). The purpose for pretreatment is to capture large debris before it enters the bioretention system in order to prevent premature clogging (CVC and TRCA, 2010). The inlet introduces a single point of entry from a large catchment area, to prevent high flows from entering the bioretention cell (Khan, 2010). Ponding allows for both contaminant removal and increased water storage during a large storm event (CVC and TRCA, 2010; Khan, 2010). Subsequently, not only does vegetation assist with the aesthetics, but it also helps in filtering pollutants (Khan, 2010; Simcock and Dando, 2013). The purpose of the mulch layer is to protect the bioretention cell, particularly the growth media, from erosion, reduce weed growth and increases water availability for the plants (Simcock and Dando, 2013). The mulch layer also assists in the removal of heavy metals, sediments, and nutrients (Davis et al., 2006; CVC and TRCA, 2010). Similar to green roofs, the growth media supports the vegetation as well as provides storage to stormwater infiltration and runoff. Finally, an optional underdrain may be implemented to transfer stormwater runoff from the bioretention cell to a connected stormwater sewer system (Khan, 2010).

2.2 Benefits

There are a range of benefits that are obtainable with the implementation of LIDs. One primary benefit is the reduction of flooding by mimicking the hydrological cycle. Figure 2.4 illustrates a schematic of the typical hydrograph comparison between a conventional roof and a green roof. When compared to impervious surfaces, such as the conventional roof or a paved road, the LIDs are able to store and slowly release stormwater infiltration. This assists in reducing the amount of water infiltrating stormwater sewer systems or reduce flooding of the nearby infrastructure. This reduction of flooding is especially required in highly dense urban cities.

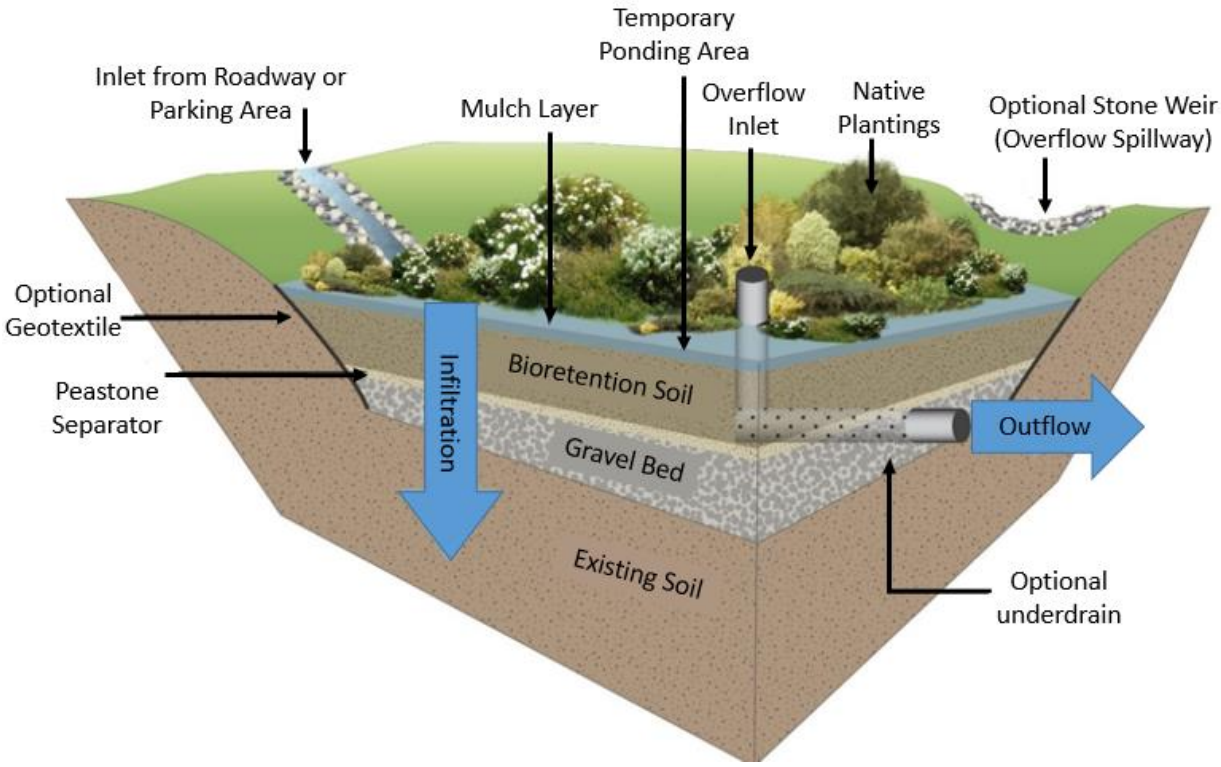

Figure 2.3: Typical bioretention schematic (retrieved from Massachusetts Department of Environmental Protection, n.d.)

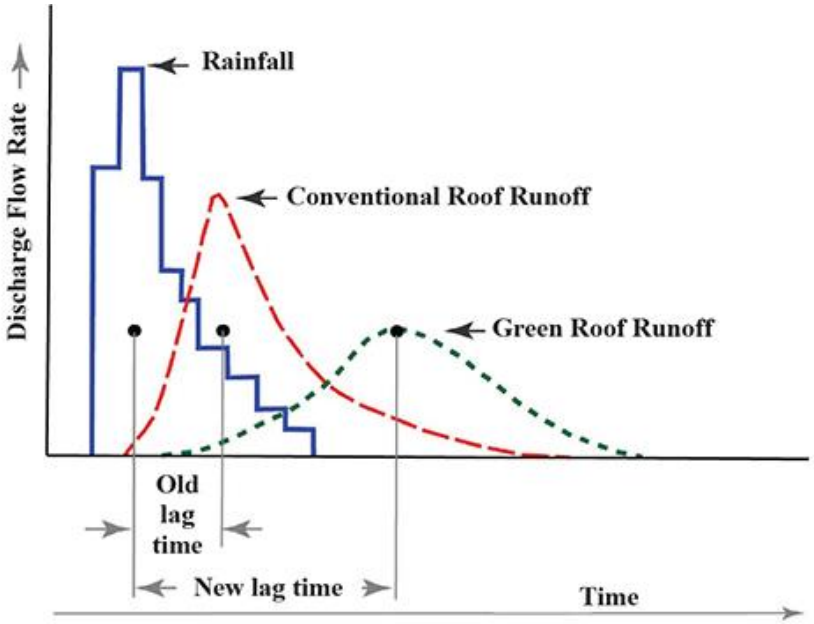

Figure 2.4: Typical hydrograph of conventional roof versus green roof runoff (from Sutton et al., 2014).

Other benefits include heat mitigation, in particular reducing the impacts of urban heat island effect (Susca et al. 2011). Removing pollutants whether by producing carbon sinks from these green spaces, or capturing it within the stormwater runoff is another benefit of LIDs (Davis et al. 2006; Yang et al. 2008). Finally, aesthetics is a benefit to the social aspect within an urban landscape.

2.3 Substrates

In order to satisfy the LID design objective of reducing flooding and/or capturing stormwater pollutants, it is necessary to use an appropriate substrate within the LID. The substrate is an engineered media that contains a mixture that is developed deliberately with specific objectives in mind. Whereas soil is a natural and native product of earth, engineered media contains enhanced properties to improve the performance, depending on the design criteria (Sandoval et al., 2017; Liu and Fassman-Beck, 2017). Although both green roofs and bioretention cells contain engineered media, the composition of both differ based on design criteria. In particular, bioretention have a greater depth and a lower saturated hydraulic conductivity in comparison to green roofs (CVC and TRCA, 2010; Liu and Fassman-Beck, 2017).

According to the Credit Valley Conservation and Toronto and Region Conservation Authority (2010), the recommended substrate depth for a bioretention cell should be between 1 and 1.25 m. On the other hand, there are two types of green roofs which are referred as intensive or extensive. Intensive green roofs have substrate depths greater than 15 cm in order to accommodate deep rooted plants and heavy foot traffic. Intensive green roofs are more complex to design as they do impose a greater load to the roofs structure. Whereas extensive green roofs have a substrate depth equal to or less than 15 cm, for a smaller vegetation cover (CVC and TRCA, 2010). Bioretention systems contain a large substrate depth in order to store a large volume of stormwater runoff during a storm event. Unlike green roofs, bioretention systems cater to a greater catchment area in addition to the direct precipitation that is captured (House et al.

2017). Furthermore, with the increase in impervious surfaces, the amount of water entering a bioretention system far exceeds that of a green roof where only direct precipitation is captured.

The other major design requirement that differs between green roofs and bioretention systems is the saturated hydraulic conductivity. Typically, the saturated hydraulic conductivity for bioretention is smaller in comparison to green roofs (Liu and Fassman-Beck, 2017). One main reason for this difference is due to pollutant removal processes. As bioretention systems gather a large amount of stormwater runoff from surrounding areas, they can be designed to handle ponding conditions. During ponding, larger particles would settle to the bottom, thus undergoing a removal process via sedimentation. However, to avoid a breeding site for mosquitoes, it is recommended that the maximum allowable surface ponding time be 24 hours after the storm event and a maximum ponding depth between 150-250 mm at the end of the storm (CVC and TRCA, 2010).

Other pollutant removal processes such as filtration, sorption, cation exchange, plant root uptake and biological activity can occur within the bioretention systems (Pitt et al., 1999). Sorption is the ability of a substance to stick to another surface. Sorption can refer to either adsorption or absorption. Adsorption refers to particles that stick to the surface of another substance whereas absorption refers to contaminants that are dissolved and absorbed or diffused within the soil. Subsequently, cation exchange capacity (CEC) relates to the total capacity of the soil to hold positively charged ions. Soil that contains a large amount of clay or organic matter have a higher CEC as they have negatively charged sites on their surface. Therefore, many nutrients, which are cations, are held at these sites by electrostatic force, thus leading to fertile soil (Brown & Lemon, 2020). Depending on the plant species, plant root uptake can also assist in capturing contaminants. Biological activity can include processes, such as denitrification, in order to break down contaminates into forms that are less harmful to the environment. For example, to assist in removing nitrate from the soil, nitrate can be converted to nitrogen gas. Adding material such as

newspaper clippings, provides an electron donor and helps drive the denitrification process under anoxic (oxygen depleted) conditions (Weiss and Gulliver, 2008; Lefevre et al. 2015).

Furthermore, the substrate should be able to support vegetation life in order to be effective. Substrates are comprised of a mixture of both large and small particle sizes in order to provide adequate air space and water holding capacity. A substrate with large particles, thus large pore spaces, will allow for rapid water flow and primarily air-filled pores after drainage. Whereas a substrate with small particles will allow for slow water flow and water-filled micropores and air-filled macropores. The proportion of air to water within the substrate is key for plant survival (Handreck and Black, 2002; Griifin, 2014). Thus, with these design specifications in mind, such as the saturated hydraulic conductivity, the ability to support vegetation, pollutant removal processes, and its water retention capacity, the engineered media is developed.

Subsequently, the growing media chosen should comply with the local climate and local availability. Griffin (2014) noted the green roof substrates varied depending on local climate and availability. For example, in North America, green roof substrates are comprised of mostly lightweight aggregates, such as slate, shale or expanded clay. Griffin (2014) also notes that green roof substrates in North America are largely manufactured aggregates, while other countries use lower carbon recycled or natural materials. For instance, New Zealand uses zeolite and volcanic rock and Northern Italy uses a blend of naturally occurring mineral material. Additionally, U.K. uses broken brick within its substrate and in Sweden naturally occurring lava or scoria is used. The Low Impact Development Stormwater Management Guide by Credit Valley Conservation and Toronto and Region Authorities (2010) provides material recommendation for LID growing media. For green roofs, a mixture of sand, gravel, crushed brick, compost, or organic matter is recommended to be combined with natural soil. For the bioretention cells, the recommendation is to use 85 to 88% sand (2.0 to 0.05 mm), 8 to 12 % fines (<0.05 mm), and 3 to 5 % organic matter (CVC and TRCA, 2010).

2.4 Soil Hydraulic Properties

The soil hydraulic properties are key in design and performance of the LIDs. Depending on the water content of the soil, the hydraulic properties can be classified as either saturated or unsaturated. Soils are considered saturated when all the void spaces are filled with water. Soils that contain air-filled voids and water-filled voids are termed either unsaturated or partially saturated soil.

2.4.1 Saturated Conditions

Under saturated conditions, the soil pores are completely filled with water. To determine the water flow, Darcy's Law (1856) for saturated soils in one-dimensional flow is as follows:

$$q = -K_s \frac{(H_2 - H_1)}{L} = -K_s \frac{dH}{L} = -K_s i \qquad [2.1]$$

where q is the Darcy flux, K_s is the saturated hydraulic conductivity, H is the total hydraulic head, L is the length of the flow path and i is the hydraulic gradient. The hydraulic gradient is the driving force for water flow. The gradient is calculated by taking the difference of the total hydraulic head for two points over the length of the flow path.

The saturated hydraulic conductivity is a key physical property that is required in water flow analysis. There are several standard methods to measure the K_s, including the constant head test or the falling head test used in the laboratory (ASTM D5856-15; ASTM D5084-16). Coarse grained soils have a greater K_s compared to fine grained soils. For instance, the range of K_s can be from 1 cm/s for gravels to 10^{-9} cm/s for clays (Freeze and Cherry, 1979).

2.4.2 Unsaturated Conditions

Richards' (1931) equation can be used to describe the uniform flow of water under unsaturated conditions. Richards' (1931) equation was derived from the Darcy-Buckingham (1907) equation, which is a modification of the Darcy (1856) equation to describe the unsaturated flow. The Darcy-Buckingham (1907) equation assumes that hydraulic conductivity is a function of soil water pressure, as following:

$$q = -K(\psi)\frac{dh}{dz} \quad [2.2]$$

Equation 2.3 is the Mixed Form of Richards' equation for uniform flow in vertical direction, which can be derived by combining the Darcy-Buckingham (1907) equation and the equation of continuity:

$$\frac{\partial\theta}{\partial t} = \frac{\partial}{\partial z}\left[K(\psi)\left(\frac{\partial\psi}{\partial z} - 1\right)\right], \quad [2.3]$$

where θ is the volumetric water content, ψ is the soil water pressure, $K(\psi)$ is the unsaturated hydraulic conductivity which is the function of the soil water pressure. Also, z is the vertical coordinate distance and t represents time.

In order to solve the Richards' equation, two nonlinear hydraulic properties are required. These are, the soil water characteristic curve (SWCC) and the unsaturated hydraulic conductivity function. The unsaturated hydraulic conductivity is the relationship of hydraulic conductivity with water content, $K(\theta)$, or pressure, $K(\psi)$. As unsaturated conditions increase, meaning a reduction in water content as a result of increasing suction, there is a decrease in hydraulic conductivity due to flow paths becoming more tortuous and flow through smaller pores. Whereas the SWCC is the relationship between water content and soil water pressure (Figure 2.5). When the soil is

saturated, the soil water pressure is zero and the water content is saturated (θ_s). Applying a small suction to the saturated soil will not immediately reduce the water content. Instead, the water content will reduce once the suction reaches the air entry value. The air entry value is the pressure when air first enters the largest pores in the saturated soil. As shown in Figure 2.5, different soil textures impact the shape of the SWCC. For instance, clay has a greater air entry value compared to sand due to its smaller pore sizes and gradual slope due to broader pore-size distribution. Whereas sand has a very steep slope due to its narrow pore-size distribution and lower air entry value due to larger pore sizes.

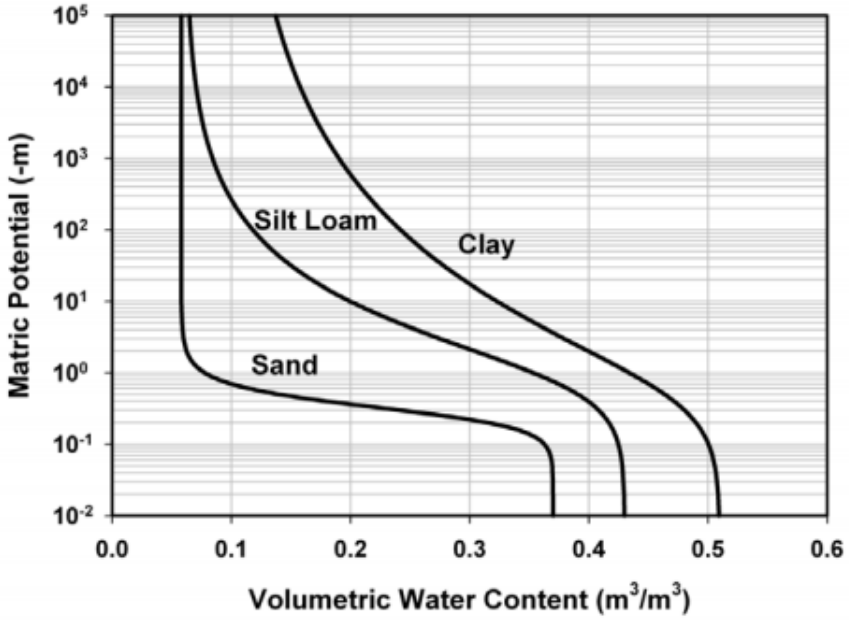

Figure 2.5: Typical soil water characteristic curve for soils of different texture (retrieved from Tuller and Or, 2003)

Various methods can be used to directly measure the SWCC. These include, using a hanging water column, pressure cells, pressure plate extractors, suction tables, soil freezing and others (Bezzera-Coelho et al. 2018). A popular method used to measure the SWCC is by conducting the simplified evaporation method (Schindler, 1980). A study conducted by Peters and Durner (2007) has shown that the simplified evaporation method is a fast, accurate and reliable method in

determining the soil hydraulic properties for coarse grained porous media. Griffin (2014), Brunetti et al. (2016), and Sandoval et al. (2017) have used the evaporation method for green roof substrate using the HYPROP apparatus. Hess et al. (2015), DelVecchio (2017), and Nichols (2018) have also used the HYPROP apparatus to measure SWCCs for bioretention media.

Once a series of water content and soil water pressure data points are measured for a porous medium, analytical functions such as those described by Brooks and Corey (1964) or van Genuchten (1980) can be fitted to the experimental data to represent the SWCC mathematically. These analytical functions once fitted to experimental data, assist in predicting the unsaturated hydraulic conductivity function. As the direct measurement of unsaturated hydraulic conductivity can be both costly and very time-consuming, these mathematical functions, along with the saturated hydraulic conductivity, can be utilized to predict the unsaturated hydraulic conductivity function (Perkins, 2011).

The van Genuchten (1980) is a very popular method to represent the SWCC (Tuller and Or, 2003). In order to express the unsaturated hydraulic conductivity, the van Genuchten function (1980) is substituted into Mualem's (1976) pore conductivity theory to obtain the van Genuchten-Mualem function (van Genuchten, 1980). Equation 2.4 represents the van Genuchten (1980) function and Equation 2.5 describes the unsaturated hydraulic conductivity based on the van Genuchten-Mualem (VGM) function.

$$Se = \frac{\theta - \theta_r}{\theta_s - \theta_r} = [1 + (\alpha|\psi|)^n]^{-m} \qquad [2.4]$$

$$K = K_s S_e^{\tau} \left[1 - \left(1 - S_e^{\frac{1}{m}}\right)^m\right]^2 \qquad [2.5]$$

where S_e is the effective saturation, θ_r and θ_s are the residual and saturated water contents, respectively, α is a fitting parameter related to the inverse of the air-entry pressure head, n and m are fitting parameters with m = 1-1/n, and τ is the pore size interaction parameter. Mualem (1976) proposed a τ value of 0.5 as an optimal value for many different soil types.

The van Genuchten (1980) model fits well for unimodal pore size distributions, however it is not capable of representing macropores found in some porous media (Dettmann et al. 2014). The SWCC demonstrates a unimodal behaviour when there is a single peak in the SWCC, and a bimodal behaviour when there are two peaks found in the SWCC. Heterogeneous soils that contain larger pores require less suction to decrease the water content, in comparison to soils with smaller pores. For example, if the soil contained clay and sand, the suction required to reduce the water content in the sand is considerably less compared to clay. Thus, a bimodal model may be a better representation of the soil hydraulic properties, if the soil exhibits a bimodal behavior.

For soil media that has a bimodal pore structure, the Durner-Mualem function can be used as a mathematical model (Brunetti et al. 2016). In order to account for the two peaks observed in the bimodal SWCC, the Durner model proposes an equation that uses linear superposition of two or more VGM functions, as presented in Equations 2.6, 2.7 and 2.8 (Liu and Fassman-Beck, 2017). Note that w is taken as a weighting factor.

$$Se = w[1 + (\alpha_1|h|)^{n_1}]^{-m_1} + (1-w)[1 + \alpha_2|h|)^{n_2}]^{-m_2} \quad [2.6]$$

$$K = K_s[wS_{e1} + (1-w)S_{e2}]\tau \frac{w\alpha_1[1 - \left(1 - S_{e1}^{\frac{1}{m_1}}\right)^{m_1} + (1-w)\alpha_2\left[1 - \left(1 - S_{e1}^{\frac{1}{m_2}}\right)^{m_2}\right]^2}{[w\alpha_1 + (1-w)\alpha_2]^2} \quad [2.7]$$

where

$$S_{e1} = [1 + (\alpha_1|h|)^{n_1}]^{-m_1} \quad [2.8]$$

$$S_{e2} = [1 + (\alpha_2|h|)^{n_2}]^{-m_2}$$

Note that the subscripts refer to the combination of two unimodal pore systems in order to represent the bimodal pore structure (Durner, 1994).

Several studies have estimated the unsaturated hydraulic conductivity of engineered media using these analytical functions. Although the VGM function is a popular method used to predict the unsaturated hydraulic conductivity, some studies (Brunetti et al., 2016; Liu and Fassman-Beck, 2017) have reported that a bimodal pore structure gives a better representation of the SWCC for some of the engineered media**.**

2.4.2.1 Prediction of SWCC

Directly measuring the SWCC can be time-consuming and expensive (Wösten et al. 2001). This has led to alternative methods to predict it using routinely measured soil properties. Pedotransfer functions (PTFs) estimate soil hydraulic properties using routinely measured soil properties, such as soil texture, grain size distribution, bulk density, or porosity. Wösten et al. (2001) conducted a thorough review of pedotransfer functions and stated that, three different types of PTF can be distinguished. The first type is predicting hydraulic characteristics based on a soil structure model. These models, also known as physicoempirical models, predict the water retention using physical principles. An example of such a model is from Arya and Paris (1981), whom predicted the SWCC using the particle size distribution due to the similarity in shapes between the SWCC and particle size distribution curves.

Subsequently, the second type of PTF is point prediction of the water retention characteristic (Gupta and Larson, 1979; Rawls et al., 1982). These PTFs are regression equations that predict

specific points of interest along the SWCC. These functions have a general form, as shown in Equation 2.9,

$$\theta_h = a * sand + b * silt + c * clay + d * OM + e * \rho_d + \cdots + x * variableX \qquad [2.9]$$

where θ_h is the water content at the soil water pressure h, OM stands for the organic matter, ρ_d is the dry bulk density, and a, b, c, d, e, and x represent the regression coefficients. Variable X is noted to be any other basic soil property that is easily measurable.

The third type of PTF is the prediction of parameters used to describe the complete hydraulic characteristics (Vereecken et al., 1992; Wösten et al., 1995). Similar to the second type, this third type also utilizes regression models. The difference between this PTF and the second type is that the second type uses point estimation whereas the third uses parametric estimation. Parametric estimations are developed by estimating the parameters of a water retention model, such as van Genuchten (1980) or Brooks and Corey (1964), by fitting it to the data and then relating the parameters to basic soil properties (Merdun, 2006).

A common method to develop a PTF and demonstrate the relationship between the inputs and outputs was the use of regression analysis. Linear regression was used initially in the development of the PTFs (Gupta and Larson, 1979). Later, the PTFs were developed using nonlinear regression models (Rawls and Brakensiek, 1985). However, once large databases of soil properties were available online for use, the amount of PTF inputs became too large to handle (Wösten et al., 2001). Artificial neural networks (ANNs) were introduced as a tool for modelling complex input-output dependencies. The ANN is composed of neurons (or nodes) and various connections between the neurons. The ANN is similar to a black-box approach where the user provides the inputs and the ANN delivers the outputs. The user does not know the internal structure of the model (Singh and Panda, 2015).

Schaap et al. (2001) have developed a computer program named Rosetta which implements five hierarchal PTFs to estimate the van Genuchten (1980) water retention parameters and the saturated hydraulic conductivity. The hierarchal approach refers to the number of inputs the user has to supply. For example, the input data for the first hierarchal model consists of a look-up table for the soil USDA textural class. Whereas the input data for the fifth model includes the percent of sand, silt and clay, the dry bulk density, and the water content at a suction of 33 and 1500 kPa. The dataset in Rosetta contains a large number of soil hydraulic data and corresponding predictive soil properties. In total, 2134 soil samples and 20 574 $\theta(\psi)$ points were inputted into Rosetta (Schaap et al., 2001).

Even though PTFs were originally developed to predict the soil hydraulic properties of natural, native soils, some studies have used PTFs to predict the soil hydraulic properties of LID substrates. For instance, Hilten et al. (2008), Palla et al. (2009), Metselaar (2012), and Castiglia Feitosa and Wilkinson (2016) have estimated the soil hydraulic properties for green roof substrates. For bioretention substrates, He and Davis (2011), Barbu (2013), and Stewart et al. (2017) have estimated the soil hydraulic properties. A majority of these studies use the soil texture class to predict the unsaturated hydraulic properties. Hilten et al. (2008) uses Rosetta to estimate the green roof substrate and Barbu (2013) has applied the physicoempirical method to estimate the bioretention substrate.

2.4.2.2 Plant Available Water and Soilless Substrates

Water exits a substrate by gravitational drainage or evaporation from the soil surface. As the soil dries, larger pores are first emptied while the smaller pores hold on tightly to the capillary water. A day or two after a storm event or irrigation, the substrate is said to be at field capacity (Handreck and Black, 2002). At field capacity, all of the smallest pores and some medium sized pores are still filled with water. The maximum amount of water that a soil can hold onto after gravitational drainage is termed field capacity. As the amount of water continues to reduce, it may reach a

point where plants are unable to extract soil moisture, thereby start wilting. This water content at which plants experience wilting is termed the wilting point.

In literature, the moisture content at field capacity and permanent wilting point are commonly assumed to be at a suction of 33 and 1500 kPa, respectively. The plant available water is taken as the difference between water content at field capacity and the wilting point. However, studies suggest that the use of 1500 kPa for growing media, or soilless substrates, is not a reliable assumption of the permanent wilting point (Stevenson, 1982)

Soilless substrates are commonly used in greenhouse crop production (Choi et al., 2019). Each substrate differs depending on desirable physical and chemical properties required to maximize greenhouse crop production (Asaduzzaman et al., 2015; Choi et al., 2019). Soilless substrates are formulated by mixing organic components such as peat moss, woodchips and bark and inorganic components such as perlite, sand, and pumice (Asaduzzaman et al., 2015; Choi et al., 2019). In order to improve drainage, reduce waterlogging, and allow for oxygen to improve root growth in containers, the soilless substrates are highly porous (Handreck and Black, 2002). For example, studies such as Choi et al. (2019) examine soilless substrates with porosities ranging from 60-85%, thus demonstrating how porous these substrates are. Griffin (2014) notes that green roof substrates are composed of primarily mineral materials therefore are similar to natural soils. However, green roof substrates are also highly porous, they can also be similar to the highly porous soilless substrates.

DeBoodt and Verdonck (1972) proposed specific plant available moisture parameters after examining SWCCs for several different soilless horticultural substrates. These plant specific parameters include easily available water (EAW, 0 to 5kPa) and water buffering capacity (WBC, 5 to 10 kPa). Handreck and Black (2002) defined readily available water (RAW) as a sum of EAW and WBC (0 to 10kPa). As these substrates are porous, the water is held less tightly and therefore require lower suctions to extract (Griffin, 2014).

2.5 Water Balance at the Ground Surface

The ground surface of the LIDs is exposed to atmospheric conditions, and is the boundary between the substrate and the atmosphere. At this boundary, water is exchanged between the ground surface and the atmosphere. Water enters the ground via precipitation, or snow melt, and exits the ground surface through evaporation or transpiration. If the rate of precipitation is more than the infiltration capacity of the soil, water may travel as surface runoff. Impervious surfaces block this natural water exchange between the soil and atmosphere leading to a decrease in ground surface infiltration and increase in stormwater runoff. The addition of LIDs assists in improving the water balance by reducing the percentage of impervious cover and allowing for an increase in infiltration (Figure 2.6). A water balance analysis at the ground surface assists in estimating the pre- and post-development infiltration and run-off conditions. Whether analyzing short-term or long-term climate conditions, the water balance will assist in identifying the performance of various LIDs at the proposed site.

Components of the water balance at ground surface include precipitation (*P*), potential evaporation (*PE*), actual evaporation (*AE*), transpiration (*T*), surface run-off (*RO*), and net infiltration (*NI*). The *NI* refers to the amount of water that enters the soil and can be written as follows:

$$NI = P - AE - RO - T \qquad [2.10]$$

These components will be discussed briefly in the following sections.

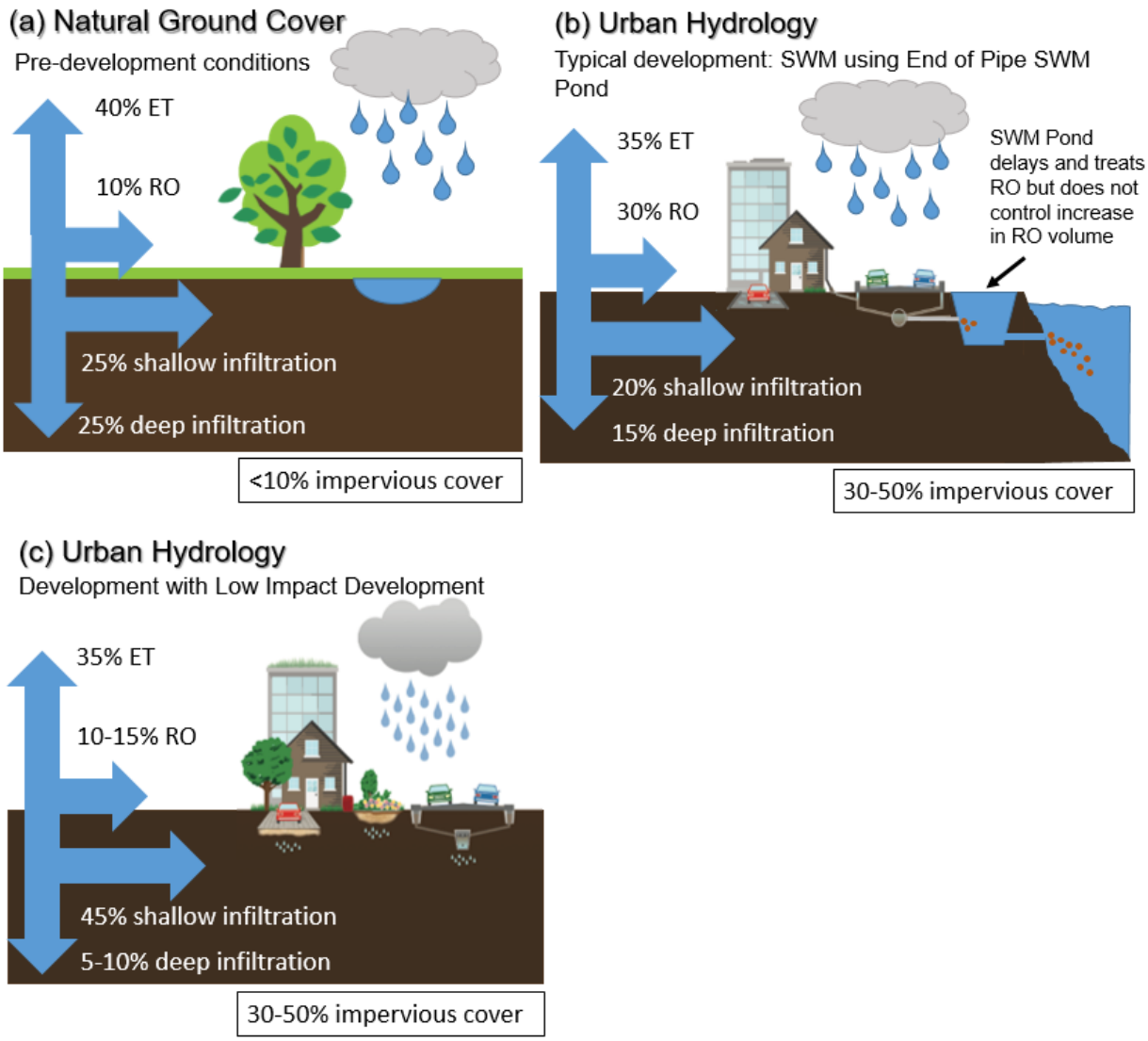

Figure 2.6: Natural versus urban water balance (modified from CVC, 2015)

2.5.1 Potential Evaporation

The potential evaporation (*PE*) refers to the amount of water removed through evaporation if ample water is available at the ground surface. The *PE* is dependent on the net radiation from the sun and the mixing effect of the wind. The *PE* is higher on sunny days as there is a reduced net radiation on cloudy days. Additionally, the *PE* is higher on windy days as the moisture is removed from the ground surface quickly. Other factors such as relative humidity, temperature, wind speed, and available water on the ground surface impact the potential evaporation.

The *PE* can be measured directly using an evaporation pan or can be estimated from measured weather variables. Methods used to estimate *PE* include Thornthwaite (1948), Penman (1948), or Pereira and Pruitt (2004). The Thornthwaite (1948) equation uses the length of daylight hours, mean monthly temperature, and an empirical constant to estimate the *PE*. Due to its simplicity and minimum input requirements, the Thornthwaite (1948) equation is used in numerous applications. However, this equation has been reported to underestimate *PE* under arid conditions (Pruitt, 1964; Pruitt and Doorenbos, 1977; Malek, 1987) and overestimate in certain humid conditions (Camargo et al., 1999). The Thornthwaite (1948) equation for daily *PE* can be written as follows (Fredlund et al. 2012):

$$PE = 0.533\left(\frac{L_d}{12}\right)\left(\frac{N}{30}\right)\left(\frac{10T_d}{I}\right)^{a_t} \quad [2.11]$$

where *PE* is the potential evaporation, L_d is the length of daylight in hours, *N* is the number of days in the month, T_d is the mean monthly air temperature in °C, *I* is the summation for 12 months of the function $(T_d/5)^{1.514}$, and a_t is a complex function of the variable *I* based on correlations to pan evaporation methods. The a_t can be defined as:

$$a_t = (6.75 * 10^{-7})I^3 - (7.71 * 10^{-5})I^2 + (1.79 * 10^{-2})I + 0.492 \quad [2.12]$$

The Penman (1948) equation uses routinely measured weather data, particularly net radiation, relative humidity, air temperature, and wind speed. Although the Penman (1948) equation has performed well for various climates, the need for many input variables limits its widespread use (Pereira and Pruitt, 2004). The Penman (1948) equation can be written as follows (Fredlund et al. 2012):

$$PE = \frac{\Gamma Q_n + \eta E_a}{\Gamma + \eta} \quad [2.13]$$

where Γ is the slope of saturation vapour pressure versus temperature curve, Q_n is the net radiation at the water (or saturated ground) surface, η is the psychrometric constant, and E_a is defined as:

$$E_a = 2.625(1 + 0.146W_w)\left(u_{vo}^{air} - u_v^{air}\right) \quad [2.14]$$

where W_w is the wind speed, u_{vo}^{air} is the vapour pressure in the air above the water (or saturated ground) surface, and u_v^{air} is the saturated vapour pressure at the mean air temperature. The Penman (1948) equation shows that the vapour pressure gradient between the water (or saturated ground) surface and the air above the water becomes the primary driving mechanism for evaporation (Fredlund et al., 2012).

The Pereira and Pruitt (2004) equation is a modified form of the Thornthwaite (1948) equation. Camargo et al. (1999) determined that using an effective temperature rather than an average temperature, the performance of the Thornthwaite (1948) equation improved. The effective temperature (T_{ef}) is described as follows:

$$T_{ef} = \frac{1}{2}k(3T_{max} - T_{min}) \quad [2.15]$$

where T_{max} and T_{min} are the maximum and minimum daily air temperature, respectively, and k is an empirical parameter, recommended as 0.69.

2.5.2 Actual Evaporation

The actual evaporation (*AE*) is the actual quantity of water that evaporates from the ground surface. The actual evaporation is dependent on the prevailing water quantity in the soil near the ground surface and is therefore, in most cases, less than the potential evaporation. The rate of actual evaporation is the same as the potential evaporation when the soil surface is saturated. As net radiation and wind reduce the moisture at the soil surface, the soil dries and holds tightly to

the available water. As the soil dries, there is an increase in soil suction leading to a decrease in evaporation, even if the atmospheric conditions dictate a greater evaporation rate. This reduced evaporation rate is the actual evaporation as it depends on both atmospheric conditions and transient moisture conditions in the soil.

There are various methods to estimate *AE* at ground surfaces (Fredlund et al. 2012). In one of such methods, *AE* is estimated by using a system-dependent atmospheric boundary condition at the top of the modeling domain. The direction and magnitude of the potential flux at the ground surface is dependent on external atmospheric conditions, such as precipitation and evaporation. While the actual flux depends on the external conditions and the soil moisture conditions. Within the context of system dependent boundary, the soil surface boundary condition may change from prescribed flux to prescribed head type condition and vice versa. An example of a system-dependent boundary is when the precipitation exceeds the infiltration capacity of the soil, resulting in either surface runoff or ponding at the surface. For this case, the infiltration capacity of the soil is controlling the infiltration rate into the soil surface rather than the precipitation rate. Similarly, if the potential evaporation rate exceeds the available water quantity at the soil surface, the evaporation rate is reduced to an actual evaporation rate. Both examples demonstrate that the soil moisture capacity controls the quantity of water entering or exiting the system in addition to the atmospheric conditions.

The system dependent atmospheric boundary condition is implemented in HYDRUS (Šimůnek et al. 2008), by using the approach recommended by Neuman et al. (1974). This boundary condition limits the absolute value of the flux such that the following two conditions are satisfied:

$$\left|-K(h)\left(\frac{\partial h}{\partial x}+1\right)\right| \leq E \qquad [2.16]$$

and

$$h_A \leq h \leq h_S \quad [2.17]$$

where E is the maximum potential rate of infiltration or evaporation under the current atmospheric conditions, h is the pressure head at the soil surface, and h_A and h_S are, respectively, the minimum and maximum pressure heads at the soil surface allowed under the prevailing soil conditions. The value for h_S is usually set to zero which would initiate instantaneous surface runoff. If h_S is set to a positive value greater than zero, it represents a layer of ponded water above the soil surface. The minimum pressure head, h_A, can be calculated from the air humidity (H_r) as follows (Šimůnek et al. 2018):

$$h_A = \frac{RT}{Mg} \ln(H_r) \quad [2.18]$$

where M is the molecular weight of water, g is the gravitational acceleration, T is temperature, and R is the gas constant. Feddes et al. (1974) have discussed details of the methods for calculating E and h_A on the basis of atmospheric data.

2.5.3 Surface Runoff

Low impact developments are designed to reduce stormwater runoff at the source. Surface runoff refers to the water that cannot infiltrate the soil during a storm event. This may be due to impervious surfaces or soil with low saturated hydraulic conductivities. With LIDs, the substrate implemented within the system is quite coarse thus allowing for easy water infiltration into the soil and the reduction in flood risk due to surface runoff.

2.5.4 Transpiration

Photosynthesis is a process that uses the radiation from the sun to convert water and carbon dioxide into oxygen and food for the plant. In order for photosynthesis to occur, carbon dioxide must enter the plant leaves through the stomata to reach the chloroplasts. There is a continuous

loss of water from the interior of the leaf through the stomata due to evaporation. As the plant cells must be moist to function, this water must be replenished by plant water uptake through the root system otherwise the plant will wilt (Radcliffe and Šimůnek, 2010).

In Richards' equation, the root water uptake can be considered as a sink term. Feddes et al. (1978) defined the sink term as:

$$S(h) = \beta(h) S_p \qquad [2.19]$$

where *S(h)* is the root water uptake as a function of soil water pressure head (*h*) or the volume of water removed from a unit volume of soil per unit time, S_p is the potential water uptake rate, and *β(h)* is a dimensionless stress response function of the pressure head ($0 \leq \beta \leq 1$).

Feddes et al. (1978) proposed a stress response function, *β(h)*, which is shown in Figure 2.7. For pressure heads greater than h_1, the water uptake is assumed to be zero close to saturation due to the lack of oxygen in the root zone. For pressure heads less than h_4, which is the wilting point pressure head, the water uptake is also zero. As shown in Figure 2.7, the *β* value is equal to one between pressure heads h_2 and h_3. The water uptake is assumed to be optimal between these two pressure heads (Radcliffe and Šimůnek, 2010). Taylor and Ashcroft (1972) and Wesseling et al. (1991) have provided values for various plants that are required for the Feddes et al. (1978) model. HYDRUS contains a database of these suggested values that users may select.

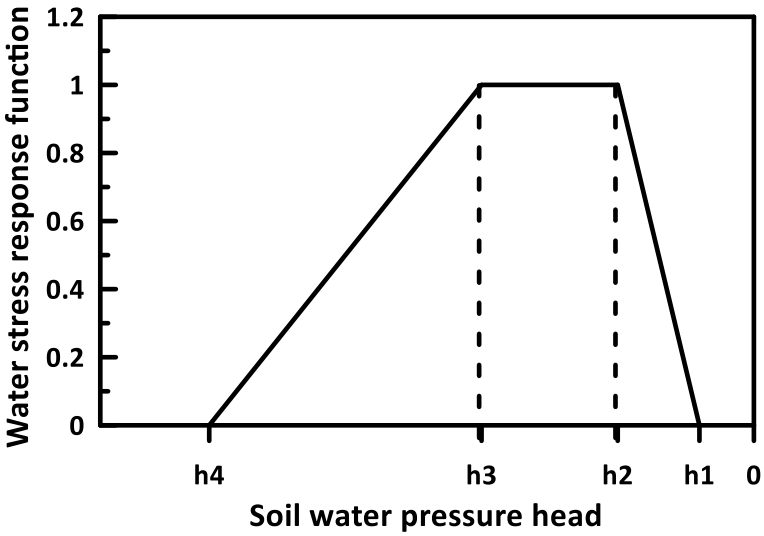

Figure 2.7: Plant water stress response function as used by Feddes et al. (1978). Modified from Radcliffe and Šimůnek (2010)

The local potential root water uptake, S_p, can be calculated from the potential transpiration rate (Brunetti et al., 2016). In order to calculate the potential transpiration rate, Beer's law is used to partition the potential evapotranspiration into potential evaporation and potential transpiration rates as follows (Ritchie, 1972):

$$PT = PET\left(1 - e^{-k*LAI}\right) = PET(SCF) \quad [2.20]$$

$$PE = PET e^{-k*LAI} = PET(1 - SCF) \quad [2.21]$$

where *PT*, *PE* and *PET* are the potential transpiration, evaporation and evapotranspiration fluxes [LT^{-1}], respectively, *LAI* is the leaf area index [-], *SCF* is the soil cover fraction [-], and *k* is the constant governing the radiation extinction by the canopy [-] as a function of sun angle, the distribution of plants, and the arrangement of leaves (between 0.5-0.75).

2.5.4.1 Leaf area index

The *LAI* is a dimensionless quantity that describes the amount of vegetation cover, or foliage, over an area of land. The *LAI* is the surface area of leaves divided by the surface area covered by soil (Fredlund et al. 2012). A large amount of plant cover leads to a higher *LAI*. This means that there is a higher transpiration rate from the plants compared to the evaporation rate from the soil. The *LAI* can be represented as a function of time, as shown in Figure 2.8. During the growing season, there is a greater *LAI* and therefore a higher transpiration rate. During the inactive season, where there is no plant growth, the *LAI* is minimal and most of the evaporation occurs from the soil.

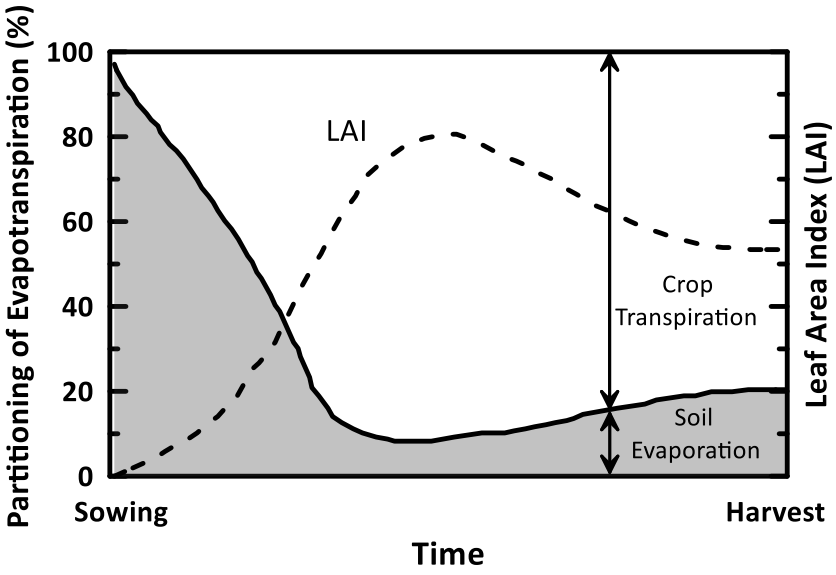

Figure 2.8: Partitioning of evapotranspiration to evaporation and transpiration over a growing period for an annual field crop (modified from Allen et al., 1998)

The Šimůnek et al. (2018) defines three ways on how the *LAI* can be calculated, as shown in Equations 2.22 – 2.24. Equation 2.22 is calculated from the crop height using the equation for grass and Equation 2.23 is calculated from crop height using the equation for alfalfa. Equation 2.24 is calculated from the soil cover fraction (SCF), where a_i is the constant for the radiation extinction by the canopy.

$$LAI = 0.24 * CropHeight \quad [2.22]$$

$$LAI = 1.5 * \log(CropHeight) + 5.5) \quad [2.23]$$

$$LAI = -\frac{1}{a_i}\ln(1 - SCF) \quad [2.24]$$

2.5.4.2 Root Distribution

In order for the plants to evaporate water via transpiration, they require the roots to extract water from the soil. The amount of water extracted is dependent on the distribution and depth of the roots (Fredlund et al., 2012). Roots that are deeper in depth can extract a greater amount of water on a sunny day compared to roots that are closer to the soil surface.

Figure 2.9 illustrates different root distribution functions adopted by researchers (Kumar et al., 2014). For these root distribution functions, the amount of water extracted varies with respect to depth. For instance, the rectangle root shape zone extracts a constant amount of water with depth while the triangular root shape zone extracts less water with depth.

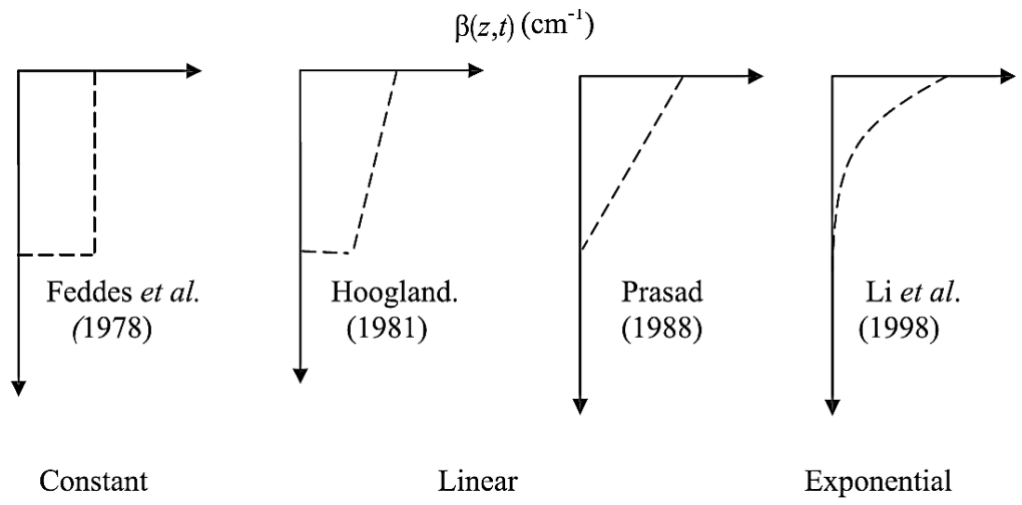

Figure 2.9: Three root distribution functions (retrieved from Kumar et al., 2014)

2.6 Climate Data

2.6.1 Climate Model

With the rapid change in climate, modelling how an engineered structure behaves in the future is a key component for good design, serviceability, and sustainability. Various climate models have been developed in order to predict the future climate under a variety of conditions such as increased green house gas (GHG) emissions. The Atmosphere-Ocean General Circulation Models (GCMs), Earth System Models (ESMs), Earth System Models of Intermediate Capacity (EMICs) and Regional Climate Models (RCMs) are all examples of climate models.

The General Circulation Models are the most commonly used climate models and are the standard climate models assessed in IPCC's Fifth Assessment Report (AR5). The primary function of GCMs is to understand the dynamics of the physical components of the climate system (atmosphere, ocean, land, and sea ice) and make projections based on future greenhouse gas and aerosol forcing (Flato et al., 2013). ESMs expand GCMs to include biogeochemical cycles such as the carbon cycle, the sulphur cycle or ozone (Flato, 2011). EMICs include relevant components of the Earth System Models, but at a lower resolution than the GCMs and ESMs to reduce computational effort. Similarly, RCMs downscale the global model simulations to a regional level to provide detailed climate information for the area of interest (Flato et al., 2013).

2.6.2 Future Emissions

The IPCC recommends that a scenario of future climates can be developed based on several assumptions concerning future GHG emissions. In IPCC's Fifth Assessment Report (AR5), a new scenario approach called representative concentration pathways (RCPs) was proposed. There are four RCPs that extend up to 2100. Each pathway leads to a specific radiative forcing, which the IPCC defined as the change in energy flux caused by a driver and is calculated at the tropopause or at the top of the atmosphere (IPCC, 2014). For RCP 2.6, the radiative forcing peaks at approximately 3W/m^2 before 2100 and then declines. For RCP 4.5 and RCP 6.0, they

are two intermediate stabilization pathways which radiative forcing is stabilized at approximately 4.5 W/m^2 and 6.0 W/m^2 after 2100. Lastly, RCP 8.5 is a high pathway where the radiative forcing reaches greater than 8.5 W/m^2 by 2100 and continues to rise for some amount of time (IPCC, 2014). By the year 2100, RCP 2.6 is considered to be the best-case scenario whereas RCP 8.5 is the worst-case scenario with the greatest concentration of radiative forces.

Chapter 3: Measured versus Predicted Soil Hydraulic Properties

3.1 Introduction

The use of pedotransfer functions are seen as a great advantage since measuring soil water characteristic curves (SWCCs) can be time-consuming and costly. Pedotransfer functions (PTFs) estimate soil hydraulic properties using routinely measured soil properties, such as soil texture, bulk density, particle size distribution, or porosity. By gathering a large quantity of measured soil data, a relationship can be developed to create a PTF.

Historically, PTFs were established with natural, native soil in mind rather than engineered substrates such as Low Impact Development (LID) substrates. Nevertheless, there are some studies that estimate rather than measure the soil hydraulic properties for LID substrates. For example, Hilten et al. (2008), Palla et al. (2009), Metselaar (2012), and Castiglia Feitosa and Wilkinson (2016) have estimated the soil hydraulic properties for green roof substrates. For bioretention substrates, He and Davis (2011), Barbu (2013), and Stewart et al. (2017) have estimated the soil hydraulic properties. A majority of these studies use the soil texture class to predict the unsaturated hydraulic properties. Hilten et al. (2008) used Rosetta Lite DLL (Schaap et al. 2001), an artificial neural network, to estimate the green roof substrate. Barbu (2013) applied the physicoempirical method to estimate the bioretention substrate.

This chapter assesses the performance of PTFs in estimating the soil hydraulic properties of various LID substrates, particularly green roof and bioretention media. The SWCC of five LID substrates, two green roof and three bioretention substrates, were measured using the HYPROP measurement system (UMS, 2015). Laboratory testing included measurement of the organic content (ASTM D2974, 2014), specific gravity (ASTM D854, 2014), particle size distribution using both the sieve test (ASTM D6913, 2017) and hydrometer test (ASTM D7928, 2017), and the saturated hydraulic conductivity using the constant head test (ASTM D5856, 2015). In addition, two published sources, Sandoval et al. (2017) and DelVecchio (2017), contained enough

available information to determine the performance of their substrates as well. Regression models, physicoempirical models, and artificial neural network were the three types of PTFs used to predict the hydraulic properties for the LID substrates. To compare the measured and predicted SWCC, statistical analysis was carried out by calculating the coefficient of determination, mean square deviation, and mean absolute deviation. To confirm the validity of the statistical analysis, a visual examination was also completed. Numerical modelling was carried out using the HYDRUS software (Šimůnek et al. 2008) to evaluate the performance of the predicted hydraulic properties to the measured hydraulic properties. Thirty years of Toronto historic climate data was used in the model.

3.2 Methodology

To illustrate an overview of the tasks that were carried out, Figure 3.1 presents a flow chart of the steps taken. LID substrates were initially provided by local suppliers. Experimental testing was completed to determine the soil and hydraulic properties of the five LID substrates. In addition, the measured soil hydraulic properties for ten LID substrates from published sources were collected. The predicted soil hydraulic properties for the LID substrates were determined using regression models, physicoempirical models, and artificial neural network. Statistical analysis was carried out to evaluate the performance of the predicted hydraulic properties to the measured hydraulic properties. Finally, numerical modelling was completed to further present the performance of predicted to measured hydraulic properties for LID media. This section discusses in detail the steps taken to reach the objective of this research.

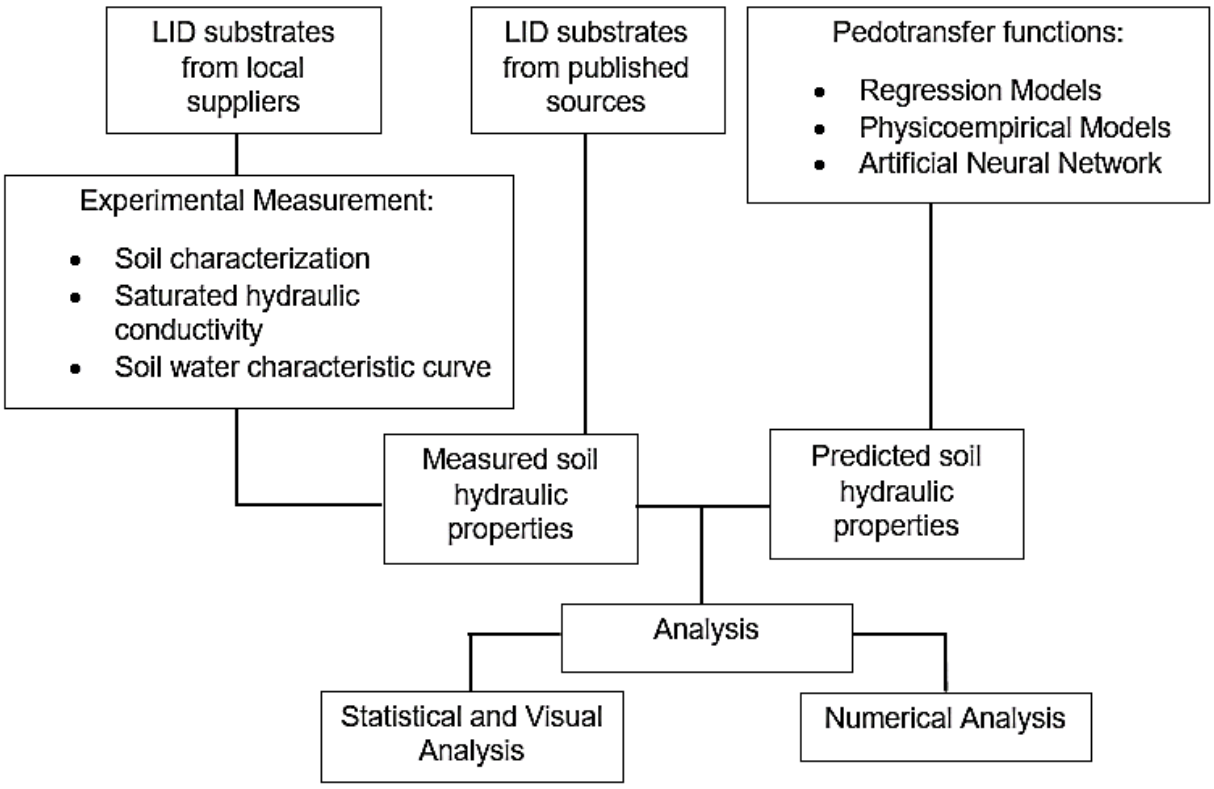

Figure 3.1: Methodology to present measured versus predicted soil hydraulic properties

3.2.1 Measured Soil Properties

3.2.1.1 Materials

The LID media presented in this research were sourced by local suppliers. The two green roof substrates were provided by LiveRoof Ontario and Gro-Bark. Gro-Bark also provided two bioretention substrates, one of which contained glass sand. The third bioretention substrate was provided by EarthCo Soil Mixtures. Overall, two green roof media (GR1, GR2) and three bioretention media (BR1, BR2, BR3) were examined.

3.2.1.2 Preparation

Before conducting any tests, it was necessary to split the soil sample. This assists in reducing any biases that may occur and obtaining an appropriate representation of the sample. In order to split the sample, a splitter was utilized. Furthermore, the LID substrate was oven dried at 65°C for

24 hours, or until the dry weight was stabilized, to determine the dried sample mass (Perelli, 2014). This ensured that the organics within the sample did not burn out.

3.2.1.3 Organic Content

To determine the organic content within the substrate, it is essential to first obtain the dried sample. Once the dried sample is acquired, the organic content was determined by dry combustion. After recording the mass of the dried sample, the sample was placed in a crucible and transferred to a muffler oven set to 550°C for approximately 2 hours (ASTM D2974, 2014; Perelli, 2014). The amount of organics within the sample was determined by taking the difference in mass before and after the dry combustion.

3.2.1.4 Specific Gravity

The specific gravity was determined using the pycnometer method (ASTM D854, 2014). To conduct this test, the mass of the empty pycnometer and the pyncometer filled with de-aired water to the designated fill line were recorded. After drying the pycnometer, approximately 50 g of oven-dried sample was poured into the pycnometer and the mass was noted. Water was added to the pycnometer until it was half filled, and then attached to a vacuum (Figure 3.2a). The sample was agitated by swirling the pycnometer occasionally in order to remove air from the sample. Once no air bubbles are visible within the pycnometer, as shown in Figure 3.2b, de-aired water was added to fill the pycnometer to the designated fill line. The mass and temperature of the filled pycnometer was recorded. Three tests for each LID substrate were conducted to verify that similar results are attainable.

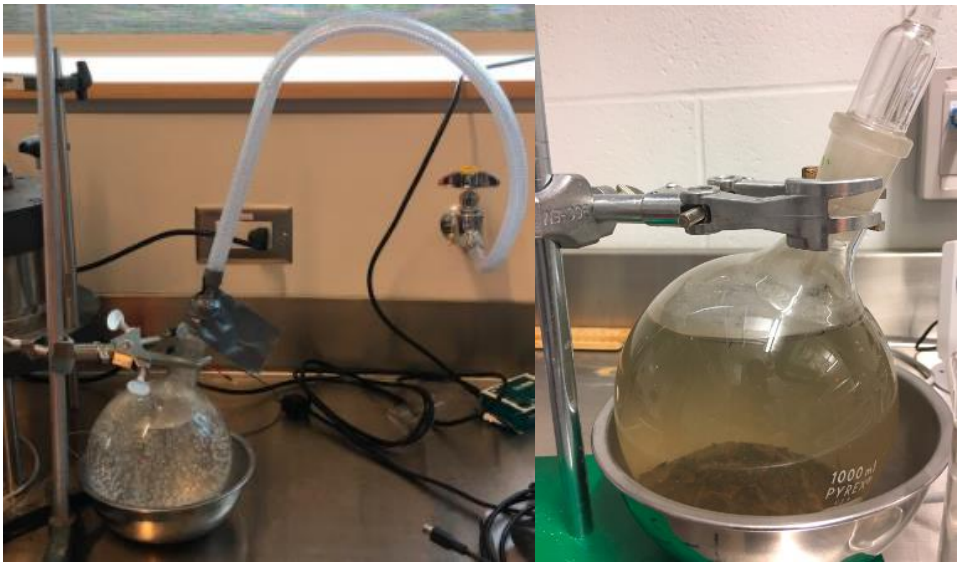

Figure 3.2: Pycnometer (a) attached to a vacuum, (b) with sample and no visible bubbles

3.2.1.5 Particle Size Distribution

In order to accurately classify the soil sample under examination, the particle size distribution (PSD) is required. Obtaining the PSD allows for comparison between samples and the determination of its textural classification through designated standards such as the U.S. Department of Agriculture (USDA) or Unified Soil Classification System (USCS), (Soil Survey Staff, 1981; ASTM D2487, 2017). To achieve an adequate range of the PSD, both the sieve test and hydrometer test were performed. The relevant ASTM designations for these tests are ASTM D6913 (2017) and ASTM D7928 (2017), respectively.

To prepare for the sieve test, approximately 500 g of oven-dried sample was weighed then washed on a No.200 sieve. The sample was washed until the water passing through the sieve was clear. The sample was then placed in the oven at 65°C. The oven-dried mass was noted and then the sample was poured into a stack of descending sieve sizes (Figure 3.3a). The stack of sieves was placed into the sieve shaker for 13 minutes. Before weighing each sieve to obtain the cumulative mass, it was important to shake each sieve by hand. This allowed for any excess sample that was unable to initially pass through the sieve to escape and enter the subsequent

sieve. If it is observed that a large amount of sample is passing through the sieve when shaken by hand, it may be essential to place the stack of sieves back into the sieve shaker. Nevertheless, 13 minutes was determined to be an appropriate time limit that worked well.

The hydrometer test is necessary to accurately determine the distribution of fine particles within the sample. The initial step for this test was to acquire 50-100g of oven-dried sample that has been screened through the No.10 (2 mm) sieve. After pouring the sample into a 250 mL beaker and recording the mass, the sample was mixed with 125 mL of hydrometric liquid, covered, and left to sit for 24 hours. The mixture was then mixed in a mechanical mixture for 2 minutes. Subsequently, the mixed sample was poured into a 1000 mL glass cylinder, filled with distilled water to the fill line, and mixed by hand for approximately one minute. After the completion of hand mixing, the cylinder was placed on a flat, stable surface where it was not disturbed for the duration of the test. After situating the cylinder and carefully placing the hydrometer into the mixture, the stopwatch was started (Figure 3.3b). For the duration of the test, hydrometer and temperature readings were taken at 1, 2, 5, 15, 30, 60, 120, 240, and 1440 minutes.

3.2.1.6 Saturated Hydraulic Conductivity

Initially, a constant head test was conducted following a procedure similar to ASTM D5856 (2015). However, challenges were discovered during the laboratory testing which led to a modified version of the constant head test. A detailed discussion of the methods followed, challenges presented, and solutions determined are presented in Appendix B. Note that a constant head test was selected rather than a falling head test as the material is very coarse. Thus, the speed of the water level within the burette for the falling head test would be too quick to record. The schematic of the constant head test is presented in Figure 3.4. The equipment used for the modified constant head test is presented in Figure 3.5a.

Figure 3.3: Determining the particle size distribution (a) sieve test, (b) hydrometer test

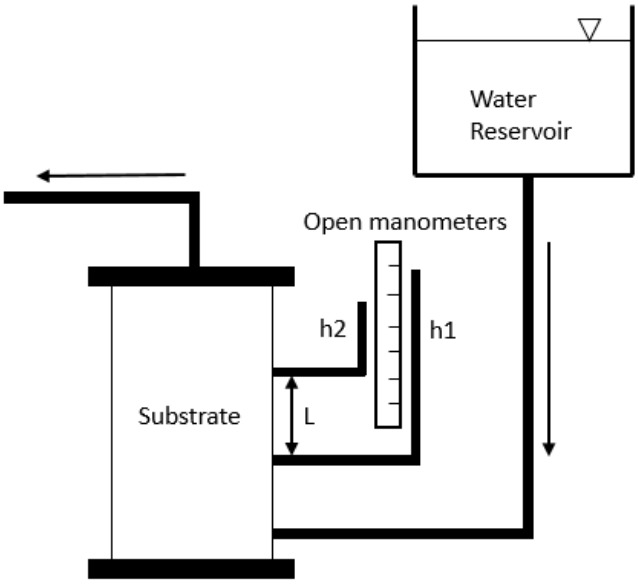

Figure 3.4: Schematic of the constant head test

To determine the saturated hydraulic conductivity, two side ports were installed into a compaction permeameter in order to attach the two open manometer tubes (Figure 3.5b). The height of the compaction permeameter is 18.0 cm and the diameter is 15.2 cm. The distance between the two

side ports is 7 cm. Before testing, it is a good practice to fill the permeameter with water to make sure that there is no leakage. Once it is confirmed that there are no visible signs of leakage, the permeameter was drained and dried, and a metal mesh and geotextile were placed at the bottom of the permeameter.

Each LID media was then packed within the permeameter to the dry bulk density of 1g/cm^3. A dry bulk density of 1g/cm^3 was used as alternative studies have obtained sample cores from live sites and used a dry bulk density of approximately 1g/cm^3 (Griffin, 2014; Perelli, 2014; Liu and Fassman-Beck, 2017; Hill et al., 2016). The oven dried sample was split into four different bowls to help reduce the sample bias. To reduce segregation, water was added so that the sample reached a gravimetric water content of 2%. A packing procedure was adopted to avoid horizontal layering. When packing, the first lift was poured in and gently compacted. The top of the layer was then lightly scraped before pouring in the next lift to avoid horizontal layering of the sample. Once the permeameter was filled, the geotextile and metal mesh were placed at the top and then were sealed with an appropriate cover (Figure 3.5c).

a)  b)  c) 

Figure 3.5: Modified constant head test, (a) geotextile and metal sheet used, (b) two ports installed into compaction permeameter, (c) permeameter filled with green roof substrate

Carbon dioxide was passed though the permeameter to assist in flushing out the air. Once the sample has been flushed with CO_2, the permeameter was attached to a water reservoir and two manometers. In order to reduce air entrapment in the system, de-aired water was used. The saturated hydraulic conductivity was determined by obtaining the volumetric flowrate by maintaining a constant head.

3.2.1.7 Measurement of SWCC using HYPROP

A popular method to measure the SWCC is the simplified evaporation method (Schindler, 1980). To measure the SWCC, the HYPROP measurement system (UMS, 2015) which employs the evaporation method was used (Figure 3.6).

With the exception of the packing procedure, the measurements were made following the procedure as described by the manufacture (UMS, 2015). For sample packing, a procedure similar to the one described for the hydraulic conductivity measurements was used. The sample was packed in three lifts. In order to reduce particle segregation during packing, the sample was wetted to a water content of 2%. The first lift is poured into the silver sample ring that is provided with the HYPROP equipment. The sample is compacted with 10 blows using a round shear box extruder and the side of the sample ring is tapped 5 times. The top of the layer was lightly scraped to avoid horizontal layering. Following a similar procedure, the second lift is poured into the sample ring. For the third lift, the excess sample at the top of the sample ring is scraped off with a straight edge (Figure 3.7a).

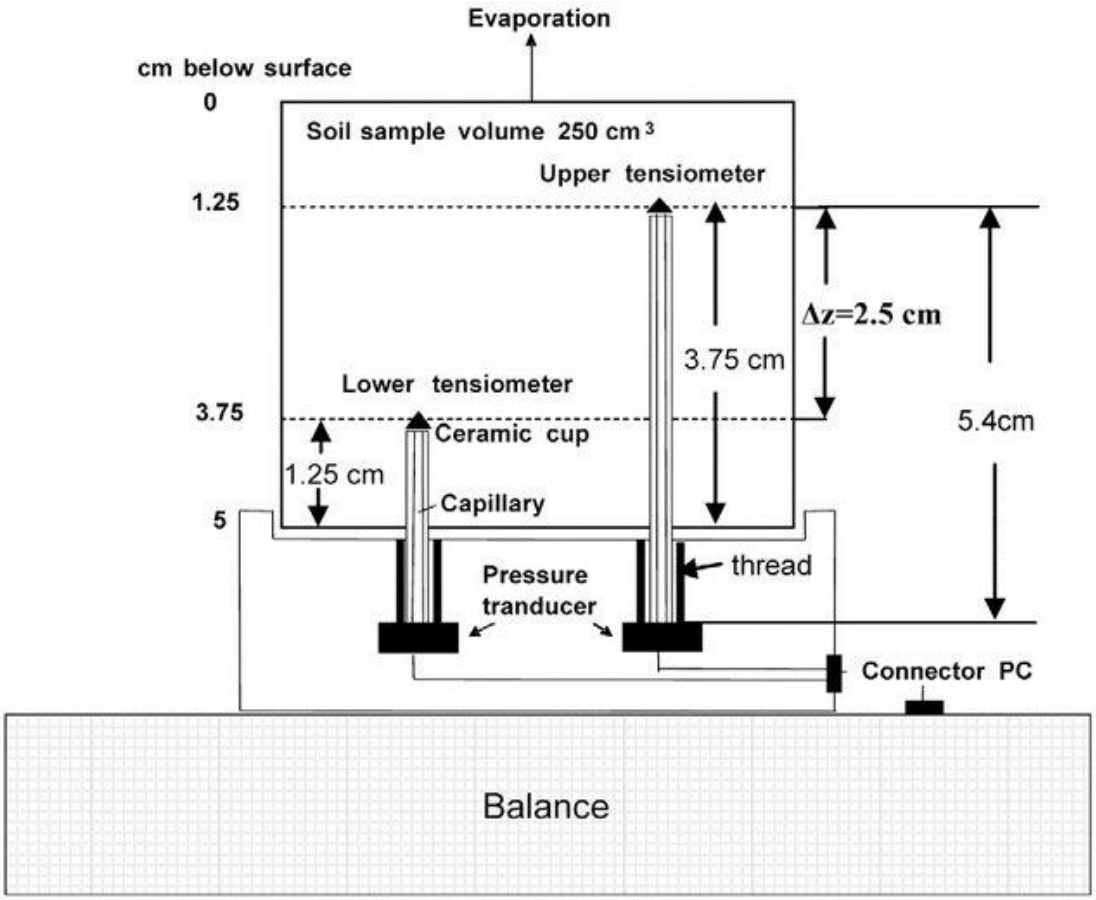

Figure 3.6: HYPROP schematic (retrieved from Bezerra-Coelho et al., 2018)

The nonwoven cloth and saturation plate supplied with the HYPROP equipment is then placed at the top of the sample ring once the packing is completed. The sample ring is flipped upside down and placed within a bowl of de-aired water to be saturated (Figure 3.7b). The plastic lid is kept on to avoid evaporative losses and the sample is left to saturate for at least 24 hours.

Figure 3.7: Sample ring used in HYPROP, (a) packed with BR3 substrate, (b) saturating in water bath

3.2.2 Soil Properties from Published Sources

The five green roof substrates examined by Sandoval et al. (2017) and the five bioretention substrates from DelVecchio (2017) contained enough available information to determine the performance of PTFs for their substrates. However, it is important to note that not all information was available, such as dry bulk density or porosity. Therefore, assumptions were made and are noted accordingly.

The SWCCs from the published data were digitized in order to determine the performance of the PTFs, as shown in Figure 3.8 and Figure 3.9. The soil parameters that are required for the PTFs are shown in Table 3.1 for Sandoval et al. (2017) and DelVecchio (2017). The particle density was not available for DelVecchio (2017) and the initial bulk density for all the soils ranged from 1.2 to 1.4 g/cm^3. Thus, an average of 1.3 g/cm^3 for all substrates from DelVecchio (2017) was used. For the green roof substrates from Sandoval et al. (2017), the compacted dry density and particle density were provided. To calculate the dry bulk density, the following equation was used:

$$\phi = 1 - \frac{\rho_d}{\rho_s} \quad [3.1]$$

where φ is porosity, ρ_d is the dry bulk density and ρ_s is the particle density.

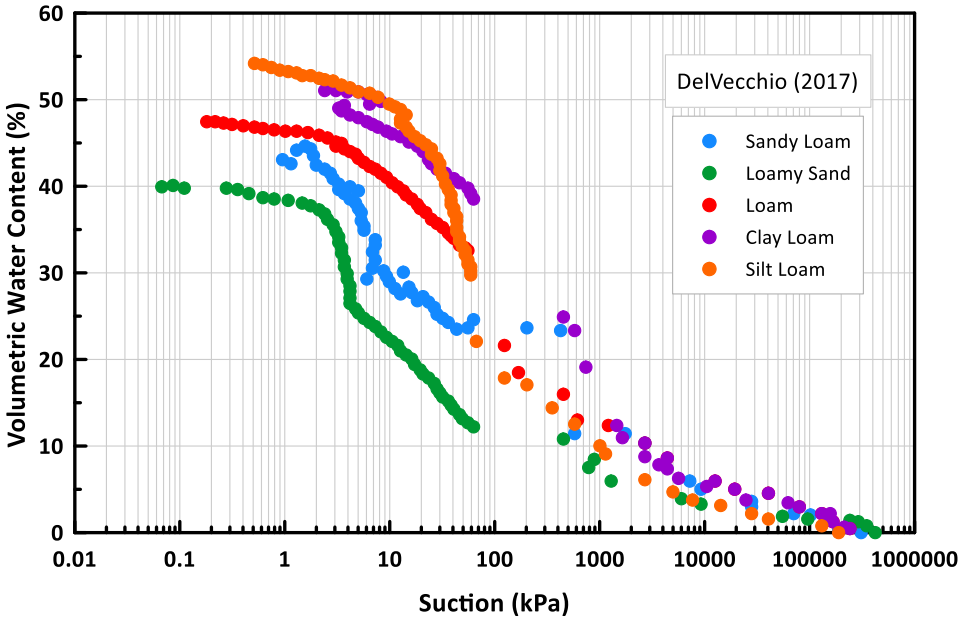

Figure 3.8: Measured SWCCs for bioretention substrates digitized from DelVecchio (2017)

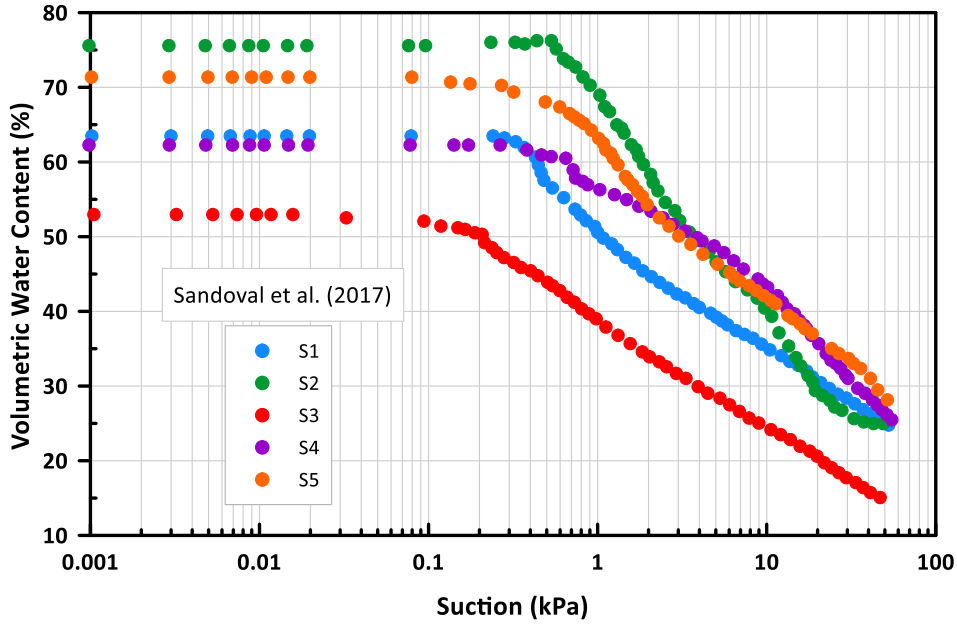

Figure 3.9: Measured SWCCs for green roof substrates, digitized from Sandoval et al. (2017)

Table 3.1: Soil parameter inputs from Sandoval et al. (2017) and DelVecchio (2017)

Source	Media	Sand (%)	Silt (%)	Clay (%)	Organic Content (%)	Dry Bulk Density (g/cm^3)	Particle Density (g/cm^3)
Sandoval et al. (2017) *Green Roof*	S1 – Sand	88.1	8.6	3.3	11.97	0.80	2.2
	S2 – Sandy Loam	65.6	29.2	5.2	30.65	0.51	2.13
	S3 – Loamy Sand	82.8	13.3	3.9	4.14	1.18	2.51
	S4 – Loam	50.7	34.4	14.9	10.24	0.92	2.44
	S5 – Sandy Loam	53.4	37.6	9	35.45	0.65	2.32
DelVecchio (2017) *Bioretention*	Sandy Loam	56	32	12	4.91	1.30	-
	Loamy Sand	80	14	6	3.57	1.30	-
	Loam	37	44	19	5.95	1.30	-
	Clay Loam	26	44	30	3.97	1.30	-
	Silt Loam	29	55	16	4.87	1.30	-

3.2.3 Pedotransfer Functions

In total, 19 different pedotransfer functions were considered for each of the LID substrates. Regression models, physicoempirical models, and the use of the artificial neural network were the three types of PTFs that were used to predict the SWCC. The ability of the PTF to predict the soil hydraulic properties of LID materials was assessed by comparing their predictions to measured hydraulic properties. Statistical analyses were used for these comparisons.

Guber and Pachepsky (2010) have developed a computer program, named CalcPTF, that utilizes regression equations to predict the unsaturated hydraulic properties from routinely measured soil properties. CalcPTF contains numerous PTFs, where some estimate the Brooks and Corey (1964) parameters and the others estimate the van Genuchten (1980) parameters. Table 3.2 provides the details of the soil inputs required for the various PTF in CalcPTF.

Table 3.2: Soil inputs required for selected PTFs in CalcPTF (Guber and Pachepsky, 2010)

#	PTF	Model	Sand	Silt	Clay	Organic Content	Dry Bulk Density
			%	%	%	%	g/cm^3
1	Saxton et al., 1986	BC[1]	+		+		+
2	Campbell and Shiosawa, 1992	BC	+		+		+
3	Rawls and Brakensiek, 1985	BC	+		+		+
4	Williams et al., 1992a	BC	+		+		+
5	Williams et al., 1992b	BC	+		+	+	+
6	Wösten et al., 1999a	VG[2]	+	+	+		
7	Varallyay et al., 1982	VG			+		+
8	Vereecken et al., 1989	VG	+		+	+	+
9	Wösten et al., 1999b	VG		+	+	+	+
10	Tomasella and Hodnett, 1998	WH[3] -> VG		+	+	+	
11	Rawls et al., 1982	WH -> VG	+	+	+	+	+
12	Gupta and Larson, 1979	WH -> VG	+	+	+	+	+
13	Rajkai and Varallyay, 1992	WH -> VG	+		+	+	+
14	Rawls et al., 1983	WH -> VG	+	+	+	+	+

[1]BC – Brooks and Corey (1964) model
[2]VG – van Genuchten (1980) model
[3]WH – water content at fixed capillary pressure

The physicoempirical models utilize the particle size distribution to predict the SWCC as they are based on the similarity of shape. The two physicoempirical models selected to be analyzed for this research are the Arya and Paris (1981) model and the Modified Kovacs Model developed by Aubertin et al., (2003).

Arya and Paris (1981) presented one of the first physicoempirical model and is especially preferred in practice as it works well with various soil types (Fredlund et al., 2012; Barbu, 2013). The Arya-Paris (AP) model divides the particle size distribution curve into fractions, where the larger particle sizes relate to a larger soil water content. The AP model estimates the volumetric water content by estimating the pore volume and determines the soil pressure by converting pore radii using the capillary theory (Arya and Paris, 1981).

The pore volume, V_p (cm^3/g) for the *i*th particle size fraction is estimated using the following equation:

$$V_p = \left(\frac{w_i}{\rho_s}\right) e \qquad [3.2]$$

where w_i is the fraction solid mass from the particle size distribution (g/g), ρ_s is the particle density (g/cm^3), and e is the void ratio. The volumetric water content (θ_i) is determined by multiplying the fraction solid mass by the total porosity, φ (cm^3/cm^3) and a ratio of the measured saturated water content to the theoretical porosity (S_w) as follows:

$$\theta_i = (\phi S_w) \sum_{j=1}^{j=i} w_j, \quad i = 1, 2, \ldots n \qquad [3.3]$$

To satisfy the capillary equation and procure the soil pressure, the pore radii, r_i (cm) is required. Equation 3.4 is used to calculate the pore radius for each particle size fraction. The number of spherical particles, n_i (g^{-1}) is determined using the particle radius, R_i (cm) as shown in Equation

3.5. The scaling parameter (α) is required for soil with non-spherical particles that are arranged randomly.

$$r_i = 0.816 R_i \sqrt{e n_i^{1-\alpha_i}} \quad [3.4]$$

$$n_i = \frac{3 w_i}{4 \pi \rho_s R_i^3} \quad [3.5]$$

Arya et al. (1998) aimed to scale the α parameter by analyzing a large set of measured data for five textural classes. The α parameter is determined using Equations 3.6 and 3.7. The *a* and *b* parameters in Equation 3.7 relate log (N_i) to log(w_i/R_i^3) and differ depending on the textural class, as shown in Table 3.3 (Arya et al., 1998).

$$\alpha_i = \frac{\log(N_i)}{\log n_i} \quad [3.6]$$

$$log N_i = \mathrm{a} + \mathrm{b} \log\left(\frac{w_i}{R_i^3}\right) \quad [3.7]$$

With all the necessary parameters determined, the pressure, *h* (cm water) is obtained using the capillary equation,

$$h_i = \frac{2\gamma \cos \Theta}{\rho_w g \, r_i} \quad [3.8]$$

where γ is the surface tension at the air-water interface (g/s^2), Θ is the contact angle, ρ_w is the density of water (g/cm^3) and *g* is the acceleration due to gravity (cm/s^2).

Table 3.3: Parameters of Eq. 3.7 for five soil textures (retrieved from Arya et al., 1998)

Textural Class	*a*	*b*
Sand	-2.478	1.490
Sandy Loam	-3.398	1.773
Loam	-1.681	1.395
Silt Loam	-2.480	1.353
Clay	-2.600	1.305

The other physicoempirical model analyzed is the Modified Kovacs (MK) Model developed by Aubertin et al., (2003). This model was found to work well with tailing materials, granular and cohesive soils (Fredlund et al., 2012). As the LID material is highly granular, it was of interest to see if this model would work well for LID materials. The major difference between the MK model and the AP model is that the MK model only uses the coefficient of uniformity (C_u) from the particle size distribution, rather than directly using all of the points measured in the PSD.

For this model, both the capillary and adhesive saturation are considered to determine the amount of water held in the soil. To determine the volumetric water content, the degree of saturation (S) is multiplied by the porosity of the soil (φ), as shown in Equation 3.9. Furthermore, Aubertin et al. (2003) defined the degree of saturation in terms of the capillary component (S_c) and the adhesive component (S_a), as shown in Equation 3.9.

$$S = \frac{\theta}{\phi} = S_c + S_a^*(1 - S_C) \quad [3.9]$$

To ensure that the adhesion saturation component does not exceed a value greater than one ($0 \leq S_a^* \leq 1$), the adhesion component S_a^* is expressed as:

$$S_a^* = 1 - \langle 1 - S_a \rangle \quad [3.10]$$

where ‹ › represents the Macauley brackets; for $S_a \geq 1$, $S_a^* = 1$ and for $S_a < 1$, $S_a^* = S_a$.

The capillary and adhesive components are defined with the following equations:

$$S_c = 1 - \left[\left(\frac{h_{c0}}{\psi}\right)^2 + 1\right]^m \exp[-m(h_{c0}\psi)^2] \quad [3.11]$$

$$S_a = a_c \left(1 - \frac{\ln\left(1 + \frac{\psi}{\psi_r}\right)}{\ln\left(1 + \frac{\psi_o}{\psi_r}\right)}\right) \frac{(h_{c0})^{\frac{2}{3}}}{e^{\frac{1}{3}}(\psi)^{\frac{1}{6}}} \quad [3.12]$$

where h_{c0} is the equivalent capillary height which is related to an equivalent pore diameter and the solid surface area; ψ is the suction head (cm); m is the pore-seize coefficient (unitless); a_c is the adhesion coefficient (unitless); e is the void ratio; and ψ_o is the suction head equal to 10^7 cm of water corresponding to dry soil conditions.

As the soil is granular, h_{c0}, ψ_r, and m are obtained using Equations 3.13 – 3.15. The adhesion coefficient (a_c) is taken as 0.01.

$$h_{c0}(cm) = \frac{0.75}{[1.17\log(C_u) + 1]eD_{10}} \quad [3.13]$$

$$\psi_r(cm) = 0.86h_{c0}^{1.2} \quad [3.14]$$

$$m = \frac{1}{C_u} \quad [3.15]$$

Where D_{10} is the diameter corresponding to 10% passing on the particle size distribution and C_u is the coefficient of uniformity, defined as the ratio of the diameter corresponding to 60% passing on the particle size distribution and D_{10}.

The third PTF type analyzed uses neural network predictions. Rosetta Lite DLL (Dynamically Linked Library) is included within the HYDRUS software (Šimůnek et al., 2008) to help predict the van Genuchten (1980) parameters and saturated hydraulic conductivity (Schaap et al. 2001). Rosetta contains five models where the inputs depend on the data availability. The first model consists of a look up table for the textural class of the soil media being analyzed. The other four models use the percentage of sand, silt and clay (SSC) along with additional inputs such as the dry bulk density (BD), the water content at 33 kPa and 1500 kPa suction values.

3.2.4 Statistical Analysis

The measured and predicted SWCC are compared using statistical analysis and through visual inspection. To confirm the validity of the statistical analysis, a visual inspection of the predicted to the measured data should be completed (Schunn and Wallach, 2005). To determine how well the trend in the data fit, the coefficient of determination (R^2) is calculated. Obtaining a R^2 of 1 refers to 100% of the predicted data matches the trend of the measured data. Nevertheless, a R^2 of 1 does not necessarily mean the predicted data matches the measured data. Thus, to determine the deviation from the actual value of the measured data, both the mean square deviation (MSD) and the mean absolute deviation (MAD) are estimated. Lower MSD and MAD values indicate less deviation between the predicted and the measured data points. The R^2, MSD and MAD are calculated as follows:

$$R^2 = \left[\frac{n \sum_{i=0}^{n} \left(\theta_m \theta_p\right)_i - \sum_{i=0}^{n} (\theta_m)_i \sum_{i=0}^{n} \left(\theta_p\right)_i}{\sqrt{\left\{ n \sum_{i=0}^{n} (\theta_m)_i^2 - \left[\sum_{i=0}^{n} (\theta_m)_i\right]^2 \right\} \left\{ n \sum_{i=0}^{n} (\theta_p)_i^2 - \left[\sum_{i=0}^{n} (\theta_p)_i\right]^2 \right\}}} \right]^2 \quad [3.16]$$

$$MSD = \frac{\sum_{i=1}^{n}[(\theta_p)_i - (\theta_m)_i]^2}{n-2} \quad [3.17]$$

$$MAD = \frac{\sum_{i=0}^{n} Abs[(\theta_p)_i - (\theta_m)_i]}{n} \quad [3.18]$$

where n is the number of data points, θ_m and θ_p are the measured and predicted volumetric water content, respectively. The difference between the MSD and MAD measure of goodness-of-fit is that the MSD squares the deviation, thus placing emphasis on points that do not fit the measure data well in comparison to points that do fit well. The MAD estimation is a more simplistic approach that puts equal weight on all deviations and is therefore suitable for relatively noise-free data.

3.2.5 Numerical Analysis

The HYDRUS 1D software (Šimůnek et al. 2008) was used to evaluate the performance of the hydraulic properties from PTFs to the measured hydraulic properties. HYDRUS is a modelling software used in the analysis of water flow and solute transport in variably saturated soils. Brunetti et al. (2017), Liu and Fassman-Beck (2017), Meng et al. (2014), Qin et al. (2016) and Stewart et al. (2017) have demonstrated that HYDRUS model presents good accuracy in producing the hydraulic response of the LID systems. In order to set-up the numerical model, the material properties, climate data, geometry, initial conditions and boundary conditions are required. The material properties used for the analysis are the measured soil properties and the predicted van Genuchten (1980) parameters from the four types of PTFs analyzed.

The models for the bioretention media were simulated with a 100 cm deep soil profile. A 15 cm soil profile was simulated for the green roof substrates, which corresponds to an extensive green roof (CVC and TRCA, 2011). The lower boundary condition was set to free drainage. The upper boundary condition was set to atmospheric boundary condition with a surface layer. Thirty years of daily records of precipitation and potential evaporation values for Toronto constituted the atmospheric boundary. Toronto historical climate data between 1981 to 2010 was collected from

Environment and Climate Change Canada portal (Environment and Climate Change Canada 2018). In total, 8250 active days were modelled, where the active period represents the time when the ground is thawed thus allowing water to infiltrate into the soil. The inactive period is when the ground is frozen and the precipitation is in the form of snow.

The allowable ponding was taken as zero for the green roof. On the other hand, bioretention are designed for ponded conditions as they cater to a greater catchment area in addition to precipitation that directly infiltrates the system. According to Credit Valley Conservation and Toronto and Region Conservation Authority (2011), the maximum ponding depth should be between 15-25 cm. Therefore, the allowable surface ponding was set to 20 cm in the models that were representative of bioretention facilities.

The amount of stormwater runoff is dependent on the catchment area and degree of imperviousness of the area for the bioretention system (Khan et al. 2013). A ratio known as the Impervious to Pervious ratio (I/P) combines these two factors in the following relationship:

$$V_i = dA_B\left(\frac{I}{P} + 1\right) \quad [3.19]$$

where V_i is the volume of the influent, d is the precipitation depth, and A_B is the area of the bioretention system. As HYDRUS 1D treats additional precipitation in units of depth rather than volume, the equation can be rewritten as follows (House et al., 2017):

$$d_i = d\left(\frac{I}{P} + 1\right) \quad [3.20]$$

where d_i is the depth of the influent. If the percentage of the catchment area was 10% and the percentage of impervious area was 60%, the I/P ratio would be 6. This would result in a depth of influent 7 times greater than the precipitation depth. It is suggested that the bioretention system should have an I/P ratio of 5 to 20 (CVC and TRCA, 2010). An I/P ratio of 6 is used for this research for the bioretention systems. For the green roof system, there is no additional stormwater

entering the system other than the precipitation directly entering the system. Therefore, the green roof system would have an I/P ratio of 0.

An initial condition of -100 cm of head was assumed for the column. As the simulations were carried out using thirty years of climate data, the initial conditions do not greatly impact the overall results over the long term. Running the thirty years of data, then applying the final conditions as the new initial conditions did not impact the overall results from the numerical simulations.

3.3 Experimental Results

3.3.1 Soil Characterization

The five LID materials were characterized by measuring their physical properties. The five substrates are shown in Figure 3.10. Visual inspection indicated that the green roof materials were coarser in comparison to the bioretention materials. The bioretention materials have a more uniform appearance with sand and wood chips being the most distinct constituents. Furthermore, the glass sand substrate (BR3) had a very strong odor indicating a large organic content.

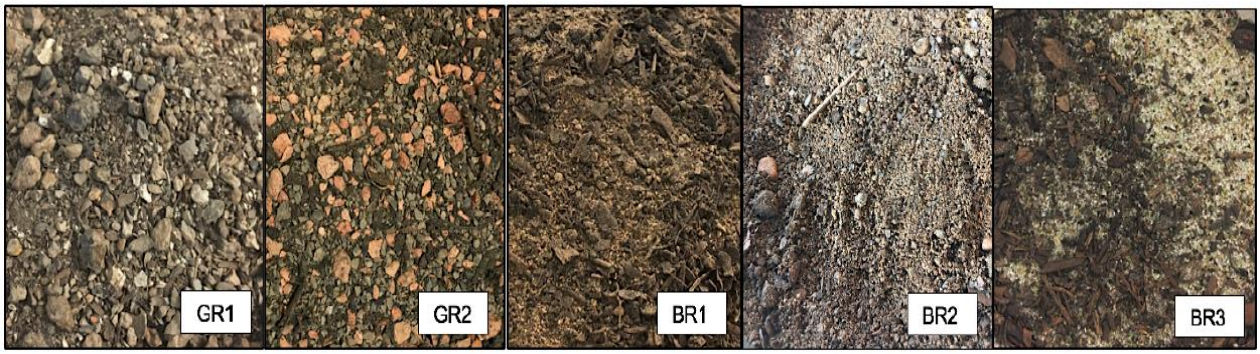

Figure 3.10: Two green roof and three bioretention substrates examined

There is an evident colour change in all of the LID substrates after dry combustion, as shown in Figure 3.11. It is clear that the wood chips are one distinct constituent within the substrate that burns up after the dry combustion. Table 3.4 shows the organic content and the specific gravity

values for all materials. The organic content of the materials ranges between 5 to 8%, with the glass sand substrate containing the greatest percentage. The addition of organic material acts as a lightweight component and is beneficial in decreasing the load on the green roof (Sandoval et al. 2017). Moreover, the organic material provides a large water storage volume (Li and Babcock, 2015) and helps deliver nutrients for plant growth (Sandoval et al. 2017). As the glass in the glass sand substrate may not contain the required nutrients, an increased percentage of organic material may assist in promoting the plant life. Furthermore, it was noted that the addition of organic material also assists in the reduction of the soil density (Sandoval et al. 2017). As shown in Table 3.4, the specific gravities of the green roof media are smaller compared to the bioretention media.

(a)  (b)  (c) 

Figure 3.11: Determining the organic content (a) BR1 before and after dry combustion, (b) BR3 before dry combustion, (c) BR3 after dry combustion

Table 3.4: Organic content and specific gravity of the five tested LID substrates

LID Substrate	Organic Content (%)	Specific Gravity
GR1	7.03	2.02
GR2	5.16	2.24
BR1	5.06	2.80
BR2	6.8	2.70
BR3	7.81	2.36

The particle size distributions (PSD) of all five substrates are shown in Figure 3.12 and further summarized in Table 3.5. From the PSD, both green roof media contains a large percentage of gravel (>2mm) in comparison to the bioretention media, which is consistent with the visual inspection done initially. The bioretention materials also contain a large percentage of sand (0.05 – 2 mm), with BR3 having 97% sand. All of the substrates analyzed were quite coarse and are expected to have high saturated hydraulic conductivity values leading to good drainage during flooding conditions.

Furthermore, both of the green roof materials had a large coefficient of uniformity (C_u), thus demonstrating that they are well-graded materials that contains a wide assortment of particle sizes. On the other hand, the bioretention materials have a C_u of 3, demonstrating that they contain particles of uniform size and have a steep gradation slope.

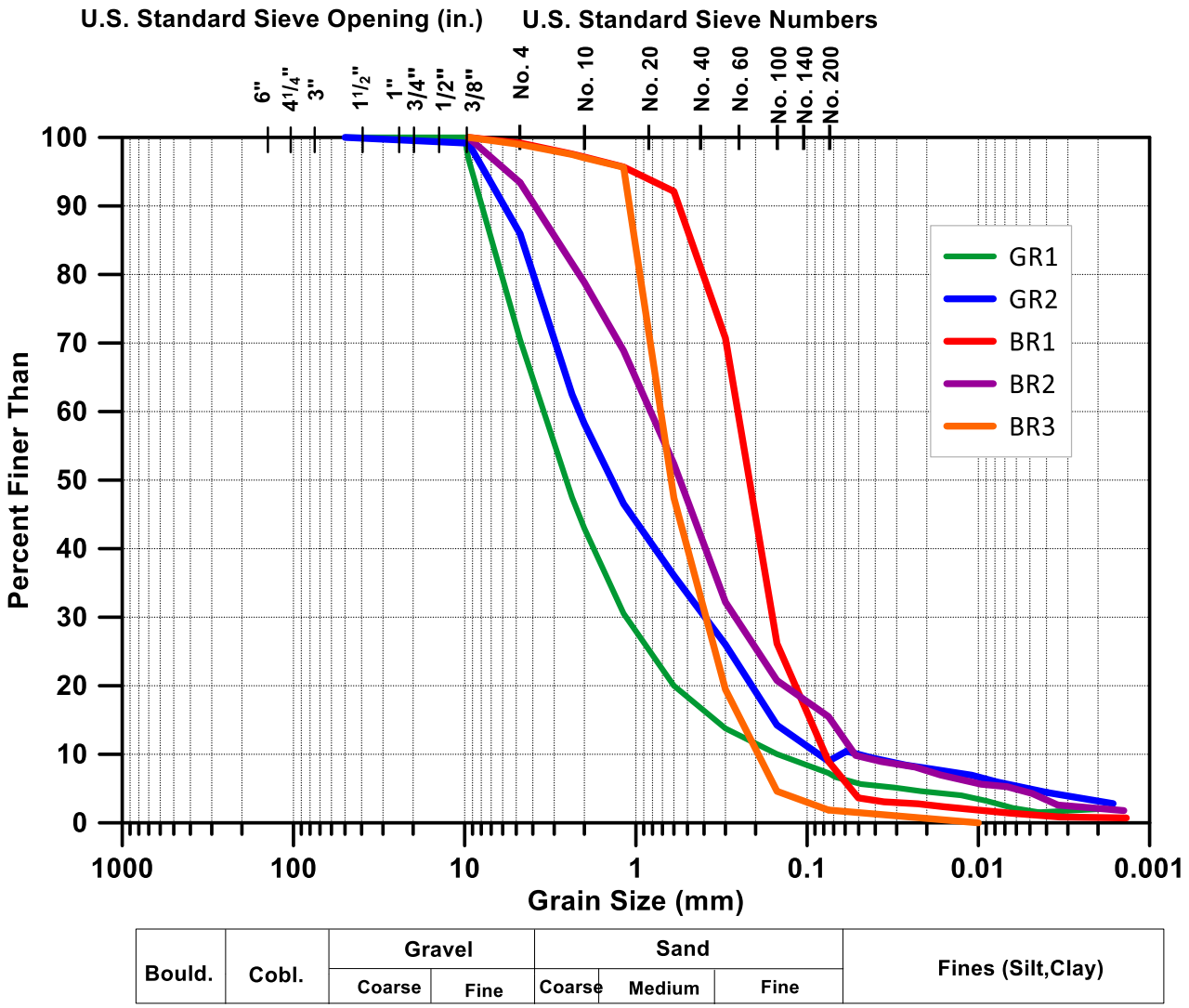

Figure 3.12: Particle size distribution curve of the five measured LID substrates

Table 3.5: Key features of the particle size distribution curve for the 5 LID substrates

	GR1	**GR2**	**BR1**	**BR2**	**BR3**
D_{10} (mm)	0.15	0.08	0.08	0.08	0.21
D_{60} (mm)	3.5	2.2	0.25	0.25	0.73
D_{30} (mm)	1.15	0.4	0.16	0.16	0.41
Coefficient of uniformity $C_u = \frac{D_{60}}{D_{10}}$	23.3	27.5	3.13	3.13	3.48
Coefficient of curvature $C_c = \frac{D_{30}^2}{D_{60}D_{10}}$	2.52	0.91	1.28	1.28	1.10
% Gravel *(d > 2 mm)*	57.1	41.8	2.86	21.2	2.98
% Sand *(0.05mm < d < 2mm)*	37.0	48.2	93.6	69.2	97.0
% Silt *(0.002mm < d< 0.05mm)*	4.00	6.50	3.00	6.70	0
% Clay *(d < 0.002mm)*	2.00	3.50	0.50	3.00	0

Subsequently, the substrates were further classified according to USDA and USCS using the data from the particle size distribution, as shown in Table 3.6.

Table 3.6: Textural classification according to USCS and USDA

LID Substrate	USCS	USDA
GR1	Well-graded sand with silt and gravel (SW-SM)	Very gravelly loamy sand
GR2	Well-graded sand with silt (SW-SM)	Gravelly loamy sand
BR1	Poorly graded sand with silt (SP-SM)	Sand
BR2	Silty sand (SM)	Gravelly sand
BR3	Poorly graded sand (SP)	Sand

Averaged saturated hydraulic conductivities (K_s) for the five LID media as well as the error bars are shown in Figure 3.13. Overall, the K_s measured for the green roof materials is one order of magnitude higher than the bioretention materials. These results are consistent with the PSD, which indicated that the green roof materials are coarser compared to the bioretention materials.

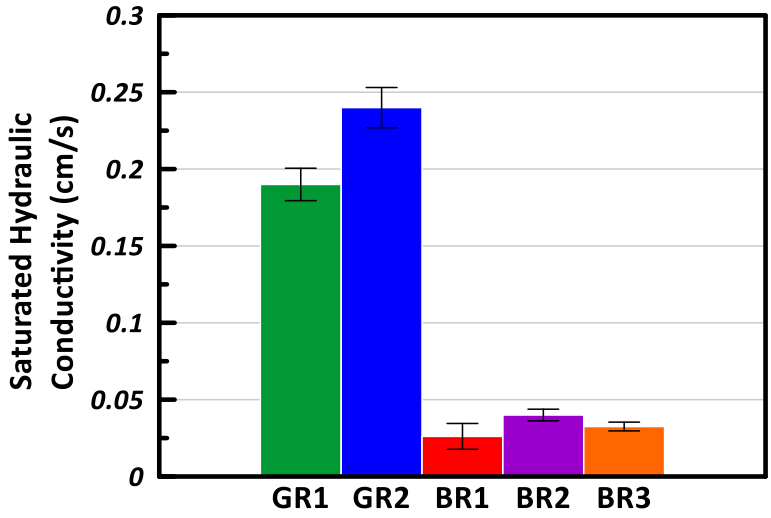

Figure 3.13: Averaged saturated hydraulic conductivity values with error bars

GR1 has a greater percentage of gravel in comparison to GR2, resulting in slightly higher K_s due to the increased void space to assist in water mobility. On the other hand, the bioretention media is designed to undergo ponding and assist in the reduction of storm water pollutants in addition to flood prevention. Thus, to capture the contaminants whether through sorption, volatilization, or filtration, a lower K_s in comparison to the green roof media is preferred (Pitt et al. 1999).

3.3.2 SWCC Results

The SWCC for the five LID materials were measured using HYPROP and are illustrated in Figure 3.14. The fitted van Genuchten (1980) parameters to the measured SWCC data are presented in Table 3.7. Figure 3.15 demonstrate how good the fit is between the experimental values and fitted curved using van Genuchten (1980) equation. Overall, the van Genuchten (1980) demonstrates a good fit to the measured SWCCs for the five LID substrates as shown in Figure 3.15.

The air entry value (AEV) is when air first enters the saturated soil. From Figure 3.14, it can be observed that BR1 and BR3 have a larger AEV compared to the other substrates. From Table 3.7, the α parameter in the van Genuchten (1980) equation is roughly equal to the inverse of the AEV. The α parameter is smaller for the bioretention materials in comparison to the green roof materials, with the exception of BR2.

The *n* parameter presented in Table 3.7 correlates with the pore size distribution. A high *n* value signifies a narrow pore size distribution, leading to a steeper SWCC as the water content drains over a narrow suction range. As observed in Figure 3.14, both BR1 and BR3 have steep curves, thus a greater *n* value. Note that BR1 and BR3 are also classified as poorly graded according to the soil classification using USCS. The green roof substrates have a smaller *n* value which allows the system to retain water over a greater suction range. Both green roof substrates are classified as well-graded according to the USCS soil classification.

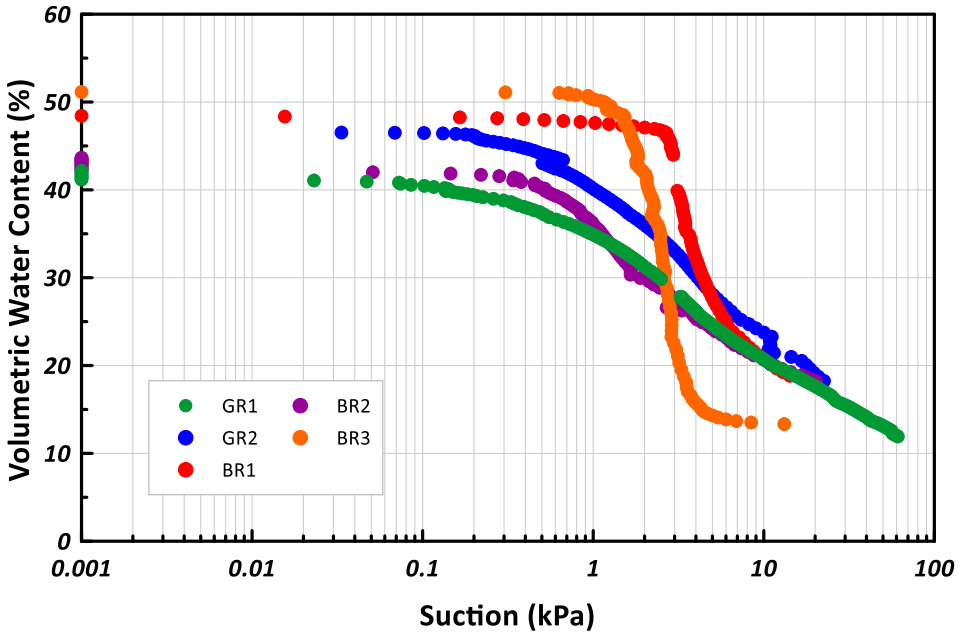

Figure 3.14: Soil water characteristic curve (SWCC) for the five measured substrates

Table 3.7: Fitted van Genuchten parameters

Media	θ_s (cm^3/cm^3)	θ_r (cm^3/cm^3)	α (1/cm)	n
GR1	0.43	0	0.24	1.21
GR2	0.47	0	0.09	1.31
BR1	0.49	0.21	0.03	5.23
BR2	0.43	0.16	0.11	1.73
BR3	0.50	0.13	0.04	5.75

From the SWCC, it can be seen that the measured points end at a suction value less than 100kPa. For example, for BR3, the HYPROP system stopped measuring at a suction value of approximately 13 kPa and a volumetric water content of 13 %. At this point, there is limited water available within the substrate leading to the end of the experiment. As the suction value for permanent wilting is typically considered to be 1500kPa, this suction value of 10kPa is quite less in comparison. However, Handreck and Black (2002) reported the suction value for unavailable

water for soilless horticultural substrates as 10kPa. Arguedas-Rodriguez (2009) conducted a study for soilless substrates, where the SWCC was measured using the tension table method with a 5 cm column. It was noted that there was a sharp decrease in water content with increasing suction between 1.25 to 10.25 kPa. At a suction greater than 10.25kPa, the curve became nearly asymptotic, meaning the remaining water within the substrate was tightly bound thus unavailable for plant uptake. Similarly, Griffin (2014) measured the SWCC for green roof substrate using the HYPROP equipment. Cavitation occurred at a suction of approximately 30kPa and a volumetric water content of approximately 18 % for the substrates analyzed by Griffin (2014).

To confirm that the SWCC is nearly asymptotic after a suction value of 10kPa, the water contents at greater suction values need to be measured. Griffin (2014) noted that the possibility of early cavitation is due to the porosity of the LID substrates. As the sample dries at the top due to evaporation, there is also macropore drainage occurring below the tensiometers due to the substrate's high porosity. This leads to the tensiometers drying faster and therefore cavitating early. Griffin (2014) had allowed the sample core to drain for 10 minutes before installing it into the HYPROP apparatus. This would empty the macropores, thereby allowing for water flow within the substrate. Although the substrate core was installed into the HYPROP apparatus immediately after the water bath, it is possible that some of the water drained out of the macropores when transferring the core to the apparatus. This may be the reason as to why the saturated water content is not equal to the porosity. Further examination is required.

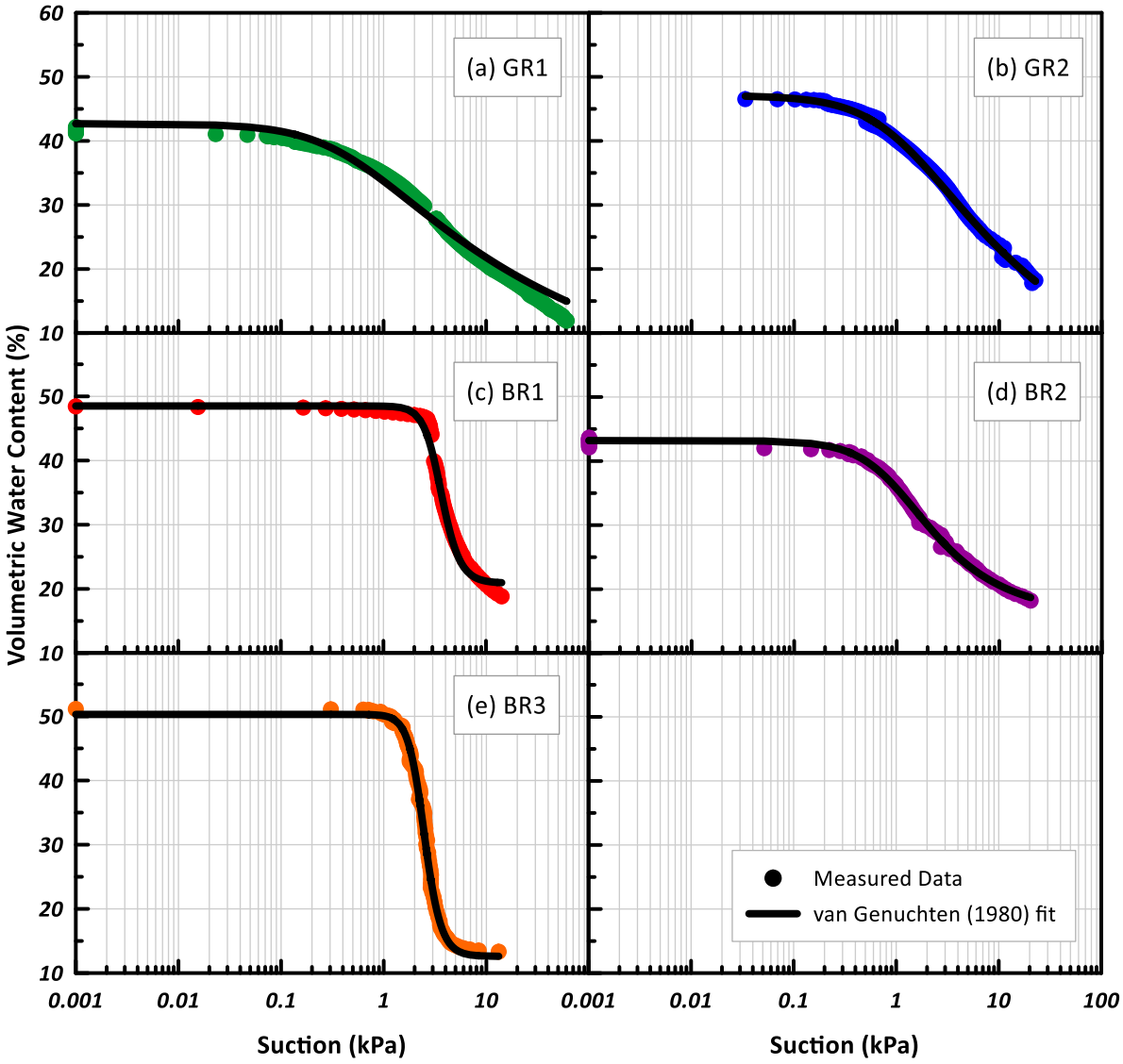

Figure 3.15: Fitted van Genuchten (1980) curves to experimental curves for five LID substrates

Liu (2016) and DelVecchio (2017) measured the SWCC at suction values greater than 100 kPa for LID substrates. Liu (2016) used the tension plate method and pressure extractor method to measure the SWCCs for both green roof and bioretention materials. The pressure extractor suction ranged between 10 – 1500 kPa. Interestingly enough, at a suction value between 10 to 100 kPa, some of the substrates analyzed by Liu (2016) have a water content of equal value, and there is no decrease in water content. However, with a suction greater than 100 kPa, the water

content reduces. This results in a SWCC that exhibits a bimodal behaviour. On the other hand, the study by DelVecchio (2017) measured bioretention substrates using both the HYPROP measurement system and WP4C Dew Point PotentiaMeter. The HYPROP data is shown to end at 60 kPa and the WP4C was used to measure the volumetric water content at suction ranges greater than 100 kPa. Similar to Liu (2016), the measured SWCC exhibited a bimodal behaviour for some bioretention substrates at a suction value greater than 100 kPa.

Therefore, it is possible that there will be a decrease in water content at a suction value greater than 100kPa for the five LID substrates analyzed, especially since the water content of the measured SWCC ends at a volumetric water content slightly greater than 10% (Figure 3.14). To know for certain and fully understand the available water, equipment such as the WP4C, Tempe cells, or pressure plate extractor would need to be used to measure the water content at a greater suction range.

3.4 Performance of PTFs to Measured LID Substrates

To compare the performance of various PTFs to the measured SWCC, the R^2, MSD and MAD values were calculated. As it can be difficult to analyze the large amount of data from the R^2, MSD, and MAD values in a tabular format, Figure 3.16 presents a scatterplot of the computed R^2, MSD, and MAD values for the green roof and bioretention substrates. The scatterplots shown in Figure 3.16 have equal scales to compare the bioretention and green roof substrates. From Figure 3.16, it can be observed that the trend relative magnitudes are captured well for both green roof substrates in comparison to the bioretention substrates. On average, both green roof substrates have an R^2 value greater than 0.90. Whereas the bioretention substrates have low R^2 values, in some cases reaching a low R^2 value of 0.30. In addition, the predicted SWCCs for the green roof substrates estimate a lower deviation from the measured SWCC in comparison to the bioretention substrates. Whereas the bioretention substrates present large deviations from the measured data compared to the green roof substrates. The MSD value for the green roof substrates, on average,

have a value less than 4. Whereas some bioretention substrates reach an MSD value of 10. Some bioretention substrates have MAD values of approximately 0.5, which means that the predicted model is off by 0.5% volumetric water content from the measured data on average. A visual examination is required to assess where the fit is most problematic.

After examining the statistical analysis of the predicted to the measured SWCC, it was concluded that some of the PTF methods work better for certain substrates compared to the others. In general, the PTFs from the CalcPTF program and from Rosetta better predicted the green roof materials measured for this research in comparison to the bioretention materials. On the other hand, the AP method performs relatively well for the bioretention materials. Overall, the MK model is observed to do poorly for all substrates considered in this research. Upon closer investigation, it can be concluded that CalcPTF and Rosetta show poor performance for materials that contain the larger percentage of sand. This leads one to the conclude that, for the most part, PTFs performance is largely dependent on the percentage of the certain particle sizes. Nevertheless, it is important to note that both the CalcPTF program and Rosetta do not take into consideration the percentage of gravel within the substrate.

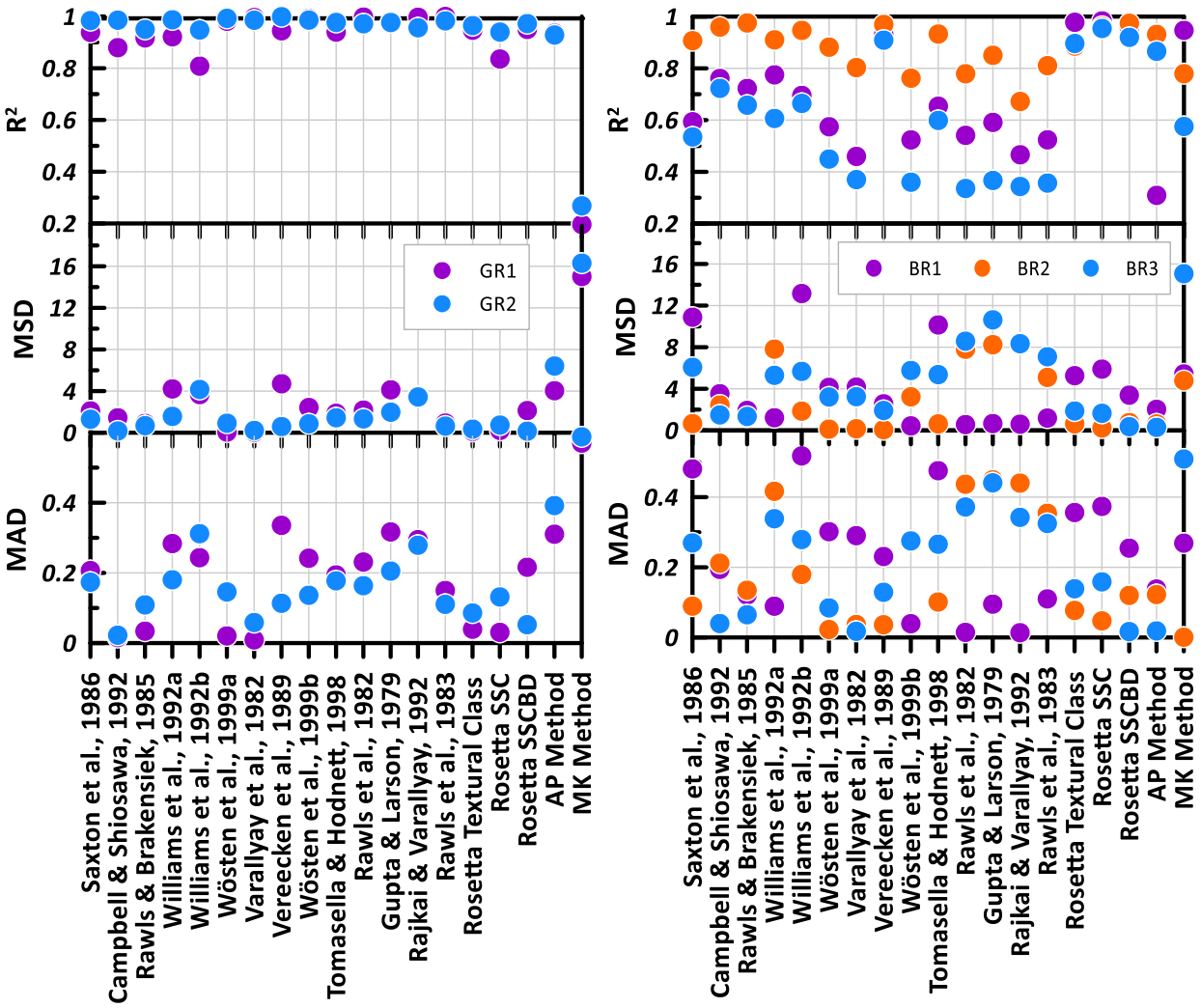

Figure 3.16: Statistical evaluation of the green roof substrates and bioretention substrates.

3.4.1 Visual Examination of the LID Substrates

Visual inspection of the measured and predicted SWCCs was carried out in order to determine an estimate that which core feature of the SWCC is not predicted well. The core features of the SWCC include the saturated and residual water contents, air entry value (AEV), and pore size distribution. The AEV is the suction value at which air first enters the saturated soil resulting in the start of desaturation. A narrow pore size distribution leads to a steeper SWCC as the water content drains over a narrow suction range. Figure 3.17 presents the five substrates and

compares the measured versus predicted SWCC for four different PTFs. As there is a large number of estimations that were considered from the CalcPTF program, the PTFs that provided a better comparison from a statistical perspective are presented in Figure 3.17. The selected PTFs from the CalcPTF program produced an R^2 value closer to 1 and a lower MSD and MAD value. Appendix C contains the measured versus predicted SWCC for all of the PTFs considered in this research.

From Figure 3.17, it can be observed that the predicted curves capture the slope of the measured SWCC fairly well. The predicted curves for BR2, GR1 and GR2 follow a gradual sloped curved, with some exceptions such as the MK method. Whereas the measured SWCCs for BR1 and BR3 have steep SWCCs which is indicative of the fact these materials drain over a narrow suction range compared to the other measured SWCCs. The predicted curves for BR1 and BR3 present a steep SWCC, similar to the measured SWCCs. Thus, the slopes of the predicted curves present a good fit to the measured curves. The AEV of the predicted SWCCs rarely overlap with the measured AEV, as shown in Figure 3.17. Predicted curves that underestimate the AEV present a relatively better fit compared to the predicted curves that overestimate the AEV. For example, the AP method presented in Figure 3.17c for BR1 overestimates the AEV, leading to an extremely poor fit. Choosing a PTF that overestimates the AEV results in an assumption that the examined substrate is able to stay completely saturated for a greater suction period.

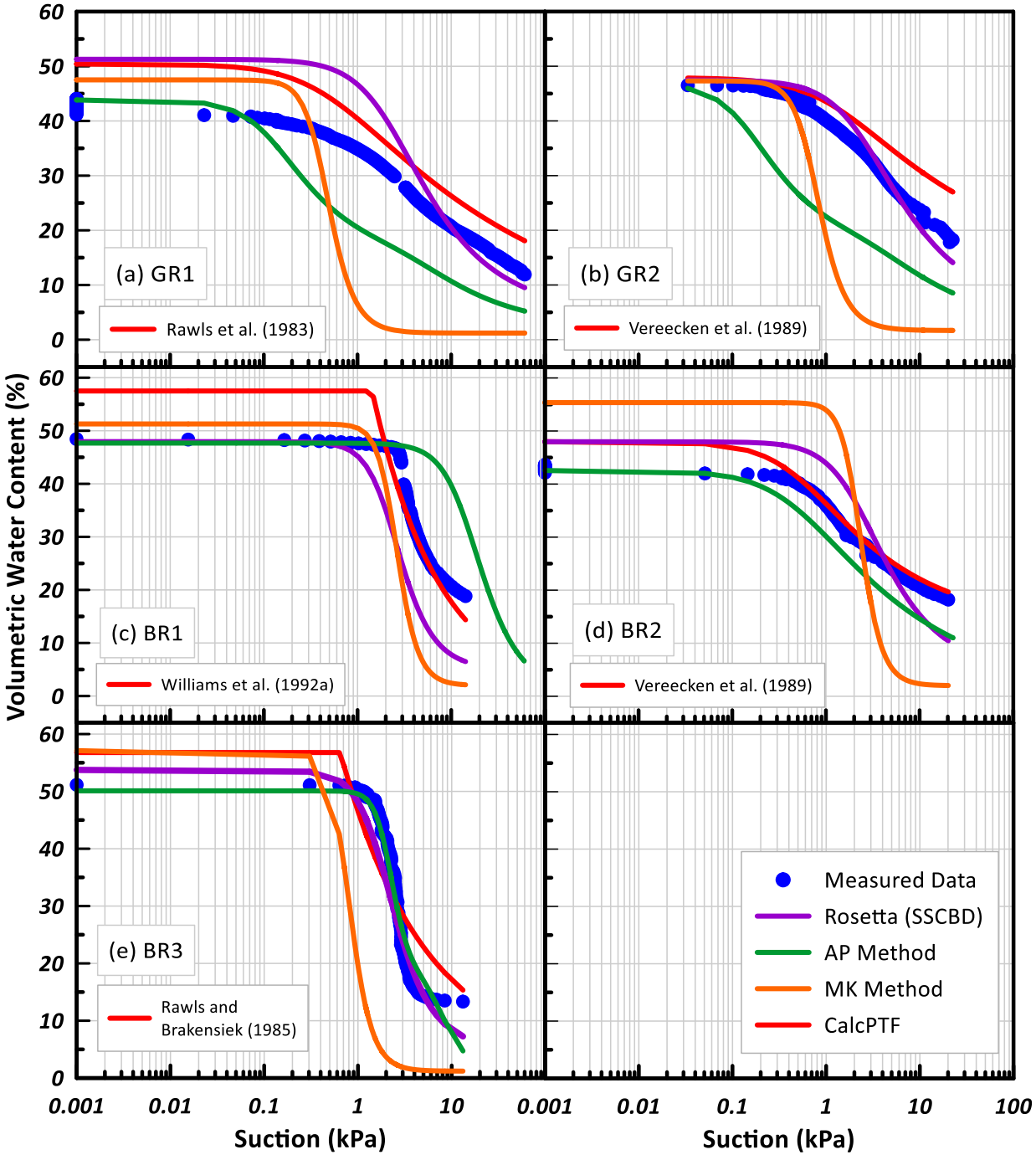

Figure 3.17: Predicted versus measured SWCC for selected PTFs for (a) GR1, (b) GR2, (c) BR1, (d) BR2, and (e) BR3

As for the saturated water content, some predicted curves overestimate the saturated water content by as much as 10%. Most of the predicted SWCCs overestimate the saturated water content, which implies that the storage of the substrate is greater than expected. There are some PTFs, particularly models 1 to 5 from Table 3.2, that use the particle density and dry bulk density to estimate the porosity. This porosity value is then assumed to be equal to the saturated volumetric water content. This tends to overestimate the saturated volumetric water content as shown in Figure 3.17. However, it should also be noted that it is somewhat difficult to achieve complete saturation during the experimental measurements. This is even after leaving the substrate core in a water bath for 24 hours. It is possible that when transferring the substrate core from the water bath to the HYPROP sensor, gravitational drainage occurs thus emptying the macropores within the porous substrate or the sample never gets completely saturated due to the air entrapment. Currently, there are no mechanisms available in the HYPROP to get rid of the entrapped air. It should be noted that even if another measurement method, such as pressure plate extractor, is to be employed and a complete saturation via vacuum or carbon dioxide flush is to be attained, complete saturation in field condition is never possible. Therefore, it can be argued that attainment of complete saturation under laboratory conditions is perhaps not the best representation of field conditions.

3.5 Performance of PTFs for Published Sources

The performance of the PTFs was further analyzed by collecting data from published sources for green roof and bioretention materials. Sandoval et al. (2017) and DelVecchio (2017) contain enough available information to determine the performance of PTFs for their substrates. In order to compare the performance of the PTFs to the measured, R^2, MSD, and MAD were estimated. To compare the performance of both substrates, Figure 3.18 presents the computed R^2, MSD, and MAD values plotted for the various PTFs. As there was a large variability between the substrates, the scale for the y-axis is not equal in Figure 3.18.

As observed in Figure 3.18, the trend relative magnitudes are captured well for the bioretention substrates from DelVecchio (2017) compared to the green roof substrates from Sandoval et al. (2017). Additionally, the predicted models for the green roof substrates presents a greater deviation in comparison to the bioretention substrates. For instance, some green roof substrates, particularly S2 and S5, have a MAD value of 50. This means that the predicted model is off by 50% volumetric water content from the measured data. Furthermore, the MSD estimated for S2 and S5 is greater than 1000 for some PTF models, which demonstrates a huge deviation in comparison to the measured model. This is quite interesting since the previous section observed that the green roof substrates performed well in comparison to the bioretention substrates. To determine why the green roof substrates performed poorly in comparison to the bioretention substrates, the models that performed poorly are analyzed is greater depth.

3.5.1 Effect of Organic Content on PTFs

From Figure 3.18, S2 and S5 are shown to have a greater deviation in comparison to the other green roof substrates. Upon closer investigation, the green roof substrates S4 and S5 have similar soil texture inputs for the percent of sand, silt and clay, (refer to Table 3.1) but their porosities and organic content are dissimilar. Both S2 and S5 are noted to have a large porosity and organic content in comparison to all of the other substrates analyzed within this research. The organic content of S2 and S5 are 30.7% and 35.5%, respectively. This organic content is far greater than the 7.8% organic content measured for BR3, which has the greatest organic content from the substrates examined in the previous section. It is concluded that most of the regression models from CalcPTF that performed poorly for S2 and S5 consider the percentage of organic content (refer to Table 3.2). Therefore, substrates with a large percentage of organic content does not perform as well as substrates with a smaller percentage.

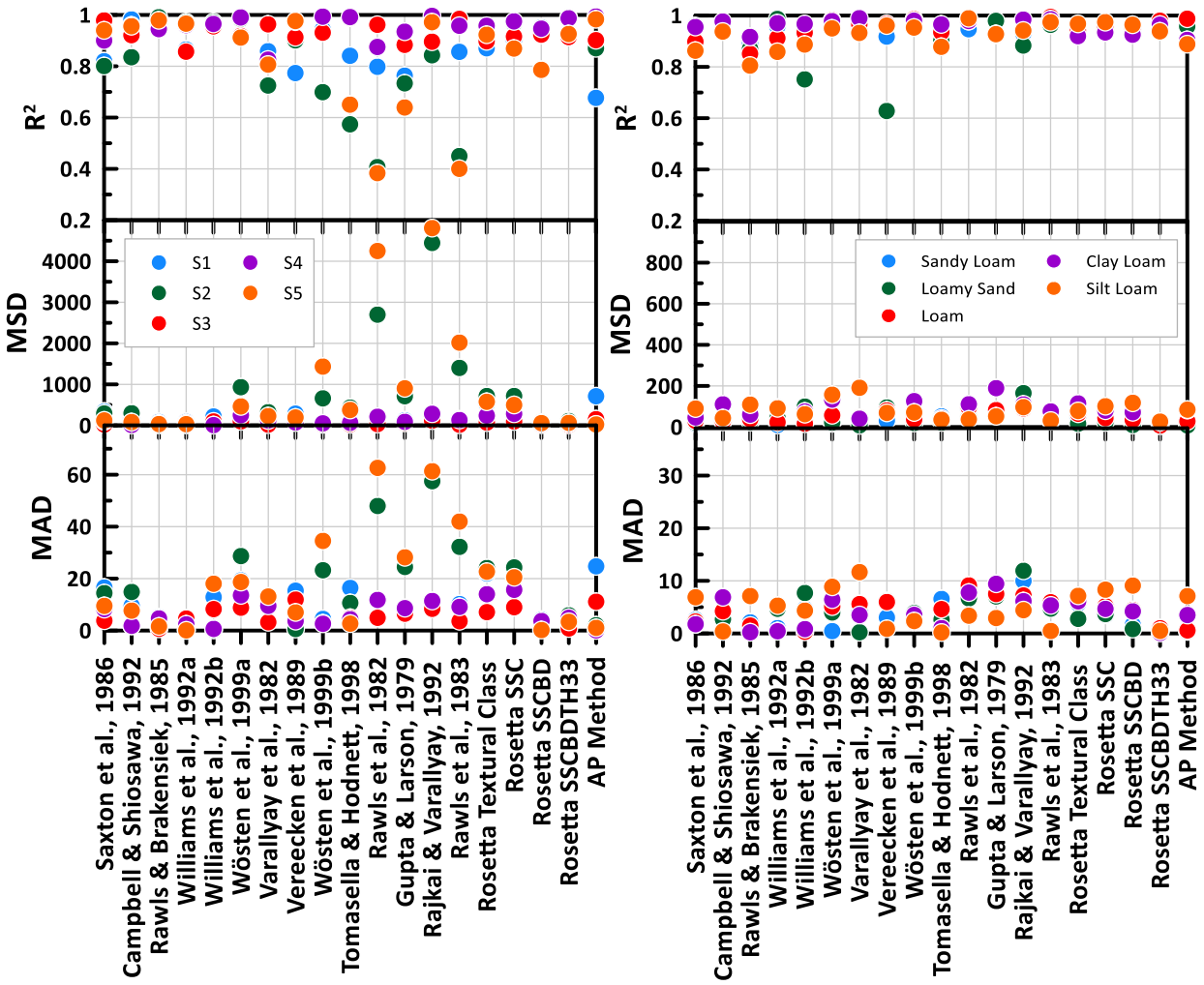

Figure 3.18: Statistical performance of (a) green roof substrates from Sandoval et al. (2017) and (b) bioretention substrates from DelVecchio (2017)

To demonstrate the impact of a large organic content on the PTF performance, the PTF developed by Rawls et al. (1983) is examined. The PTF developed by Rawls et al. (1983) considers the organic content and performed poorly for S2 and S5. Figure 3.19 presents the measured SWCC for S4 and S5 as well as the predicted SWCC using the regression equation developed by Rawls et al. (1983). Note that S4 has an organic content of 10.2%. As shown in Figure 3.19b, the predicted SWCC for S5 overestimates the saturated volumetric water content and the air entry value. However, using the same regression equation developed by Rawls et al. (1983) for S4

results in a relatively good fit in comparison, as shown in Figure 3.19a. Thus, the large organic content results in overestimation of the volumetric water content when using the regression equation developed by Rawls et al. (1983). With an increase in organic content, there is an increase in the predicted saturated volumetric water content.

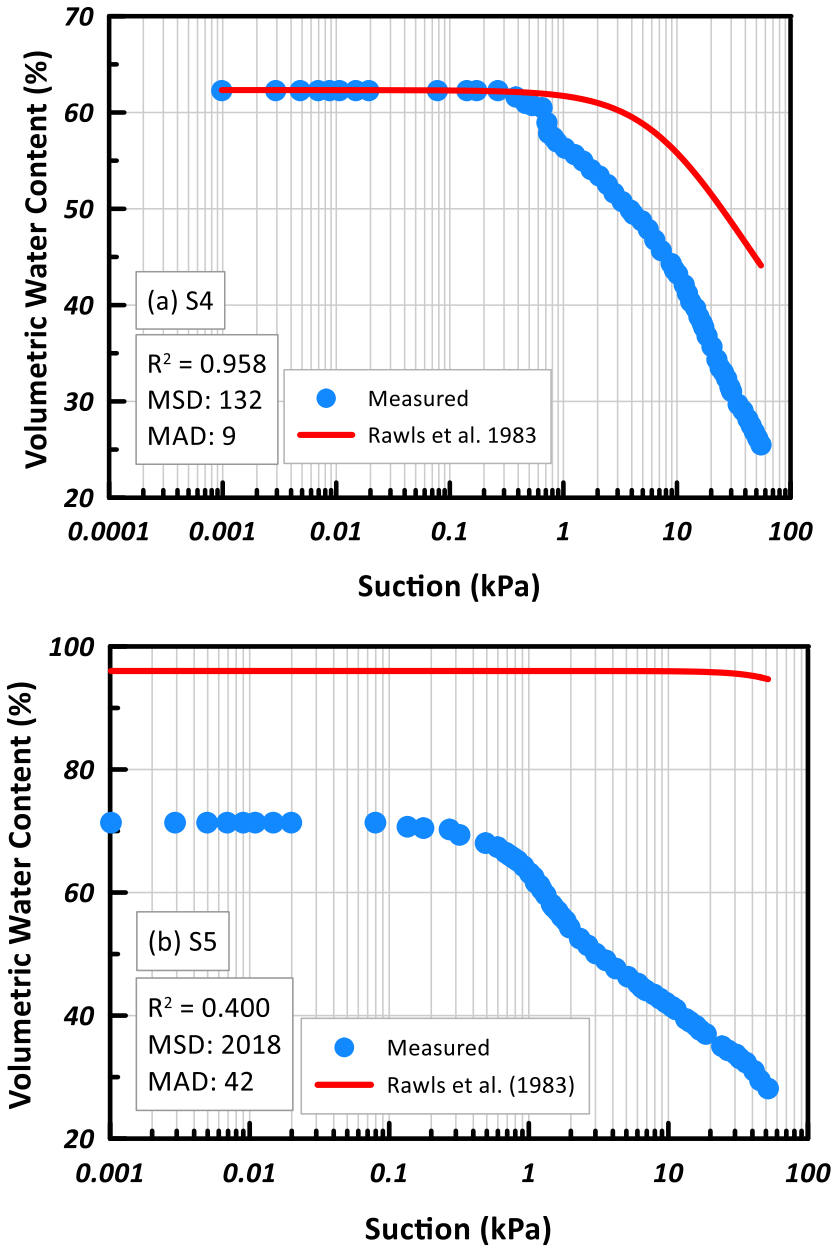

Figure 3.19: Measured SWCC and predicted using Rawls et al. (1983) for (a) S4 and (b) S5 green roof substrate retrieved from Sandoval et al. (2017)

To further demonstrate the impact of organic content on the performance of the PTFs, the organic content for S5 was reduced from 35.5%. Figure 3.20 presents the predicted SWCCs for S5 with a reduced organic content of 20% and 10% using the PTF developed by Rawls et al. (1983). From Figure 3.20, it can be seen that reducing the organic content results in a closer prediction to the measured SWCC. Both the saturated volumetric water content and the AEV are reduced with the reduction of organic content.

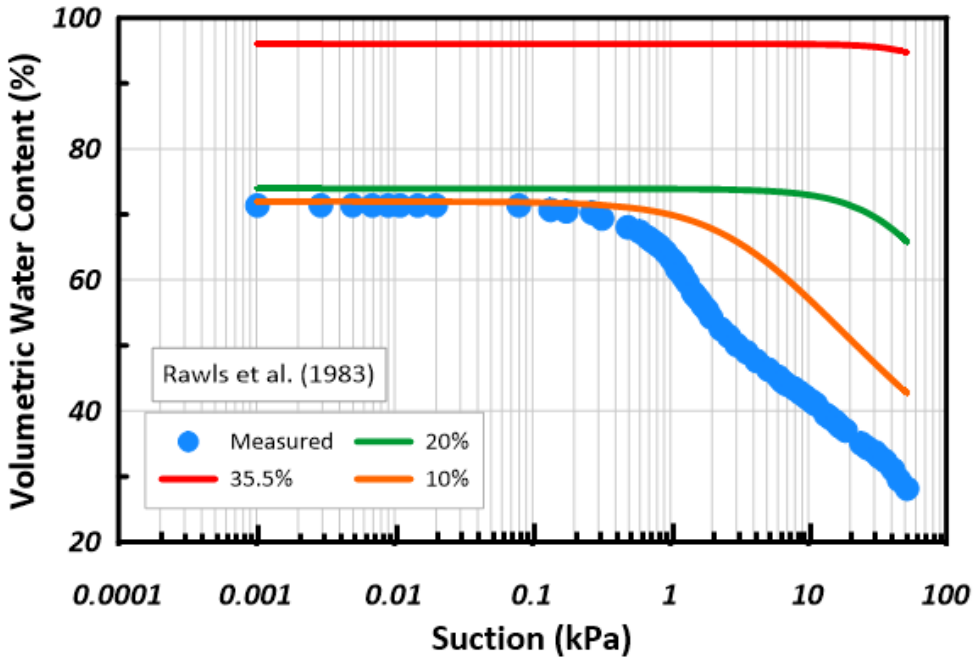

Figure 3.20: Reducing organic content using PTF developed by Rawls et al. (1983) for S5 substrate

Subsequently, the PTF developed by Rajkai and Varallyay (1992) is another regression equation that considers organic content. It performed poorly due to the *n* parameter prediction resulting in a value less than one. As these regression equations compute the *m* parameter from the van Genuchten equation as *m=1-1/n*, an *n* parameter less than one results in a negative *m* parameter. By keeping the soil inputs the same but changing the organic content, it was observed that with

an increase in organic content there was a decrease in the *n* value for the PTF developed by Rajkai and Varallyay (1992).

Overall, the green roof substrate from Sandoval et al. (2017) performed poorly in comparison to the other LID substrates examined due to the large organic content present within the substrates. Reducing the organic content in the substrates S2 and S5 resulted in a better statistical performance of the PTFs. This can be further demonstrated by reducing the organic content for S2 and S5 to 10% and plotting the statistical performance on the same scatterplot as shown previously in Figure 3.18. Figure 3.21 has the same axis used in Figure 3.18 and demonstrates an improved statistical performance after reducing the organic content of S2 and S5.

3.5.2 Visual Examination of LIDs from Published Sources

A visual analysis was carried out to further examine features of the SWCC and determine the most problematic feature between the measured and predicted SWCCs. Figure 3.22 presents the measured versus predicted SWCCs for the green roof substrates from Sandoval et al. (2017). Whereas Figure 3.23 presents the measured versus predicted SWCCs for the bioretention substrates from DelVecchio (2017). Similar to Section 3.3.1, the PTF that produced a better comparison from a statistical perspective is presented in Figure 3.22 and Figure 3.23 as there is a large number of PTFs considered in CalcPTF.

The predicted SWCCs show a relatively good fit with some exceptions. For instance, it can be seen that the saturated volumetric water content is underestimated using Rosetta. This is interesting as previously a majority of the predictive models overestimated the saturated volumetric water content. However, it is important to note that the dry bulk density was estimated by assuming the porosity is equal to the saturated volumetric water content from the measured SWCC. This resulted in a fit to the θ_s for the predictive methods from CalcPTF since CalcPTF allows the user to input both dry bulk density and particle density. Whereas Rosetta uses only the dry bulk density along with the soil textures to predict the SWCC. If the porosity is greater than

the measured θ_s from the SWCC, then the calculated dry bulk density would be smaller than the estimated value, using Equation 3.1. To check this theory, a smaller dry bulk density value was inputted into Rosetta for S2 and resulted in a greater θ_s.

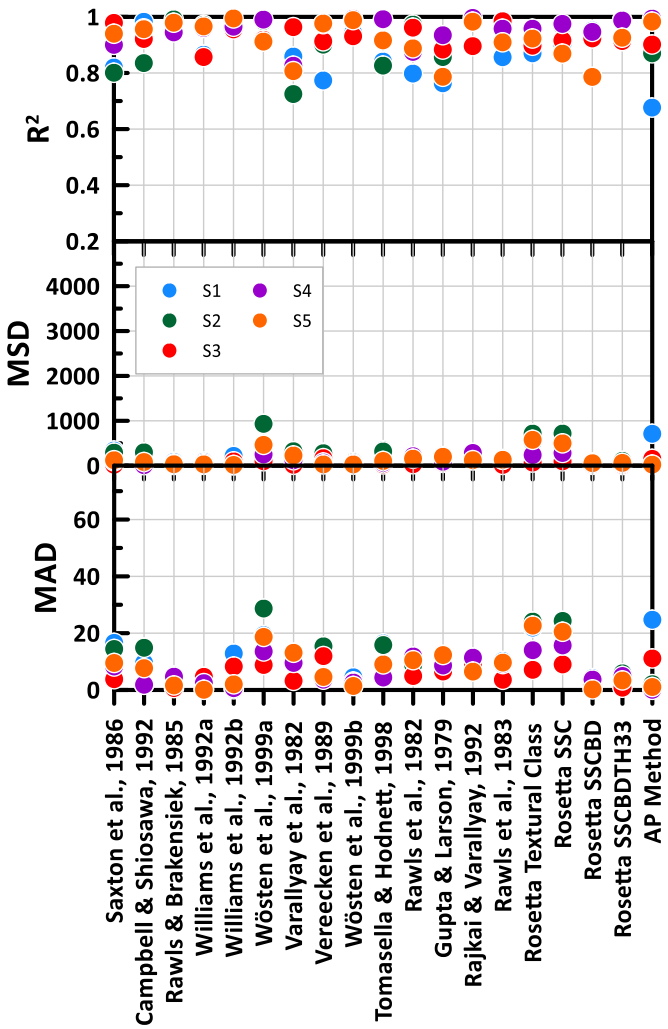

Figure 3.21: Statistical performance of green roof substrates from Sandoval et al. (2017) after reducing the organic content for S2 and S5

From Figure 3.22 and Figure 3.23, the measured SWCCs drain gradually over a greater suction range, unlike BR1 and BR3 from the previous section. The slope of the predicted curves presents

a good fit to the measured curves, with few exceptions such as the AP method used for the clay loam substrate in Figure 3.23. The AEV of the predicted curves rarely overlap the measured curves, which was also observed in the previous section. Additionally, a clear feature noted between Figure 3.22 and Figure 3.23 is the pore structure. A bimodal pore structure can be seen in Figure 4.13 for the bioretention substrates. The effect of the bimodal pore structure will be discussed in more details in the next section.

3.5.3 Effect of Bimodal Pore Structure on PTF Performance

An immediate observation noted between all of the substrates examined is the pore structure. In the analysis of the bioretention substrates from DelVecchio (2017), it was determined that these substrates exhibited a bimodal behaviour in the measured SWCC. This is important as Rosetta estimates van Genuchten (1980) parameters and CalcPTF estimates both Brooks and Corey (1964) and van Genuchten (1980) parameters. These two analytical functions fit well for soils that have a unimodal pore structure, meaning the SWCC has one peak. Whereas a SWCC that has two peaks exhibits a bimodal pore structure.

To demonstrate the impact of the bimodal pore structure on the PTF performance, Figure 3.24 presents the measured to the predicted volumetric water content of the sandy loam substrate from DelVecchio (2017). Note that according a study performed by Piñeiro et al. (2008), the predicted values should be on the x-axis and the measured on the y-axis. This is because Piñeiro et al. (2008) observed that there was an underestimation of the slope and overestimation of the y-intercept when the measured values were on the x-axis and the predicted on the y-axis. The PTFs used to predict the volumetric water content and are presented in Figure 3.24 are Rosetta and Campbell and Shiosawa (1992), which is a model from CalcPTF. Both of these models have a similar response between the measured volumetric water content of 25-35%, where there is a slight deviation from the 45° line. This deviation is where the second peak in the SWCC is found, thus demonstrating that the PTFs were unable to capture the bimodal behaviour of the substrate.

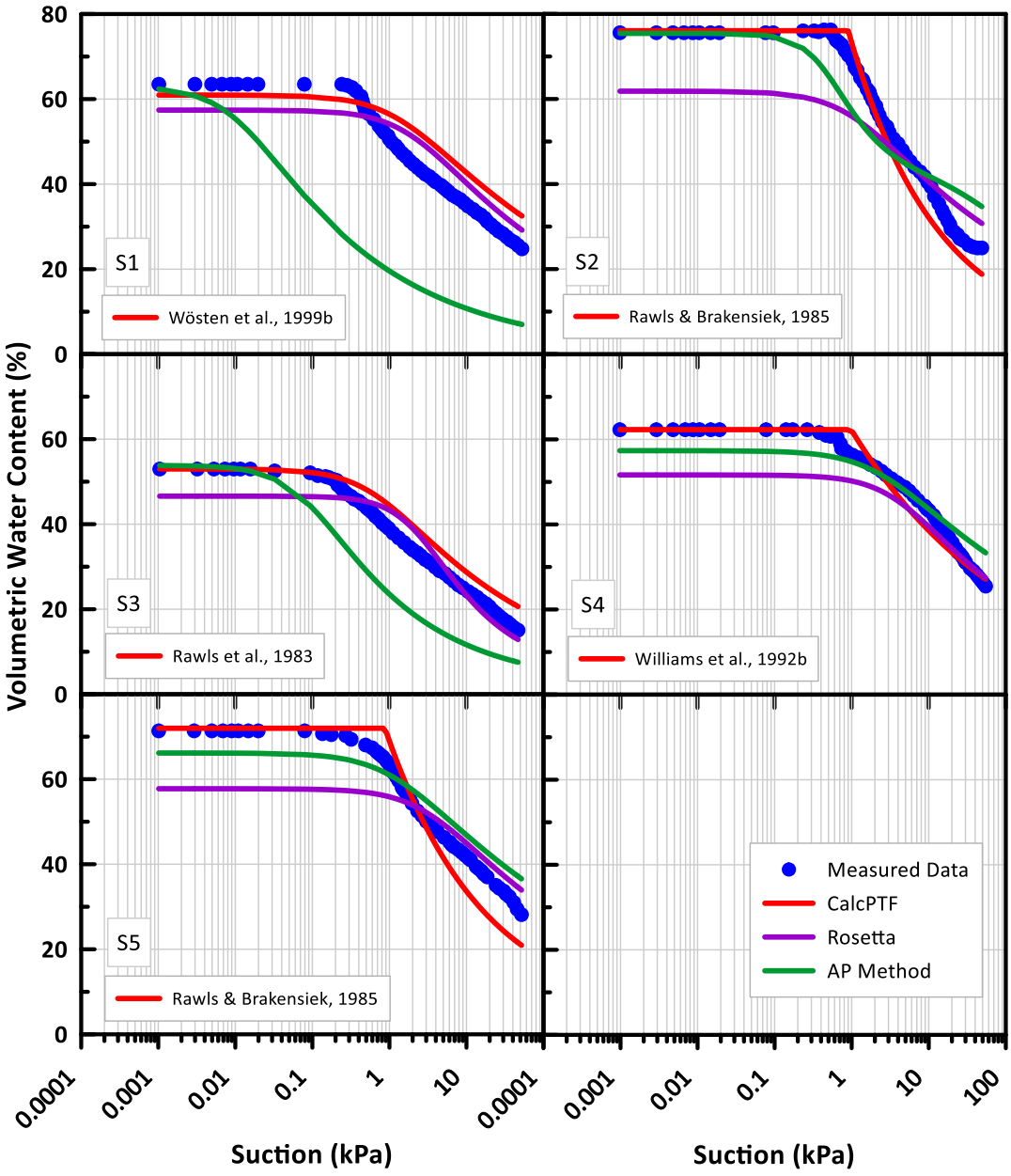

Figure 3.22: Visual examination of measured versus predicted SWCCs for green roof substrates from Sandoval et al. (2017)

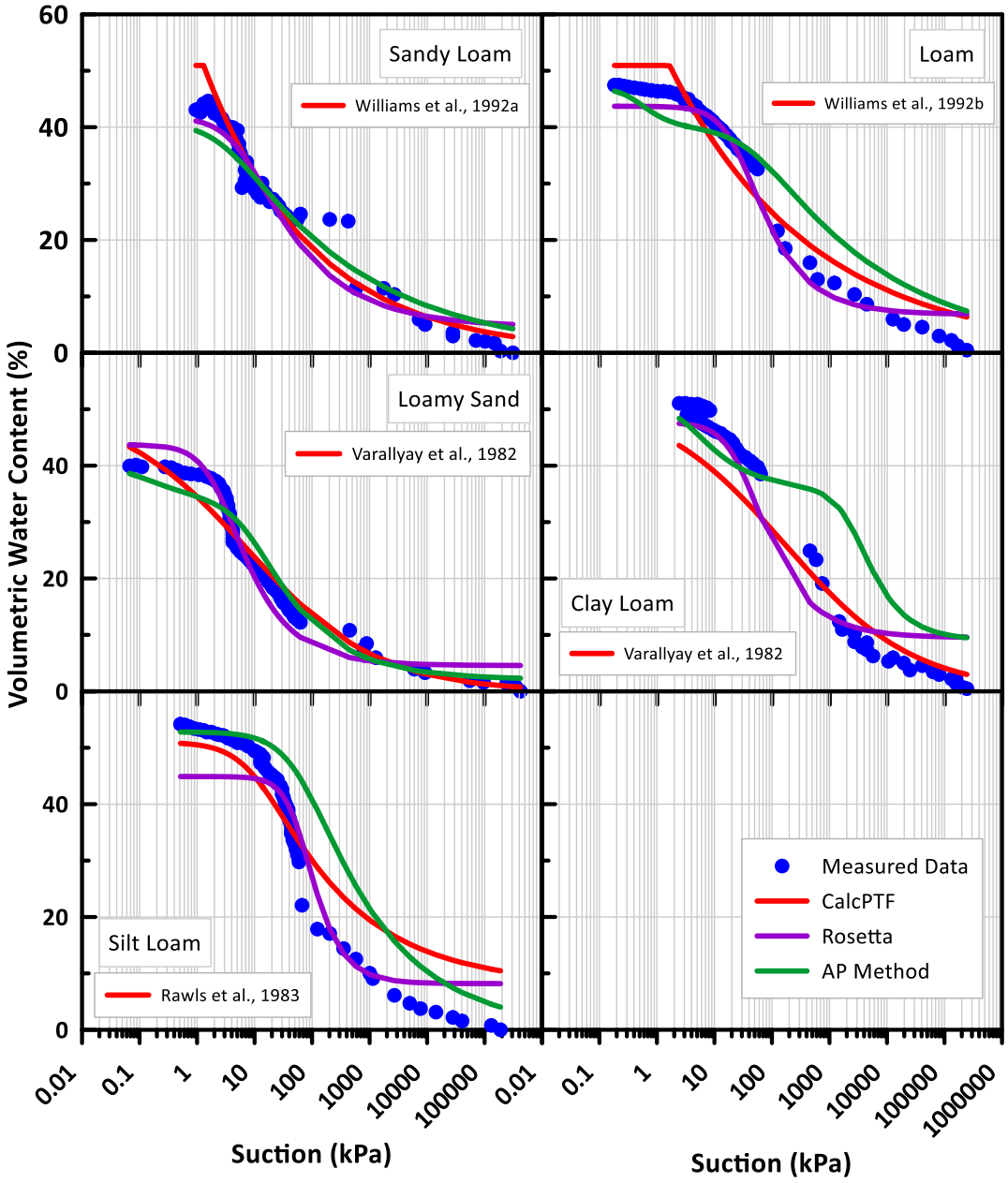

Figure 3.23: Visual examination of measured versus predicted SWCCs for bioretention substrates from DelVecchio (2017)

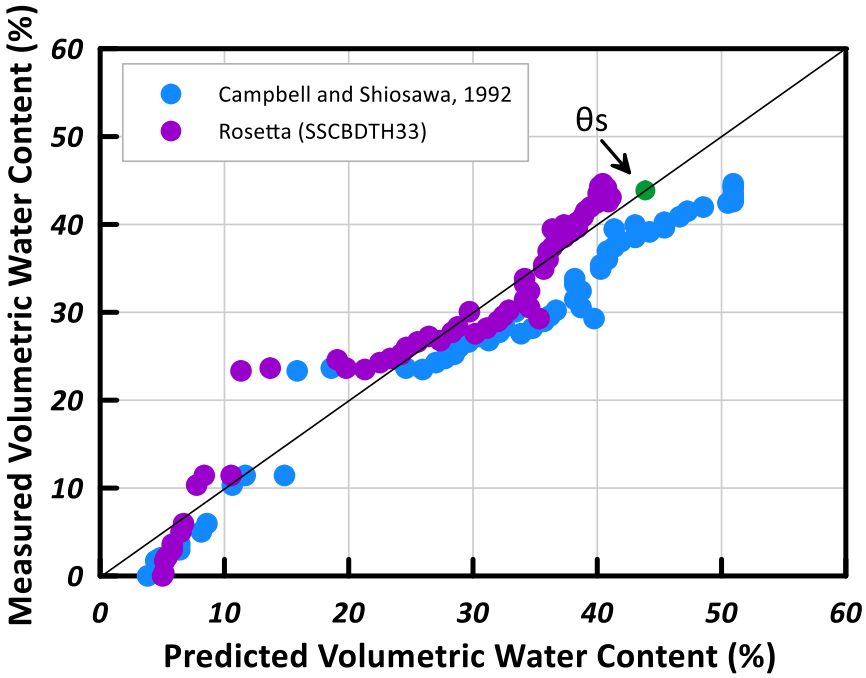

Figure 3.24: Predicted versus measured volumetric water content for Sandy Loam substrate (DelVecchio, 2017)

Unlike Rosetta and the CalcPTF models, the AP model uses the particle size distribution to estimate the SWCC. The AP model divides the particle size distribution curve into fractions, where larger particle sizes relate to larger soil water content. Therefore, it is able to have a better understanding of the physical characteristics of the soil and apply it when predicting the SWCC. Programs, such as SWRC-Fit (Seki, 2007), are used to fit an appropriate analytical function to the predicted data points from the AP method. This means that the AP model is not limited to just the van Genuchten (1980) model or Brooks and Corey (1964) models like Rosetta and CalcPTF. For example, the clay loam bioretention substrate shown in Figure 3.23 presents a bimodal pore structure using the AP method and is fitted using Durner (1994) model. The Durner (1994) model uses linear superposition of two or more VGM functions to account for the second peak in the SWCC.

Overall, the AP method performed fairly well for the bioretention substrates shown in Figure 3.23. The clay loam and silt loam substrates showed a lower statistical performance in comparison to the other three substrates. The clay loam, silt loam and loam overestimate the volumetric water content after a suction value of approximately 100kPa. For the clay loam, the data points calculated from the AP method demonstrate a distinct bimodal behaviour. However, the measured SWCC data for the clay loam exhibit a unimodal behaviour rather than bimodal. Still, there is no measured data between 70 kPa and 400 kPa, which may be a possible location for a second peak in the SWCC.

The overestimation of volumetric water content after a suction value of approximately 100 kPa seen for the clay loam, loam and silt loam substrates could be as a result of the scaling parameter (α) required in the AP method. Arya et al. (1999) aimed to scale the α parameter by analyzing a large set of measured data for five textural classes (Table 3.3). The α parameter is determined using Equations 3.6 and 3.7. The *a* and *b* parameters in Equation 3.7 relate log (N_i) to log(w_i/R_i^3) and differ depending on the textural class, as shown in Table 3.3.

As the α parameter for the clay loam texture class is not available in Arya et al. (1999), the *a* and *b* parameters for silt loam were used. Figure 3.25 demonstrates the difference in using the *a* and *b* parameters for silt loam versus clay were used for the clay loam substrate. From the Figure, using the clay parameters results in an overall decrease in pressure head. For instance, at the same volumetric water content of 20%, the silt loam parameters estimate a pressure head of approximately 6000 kPa while the clay parameters estimate a pressure head of 3000 kPa. Although using the clay parameters may lead to a closer estimation of the volumetric water content in the dry range, it also resulted in an underestimation of the pressure head in the wet range. Still, this is due to the overall shape of the predicted SWCC rather than the use of the *a* and *b* parameters.

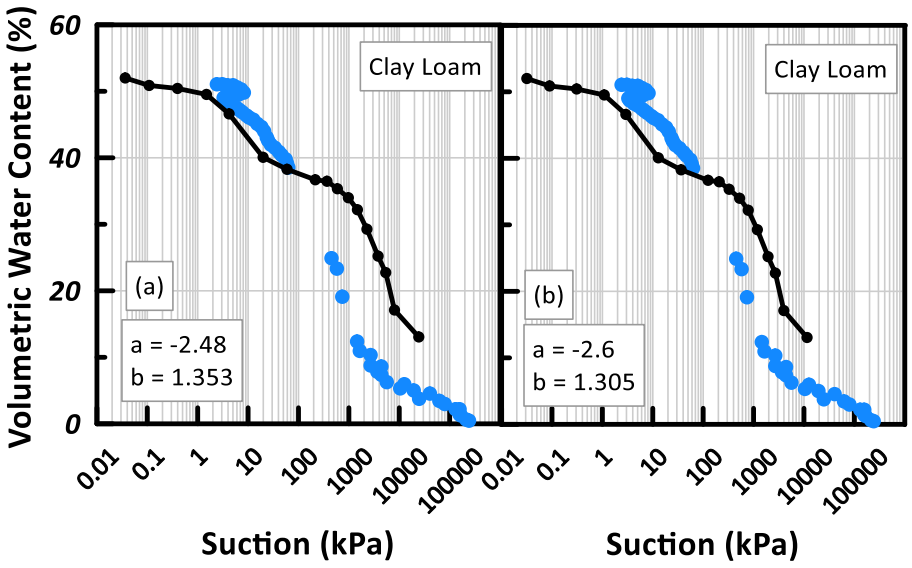

Figure 3.25: Arya and Paris scaling parameter for (a) silt loam and (b) clay used to predict the clay loam bioretention substrate

3.6 Numerical Modelling Results

The water balance at the ground surface describes the amount of water that moves across the soil-atmosphere boundary. Through the assessment of a water balance, relevant components such as water storage capacity, infiltration or drainage can be quantified. This assists in the design and analysis of the substrates performance when used in LID applications. Components of the water balance at the ground surface include precipitation (*P*), potential evaporation (*PE*), actual evaporation (*AE*), transpiration (*T*), surface run-off (*RO*), and net infiltration (*NI*). The *NI* refers to the amount of water that enters the soil surface overcoming the evaporation and surface runoff. It can be described as:

$$NI = P - AE - RO \qquad [3.21]$$

The *AE* is also dependent on prevailing water quantity in the near surface soil layer and is therefore always less than the *PE,* if the surface does not remain saturated. HYDRUS estimates *AE* by using a system-dependent atmospheric boundary condition at the top of the modeling domain. The potential flux is dependent on external conditions, such as precipitation and

evaporation, while the actual flux depends on the external conditions as well as the transient soil moisture conditions.

As shown in Equation 3.21, if the actual evaporation is high, the *NI* decreases accordingly. Higher precipitation intensities might result in exceeding the infiltration capacity of the soil resulting in surface run-off, thus decreasing the *NI*. Generally, a higher soil water retention and low saturated hydraulic conductivity (K_s) tends to increase the *AE*, thus decreasing *NI*. A lower K_s and higher air entry value implies that it would take longer for water to move deeper into the soil, thereby allowing evaporation to occur as the water remains near the surface.

The HYDRUS 1D software was used to evaluate the performance of the hydraulic properties from PTFs to the measured hydraulic properties using thirty years of Toronto historical climate data. The water balance at the surface using the measured and predicted soil hydraulic parameters are presented in Figure 3.26. Note that the water exiting the system is assumed to be negative while the water entering the system is considered positive. Table 3.8 contains the van Genuchten (1980) parameters used in the numerical simulations for GR2 and BR2's water balances. As there were many regression equations contained within CalcPTF, the source that produced a better comparison from a statistical perspective (high R^2, low MSD and MAD) was chosen. Additionally, no surface runoff was observed for any of the substrates as they have a high saturated hydraulic conductivity.

From Figure 3.26a, it can be observed that the PTFs overestimate the *NI* for green roof material. The difference in *NI* calculated from measured and estimated (MK method) hydraulic properties is 500cm at the end of the 30-year period. This comes out to be 167 mm every year on average. This is consistent with the statistical analysis for GR2, where the MK model performs poorly in comparison to CalcPTF. The difference between CalcPTF and the measured hydraulic properties for *NI* is 50cm, which is quite small in comparison. The greater *NI* results in a greater bottom flux (*BF*) leading to overdesign for a green roof. The *BF* describes the outflow at the bottom of the

substrate as free drainage was assumed at the bottom boundary. During a storm event, it is ideal to mitigate the water travelling out of the green roof. As reducing peak flow during storm events is a key design criterion for LIDs, a decreased *BF* for green roofs is preferred.

Table 3.8: van Genuchten (1980) parameters used in measured versus predicted numerical simulations for GR2 and BR2

Substrate	PTF	Source	θ_r	θ_s	α (cm^{-1})	n
GR2	Measured	Van Genuchten fitted	0.00	0.47	0.09	1.31
	CalcPTF	Vereecken et al. (1989)	0.12	0.48	0.08	1.29
	Rosetta	SSCBD	0.05	0.48	0.04	1.67
	AP Method	Arya and Paris (1981)	0.01	0.48	0.96	1.34
	MK Method	Aubertin et al. (2003)	0.02	0.47	0.13	3.48
BR2	Measured	Van Genuchten fitted	0.16	0.43	0.11	1.73
	CalcPTF	Vereecken et al. (1989)	0.13	0.48	0.20	1.44
	Rosetta	SSCBD	0.05	0.48	0.05	1.90
	AP Method	Arya and Paris (1981)	0.00	0.43	0.21	1.35
	MK Method	Aubertin et al. (2003)	0.02	0.55	0.04	4.29

Figure 3.26b presents the water balance for BR2. The water balance of the predicted and measured hydraulic properties shows similar results. Whereas the PTFs overestimated the *NI* for GR2, the PTFs for BR2 underestimate the *NI*, with the exception of the MK model. CalcPTF has the closest results to the measured simulation, with a *NI* difference of 165 cm at the end of the 30-year simulation. The performance of the PTFs is consistent with their ability to predict hydraulic properties. Similar observations were made for BR1 and BR3, where simulations using predicted and measured hydraulic properties resulted in relatively close *NI* values. Therefore, it can be concluded that the *NI* estimates are less sensitive to soil hydraulic properties for LID systems that accept a large quantity of water.

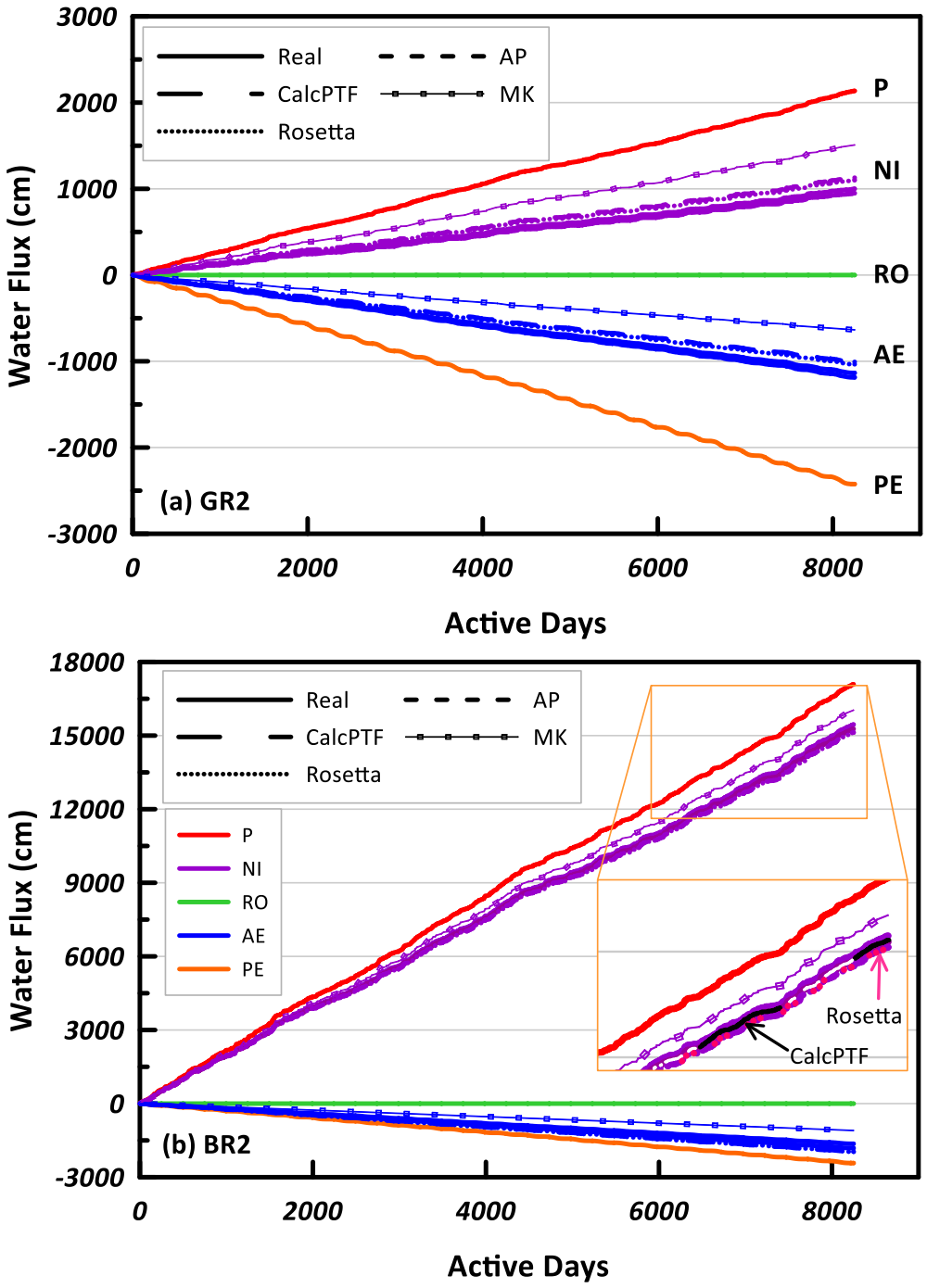

Figure 3.26: Water balance of measured and predicted SWCC for 30-year Toronto historic climate data for (a) GR2 and (b) BR2

To further analyze the water balance results, the percent difference for each PTF and the cumulative *NI*, *AE*, and *BF* are examined and shown in Figure 3.27. The cumulative values for *NI*, *AE*, and *BF* using the measured soil hydraulic properties is used as the baseline. It is evident that

there is a greater percent difference between the *NI* and *BF* for the green roof substrates whereas the bioretention substrates have a small, almost negligent, percent difference. This further demonstrates that the effects of the soil hydraulic properties get muted when large quantities of water enter the system. There is also a great percent difference in *AE* for the bioretention that is not as noticeable in the water balance shown in Figure 3.26b.

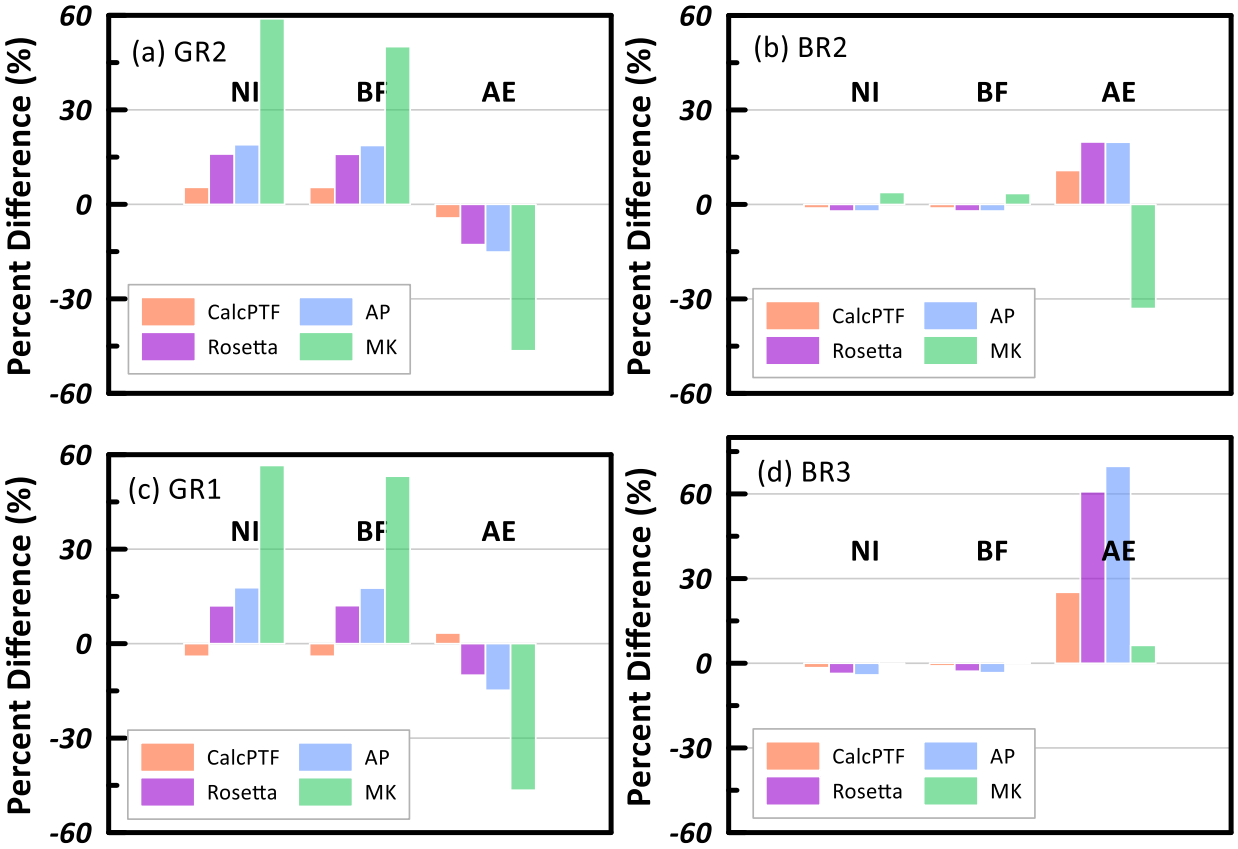

Figure 3.27: Percent difference for predicted versus measured soil hydraulic properties of cumulative NI, BF, and AE for (a) GR2, (b) BR2, (c) GR1, and (d) BR3

3.7 Conclusions

Two green roof and three bioretention substrates were examined and characterized using routinely used soil testing such as the sieve test and hydrometer test to acquire the particle size distribution curve. Other tests include dry combustion to determine the organic content, the

pycnometer method to determine the specific gravity, and the constant head test to measure saturated hydraulic conductivity. Some highlights from these test results are noted as follows. The bioretention material BR3 contained the greatest percentage of organic content, possibly due to it containing glass sand. The green roof materials had a smaller specific gravity compared to the bioretention materials. The green roof media had a greater percentage of gravel whereas the bioretention media had a greater percentage of sand. From the coefficient of uniformity, the green roof media are classified as well-graded and the bioretention media are uniformly-graded with a steep gradation curve. All of the LID substrates are quite coarse and are expected to have good drainage during a storm event. From the constant head test, the green roof substrates have a greater K_s compared to the bioretention substrates. The average K_s for GR1, GR2, BR1, BR2, and BR3 are 0.24, 0.19, 0.03, 0.04, and 0.03 cm/s, respectively. As the bioretention systems are designed for ponded conditions, a smaller K_s, in comparison to the green roof media, allows for the contaminant capture. Finally, the SWCC was measured using the HYPROP apparatus (UMS, 2015). The well-graded green roof substrates retained water over a greater suction range, whereas the poorly-graded bioretention substrates retained water over a narrow suction range. The samples for the green roof and bioretention materials obtained from different suppliers indicated that there is a wide variability in composition, geotechnical and hydraulic properties of these materials. Measurement of unsaturated soil hydraulic properties for LID materials is costly, and time intensive leading to predictive methods such as pedotransfer functions. The use of these predictive methods for LID materials were examined in detail within this research.

Overall, there is a high level of uncertainty when using PTFs for LID materials. There is no one particular PTF model that works best for the all the LID material that were considered. For example, even though BR1, BR2 and BR3 are all bioretention substrates, the PTF that performed best statistically for each substrate is different. Furthermore, it was observed that the green roof substrates, GR1 and GR2, performed better using the PTFs from CalcPTF and Rosetta compared

to the bioretention substrates, BR1, BR2, and BR3. However, for the published literature analysis, the green roof substrates from Sandoval et al. (2017) did not perform as well as the bioretention substrates from DelVecchio (2017). Therefore, there is no PTF model that would work universally in the estimation of LID substrates. As there is a large variability of the materials used in LID substrates, depending on the design criteria of the system, a PTF model that works well for one LID substrate may not work well for another. The PTF models were designed by gathering a large quantity of measured soil data and creating a relationship. However, the soil data that is used to create the PTF models are typically natural soil and not the engineered soil used in LID systems. Thus, with the combination of the variability of materials used in each LID system and the PTF originally developed for native soil, there is no PTF model that can estimate all LID substrates.

The core features of the SWCC, including the air entry value, the saturated volumetric water content and the pore size distribution, were examined through visual analysis. For many of the examined substrates, the air entry value of the predicted SWCCs rarely overlapped the measured SWCC. Overestimating the AEV implies that the substrates is able to stay completely saturated under a greater suction value. Whereas the slopes of the predicted SWCCs generally had a good fit to the measured SWCCs. The PTFs were mostly able to predict whether the slope of the measured SWCC is steep or gradual. The saturated volumetric water content was overestimated for many of the examined substrates, sometimes as much as 10%. This would imply that the storage of the substrate is greater than expected.

Other aspects to consider from this section include the impact of a greater percentage of organic content on the PTF. With an increase in organic content, the *n* parameter used in the van Genuchten equation was seen to decrease to a value below 1 in the PTF model by Rajkai and Varallyay (1992). The increase in organic content also resulted in an overestimation of the saturated volumetric water content and air entry value in the PTF model by Rawls et al. (1983).

Therefore, PTFs that use regression equations did not perform well when estimating LID substrates with an organic content greater than 25%.

In addition, some substrates from DelVecchio (2017) exhibited bimodal characteristics. A bimodal SWCC has two peaks whereas a unimodal SWCC has one. The CalcPTF and Rosetta PTFs provide a unimodal SWCC prediction as they provide parameters for the Brooks and Corey (1964) and van Genuchten (1980) analytical functions. The AP model is not limited to the Brooks and Corey (1964) or van Genuchten (1980) analytical functions as it is derived from the particle size distribution which can exhibit bimodal behaviour. For the clay loam substrate from DelVecchio (2017), there is a clear indication that the AP method predicted a bimodal behaviour for the SWCC. However, the predicted curve did not fit well to the measured either due to missing data points between 70 to 400 kPa to indicate a measured bimodal SWCC or due to the scaling parameter used in the AP method.

In general, the PTFs have a limited capability to accurately estimate the SWCC of the engineered media. These substrates differ vastly when compared to natural, non-engineered soil as they are mixed to meet a specific design criterion. To examine the performance of the use of PTFs, long term simulations using HYDRUS 1D was completed. Through numerical modelling, it was determined that measured soil hydraulic properties are more relevant for green roof systems in comparison to bioretention systems. This was observed by examining the percent difference of the measured cumulative net infiltration, actual evaporation and bottom flux to the predicted values. Using the AP method and Rosetta resulted in a percent increase of 15% in cumulative net infiltration for the green roof substrates. Using the MK method, a 60% increase in the cumulative net infiltration was observed for the green roof substrates. Whereas the bioretention media presented a small, negligent percent difference for all PTFs considered. As field and laboratory measurement of unsaturated hydraulic properties can be expensive and cumbersome, the use of PTFs can be seen as a great advantage. However, from a design perspective, accurate

soil hydraulic properties are more important for systems that manage less water, such as green roof systems.

Chapter 4: Design and Performance of Low Impact Developments Under Changing Climate

4.1 Introduction

According to the Intergovernmental Panel on Climate Change (IPCC), climate is changing around the world, particularly due to economic and population growth rapidly increasing anthropogenic greenhouse gases (IPCC, 2014). Adverse effects of climate change are noted by the atmosphere and ocean warming, the amount of snow and ice diminishing, and the sea level rising. Canada is not exempted from the changing climate. Recent studies have shown that Canada is becoming warmer as the annual mean temperature averaged over the land has increased by 1.7°C from 1948 to 2016 (Vincent et al. 2018; Zhang et al. 2019). It is projected that the number of growing days will also increase with this change in mean temperature across Canada. Additionally, there has been observed trends of increasing annual mean precipitation in Canada. Under a low emission scenario, the annual mean precipitation is projected to increase 7% by the late 21st century. Under a high emission scenario, the annual mean precipitation is projected to increase by 24% (Zhang et al. 2019). With the increase in temperature and frost-free days, there will be a shift from snow to rain in the spring and fall seasons.

With the increase in both intensity and frequency of extreme precipitation events due to climate change, the risk of flooding rises in dense cities such as Toronto, ON, Canada. In order to counter the risk of flooding, engineers have developed ingenious stormwater management solutions such as the use of Low Impact Developments. Low Impact Developments (LIDs) are defined as a stormwater management strategy that aims to mitigate the impacts of increased runoff and stormwater pollution by managing runoff as close to its source as possible (U.S. EPA, 2007). With LIDs, stormwater can be treated as a resource in helping to preserve and recreate natural landscapes, rather than as a waste that needs to be rerouted from its source (U.S. EPA, 2018).

LIDs assist in developing sustainable cities and include systems such as permeable pavements, green roofs, bioretention cells, and rain barrels.

The amount of research conducted on the performance of LIDs under changing climate is minimal. Hathaway et al. (2014) noted that the evaluation of the performance of urban stormwater control measures under climate change projections have not been thoroughly examined. Using base scenario data between 2001 to 2004 and future scenario data between 2055 to 2058 under two climate emission pathways, Hathaway et al. (2014) determined that the frequency and magnitude of overflow from a bioretention system in North Carolina, USA is projected to increase substantially under future climate scenarios. Borris et al. (2016) investigated the runoff quality of bioretention in urban and suburban catchments in Ostersund, Sweden for future scenarios under different greenhouse gas (GHG) emissions and socio-economic pathways. Wang et al. (2019) analyzed the performance of bioretention under changing climate in Guangzhou, China. Performance factors included reduction of runoff volume, peak flow and first flush. The effect of first flush is defined as the high concentration of contamination in the initial portion of the surface runoff (Wang et al. 2019). In the highly-dense urban city, Wang et al. (2019) noted that the performance of bioretention systems decreases with climate change and cannot replace older stormwater management systems.

Subsequently, Stovin et al. (2013) conducted a 30-year continuous simulation to examine the performance of green roofs for four UK locations under different climatic regimes. Viola et al. (2017) attempted to quantify the retention performance of green roofs worldwide by considering several climate conditions using a simple stochastic weather generator. Both Stovin et al. (2013) and Viola et al. (2017) do not consider the impact of climate change for these long-term conditions. A study by Herrera-Gomez et al. (2017) considered the impact of climate change in Spain. The study was related to the mitigation of urban heat island effect using green roofs. Berkompas et al. (2008), Fassman-Beck et al. (2013), Schultz et al. (2018), and Voyde et al. (2010) have completed

studies on the performance of extensive green roofs, particularly the stormwater retention performance. From these studies, it can be noted that the storage, and therefore the run-off performance, is dependent on the size of the storm, rather than solely the substrate depth. Thus, the change in climate should be taken into consideration when designing these LID systems as increased storm sizes and intensities are projected in many parts of the world.

Understanding that the quantity and intensity of rainfall is projected to increase, analysis of LIDs under changing climate is essential. This research has conducted an examination of green roof and bioretention substrates under changing climate to determine if current and future LID systems are required to be modified. This research also presents a methodology to analyze the LID designs for the changing climate. Various design aspects of the LID systems are examined, including future quantities of water that would enter the system, peak intensity delay, peak time delay, run-off, ponding and overflow within the bioretention facilities, residence times, storage capacity, and substrate thickness. This research assesses green roof and bioretention systems under changing climate for ten different locations in Ontario, with specific focus on Toronto, Ontario. Furthermore, both future long-term and extreme precipitation events are examined and compared to historical climate data for these ten locations in Ontario. Numerical modelling was carried out using HYDRUS software (Šimůnek et al. 2008).

4.2 Methodology

This section describes the steps taken to complete the analysis of LIDs under changing climate. When designing for LIDs, the use of Darcy's equation for saturated flow may lead to inaccurate results such as ponding or overflow within the soil media (Liu and Fassman-Beck, 2017). Rather, it is more likely that unsaturated flow conditions dominate both green roof and bioretention systems (Barbu and Ballestero, 2014; Liu and Fassman-Beck, 2017; Perelli, 2014). The HYDRUS software (Šimůnek et al. 2008) is chosen to evaluate the performance of green roof and bioretention substrates under changing climate. HYDRUS is a modelling software used in the

analysis of water and energy flow and solute transport in variably saturated soils. The software can be used to simulate 1-, 2- and 3-dimensional movement of water, heat, and multiple solutes in variable saturated media. The program solves the Richards' equation for saturated-unsaturated water flow and convection-dispersion type equations for heat and solute transport (Šimůnek et al. 2008). Brunetti et al. (2017), Liu and Fassman-Beck (2017), Meng et al. (2014), Qin et al. (2016), and Stewart et al. (2017) have demonstrated that HYDRUS model presents good accuracy in producing the hydraulic response of the LID system.

In order to set-up the numerical model in HYDRUS, the material properties, climate data inputs, geometry, and initial and boundary conditions are required. These will be discussed in more detail in the following sections. Additionally, Figure 4.1 presents an overview of the tasks completed to achieve the objectives of this research. Extreme precipitation events and long-term climate data were compiled for historic and future climate scenarios. The material properties of the green roof and bioretention media were measured in the laboratory. The numerical model geometry was developed for both the green roof and bioretention media. Analysis of the green roof and bioretention media was carried out for in terms of both long-term analysis and extreme precipitation analysis. Performance factors included the total quantity of water, the peak storm delay, the total ponding depth and time, and the total run-off.

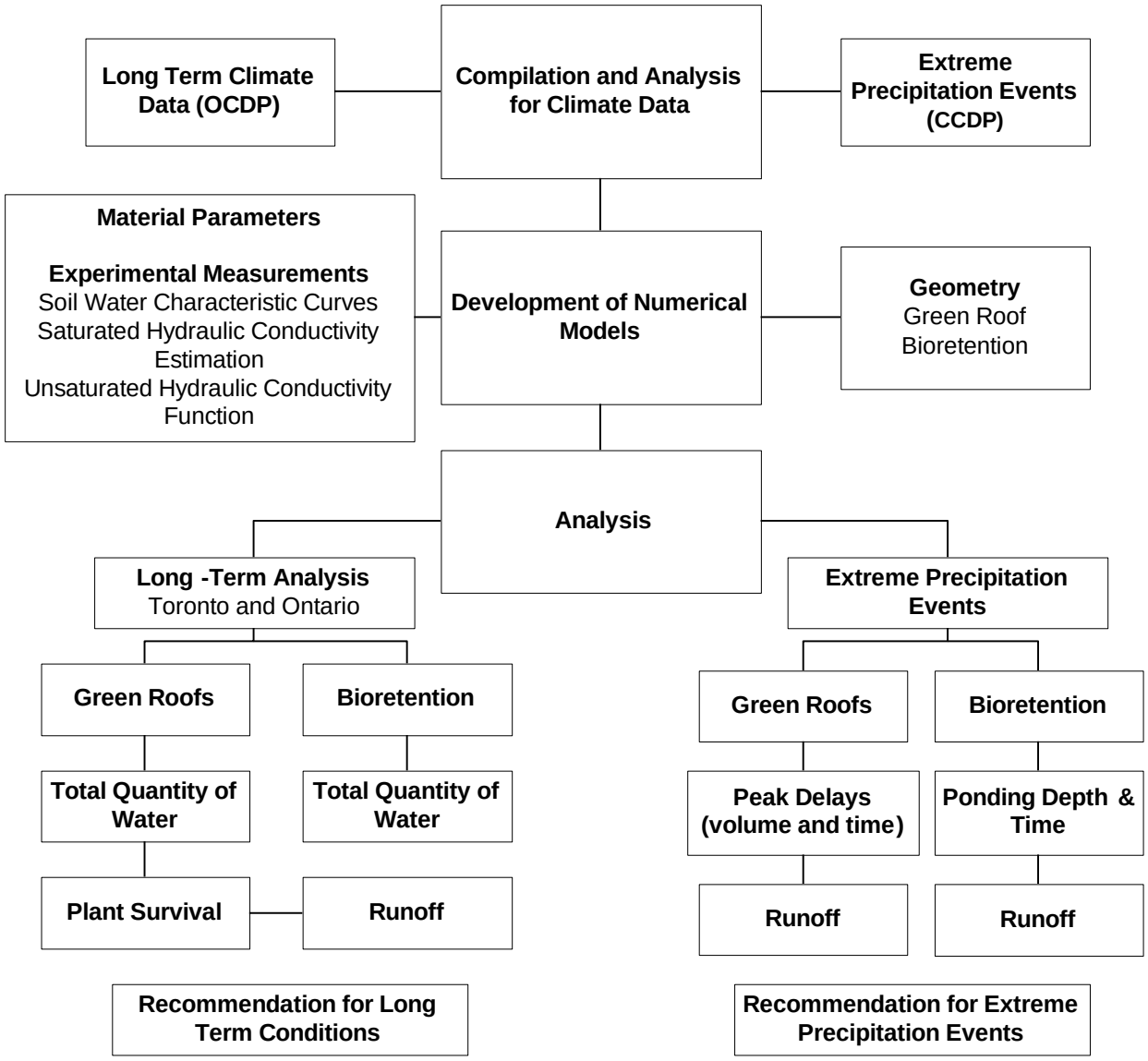

Figure 4.1: Methodology to analyze LID design under changing climate

4.2.1 Material Properties

Green roof and bioretention substrates were sourced from local suppliers. These substrates were tested in the laboratory to determine their soil properties. Laboratory testing included measurement of the organic content (ASTM D2974, 2014), specific gravity (ASTM D854, 2014), particle size distribution using both the sieve test (ASTM D6913, 2017) and hydrometer test (ASTM D7928, 2017), and the saturated hydraulic conductivity using the constant head test

(ASTM D5856, 2015). The soil water characteristic curve was measured using the HYPROP measurement system (UMS, 2015). Details regarding the soil hydraulic and geotechnical properties are provided and discussed in Chapter 3.

Table 4.1 presents the hydraulic properties used in the numerical analysis for one of the green roofs and bioretention substrates, respectively. The green roof's saturated hydraulic conductivity (K_s) was measured to be one order of magnitude greater than the bioretention media. A smaller K_s for the bioretention compared to the green roof is desirable as it assists in pollutant removal processes, such as filtration. A large K_s for the green roof assists in reducing the risk of surface runoff leading to a greater roof load.

The van Genuchten (1980) equation was used to mathematically represent the measured soil water characteristic curve. The van Genuchten (1980) equation is written as follows:

$$Se = \frac{\theta - \theta_r}{\theta_s - \theta_r} = [1 + (\alpha|\psi|)^n]^{-m} \quad [4.1]$$

where S_e is the effective saturation, θ_r and θ_s are the residual and saturated water contents, respectively, α is a fitting parameter related to the inverse of the air-entry pressure head, n and m are fitting parameters with m = 1-1/n. In order to express the unsaturated hydraulic conductivity, the van Genuchten function (1980) is substituted into Mualem's (1976) pore conductivity theory to obtain the van Genuchten-Mualem function (van Genuchten, 1980).

Table 4.1:Hydraulic Parameters of Green Roof and Bioretention Media

Media	Saturated hydraulic conductivity, K_s (cm/s)	Fitted van Genuchten (1980) Parameters			
		θ_s (cm^3/cm^3)	θ_r (cm^3/cm^3)	α (1/cm)	n
Green Roof	0.19	0.47	0	0.09	1.13
Bioretention	0.04	0.43	0.16	0.11	1.73

4.2.2 Climate Data

The historical or baseline climate data is used as a reference point to demonstrate the changes in the future climate data. Climate data for ten different locations across Ontario was compiled. These locations are Toronto, Niagara, Kingston, Ottawa, Timmins, Kenora, Thunder Bay, North Bay, London, and Windsor (Figure 4.2). Historical climate data between 1981 to 2010 was collected from Environment and Climate Change Canada portal (Environment and Climate Change Canada 2018). The dataset comprises of the daily values of precipitation, relative humidity, temperature, wind speed, and net radiation. The compiled climate datasets were statistically analyzed to compute historical averages, maximum and minimum values, and other pertinent information for various climate variables over the 30 years (Baninajarian et al. 2019; Baninajarian, 2020; Baninajarian et al. 2021; Bashir et al. 2020; Pk et al. 2020).

Future climate data was collected from published sources. In particular, the future climate data from Ontario Climate Data Portal (OCDP) published by the laboratory of mathematical parallel systems (LAMPS) at York University was determined to perform the best when back predicting the historical climate data (Baninajarian et al. 2019; Baninajarian, 2020; Baninajarian et al. 2021; Bashir et al. 2020; Pk et al. 2020). The OCDP provides future climate data for the period of 2011 to 2100. The portal contains projections for four climate variables, daily precipitation, maximum, minimum, and average temperatures on a 10 x 10 km grid resolution for Ontario. In order to estimate the potential evaporation, Baninajarian (2020) and Pk (2017) have compared the Pereira and Pruitt (2004) method to the Penman (1948) method for the determination of daily potential evaporation values. They reported that the Pereira and Pruitt (2004) method estimated similar values as the Penman (1948) method. Moreover, the Pereira and Pruitt (2004) method has a greater advantage as it only requires daily minimum, mean, and maximum temperature data for estimation of potential evaporation.

Figure 4.2: Map of the ten locations in Ontario considered for climate data analysis

There are 33 general circulation models (GCMs) for four representative concentration pathways (RCP 2.6, RCP 4.5, RCP 6.0, and RCP 8.5) contained within the OCDP. The GCMs are the standard climate models used based on the IPCC's Fifth Assessment Report (IPCC, 2014). The primary function of a GCM is to understand the dynamics of physical components of the climate system (atmosphere, ocean, land, and sea ice) and make projections based on future greenhouse gas and aerosol forcing (Flato et al., 2013). Whereas the RCPs are proposed in IPCC's Fifth Assessment Report as scenarios to project future climate on several assumptions concerning future greenhouse gas emissions. Each pathway leads to a specific radiative forcing, which the IPCC defined as the change in energy flux caused by a driver and is calculated at the tropopause or at the top of the atmosphere (IPCC, 2014). By the year 2100, RCP 2.6 is considered to be the

best-case scenario whereas RCP 8.5 is the worst-case scenario, with the greatest concentration of radiative forces.

4.2.2.1 Selection of Long-Term Climate Data

From the 33 GCMs contained within the OCDP, Baninajarian (2020), Bashir et al. (2020) and Pk (2017) determined that CCSM4, GFDL-ESM2M, NorESM1-M, and Had GEM2-ES are the four GCMs that performed best when predicting the historical data for different cities within Ontario. Therefore, these four GCMs are used in long-term analysis of future climate projections. For each of the four GCMs, 90 years of future climate data (2011-2100) were subdivided into 30-year periods. This resulted in 48 future climate ensembles (*CE*) for the four RCPs (Figure 4.3). The historical climate data for the period of 1981 to 2010 is designated as *CE*#1. Further examination of this climate data can be found in Baninajarian (2020), Baninajarian et al. (2021), Bashir et al. (2020), Pk (2017), and Pk et al. (2020).

As the climate data for ten locations for four GCMs and four emission pathways results in 490 thirty-year daily climate datasets, the selection of an appropriate design climate is recommended (Baninajarian 2020). It was decided that for Toronto, all 48 future climate ensembles presented in Figure 4.3 will be used to examine the performance of LIDs. Considering that Toronto is the biggest urban centre in Canada, this was accomplished for a comprehensive assessment. Considering the computational resources, the time required to analyze all of the results and review of the assessment for Toronto, indicated that selection of a design climate based on the wettest condition is an appropriate strategy for other urban centres. In order to choose an appropriate climate scenario from the four different GCMs and RCPs, the future climate scenario that produces the wettest condition in the LID substrates can be considered for other locations. Baninajarian (2020) noted that simply choosing the climate ensemble that produces the highest increase in precipitation and annual moisture index has two inherent shortcomings when selecting the climate scenario that produces the wettest conditions within the soil. First, choosing the

greatest precipitation and annual moisture index only considers the water availability from atmospheric conditions. Bashir et al. (2016) has demonstrated that the water balance at ground level is a function of the soil hydraulic properties. Secondly, Baninajarian (2020) indicated that the water balance at ground surface is a function of a sub-daily temporal scale as well. This means that the amount of water entering the ground surface differs if one were to use a daily resolution versus a sub-daily resolution of precipitation data, due to the hydraulic conductivity of the soil. Thus, Baninajarian (2020) completed numerical simulations using the same climate data for the ten locations in Ontario to determine the critical scenario for sand and silt materials. The critical scenario was determined to be the climate data that produced the largest degree of saturation as this would decrease the factor of safety of the embankment from a stability perspective. For this research, the scenarios that produced the largest degree of saturation for the sand material from Baninajarian (2020) are used and are presented in Table 4.2. As the LID media are coarse-grained materials, the scenarios are selected for the sand material rather than the silt material.

4.2.2.2 Extreme Precipitation Events

According to the IPCC (2013), the frequency and intensity of extreme precipitation events have increased since 1950 in North America. The increase in extreme events can cause heavy economic, social, and environmental hazards. In order to design infrastructure and stormwater management systems for a region, intensity-duration-frequency (IDF) curves are used to determine the probability of a storm event occurring under certain intensities. Environment and Climate Change Canada (2014) provides historic IDF curves for the province of Ontario. Whereas future IDF curves are published by various sources. Baninajarian (2020) determined that the future IDF curves published by Ontario Climate Change Data Portal (CCDP, 2018) using the regional climate model, RegCM, predict higher intensities compared to other published sources and are therefore used for this research. The RegCM uses the outputs from HadGEM2-ES GCM and predictions for RCP 8.5 emission scenario, which are considered in this research.

Table 4.2: Selected long-term climate scenarios for ten locations

Location	General Circulation Model	Representative Concentration Pathway
Windsor	Nor	8.5
London	Had	8.5
Niagara	GFDL	2.6
Toronto	Had	8.5
Kingston	Had	6.0
Ottawa	GFDL	4.5
North Bay	Had	8.5
Timmins	CCSM	4.5
Thunder Bay	GFDL	2.6
Kenora	GFDL	8.5

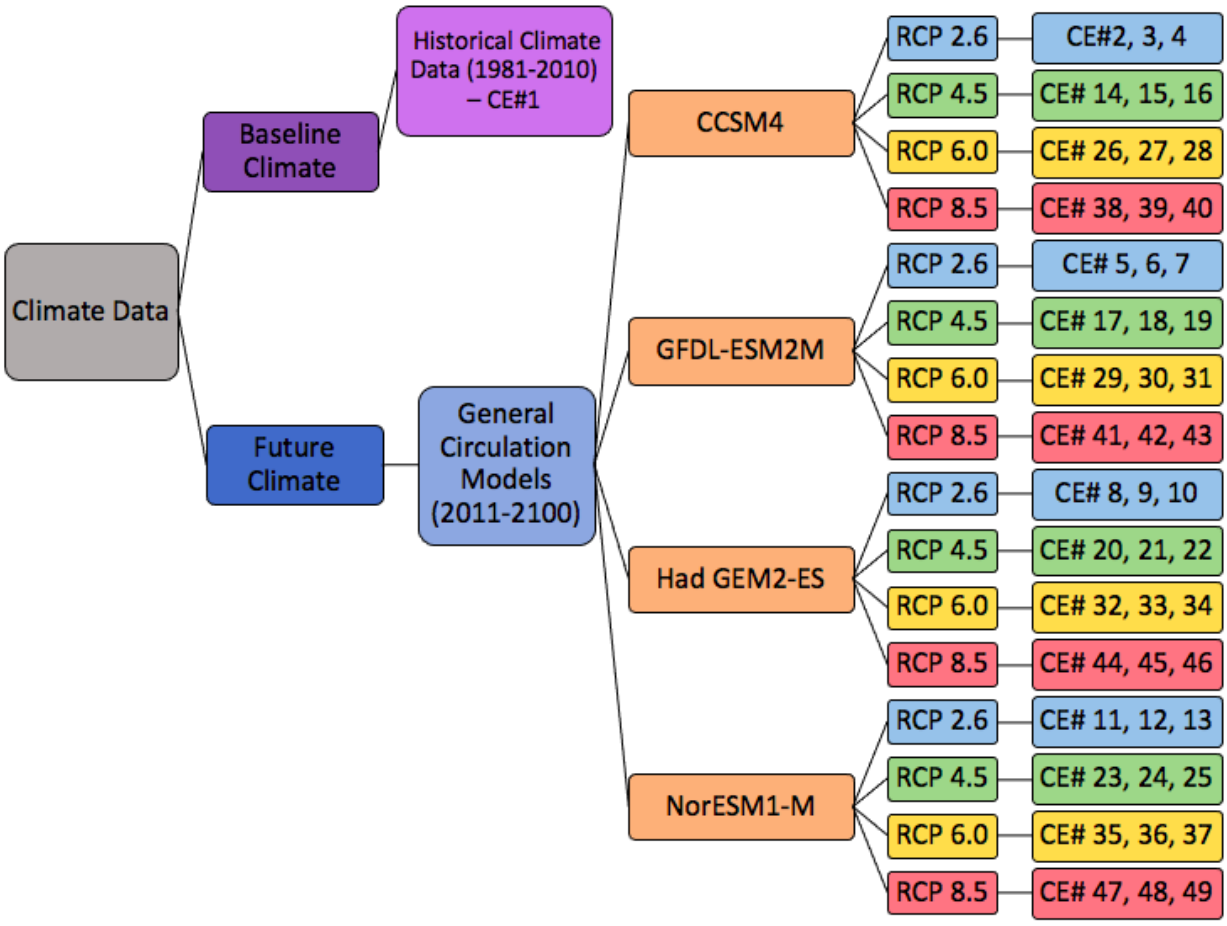

Figure 4.3: Flow chart of baseline and future climate data used in long-term analysis

Baninajarian (2020) compiled and compared IDF curves for ten different locations in Ontario. These locations include Windsor, London, Niagara, Toronto, Kingston, Ottawa, North Bay, Timmins, Thunder Bay, and Kenora (Figure 4.2). According to the analysis conducted by Baninajarian (2020), there is a greater percent change for most locations observed for the 6- and 24-hour durations as compared to the 1-hour storm duration. In addition, all locations project an increase in the intensity of extreme events, with the exception for the city of Kenora. Figure 4.4 illustrates the percent change between the base and future precipitation for 1, 6, and 24-hour

storm durations for the ten locations in Ontario, arranged from most southerly to most northerly location. It can be observed that for 24-hour, 100-year storm events, the city of Niagara has the greatest percent increase of 158%. The city of Kingston also has a large percent increase of 150%. There is a similar trend observed for most locations with the exception of the cities of Toronto, Timmins and Ottawa, for the 24-hour storm events. For Toronto, Timmins and Ottawa, there is a greater increase in the storms with a 2-year return period compared to the 100-year return period. This means that in the future, Toronto, Timmins and Ottawa will have an increase in smaller intensity storms that have a greater probability of occurring within a given year compared to the other locations. Additionally, both Toronto and North Bay have minimal change in precipitation for the 6-hour storm event compared to the other locations. It can also be noted that the cities located northern part of Ontario with 100-year return periods have a smaller change in precipitation compared to the locations in the southern part of Ontario.

With the acquired IDF data, synthetic design storms can be developed to be used in the numerical analysis. Kiefer and Chu (1957) proposed a method, also known as the Chicago design storm, that uses the IDF data to develop the synthetic design storm. The Chicago method uses the entire IDF curve to develop the design storm, unlike the rectangular or triangular hyetographs (Yen and Chow, 1980), where a single point on the IDF curve is used (Prodanovic and Simonovic, 2004). The method proposed by Kiefer and Chu (1957) is suggested for urban storm designs by the Ministry of Transportation of Ontario (MTO, 1997), and was used for this research. Figure 4.5 demonstrates an example of a design storm developed using the Chicago method from a Toronto historical IDF curve.

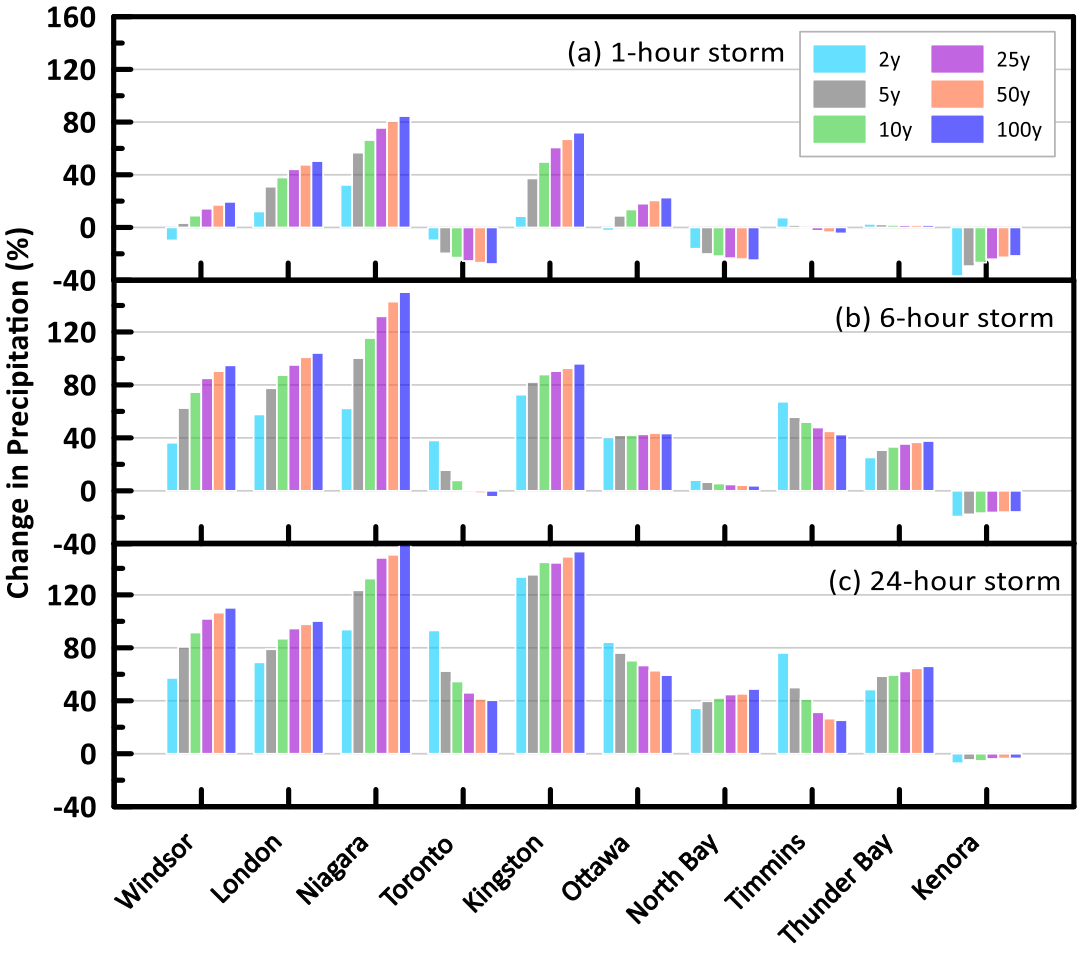

Figure 4.4: Percent change between base and future (a) 1-hour, (b) 6-hour, and (c) 24-hour storm durations

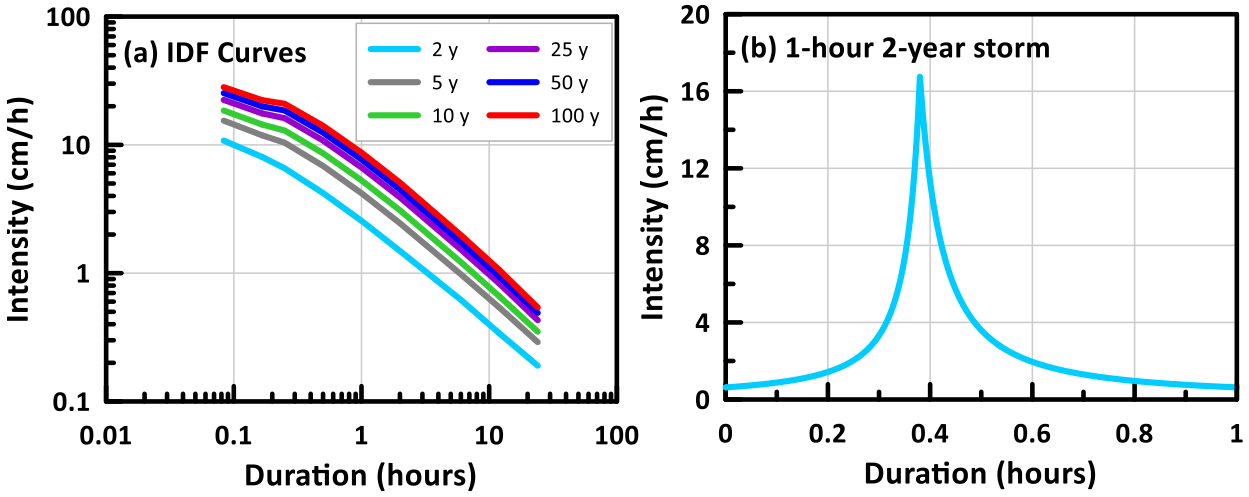

Figure 4.5: Example of design storm development from (a) IDF data using the (b) Chicago method

4.2.3 Initial and Boundary Conditions

The initial conditions could play a significant part in design storm analysis. A substrate with wet initial conditions would lead to a greater runoff or ponding depth in comparison to drier initial conditions. Long-term 30-year simulations were carried out using the historical and future climate datasets. Average soil water pressure conditions were extracted from 30 years of Toronto historical data simulation and were used as the initial conditions for the design storm simulations. To complete a comparison for all locations considered in Ontario, the initial conditions for each location was taken as the same.

For the lower boundary condition, both LID substrates were simulated with a free drainage boundary condition. The upper boundary condition was set to atmospheric with a surface layer. Daily records of precipitation and potential evaporation values constituted the atmospheric boundary. The allowable ponding was taken as zero for the green roof. On the other hand, bioretention facilities cater to a greater catchment area in addition to the precipitation that directly infiltrates the system. According to CVC and TRCA (2010), the maximum ponding depth should

be between 15-25 cm. Therefore, for the bioretention facilities models, allowable surface ponding was set to 20 cm.

The water balance at the ground surface describes the water that moves across the soil-atmosphere boundary. Components of the water balance at the ground surface include precipitation (*P*), potential evaporation (*PE*), actual evaporation (*AE*), surface run-off (*RO*), and net infiltration (*NI*). The net infiltration refers to the amount of water that enters the soil and can be described as:

$$NI = P - AE - RO \quad [4.2]$$

The *AE* is dependent on prevailing water quantity in the soil near the ground surface and is therefore, in most cases, less than the potential evaporation. To estimate the actual evaporation, HYDRUS uses a special type of boundary where the flux is not known a priori. With the system-dependent atmospheric boundary condition at the top of the modelling domain, the direction and magnitude of the potential flux at the ground surface is dependent on external atmospheric conditions, such as precipitation and evaporation. The actual flux is dependent on the external conditions and the soil moisture conditions. Within the context of system dependent boundary, the soil surface boundary condition may change from prescribed flux to prescribed head type condition and vice versa.

4.2.3.1 Impervious to Pervious Ratio

Bioretention systems are designed for ponded conditions as they cater to a greater catchment area in addition to the precipitation directly falling onto the system. The amount of stormwater runoff is dependent on the catchment area and degree of imperviousness of the area (Khan et al. 2013). A ratio known as the Impervious to Pervious ratio (I/P) combines these two factors in the following relationship:

$$V_i = dA_B\left(\frac{I}{P}+1\right) \quad [4.3]$$

where V_i is the volume of the influent, d is the precipitation depth, and A_B is the area of the bioretention system. As HYDRUS treats additional precipitation in units of depth rather than volume, the equation can be rewritten as follows (House et al., 2017):

$$d_i = d\left(\frac{I}{P}+1\right) \quad [4.4]$$

where d_i is the depth of the influent. If the percentage of the catchment area was 10% and the percentage of impervious area was 60%, the I/P ratio would be 6. This would result in a depth of influent 7 times greater than the precipitation depth. It is suggested that the bioretention system should have an I/P ratio of 5 to 20 (CVC and TRCA, 2010). Therefore, an I/P ratio of 6 is used for this research for the bioretention systems. For the green roof system, there is no additional stormwater entering the system other than the precipitation directly falling on the system. Thus, the green roof system would have an I/P ratio of 0.

4.2.4 Geometry

The HYDRUS software family is able to simulate 1-, 2- and 3-dimensional movement of water, energy and solute in variably saturated media. For this research, both 1D and 2D analysis of the LID geometry are examined. For 1-dimensional analysis, HYDRUS 1D version 4.17 is used (Šimůnek et al. 2018a). HYDRUS (2D/2D) version 3.01 is used for the 2-dimensional analysis (Šimůnek et al. 2018b). A triangular mesh was used for the two-dimensional analysis where a finer mesh was applied to the top of both the green roof and bioretention systems.

An extensive green roof has a substrate depth equal to or less than 15 cm for a smaller vegetation cover. Whereas intensive green roofs, have a substrate depth greater than 15 cm to accommodate deep rooted plants and heavy foot traffic (CVC and TRCA, 2010). For this research, the green roof was simulated with a 15 cm soil profile. Li (2014) simulated a green roof

configuration using HYDRUS 2D. As this configuration is a generic geometry of a green roof, it is used for the 2D analysis. Figure 4.6a and Figure 4.7 illustrates the geometry used for the 1D and 2D green roof configurations. For the 2D geometry, depressed water storages and raised drainage openings can be observed in Figure 4.7.

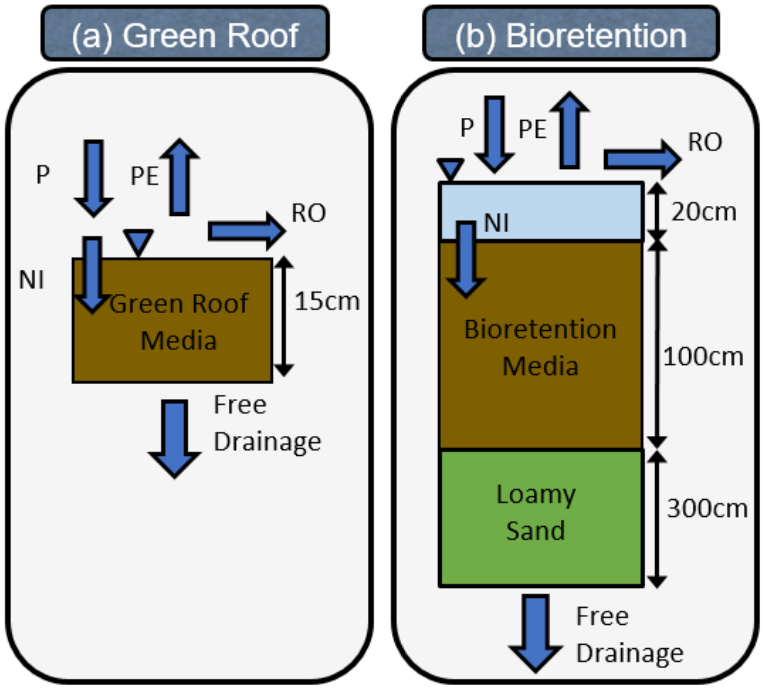

Figure 4.6: One-dimensional configuration of (a) green roof, and (b) bioretention media

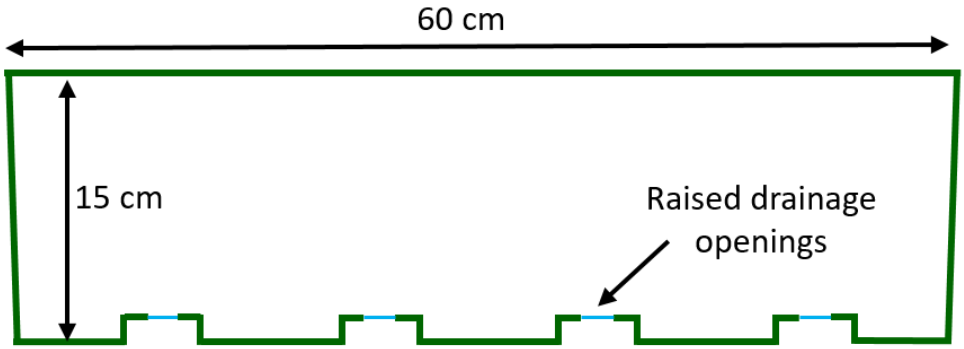

Figure 4.7: Two-dimensional green roof configuration (from Li, 2014)

For the bioretention system, CVC and TRCA (2010) recommend that the substrate depth should be between 1 and 1.25 m. In addition, bioretention facilities can be located above any soil type, however for soils with an infiltration rate less than 15mm/h (hydraulic conductivity less than 10^{-6} cm/s), an underdrain is required (CVC and TRCA, 2010). Therefore, the bioretention system is simulated with a 100 cm soil profile above 300 cm of loamy sand (Figure 4.6b). The hydraulic properties of the loamy sand were predicted using Rosetta Lite DLL (Dynamically Linked Library) which is included in the HYDRUS software (Šimůnek et al., 2008) to predict the van Genuchten (1980) parameters and saturated hydraulic conductivity (Schaap et al. 2001). The hydraulic properties for the loamy sand media are presented in Table 4.3.

Table 4.3: Hydraulic properties of loamy sand

Saturated hydraulic conductivity,	Fitted van Genuchten (1980) Parameters			
K_s (cm/h)	θ_s (cm^3/cm^3)	θ_r (cm^3/cm^3)	α (1/cm)	n
4.38	0.3904	0.0485	0.0347	1.7466

For the 2-dimensional analysis, a typical bioretention configuration was constructed and is presented in Figure 4.8. The main difference between the 1D and 2D geometry for the bioretention is that for 2D geometry there will also be lateral movement of water. The side slope of 4H:1V in 2D geometry is noted to be best suited for urban areas, particularly for pedestrian comfort (NACTO, 2013).

4.3 Results

4.3.1 Comparison of One and Two-Dimensional Analysis

To compare the 1D and 2D geometry, 30-years of the city of Toronto's historical climate data was used in the simulation for both the geometries. The cumulative net infiltration, actual evaporation and bottom flux were analyzed and compared. Figure 4.9 demonstrates the comparison of the

cumulative net infiltration, actual evaporation, and bottom flux (*BF*) from the 1D and 2D analyses for the green roof system. For the 2D analysis, the drainage openings with 1, 2, and 3 cm diameters were simulated. With the increasing diameter sizes, the cumulative water balance components for the 1D and 2D results in similar values. The percent difference between the 1D and 2D cumulative values for *NI, AE,* and *BF* are minimal demonstrating the similarity in the results.

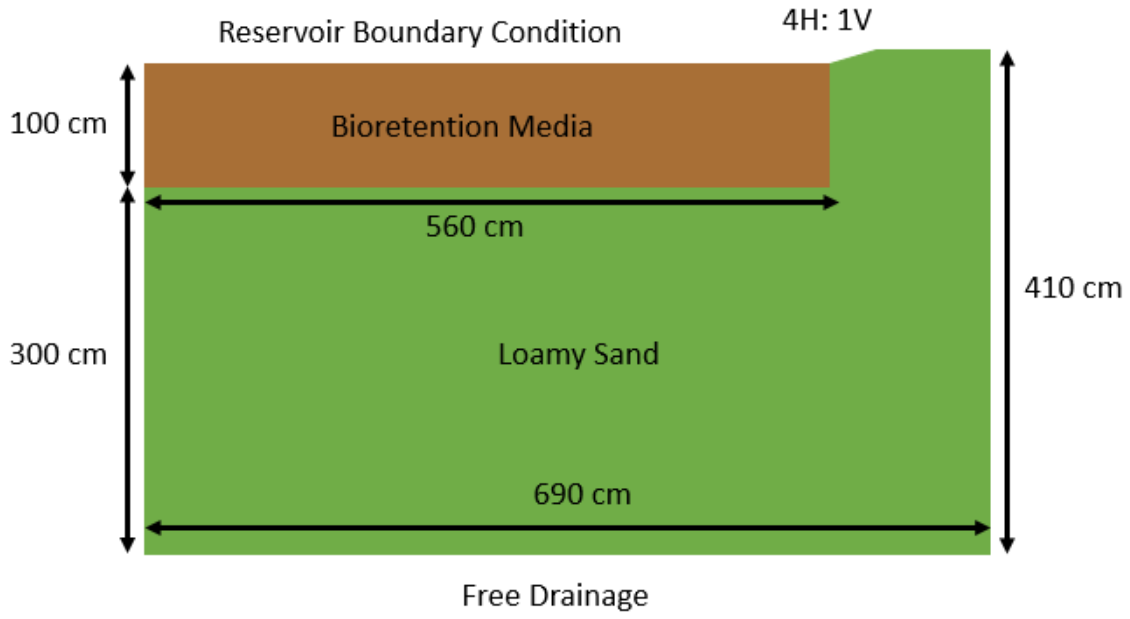

Figure 4.8: Two-dimensional bioretention configuration

For the bioretention system, Figure 4.10 presents the cumulative actual evaporation and net infiltration simulated from both the 1D and 2D analysis. Similar values of actual evaporation and net infiltration can be observed for both 1D and 2D bioretention analysis. Therefore, it can be concluded that the simulations for the green roof and bioretention analysis can be reasonably simulated using one dimensional domain. All additional simulations were completed using HYDRUS 1D.

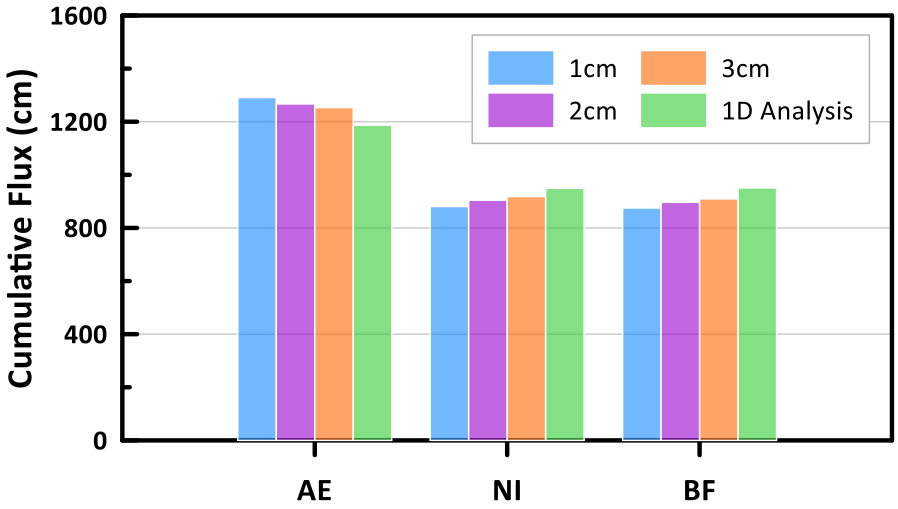

Figure 4.9: Comparison of cumulative fluxes for 1 and 2-dimensional green roof analysis

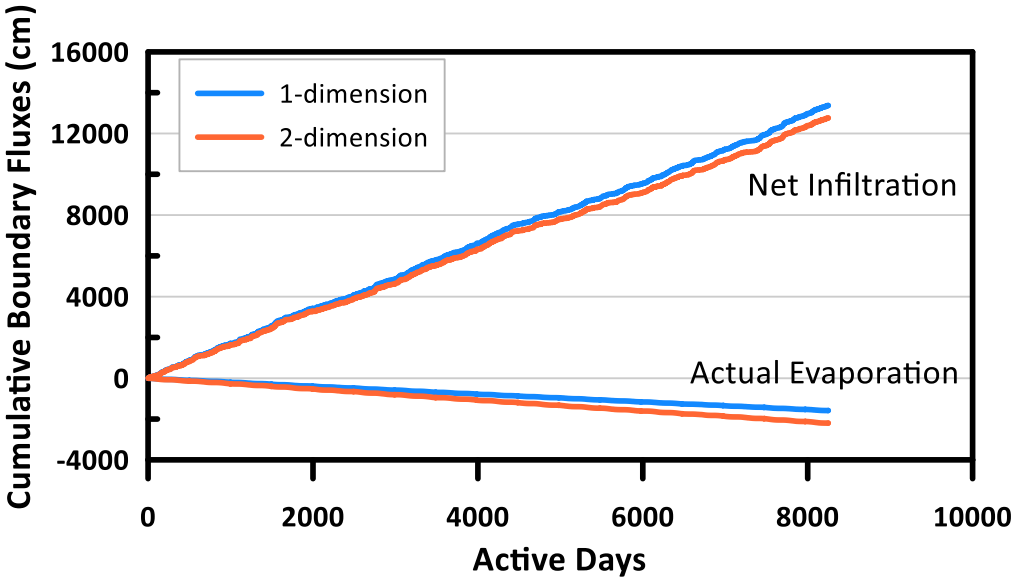

Figure 4.10: Comparison of cumulative fluxes for 1 and 2-dimensional bioretention analysis

4.3.2 Long-Term Analysis

As LIDs are relatively new in stormwater management techniques (CVC and TRCA, 2011), there are uncertainties about their performance under changing climate. Through the assessment of long-term climate analysis, the future quantity of water the LID systems are projected to handle

is examined and compared to the historical climate data. This provides an understanding of whether the LID systems may require additional design modifications to handle the increased quantity of water projected for the future. Over or under design of the LID system could be costly in the future and therefore should be examined thoroughly to avoid economical, social, or environmental risks.

In order to design and implement stormwater management systems to manage water for future climatic conditions, long-term simulations were carried out. To assess the behaviour of the green roof and bioretention substrates under the various climate ensembles, annual net infiltration values from different simulations are presented in the form of box and whisker plots. The box and whisker plots provide meaningful statistical estimates to study the possible trends for the future climate data for different GCMs and RCPs. This also assists in statistical quantification that which climate ensemble would likely produce unfavourable conditions, such as a large increase in the quantity of water in the future compared to the baseline.

For the first portion of this section on long-term analysis, specific focus on the annual net infiltration for Toronto using the four different GCMs for four RCPs is presented. This is followed by the annual net infiltration assessment for the other locations for climate ensembles that are identified to create the wettest conditions.

4.3.2.1 Long-Term Analysis for Toronto

The annual net infiltration values for 48 future climate ensembles for Toronto were compared to the value from baseline climate ensemble. Figure 4.11 and Figure 4.12 present the box and whisker plots for the green roof and bioretention substrates, respectively. The lower and upper ends of the box show the first and third quartiles, whereas the whiskers represent the maximum and minimum values of annual net infiltration. The dotted line in the centre represents the median of the base climate ensemble.

From Figure 4.11 and Figure 4.12, it can be observed that the GCM HadGEM2-ES predicts higher estimates of the annual net infiltration compared to the other three GCMs. Additionally, higher estimates of the annual *NI* are projected to occur under RCP 8.5 emission scenario. With the increase in time and RCP number, an increase in annual *NI* can be observed. This means that the annual net infiltration is projected to significantly increase later in the 21st century (2071-2100) under RCP 8.5 emission scenario. There is also no substantial change in median, first and third quartile values, with the exception of GCM HadGEM2-ES as well as NorESM1-M under RCP 8.5 emission scenario. There is, however, a large increase in maximum and minimum values projected in the future compared to the baseline predictions. A majority of the green roof future climate ensembles have a maximum annual net infiltration greater than the baseline. Whereas for the bioretention future climate ensembles, the maximum annual net infiltration for some ensembles are shown to be equal to the base third quartile.

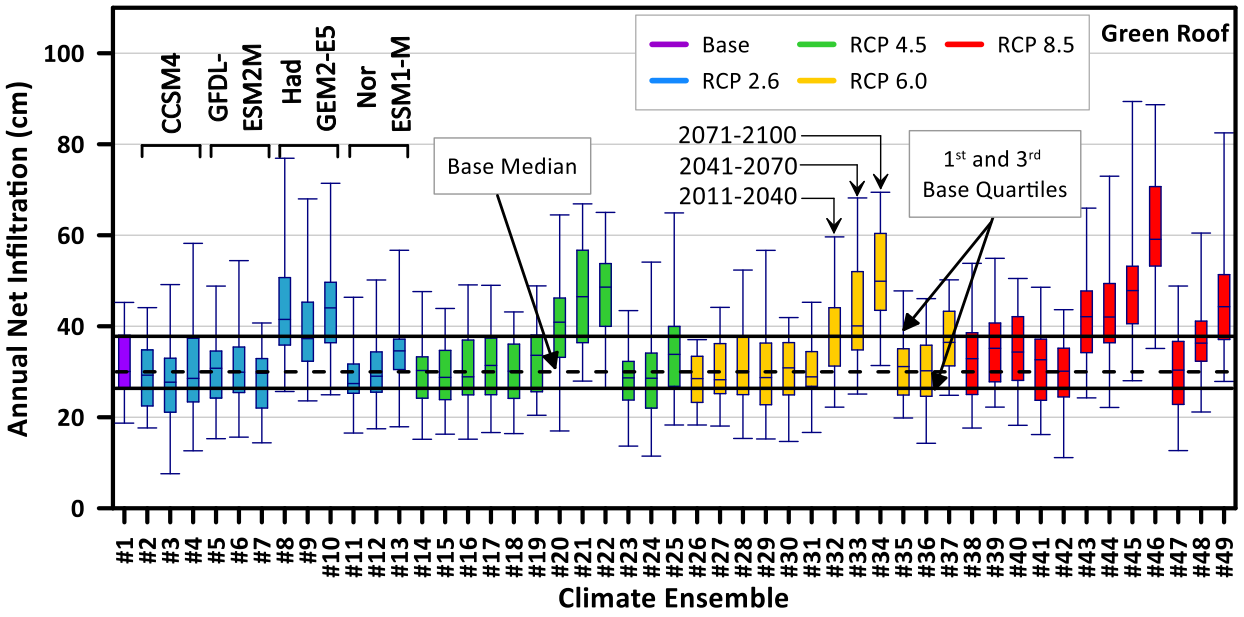

Figure 4.11: Comparison of annual net infiltration of green roof media in Toronto

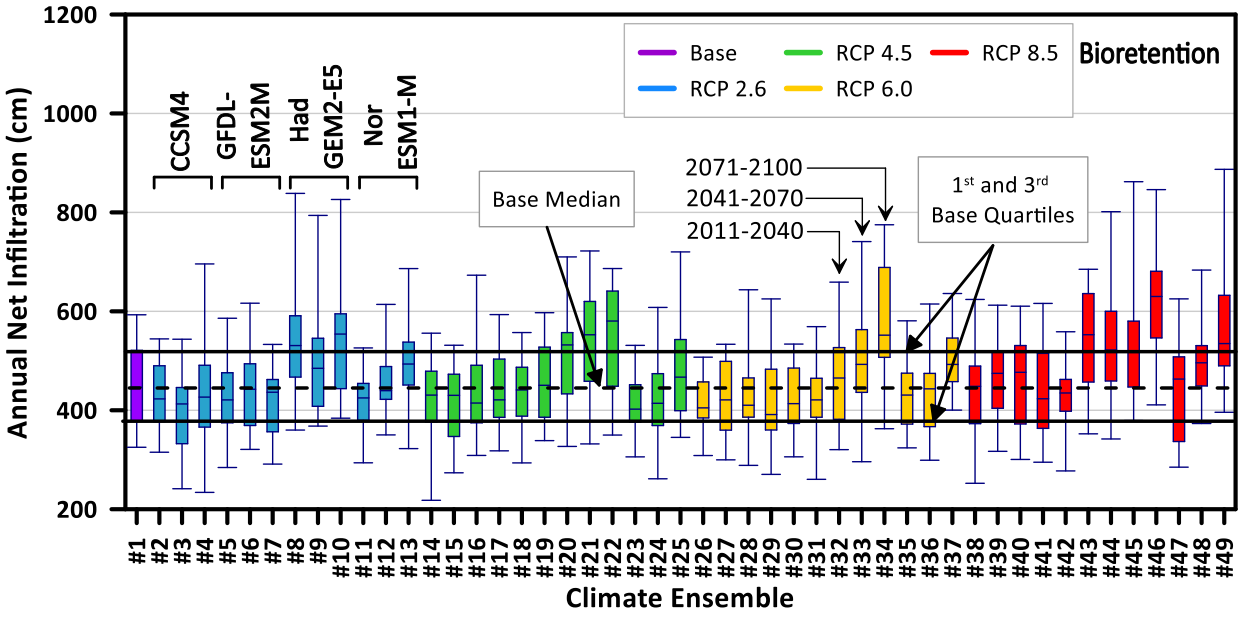

Figure 4.12: Comparison of annual net infiltration of bioretention media in Toronto

The base climate ensemble for the green roof substrate has a minimum and maximum annual net infiltration of 19 and 45 cm, respectively. Climate ensemble #3 has a minimum annual *NI* of 7.6 cm and climate ensemble #45 has a maximum annual *NI* of 89 cm. The percent difference between the maximum and minimum baseline and future climate ensembles are 98 and -59%, respectively. For the bioretention system, the base climate ensemble has a minimum and maximum annual net infiltration of 325 and 593 cm, respectively. Climate ensemble #14 has a minimum annual *NI* of 218 cm and climate ensemble #49 has a maximum annual *NI* of 887 cm. The percent difference between the maximum and minimum base and future climate ensembles are 50% and -33%, respectively. This large increase in annual net infiltration compared to the historic climate conditions can lead to reduced hydrological performance of the LID system.

When comparing the percent change between the base and future ensembles for the green roof and bioretention, the bioretention substrate has a smaller percent change for the maximum annual *NI* compared to the green roof media. The percent increase of the maximum annual *NI* compared

to the baseline for the green roof is +98% whereas for the bioretention it is +50%. Although both of these percent differences between the baseline and future ensemble is quite large, the percent change for the bioretention is smaller, even with a greater quantity of water entering the system. This means that the annual actual evaporation plays a key role for the quantity of water entering the system. As there is no run-off calculated for these simulations, the net infiltration is directly impacted by the actual evaporation, in addition to the precipitation.

Under the RCP 8.5 scenario, the temperature is projected to substantially increase in the future due to the increase in GHG emissions (IPCC, 2014; Baninajarian, 2020). This means that the potential evaporation is projected to increase with increasing temperatures. Although the potential evaporation is projected to increase, the actual evaporation is also dependent on prevailing water quantity in the soil near the ground surface and is therefore, in most cases, less than the potential evaporation. Even though the bioretention media has a greater quantity of annual *NI* compared to the green roof, the percent difference between the baseline and maximum annual *NI* is noted to be less. This means that the soil hydraulic properties are significant to the total annual *NI*. It is important to note that the actual evaporation is a system dependent boundary and is therefore dependent on external conditions as well as soil moisture conditions. Therefore, since the infiltration capacity of the bioretention media is smaller than the green roof, it also controls the quantity of *NI* and *AE* at the ground surface, in addition to the external atmospheric conditions. Thus, the total quantity of annual *NI* for the bioretention system far exceeds that of the green roof. However, the percent increase in future maximum annual *NI* compared to the baseline is smaller for the bioretention due to the system-dependent actual evaporation.

The annual actual evaporation for the green roof and bioretention media simulated using the 49 climate ensembles are presented in Figure 4.13 and Figure 4.14. The quantity and trend for the bioretention is immediately noted to differ from the green roof substrate. For the green roof media, there is a slight increase in actual evaporation with RCP and with time. However, this increase is

not as significant as the bioretention media, shown in Figure 4.14. For the bioretention media, a majority of the future climate ensembles exceeds the maximum annual actual evaporation of the historical climate ensemble. The bioretention media has available water at the ground surface that is able to reach a rate close to the potential evaporation rate. It is also noted that the GCM Nor ESM1-M for the later part of the 21st century projects higher estimates of the annual actual evaporation.

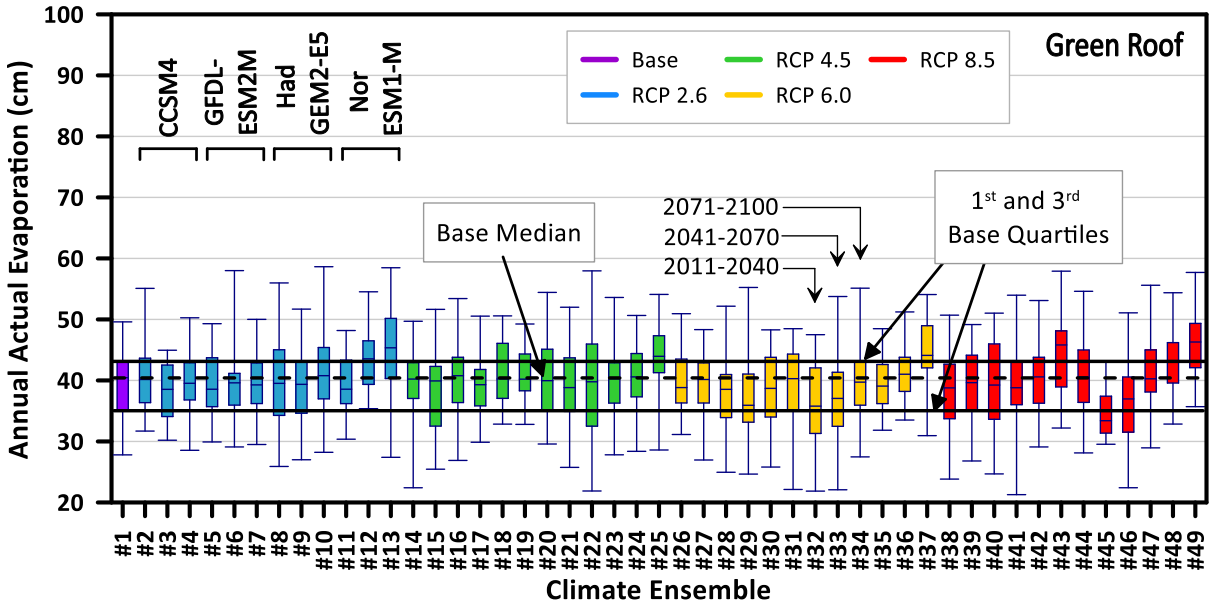

Figure 4.13: Comparison of annual actual evaporation of green roof media in Toronto

4.3.2.1.1 Significance of Active Days and Water Availability

The annual net infiltration of LID systems for the future is also observed to be dependent on the number of active days. The active period represents the time when the ground is thawed, thus allowing water to infiltrate into the soil. The inactive period is when the ground is frozen and the precipitation is in the form of snow. To demonstrate the significance of the number of active days on the annual *NI*, Figure 4.15 presents the future climate ensembles that have a greater active period compared to the baseline for the green roof media. Whereas the future climate ensembles

with a smaller active period compared to the baseline are presented in Figure 4.16. It is noted that a majority of the climate ensembles with a greater number of active days occurs in the later part of the 21st century (2071-2100). From Figure 4.15, it can be observed that the future climate ensembles with a greater active period have median annual *NI* values equal to or greater than the baseline. With the exception to *CE*#4, all future climate ensembles with a greater number of active days have a greater first quartile and median than the baseline. Additionally, the maximum annual *NI* for the future climate ensembles with a greater active period all exceed the baseline. This demonstrates that in the future, the increase in active days' results in a greater quantity of water entering the green roof system.

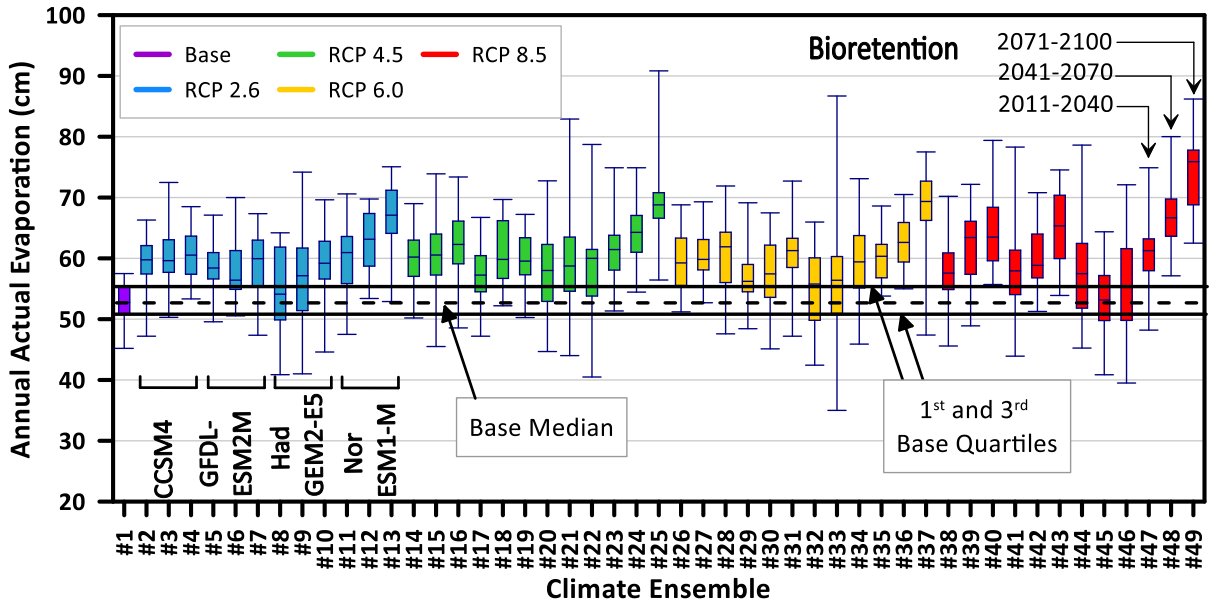

Figure 4.14: Comparison of annual actual evaporation of bioretention media in Toronto

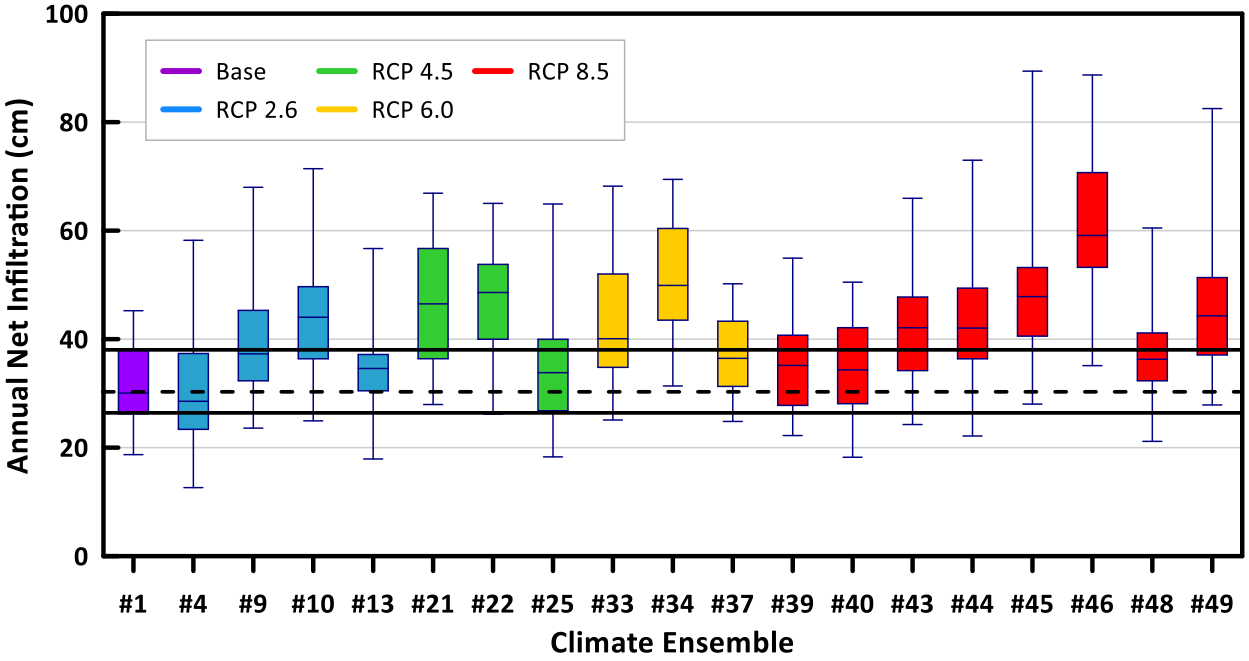

Figure 4.15: Comparison of green roof annual net infiltration for greater number of active days

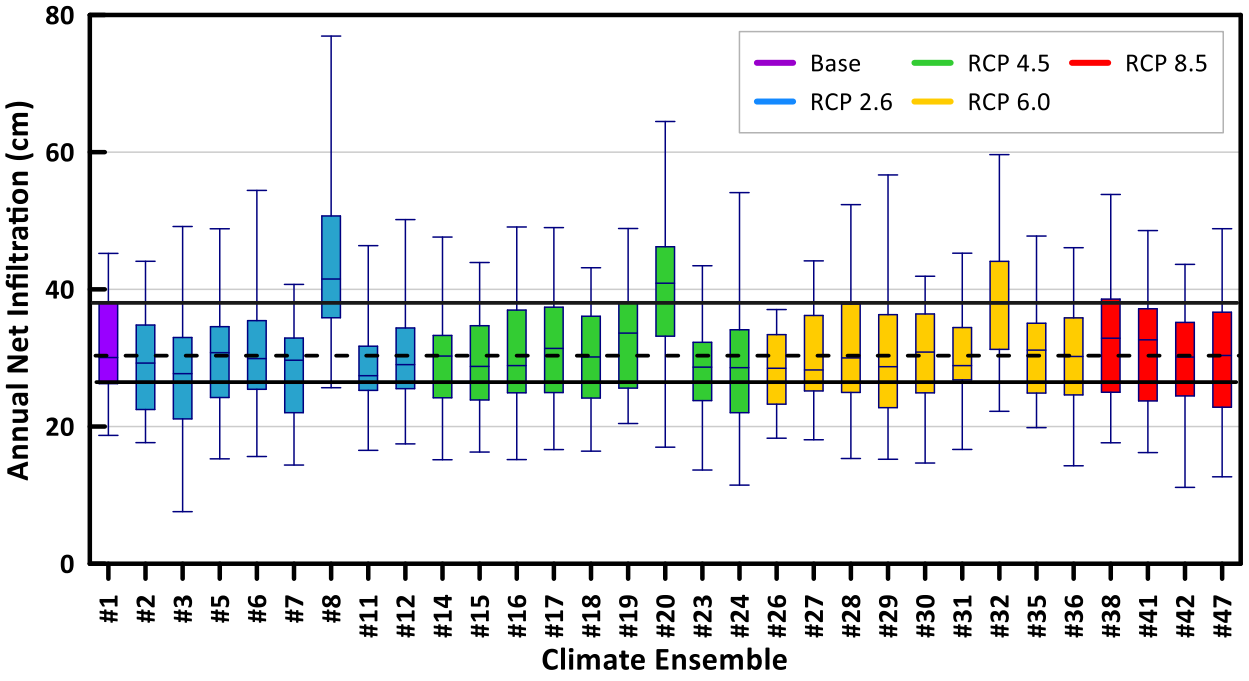

Figure 4.16: Comparison of green roof annual net infiltration for smaller number of active days

From Figure 4.16, a majority of the future climate ensembles have a third quartile equal to or less than the baseline third quartile. Exceptions are made for *CE* #8, 20 and 32, which have a smaller active period compared to the baseline, but a greater third quartile and median annual net infiltration. Note that *CE*#8, 20, and 32 are for the early part of the century (2011-2040) using HadGEM2-ES for RCP 2.6, 4.5 and 6.0, respectively. These exceptions are possibly due to the fact that this climate ensemble has a large annual moisture index (I_m). The Thornthwaite climate classification system (Thornthwaite, 1948; Thornthwaite and Hare, 1955) is determined by calculating the annual moisture index. The I_m is expressed as follows (Thornthwaite and Hare, 1955):

$$Im = 100\left(\frac{P}{PE} - 1\right) \quad [4.5]$$

where *P* is the annual precipitation and *PE* is the annual potential evaporation. An I_m of zero indicates that the annual precipitation and potential evaporation are equal. A positive I_m signifies a surplus of net water and a negative I_m implies a scarcity of net water. A positive I_m with the value between 0 to 20, 20 to 100, or greater than 100 has a climate condition of moist humid, humid, or pre-humid conditions, respectively. A negative I_m with the value between 0 to -33, -33 to -67, or -67 to -100 has a climate condition of dry subhumid, semi-arid or arid conditions, respectively. Note that the I_m refers to the water availability, not the total amount of water entering the system. Referring to Equation 4.2, the *NI* is dependent on the actual evaporation which, in turn, is dependent on the soil moisture conditions and the external atmospheric conditions.

A comparison of the annual moisture index of the base climate ensemble to the future climate ensembles is presented in Figure 4.17. The base climate ensemble is classified as dry subhumid conditions. On average, the future climate ensembles for Toronto stay within the dry subhumid range. The box and whiskers plot for the annual I_m demonstrates that the total precipitation far exceeds the potential evaporation for *CE* #8 leading to a surplus in net water. As *CE* #8, 20, and

32 are all for the early part of the century, there may be little change to the increase in temperature leading to more water availability. Additionally, as *CE*#8 is for RCP 2.6, the water availability is far greater with smaller temperature changes, leading to greater *NI*, even with a smaller active period compared to the baseline.

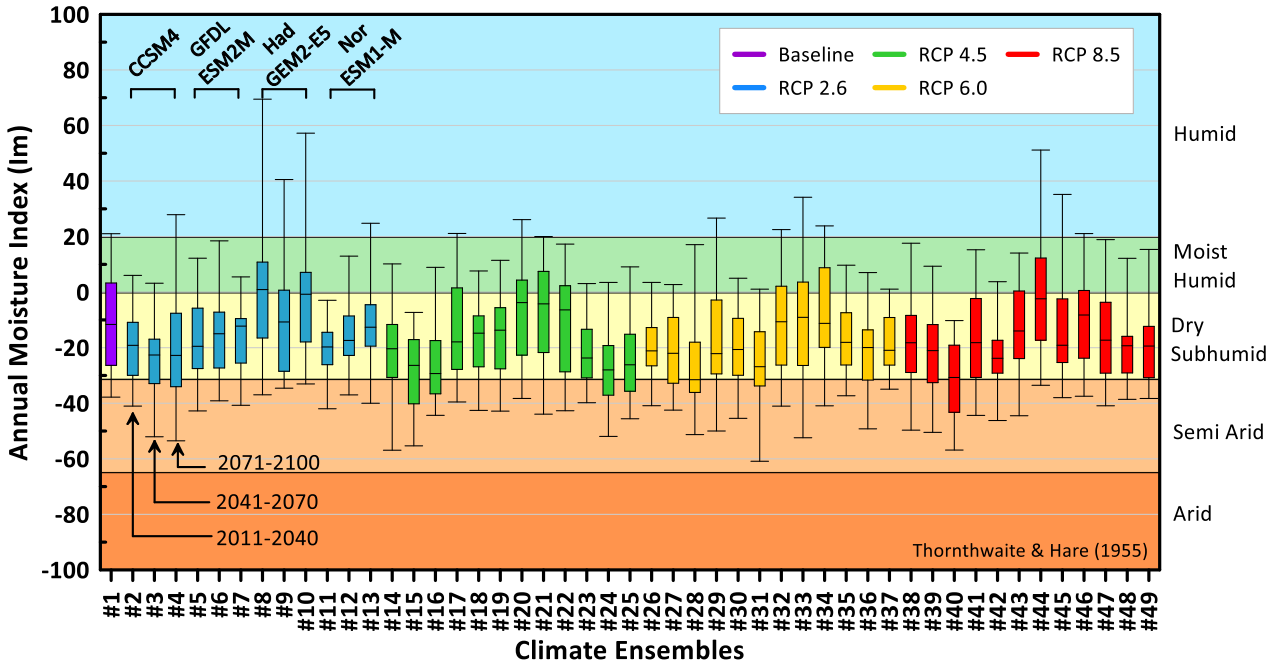

Figure 4.17: Comparison of green roof annual moisture index for base and future climate ensembles

Similarly, the climate ensembles for the bioretention media were also separated according to the number of active days. Figure 4.18 presents the climate ensembles with a greater active period compared to the baseline, and Figure 4.19 presents the climate ensembles with a smaller active period. Similar to the green roof media, Figure 4.18 demonstrates that all of the future climate ensembles have a greater median compared to the baseline, with the exception to *CE*#4. Moreover, the maximum annual *NI* for all future climate ensembles exceed the baseline for the climate ensembles with a greater active period.

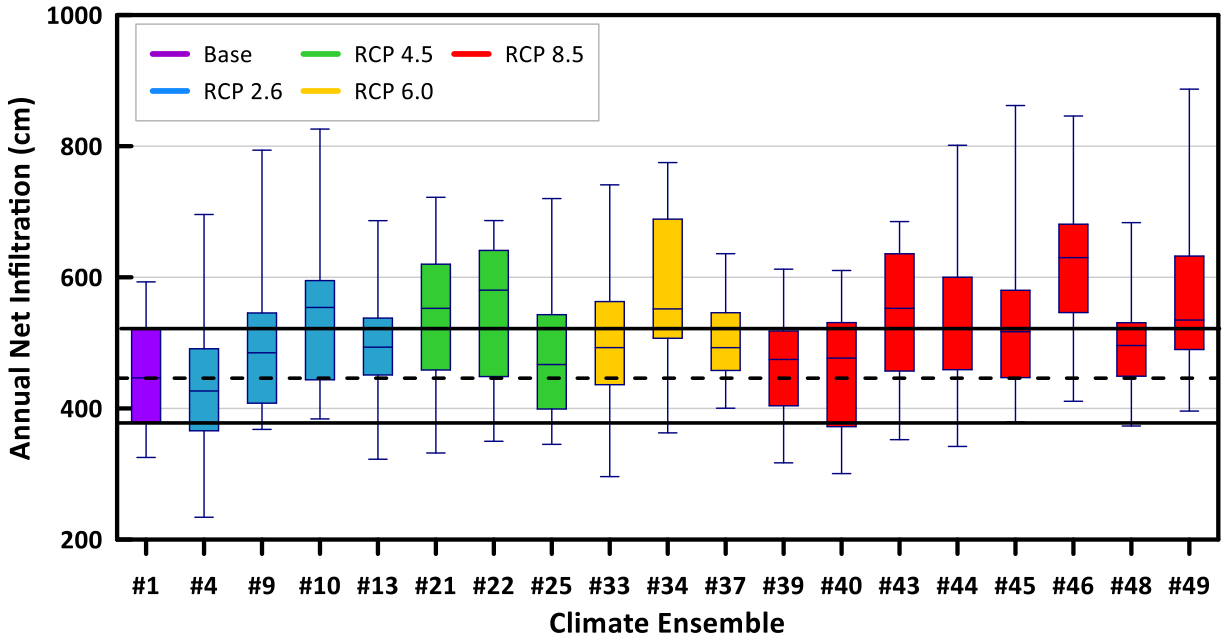

Figure 4.18: Comparison of bioretention annual net infiltration for greater active period

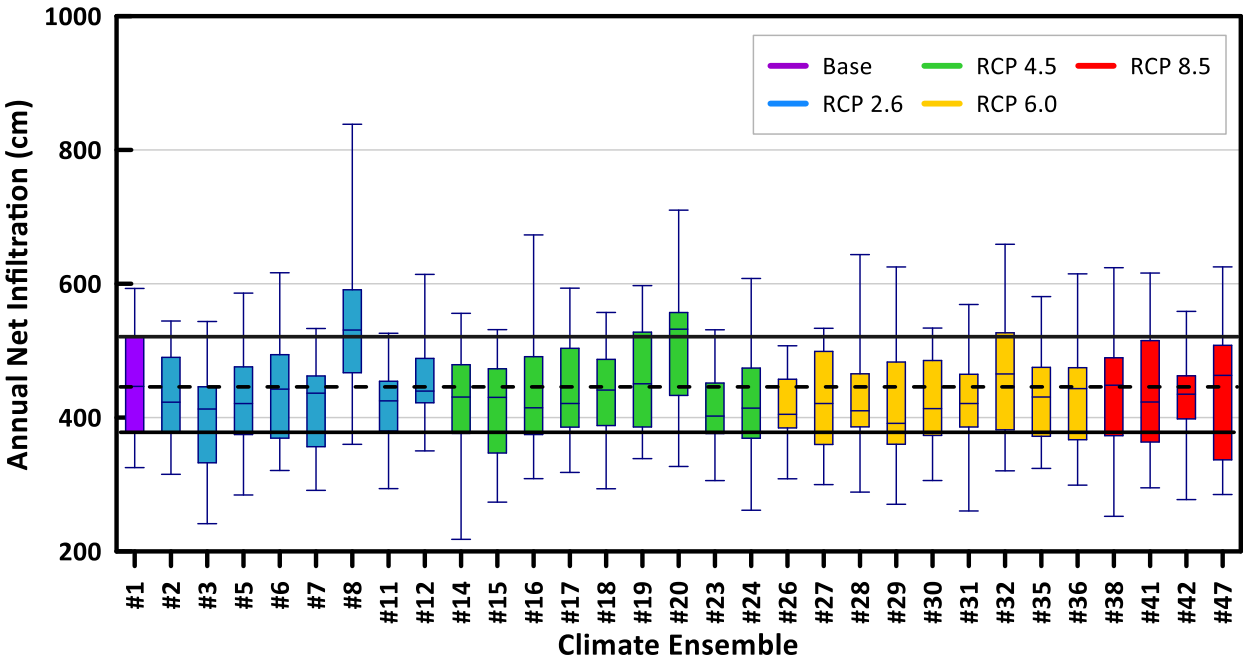

Figure 4.19: Comparison of bioretention annual net infiltration for smaller active period

From Figure 4.19, the bioretention media presents some dissimilarities when compared to the green roof media. For example, for the bioretention media, *CE*#8 and 20 have a third quartile greater than the baseline third quartile. Whereas *CE*#32 is only slightly greater than the baseline third quartile, which is unlike the green roof media. Furthermore, it is noted that there are less climate ensembles that have a maximum annual *NI* greater than the baseline for the bioretention media future ensembles compared to the green roof media. For a smaller active period, there are thirteen climate ensembles that exceed the baseline maximum annual *NI* for the bioretention. For the green roof, there are nineteen climate ensembles that exceed the baseline maximum annual *NI*. The annual moisture index for the bioretention media would demonstrate a surplus of water due to the I/P factor considered for the precipitation. Thus, the dissimilarities between the green roof and bioretention in annual *NI* once again stems from the soil moisture conditions.

Overall, the number of active days, the water availability, and soil moisture conditions are significant in assessing the quantity of water entering the LID system. Critical future scenarios that project an increased number of active days and water availability will lead to large quantities of water entering the LID system.

4.3.2.1.2 Long-Term Plant Survivability

As there are negative annual moisture indices for some climate ensembles in the future, there is a possibility that there may not be adequate water for plant survival. As the green roof system has a large saturated hydraulic conductivity to avoid ponded conditions, it is more likely to experience unsaturated conditions compared to the bioretention. Thus, the plant survivability is checked for green roof long-term future climate analysis.

In order to simulate the plant survivability in HYDRUS, the model set-up is required to be updated to consider root water uptake. The soil profile is updated with the addition of roots. The amount

of water extracted is dependent on the distribution and depth of the roots (Fredlund et al. 2012). A triangular distribution would extract less water with depth, whereas a rectangular distribution would extract a constant amount with depth (Kumar et al., 2014). As the green roof substrate has a depth of only 15 cm, a constant or triangular root distribution does not result in a large difference.

To partition the potential evapotranspiration to potential evaporation and transpiration, the leaf area index (LAI) is used. The LAI is a dimensionless quantity that describes the amount of vegetation cover over an area of land. A large amount of plant cover indicates a higher LAI as there is a higher transpiration rate from the plants compared to the evaporation from the soil. The LAI can be approximated as follows (Šimůnek et al. 2018):

$$LAI = 0.24 * CropHeight \quad [4.6]$$

The LAI was approximated to be 1.2 as it was assumed that the vegetation on the green roof is grass with a height of 5 cm. Furthermore, Brunetti et al. (2016) assumed an LAI value of 2.29 for Sedum mix for a green roof located in Italy. Therefore, an approximated LAI of 1.2 seems reasonable.

The LAI is applied when there is vegetation cover, therefore the growing season is required to be defined. The inactive period is when the ground is frozen and the precipitation is in the form of snow. The active period is when the ground is thawed allowing for the infiltration of water into the soil. The growing season is not equal to the active period, rather it is the period during which the weather conditions are preferable for plant growth. The growing season length is calculated as the number of days between the last occurrence of 0°C in the spring and the first occurrence of 0°C in the fall (Government of Canada, 2020). Figure 4.20 illustrates the active period, inactive period, and growing days for Toronto baseline data. In Toronto, the baseline climate data has 275 active days, from March 26th to December 26th. The length, start and end of growing season, is contained within the 4th Edition (1974) of the National Atlas of Canada. The length of the growing

season is 200 days, starting on April 15th and ending on October 31st. The LAI value is applied during the growing season.

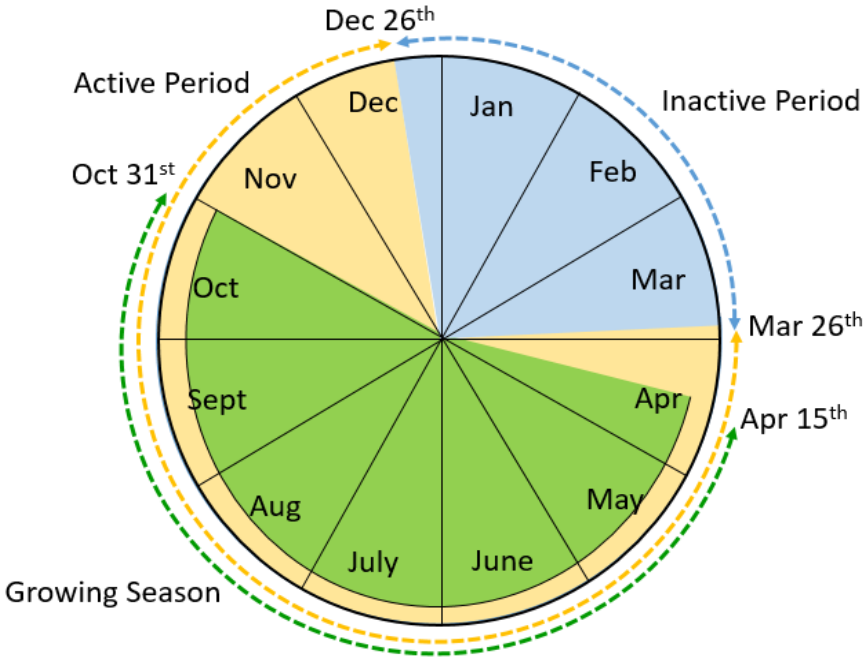

Figure 4.20: Illustration of active, inactive and growing period in Toronto

Thirty years of Toronto historic climate data is initially simulated using the root water uptake function in HYDRUS. From the unsaturated hydraulic properties, the field capacity and permanent wilting point are defined. The field capacity is the amount of water content held in the soil substrate after gravitational drainage has occurred. Typically, the field capacity is the water content at a soil water pressure of 33 kPa. Whereas the wilting point is the water content at a soil water pressure of 1500 kPa. If the soil water pressure exceeds this point, the plant will not recover and will wilt. From the green roof unsaturated hydraulic properties, it was determined that the volumetric water content at 33 kPa and 1500 kPa is 16.1% and 4.89%, respectively.

Figure 4.21a demonstrates the volumetric water content for the base climate ensemble. From the analysis, the volumetric water content does not fall below the permanent wilting point. Still, the

volumetric water content does reach a minimum value 5.69% and may require irrigation to avoid wilting of certain plant species. The future climate ensemble #40 is examined as well since it has the lowest annual moisture index value on average. The active period for climate ensemble #40 starts on February 22 and ends December 28. The growing season would also need to be adjusted for the future. An approximation of the growing season was completed using the average temperatures for that climate ensemble. The start of the growing season is taken as April 15th and the end is November 19th. Figure 4.21b demonstrates that the volumetric water content from the 30 years of CE#40 also does not pass the permanent wilting point. The volumetric water content reaches a minimum value of 5.61%. Therefore, according to this analysis, the future volumetric water content does reach a value slightly less than the base, but it does not pass the wilting point. If the volumetric water content did pass the permanent wilting point, a greater substrate depth would be required to increase the storage capacity.

4.3.2.1.3 Annual Runoff Reduction for Green Roof Media

In 2006, Toronto approved the Wet Weather Flow Master Plan (WWFMP). This plan is a long-term goal with the aim of reducing and ultimately eliminating the adverse impacts of wet weather flow in Toronto's environment. The WWFMP contains four categories; water quality in local waterways, water quantity, natural areas and wildlife, and sewer system (Toronto Water, 2017). Within the WWFMP, a water balance target states that the maximum allowable annual runoff volume from any development site should be 50% of the total average annual rainfall depth. As it is expected that climate change will likely result in an increase in annual rainfall depth, the green roof substrate is examined to determine whether it can accomplish this water target.

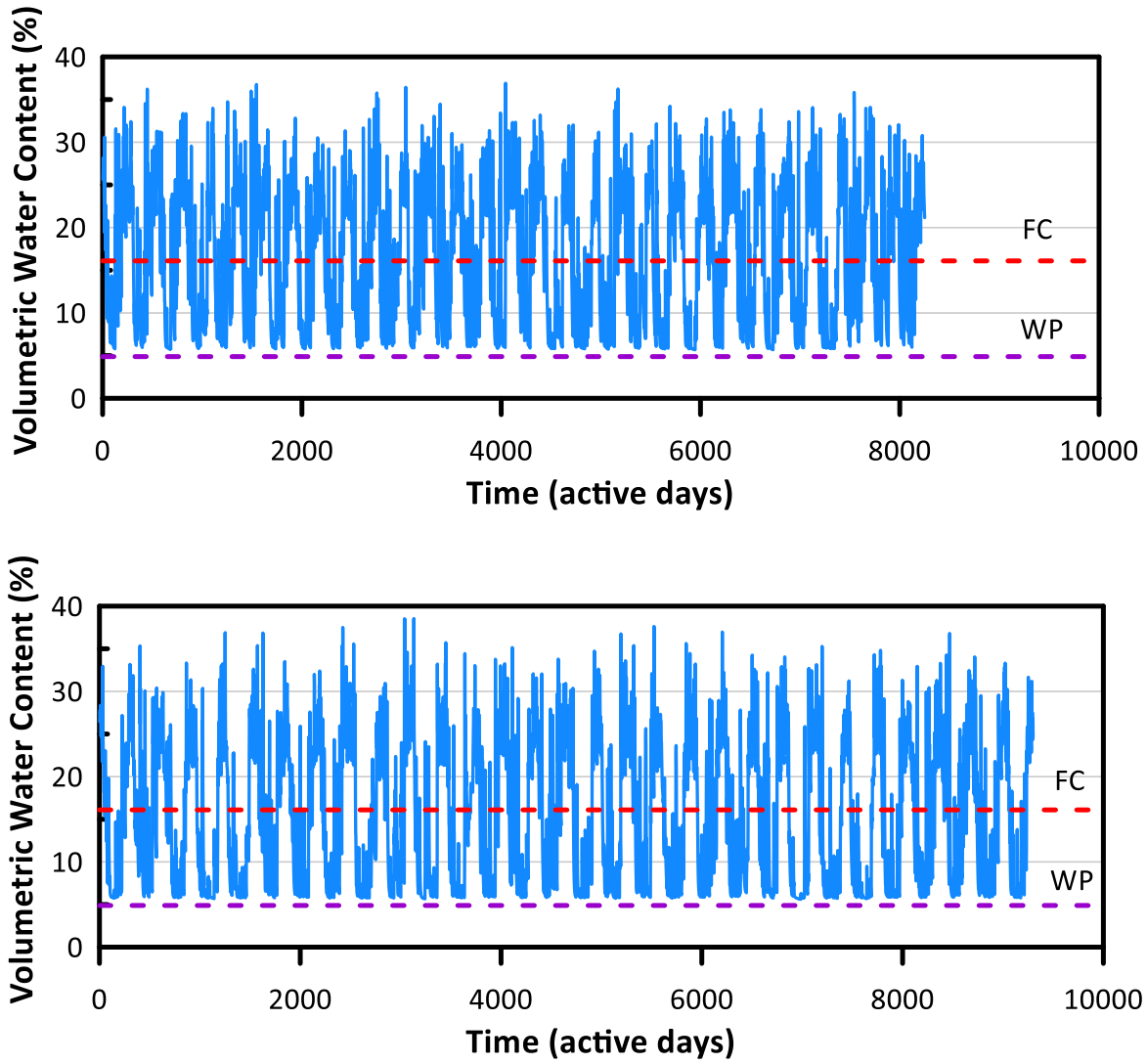

Figure 4.21: Analysis of plant survivability in green roof media under (a) base, and (b) future climate scenarios

The percent difference of the average annual precipitation and runoff from the green roof substrate for all 49 climate ensembles is plotted in Figure 4.22. Note that the runoff from the green roof is the bottom flux and not the surface runoff. The 50% threshold line is represented by a black dotted line. If the value is below 50%, the runoff from the green roof is greater than 50% of the average annual rainfall depth. Furthermore, Figure 4.22 is separated by future emissions as RCP 2.6, RCP 4.5, RCP 6.0, and RCP 8.5. Overall, it can be seen that in the future the water balance

target is not always met. In particular, the percent difference of the average annual precipitation and runoff under RCP 8.5 emissions has the smallest percent difference. For instance, in the year 2094 for *CE* #46, the total annual precipitation is projected to be 101 cm, whereas the total annual runoff was simulated to be 74.8cm. The percent difference is 26%, which is far below the water balance target. This demonstrates that due to climate change in the future, the site may not be able to meet the maximum allowable runoff.

To further present the impact of climate change on the current water balance targets, the number of times the annual runoff is more than 50% of the annual precipitation is shown in Figure 4.23. Within Figure 4.23, the climate ensembles are arranged according to the GCM source rather than the RCP emission. From the bar chart, the GCM Had GEM2-ES results in the greatest number of times the annual runoff surpasses the allowable site runoff. When compared to the base, there is a general increase in the number of events leading to reduction in site performance to the water balance target. With increasing time and RCP emissions, there is a greater number of events, where the annual runoff is greater than the 50% annual precipitation. Therefore, developers may want to consider alternative LID measures at the site to account for the climate change resulting in water balance targets not being met. As excessive runoff leads to flooding, erosion, and degraded water quality in receiving waters, this results in negative impacts to property owners, downstream ecosystems, and water users (Li, 2014). Therefore, it is ideal to meet the criteria in reducing the stormwater runoff generated during a rainfall event by designing for climate change.

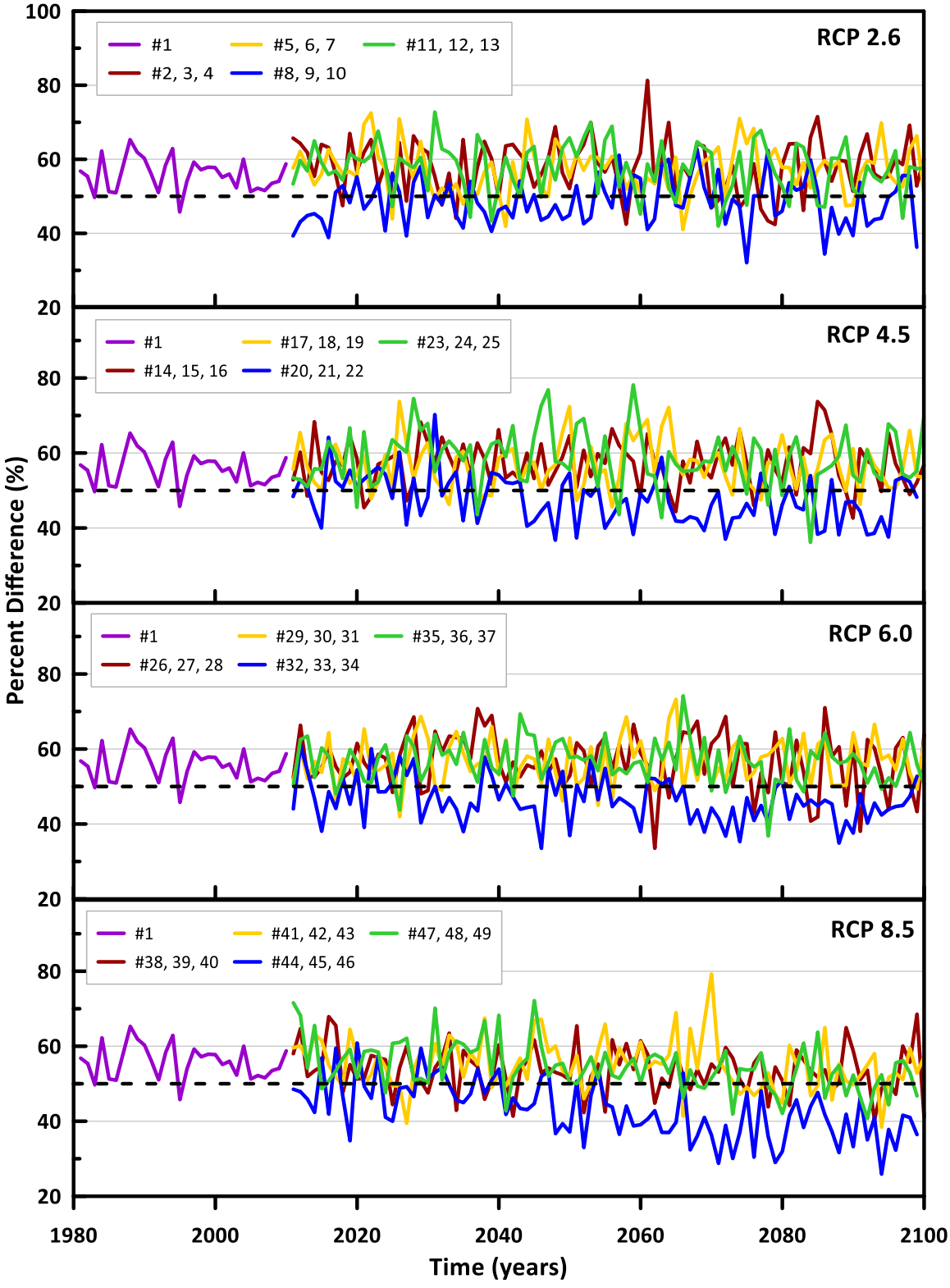

Figure 4.22: Percent difference of average annual precipitation to average annual runoff from the green roof media for difference emission pathways

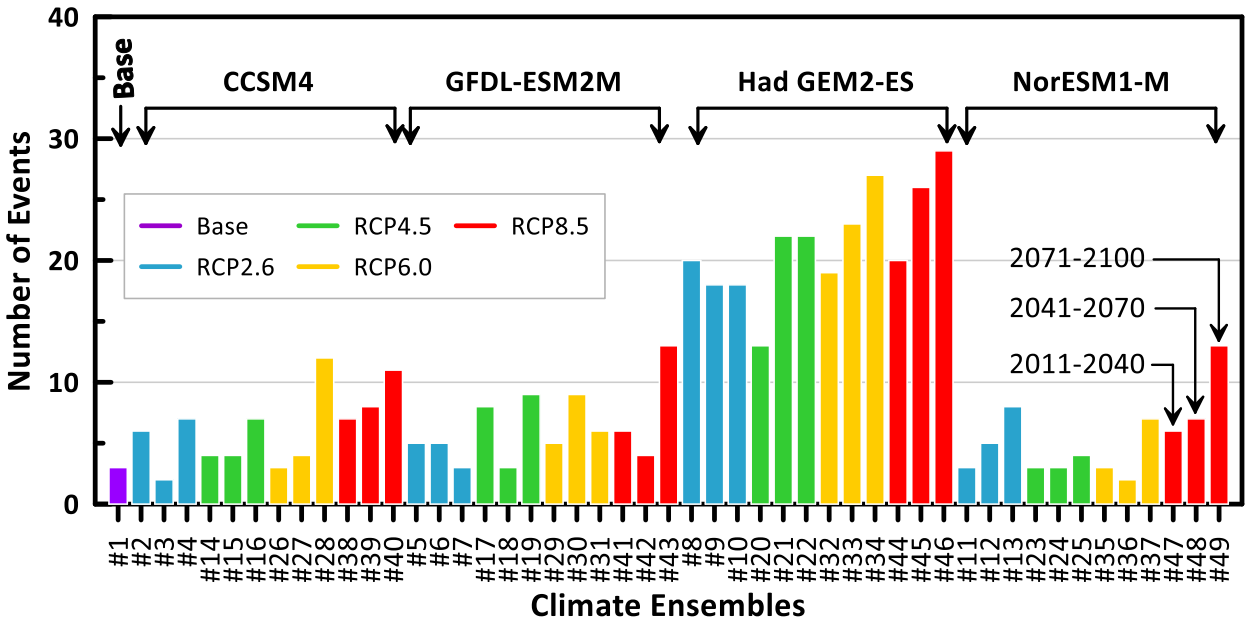

Figure 4.23: Comparison of how often the annual runoff is greater than the 50% annual precipitation limit

4.3.2.2 Long-Term Analysis for Ontario

The change in the quantity of water for all the ten locations in Ontario were examined for both the green roof and bioretention media. Figure 4.24 and Figure 4.25 presents the baseline and future annual net infiltration for the ten locations in Ontario in the form of box and whisker plots. The lower and upper ends of the box show the first and third quartiles, whereas the whiskers represent the maximum and minimum values of annual net infiltration. The line in the centre of the box represents the median climate ensemble. Furthermore, the future climate data was separated into 30-year periods; 2011 to 2040, 2041 to 2070, and 2071 to 2100.

From Figure 4.24 and Figure 4.25, it is noted that the three cities located in the north part of Ontario have the smallest quantity of annual net infiltration for both the green roof and bioretention media compared to the other locations. These cities are Timmins, Thunder Bay and Kenora. Additionally, in the later part of the century, the amount of annual net infiltration is shown to

increase for a majority of the cities. The maximum annual net infiltration for all the cities is greater in the future compared to the baseline. The 2071 to 2100 period for Kingston is shown to have the greatest maximum annual net infiltration for both the green roof and bioretention media. Furthermore, Niagara is the only city that has a maximum annual *NI* for the 2071-2100 period less than the maximum annual *NI* for the baseline.

The location that has the greatest percent change between the maximum annual net infiltration in the future compared to the baseline is Toronto for the green roof media and Kenora for the bioretention media. The maximum annual *NI* for the base and future (2041-2070) for Toronto is 45 and 89 cm, respectively. This results in a percent increase of 98%. For the bioretention media, the maximum annual *NI* for the base and future (2041-2070) for Kenora is 575 and 889 cm, respectively. This results in a percent increase of 55%.

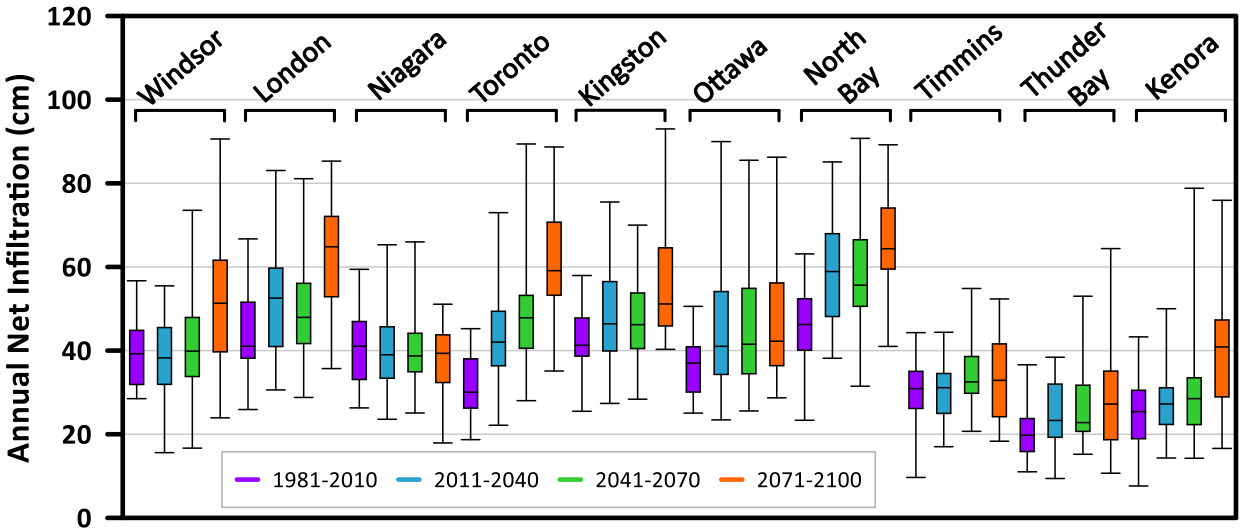

Figure 4.24: Comparison of green roof annual net infiltration in Ontario

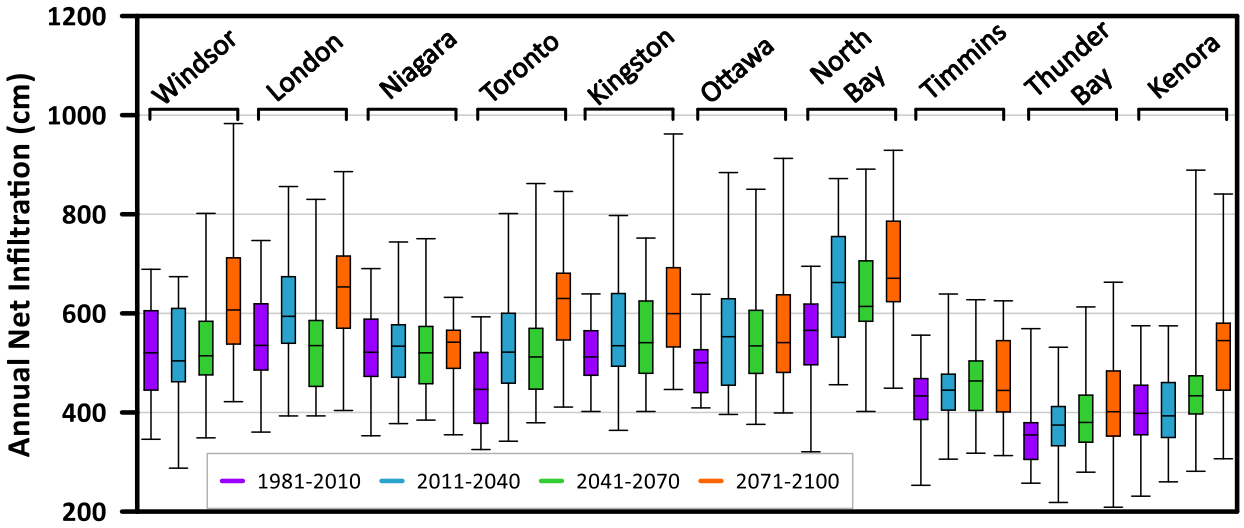

Figure 4.25: Comparison of bioretention annual net infiltration in Ontario

Similar to the assessment conducted for Toronto, the number of active days and the moisture indices are examined for all the ten locations in Ontario. Figure 4.26 to Figure 4.29 present the active days for the historic, 2011-2040, 2041-2070, and 2071-2100 ensembles for all ten locations. The blue arrows in the future ensembles represents a decrease in active days compared to the baseline. Whereas the red arrows signify an increase in active days.

From Figure 4.26, a notable observation is that the northern locations have a smaller number of active days compared to the southern locations. Ottawa, North Bay, Timmins, Thunder Bay, and Kenora have a smaller number of active days, starting later in April and ending in November. From Figure 4.27, the cities of Toronto and Ottawa, are shown to expect increase in the number of active days. Whereas the other locations have a smaller number of active days compared to the baseline. In Figure 4.28, Toronto, Ottawa, North Bay and Kenora are all seen to increase in the number of active days compared to the baseline. Finally, Figure 4.29 presents the later portion of the 21st century where a majority of the locations have an increased number of active days. An exception can be made for Niagara, Timmins and Thunder Bay. After Toronto, North Bay has the greatest increase in active days of 31 days for the 2071-2100 period. Whereas Niagara has the

greatest decrease in active days of 31 days for the 2071-2100 period. As the maximum annual *NI* for the 2071-2100 period for Niagara is the only city smaller than the baseline, this is possibly due to the reduced active period.

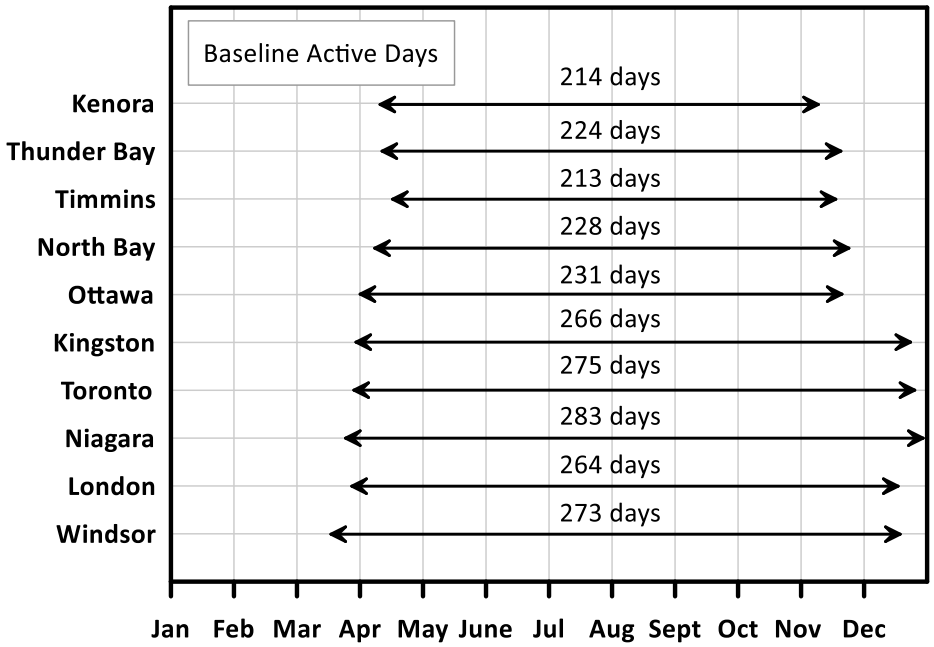

Figure 4.26: Historic (1981-2010) active days for ten locations in Ontario

The annual moisture index for all the ten locations in Ontario are presented in Figure 4.30. North Bay is observed to have the greatest annual moisture index for both the baseline and future climates, resulting in humid climatic conditions. This correlates to the large annual net infiltration presented in Figure 4.24 for North Bay. The median, first and third quartiles for a majority of the cities are located within the moist humid and dry subhumid range. The maximum and minimum extremes reach the humid and semiarid conditions. Kenora is observed to have a large difference in extremities, with the maximum I_m stretching to humid conditions and the minimum I_m reaching semiarid conditions.

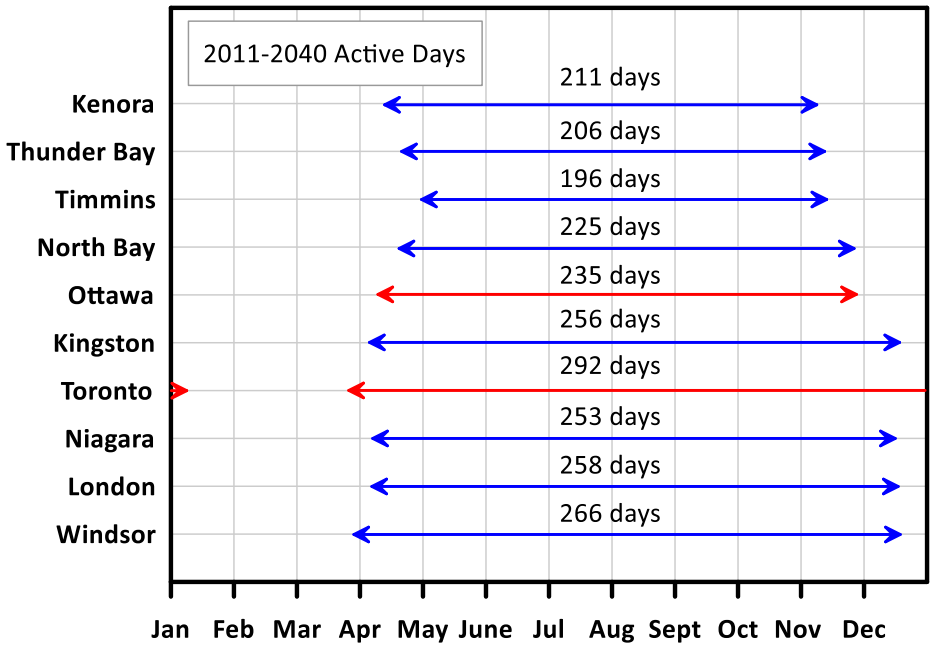

Figure 4.27: Future (2011-2040) active days for ten locations in Ontario

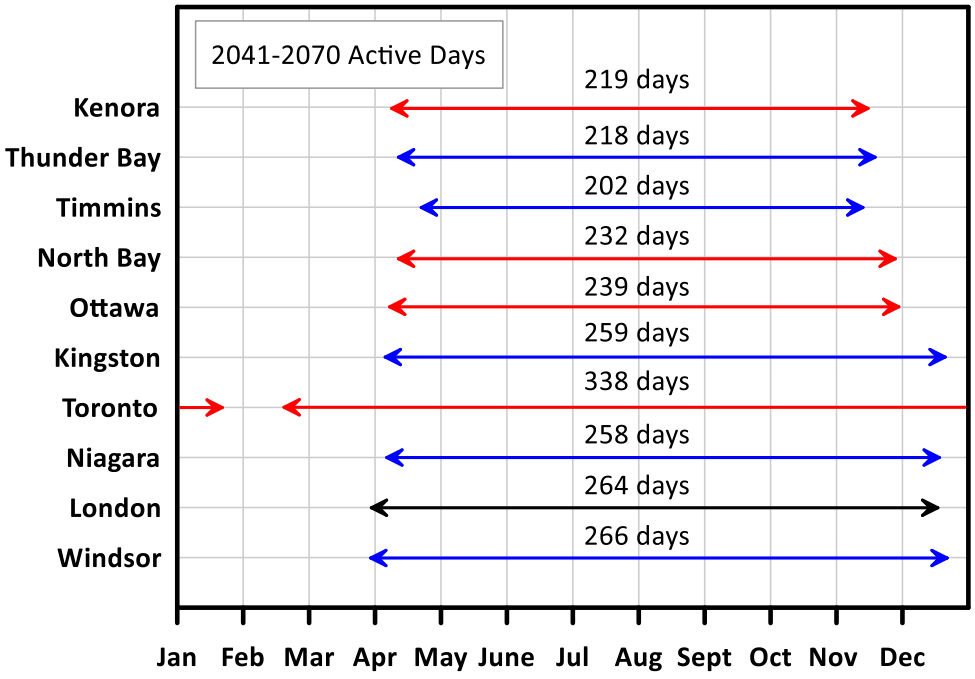

Figure 4.28: Future (2041-2070) active days for ten locations in Ontario

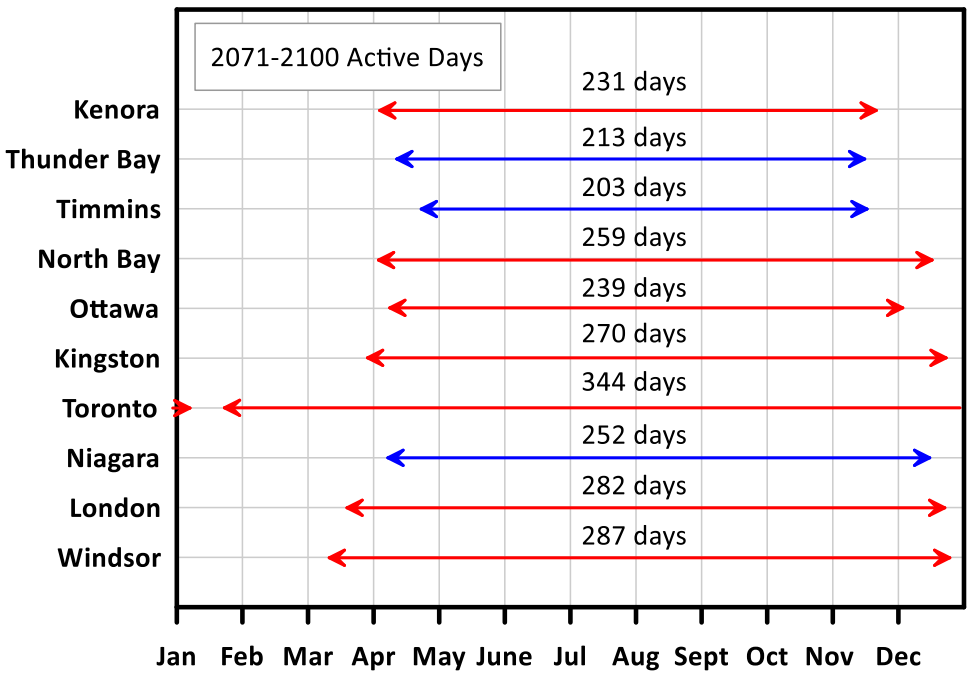

Figure 4.29: Future (2071-2100) active days for ten locations in Ontario

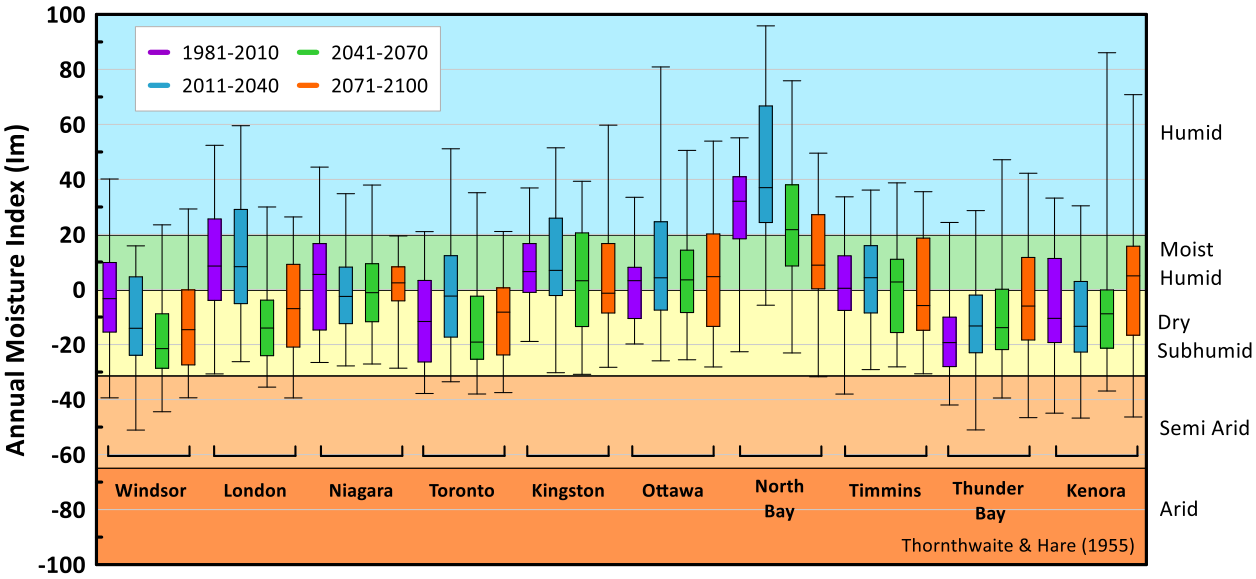

Figure 4.30: Comparison of annual moisture index for ten locations in Ontario

It is also interesting to note that a majority of the cities have a reduction in water availability as the time period increases. For example, for Windsor, the future climate ensembles have a median value less than the baseline. This is due to the increase in temperatures with time, resulting in greater values of potential evaporation. Figure 4.31 and Figure 4.32 presents the annual actual evaporation for the green roof and bioretention media. From this figure, Windsor has a maximum annual actual evaporation greater than the other nine locations for the period 2071 to 2100. For most of the cities, there is an increase in annual actual evaporation with time. The median, first and third quartiles for the green roof annual *AE* stays within 30 to 50 cm for all locations, except Windsor. For the bioretention, the median, first and third quartiles of the annual *AE* ranges between 50 to 70 cm. For most locations, an increase in *AE* is expected, however an increase in quantity of precipitation and active period will still result in increased *NI* values.

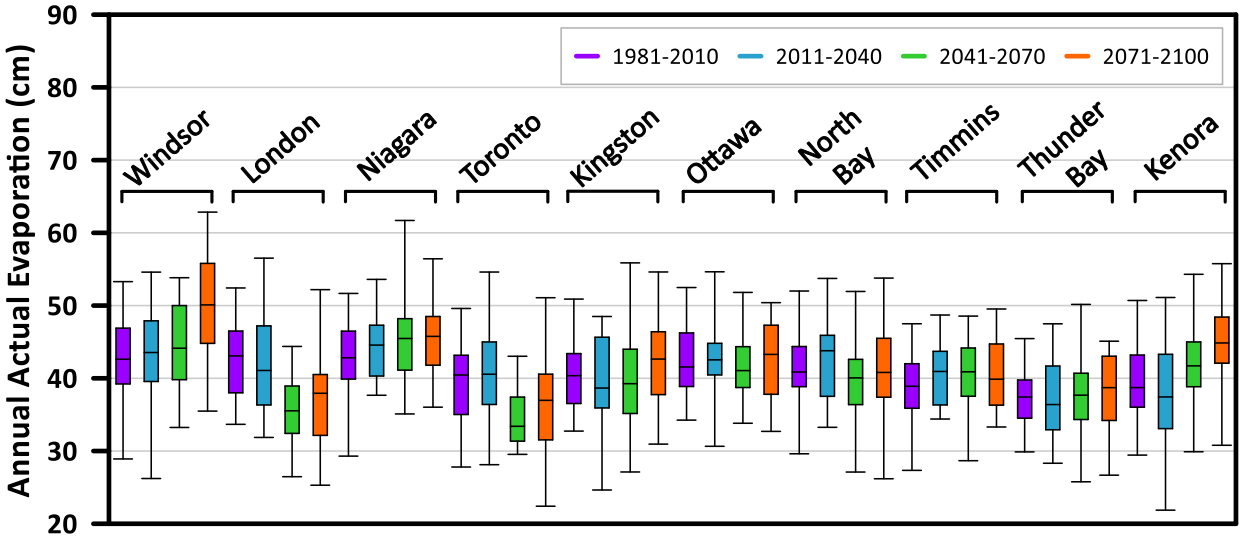

Figure 4.31: Comparison of green roof annual actual evaporation in Ontario

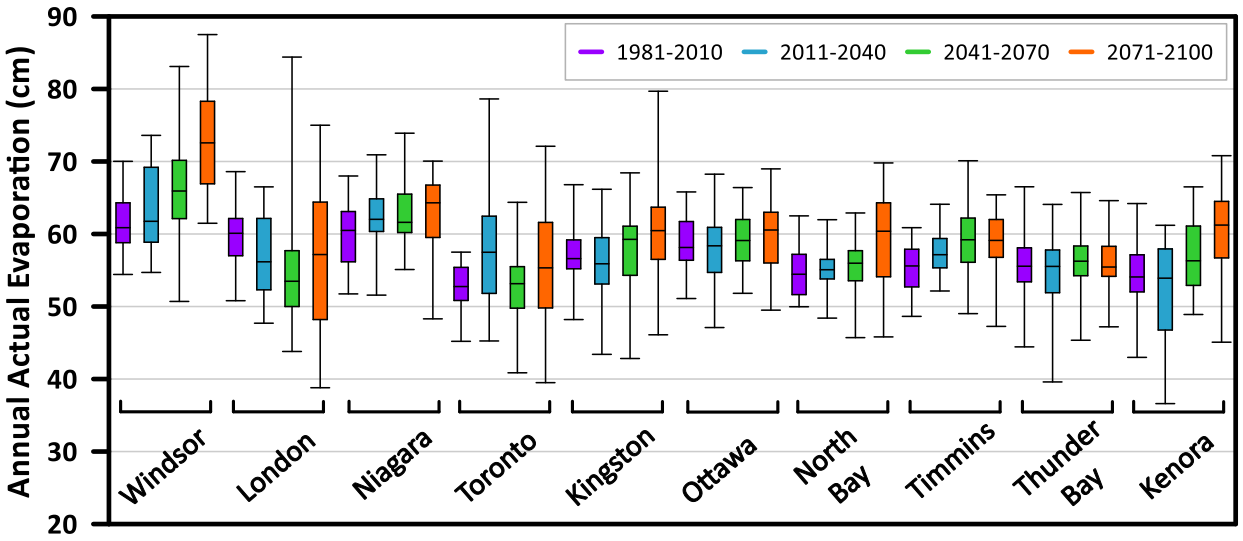

Figure 4.32: Comparison of bioretention annual actual evaporation in Ontario

4.3.3 Performance of LIDs under Extreme Precipitation Events

The performance of the LID systems is also examined under extreme precipitation events. Long-term analysis using daily climate data provides estimates and are beneficial to estimate the total quantities that the LID systems will be expected to handle. On the other hand, storm events have a greater chance of presenting runoff or ponded conditions due to the large intensity occurring under small durations. With climate change, the intensity of storm events is projected to increase leading to a greater risk in flooding. Thus, in this section, the green roof and bioretention media performance will be examined under extreme precipitation events.

4.3.3.1 Hydrological Performance of Green Roofs under Extreme Precipitation Events

Through the analysis of the system boundary fluxes, the mass balance of the green roof system during a storm event is primarily examined. The fluxes at the ground surface and bottom boundary for a 48-hour storm event in Toronto are presented in Figure 4.33. As the effects of evaporation were not taken into consideration for the storm events, the net infiltration and surface runoff are the two water balance components considered for water balance at the ground surface. Due to

the high permeability of the green roof substrate, there is no surface runoff computed. Therefore, the net infiltration is equal to the quantity of the precipitation entering the system.

As shown in Figure 4.33, the net infiltration and bottom flux for the future design storms are greater than the baseline, which is consistent with the climate data analysis presented earlier. Moreover, the bottom flux and net infiltration values are very similar to each other. It can also be observed that lag time between the water entering the green roof system and exiting is minimal. There are number of reasons for this such as small thickness of green roof (15 cm), high hydraulic conductivity of the green roof material, and near saturation conditions. Additional simulations were run with 10, 20, and 30 cm media depths.

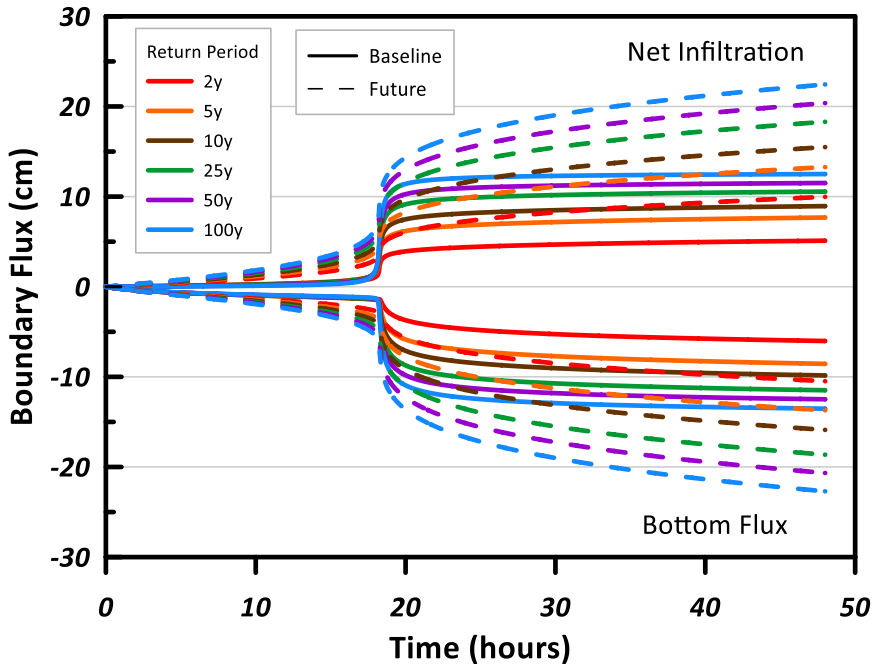

Figure 4.33: Green roof boundary flux for Toronto

Figure 4.34 presents the water balance for different green roof media depths. These results are for 48-hour 2-year and 100-year historical storm events for the city of Toronto. It can be observed that with the increase in substrate depth, the quantity of bottom flux is reduced and the detention

time increases. This implies that the increased substrate depth leads to a greater storage and increased detention time. For example, there is a more gradual increase in the bottom flux for the 30 cm 2-year event after a time of approximately 20 hours. Whereas the 10 cm 2-year event releases a large quantity of water at a time of approximately 18.2 hours. For the 100-year event, there is a large quantity of water released near the peak of the storm for all three substrate depths. However, the cumulative bottom flux is smaller for the 30 cm substrate depth as it has greater storage.

Low impact developments are also implemented to assist in the reduction of peak flow rates to reduce flooding or assist overwhelmed older storm water systems during a storm event. Therefore, a thinner soil substrate may not be ideal for a sudden, short-term storm event with a large quantity of water, as it has a smaller storage. A thicker substrate will delay the peak flow, thus assisting in the reduction of peak flow and flooding at nearby impervious structures. The water that is stored will then either be evaporated or drain after the peak of the storm event.

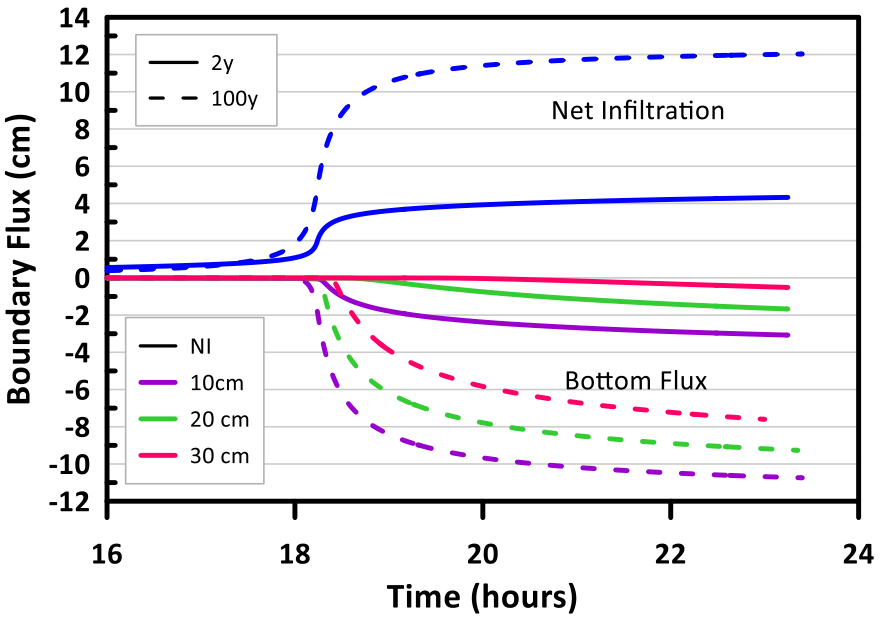

Figure 4.34: Impact of green roof thickness on boundary fluxes

4.3.3.1.1 Green Roof Peak Reduction

Green roofs assist in reducing the peak flow of a storm event when compared to the conventional roof (Berndtsson, 2010). The peak reduction can be determined by taking the percent difference between the peak of the storm event and the peak of the runoff. Figure 4.35 illustrates a hydrograph for a 48-hour 2-year storm using Toronto base and future climate data. From this figure, one can see that the green roof system does in fact assist in reducing the peak intensity of the storm event. This helps in not overwhelming the older storm water systems, such as combined sewer overflows, during a storm event. It can also reduce erosion of nearby streams or reduce flooding during the time of the storm. Nevertheless, it is projected that the peak reduction will be smaller in the future. This will lead to a greater intensity in the peak runoff, compared to baseline storm events. Figure 4.35 demonstrates the decrease in peak reduction for a future 48-hour 2-year storm event in Toronto. The peak reduction for the future event drops 22% when compared to the historical event. The 48-hour 2-year historic and future events have a peak reduction of 91% and 69%, respectively. This demonstrates the large decrease in peak reduction and can lead to a greater risk in flooding around the site that was not initially expected when designing the green roof using historical climate data.

As design storm data for other ten locations in Ontario are also available, each location for a 48-hour storm with six different return periods (2, 5, 10, 25, 50, and 100-year) are also simulated. The peak reduction for each location were computed for the baseline and future design storms. It was determined that the peak reduction for the base ranges between 20% (100-year storm) and 96% (2-year storm). Whereas the peak reduction for the future ranges between 11% (100-year storm) and 82% (2-year storm). The difference between the future and base peak reduction was then calculated and is presented in Figure 4.36. A negative difference implies that the future has a smaller peak reduction compared to the base climactic condition. For example, Niagara 48-hour 2-year base and future event has a peak reduction of 88% and 61%, respectively. The difference

of the future and the base equals -27%, signifying that there is a smaller peak reduction in the future. From Figure 4.36, it can be observed that, overall, there is a smaller peak reduction in the future compared to the base. This means that the runoff peak intensity will be higher for future events. The are some exceptions for the cities of Toronto, Kenora, and North Bay.

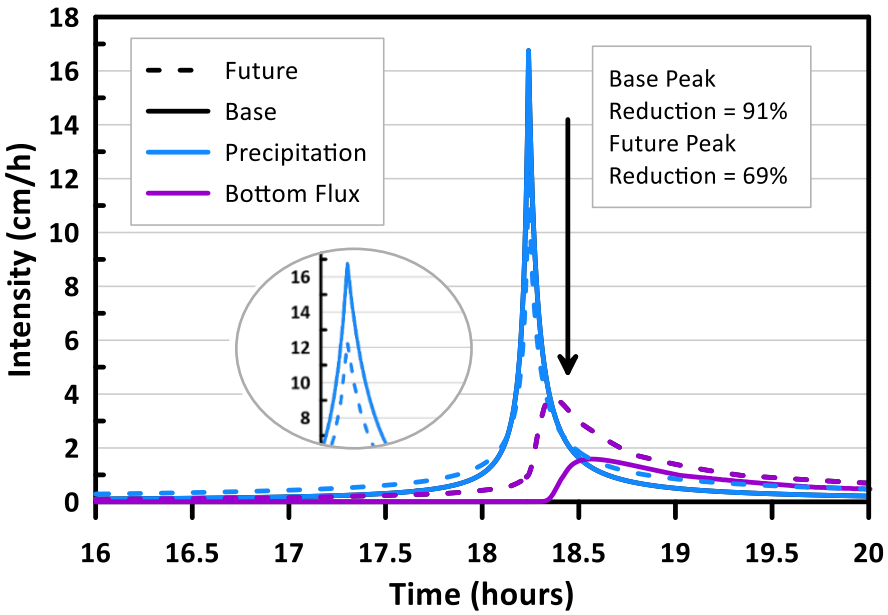

Figure 4.35: Precipitation and runoff hydrograph for Toronto 48-hour 2-year base and future event

Subsequently, Toronto with return periods of 25, 50 and 100 years does not follow a similar trend as the other locations. Rather, there is a greater peak reduction in the future for these return periods. Still, the difference in peak reduction for these return periods are fairly small. Figure 4.37 presents the hydrograph for Toronto 48-hour 100-year event using the Chicago storm method. The figure demonstrates that the runoff peak for the baseline event is greater than the future event. Initially, there is a greater quantity of runoff for the future storm, as there is a greater quantity of future precipitation projected. At a time of approximately 18 hours, the precipitation intensity of the historic storm surpasses the precipitation intensity of the future. The future storm for Toronto, as described by the Chicago method, results in a more gradual storm. Whereas the

historic storm results in sudden increase in storm intensity. Due to the storm distribution, the historic storm for Toronto has a smaller peak runoff reduction compared to the future storm. This highlights the fact in addition to the intensity and duration of the storm, the distribution of the storm is also very important. In this research only one method of storm distribution (Chicago method) was investigated. Therefore, it is recommended that for such analyses, more than one method of storm distribution should be considered.

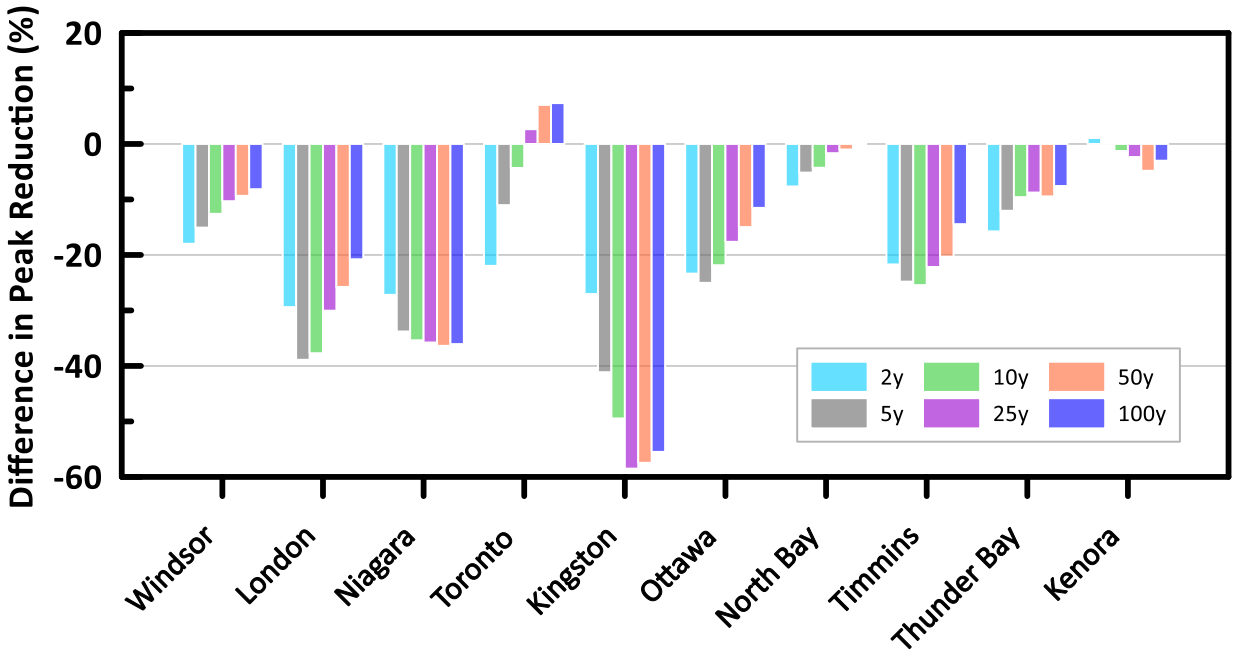

Figure 4.36: Difference in peak reduction of base and future design storms in Ontario

4.3.3.1.2 Green Roof Peak Time Delay

In addition to peak reduction, the peak time delay is significant in delaying the stormwater runoff quantity during a storm event. This can once again assist in reducing erosion, flooding, or overwhelming nearby stormwater management systems, in comparison to the conventional roof. The delay allows for systems, such as the combined sewer overflow, to deal with the precipitation from the storm event and then take the additional water that was delayed by the LID facility. The

time delay was determined by subtracting the time of the peak runoff from the peak of the storm event. For example, for Toronto 48-hour 2-year event, the peak time delay for the base and future storm events are 19.6 minutes and 7.2 minutes, respectively. The difference is 12.4 minutes, which is presented in Figure 4.38. The difference between the time delay from the base and future are presented in Figure 4.38 for the ten locations in Ontario.

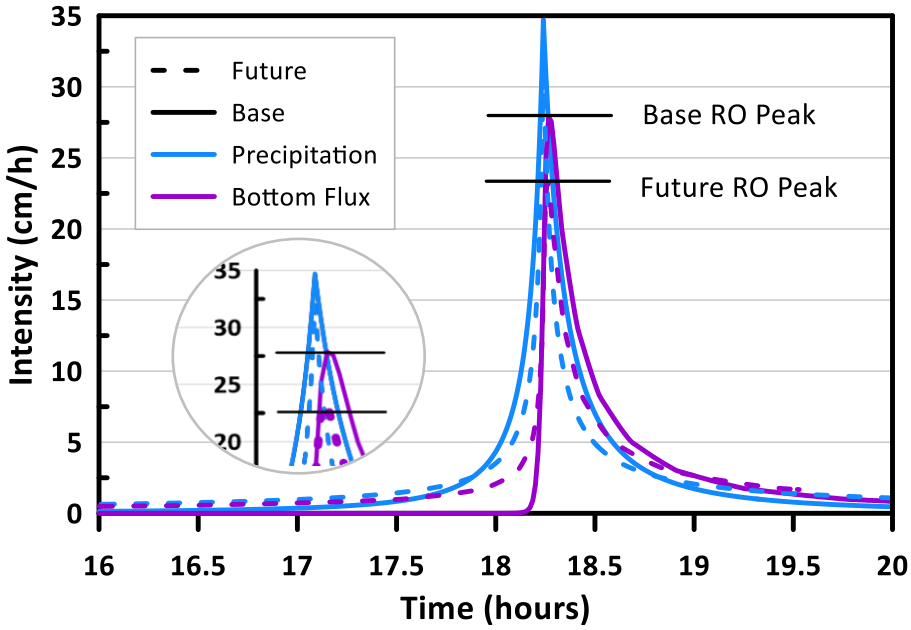

Figure 4.37: Base and future hydrograph for Toronto 48-hour 100-year storm

With the exception of Kenora and North Bay, eight locations in Ontario follow a similar trend. Interestingly enough, there is a greater difference in the base and future for the 2-year storm events. This large difference in time delay between the base and future for 2-year storms implies that frequent storm events, or storms with a greater probability of occurrence, will have a smaller time delay between the storm peak and runoff peak in the future compared to 100-year storms. Nevertheless, there is still a reduced time delay in the future leading to adverse effects of

stormwater runoff. For instance, Kingston and Timmins have the greatest time difference of 26 minutes. This means that the peak will occur 26 minutes earlier in the future.

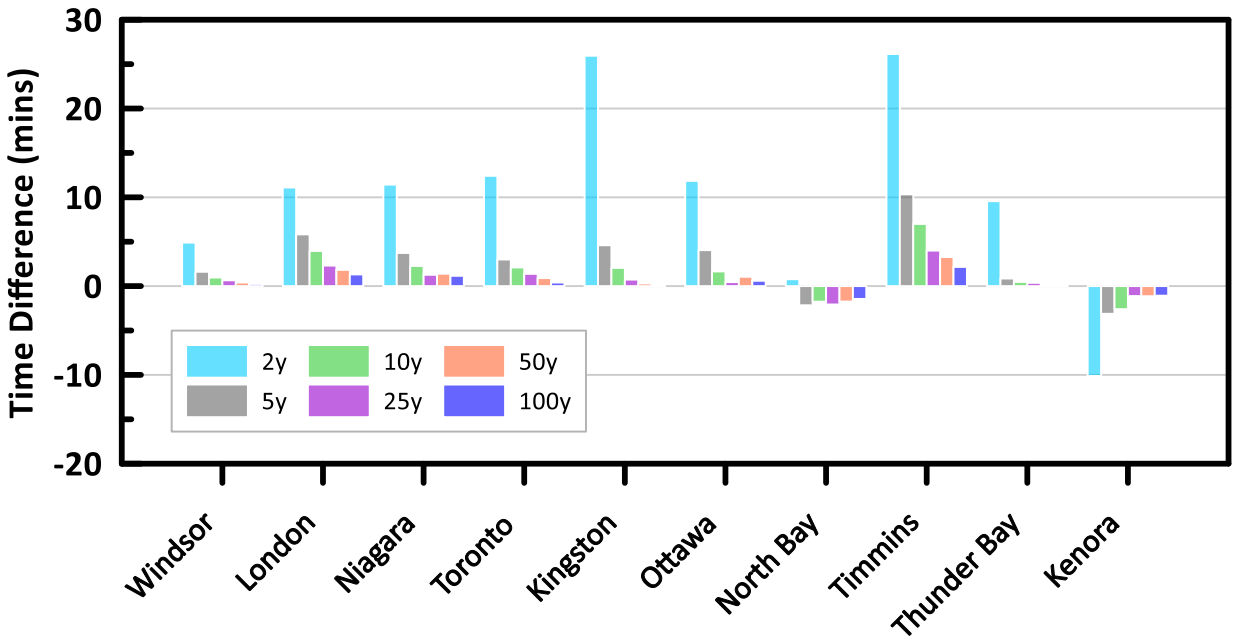

Figure 4.38: Time difference (minutes) between the base and future peak storm delay

For large return periods, the difference between the base and future is small. However, the time delay between the peaks for the base was not large to begin. For example, the 100-year base and future time delay for Timmins is 4.6 minutes and 2.4 minutes, respectively. This may result in a smaller time difference of 2.2 minutes, compared to the maximum difference of 26 minutes. However, this does imply a percent difference of 47% between the base and future events for Timmins. Figure 4.39 presents the percent difference between the base and future time delay. The greatest percent difference is computed for London 100-year storm (88%), demonstrating the large change between base and future storm events.

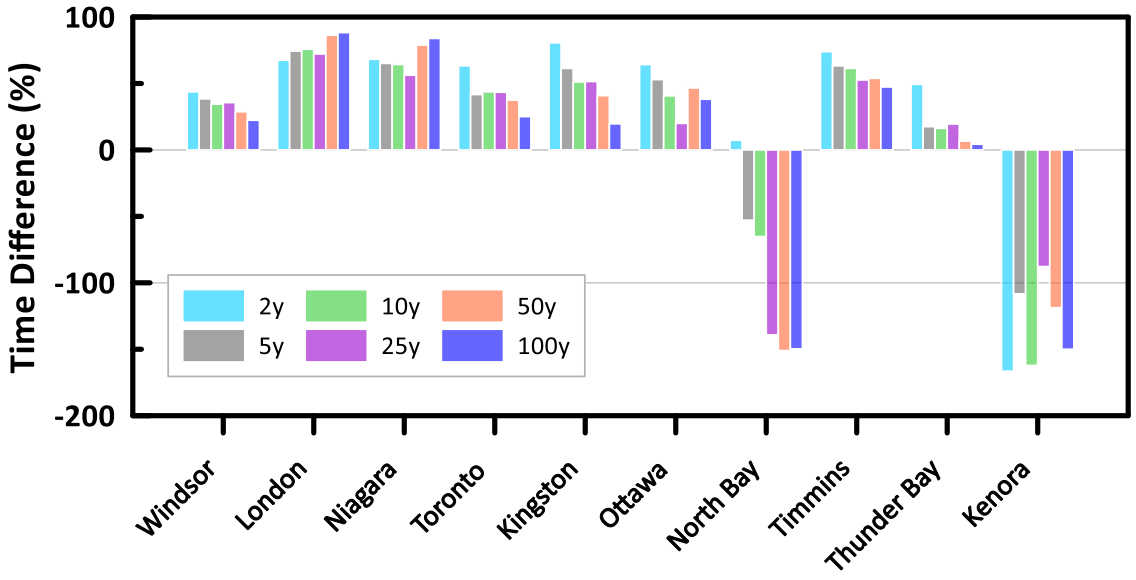

Figure 4.39: Percent Change between the base and future peak storm delay

Kenora and North Bay are once again the exception with a large peak delay in the future compared to the base. Kenora has a reduction in storm quantity in the future compared to the base leading to the reduced time difference. For North Bay, however, the total storm quantity is projected to be greater in the future compared to the base. Examining the hydrograph, it is noted that the peak intensity of the future storm is quite low in comparison to the historic, as shown in Figure 4.40. Thus, the development of the storm distribution impacts the assessment of the LID hydrological performance.

4.3.3.2 Hydrological Performance of Bioretention Systems under Extreme Precipitation Events

A key design aspect for bioretention facilities includes the ability to allow for surface ponding as these systems collect a large quantity of stormwater runoff from a large catchment area. Additionally, the surface ponding assists in stormwater pollutant removal processes, particularly

via sedimentation. Still, there are regulations to follow when designing for ponding within the bioretention system, such as the maximum ponding depth and allowable ponding time. CVC and TRCA (2010) require a maximum ponding depth between 15 to 25 cm and a maximum allowable surface ponding time of 24 hours after a storm event since it is less than the time required for one mosquito breeding cycle. With these constraints in mind, the surface ponding depth and time are investigated.

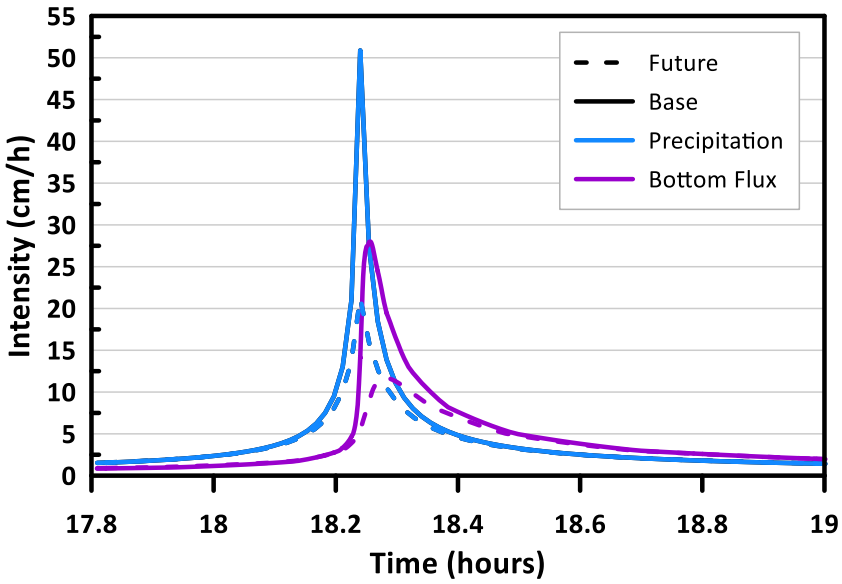

Figure 4.40: Comparison of North Bay 48-hour 100-year base and future storm event

Before conducting an examination of the other nine locations, the ponded conditions for Toronto were examined in detail. The surface head for the city of Toronto 48-hour storm with six return periods is presented in Figure 4.41. From Figure 4.41, the surface head for the future initially reaches a higher value of saturation compared to the base. For example, at a time of 1 hour, the surface head for the 100-year base and future event is -74 cm and -22 cm, respectively. Due to the storm distribution, there is a greater quantity of water initially entering the bioretention system for the future. After the peak of the storm, the future has a greater surface head compared to the base, once again due to the storm distribution. This is a notable observation since the initial

conditions of the next storm event can be impacted. For example, if there is a storm immediately after the storm events presented in Figure 4.41, the initial conditions for the future storm have a greater surface head compared to the base. Thus, the substrate is initially more wet in the future leading to ponded conditions in a shorter period of time. Furthermore, close to the peak of the storm, ponding is observed as well as runoff since the surface head surpasses the 20 cm ponding limit.

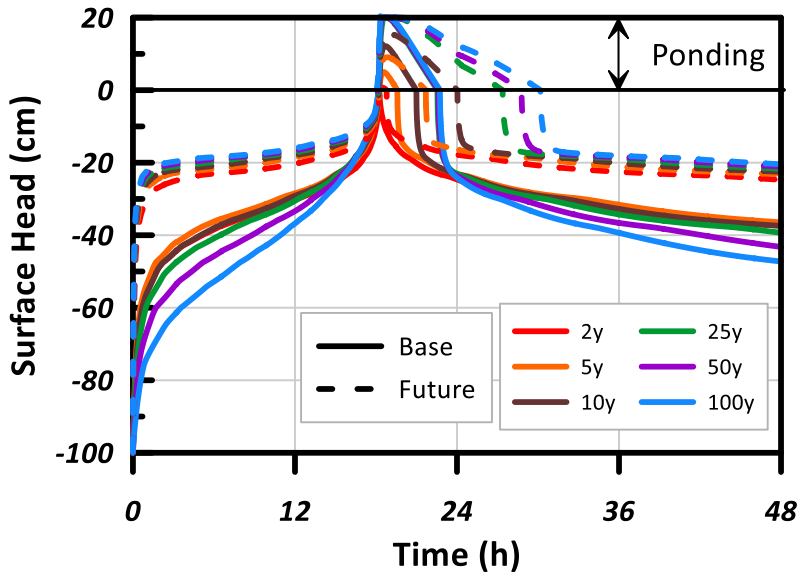

Figure 4.41: Bioretention surface head for Toronto 48-hour storms

The ponded conditions for Toronto 48-hour storm and is presented in Figure 4.42. Simulations conducted using the future storm events results in a large increase in both ponding time and ponding depth. For Toronto, there is also runoff observed for the 25, 50 and 100-year storms as it surpasses the 20 cm ponding limit. With the increase in return period, there is an increase in ponded conditions. In addition, there is more than double the amount of total ponding time for a 48-hour 100-year future storm event compared to the base. This is concerning as adverse impacts of long-term standing water include insect hot-spots or increased stormwater runoff and heavy flooding surrounding the bioretention system due to multiple storm events. If the bioretention was

initially designed for a base 48-hour 100-year storm event, which has an expected ponding time of 4.5 hours, it may not be able to withstand the future scenario of 12 hours of ponding time due to climate change. Still, the Toronto 48-hour storms for the six return periods did not surpass the 24-hour maximum ponding time defined by CVC and TRCA (2010).

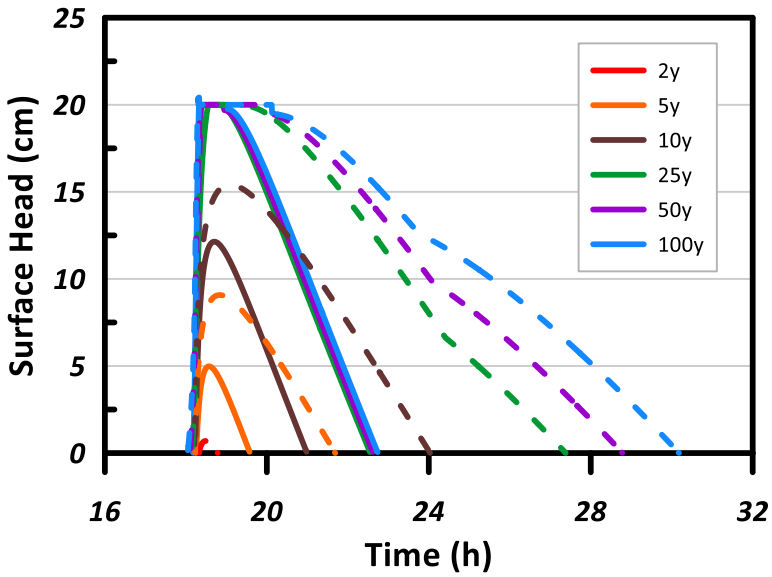

Figure 4.42: Ponding for Toronto bioretention under 48-hour storm durations

4.3.3.2.1 Ponded Conditions for Ontario

The performance of the bioretention media under extreme precipitation events is also examined for the ten locations in Ontario. Figure 4.43 presents the ponding depth difference between base and future events for the ten locations in Ontario. A positive value in ponding depth difference indicates that the future has a greater ponding depth. For example, the historic 10-year event for Kingston has a maximum ponding depth of 3.8 cm. Whereas the future 10-year event for Kingston reached the maximum ponding depth of 20 cm. The difference of 16.2 cm can be observed in Figure 4.43.

Overall, a majority of the locations in Ontario have an increased ponding depth projected for the future, with the exception of Kenora and North Bay. There is little to no ponding difference for the 2-year storms for all ten locations. Toronto has minimal difference in ponding depth between the base and future. The 5-year storm event for London has the greatest increase of 18 cm in ponding depth.

Furthermore, it can be observed that the 5-year and 10-year storm events have a large increase in comparison to the storms with a greater return period. This is due to the fact that there was no difference in the ponding for the storms with a greater return period as both the historic and future storm events reached the maximum 20 cm ponding depth. Thus, the stormwater runoff from the bioretention system is also examined.

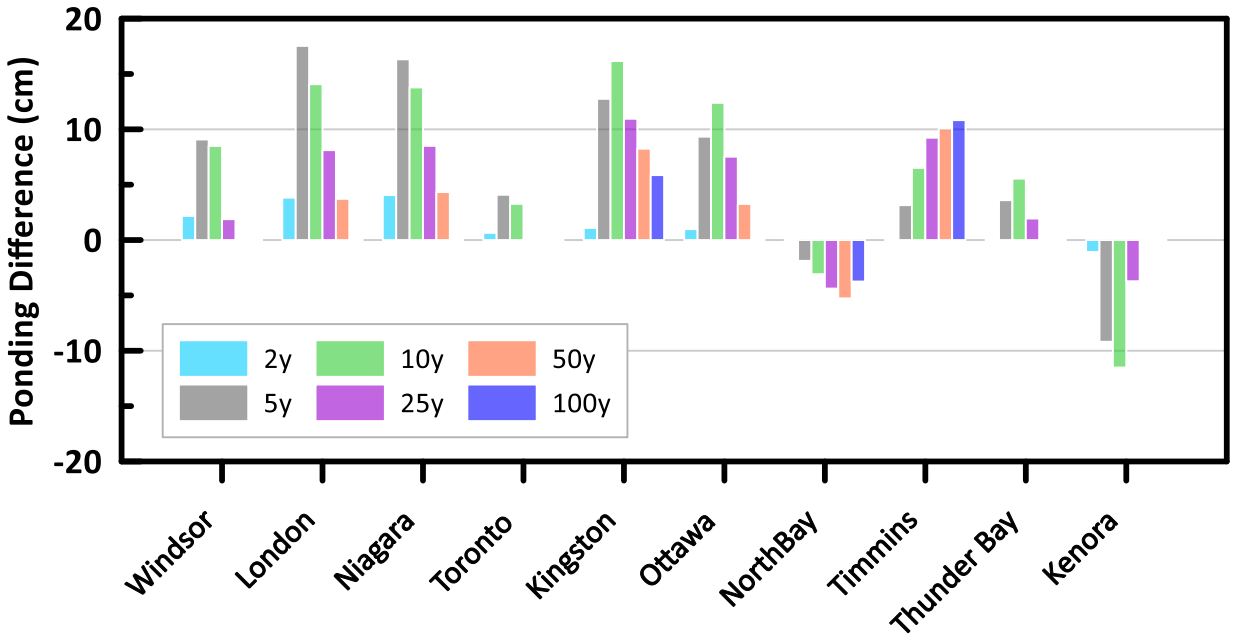

Figure 4.43: Ponding depth difference (cm) between base and future for bioretention media

The difference in runoff between the historic and future climate for the ten locations is shown in Figure 4.44. Similarly, a positive value in runoff difference indicates that the future has a greater

stormwater runoff quantity. The 2-year and 5-year storms did not result in runoff for either the historic or future events. Moreover, there is little to no stormwater runoff observed for North Bay, Timmins and Toronto. Also, Kenora has a negative difference as there is a reduction in runoff observed for the future.

The 100-year storms result in a large increase in runoff for the future. London and Niagara 100-year storm have the greatest increase in ponding depth, with an approximate 50 cm increase. This is definitely concerning as the bioretention system may fail and the configuration would need to be updated, such as the addition of an underdrain, to avoid flooding around the bioretention facility. This overflow also leads to an increase in untreated stormwater runoff, which will have adverse impacts to nearby streams and waterbodies.

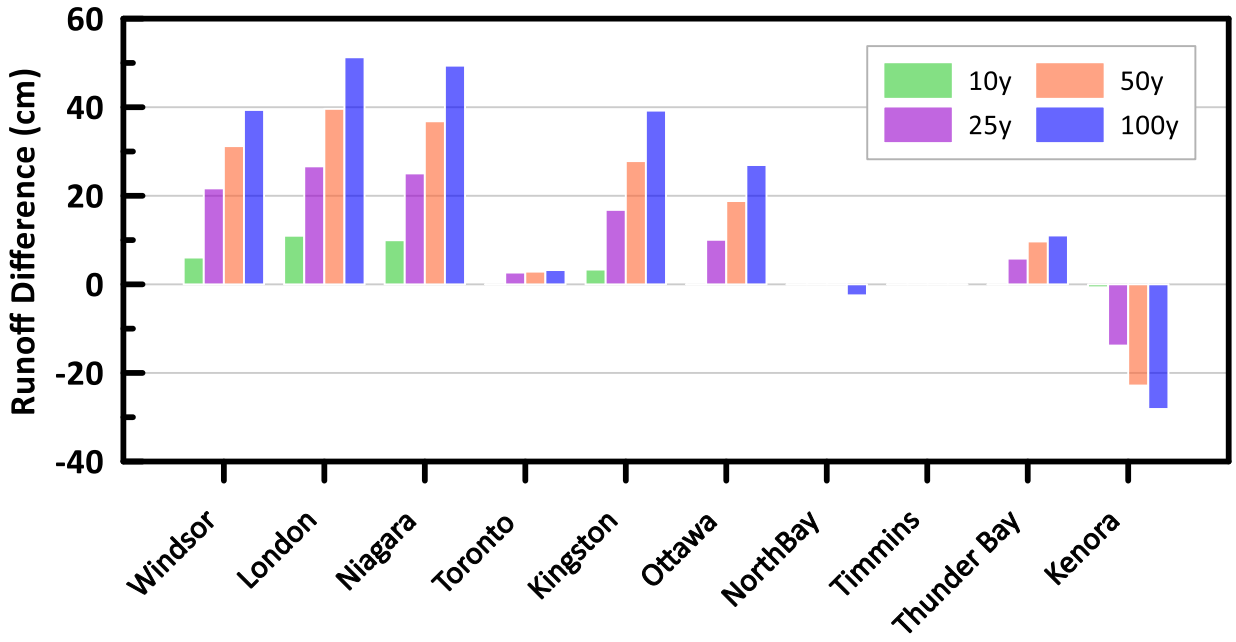

Figure 4.44: Runoff difference (cm) between base and future for bioretention media

The next bioretention performance criteria that is examined is the total ponding time. The ponding time difference between the base and future storm events for the ten locations are examined and

presented in Figure 4.45. There is a general increase in ponding time for most locations in the future, with the exceptions of North Bay and Kenora. Windsor, with a 100-year return period, has the largest increase in ponding time (13 hours) compared to the base. There is a large increase in storm events with 100-year return periods and minimal time difference for storms with a 2-year return period. Still, none of locations exceed the 24-hour ponding time limit defined by CVC and TRCA (2010). The future 100-year Windsor storm has the greatest ponding time of 22 hours, which is fairly close to that limit.

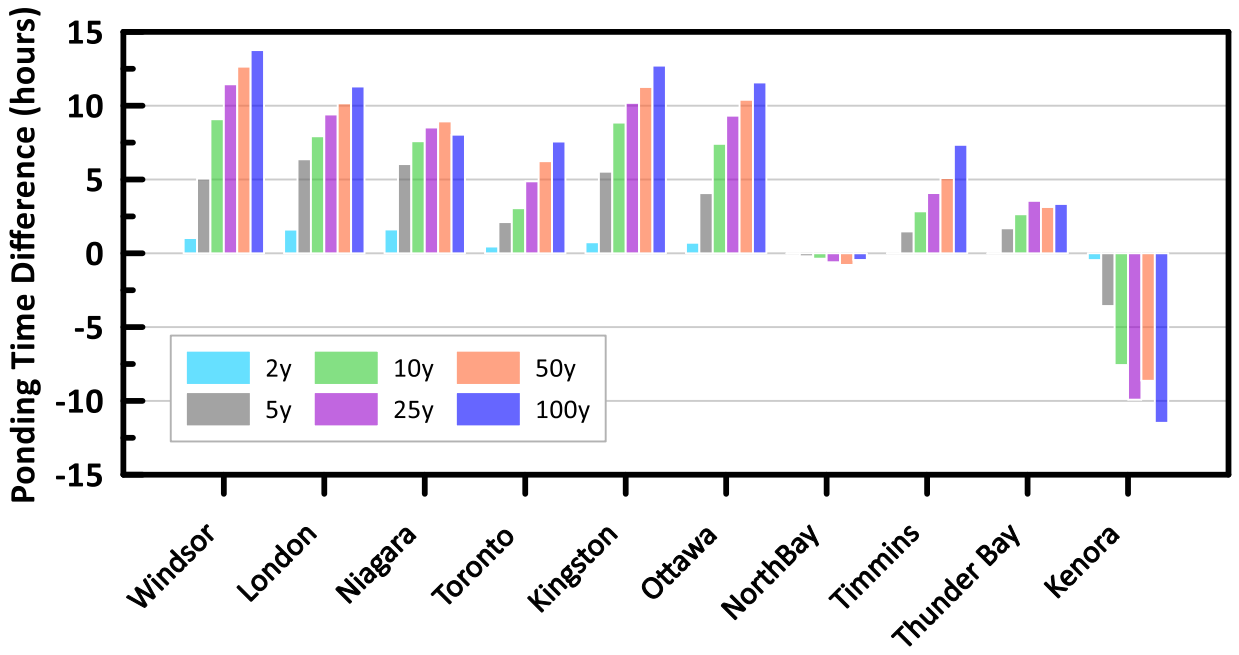

Figure 4.45: Ponding time difference (hours) between the base and future

4.4 Conclusions

This chapter presents an examination of green roof and bioretention media under changing climate. Both long-term climate (2011-2100) and extreme precipitation (48-hour storm) analyses were conducted to assess the performance of LIDs under changing climate.

To begin, long-term simulations were carried out to investigate LID performance for Toronto using four GCMs for all four RCPs. In total, 48 future climate ensembles consisting of 30-years of climate data was examined for the city of Toronto. Through comparison of the annual net infiltration using box and whisker plots, it was observed that the GCM HadGEM2-ES predicted higher estimates of the annual net infiltration compared to the other three GCMs examined. Additionally, higher estimates of the annual net infiltration were noted for RCP 8.5 emission scenario especially for the later part of the 21st century (2071-2100). An increase in maximum and minimum annual net infiltration values for the future compared to the historic climate ensemble were also observed.

The significance of the number of active days, water availability and soil moisture conditions were investigated. It was observed that with an increase in active period, there is an increase in annual net infiltration. Exceptions were observed for climate ensembles #8, 20 and 32, where the active period was less than the baseline, but a greater annual net infiltration was observed. This is due to the large annual moisture index observed, where a greater quantity of precipitation compared to potential evaporation is expected in the future resulting in humid climatic conditions. Also, these three ensembles contain climate data for the early part of the century (2011-2040), where the potential evaporation is expected to be lower compared to the later part of the century.

A major difference between the annual net infiltration quantities for the green roof and bioretention systems was noted. Although the bioretention systems manage large quantities of water than the green roof systems, increase in net infiltration values for the future would see a larger increase in the case for the green roof. It is projected that the percent increase of the maximum annual net infiltration in the future for the bioretention and green roof is 50% and 98%, respectively. This is related to the difference in the way green roofs and bioretention systems function. Green roofs are designed for no surface runoff conditions and are relatively thin, while bioretention systems are designed for ponded conditions. The ponded conditions and large quantities of water that the bioretention systems have to handle results in conditions where larger quantities of water are

available in the near surface layers of the system for longer periods, resulting in actual evaporation values closer to potential values. This, together with the generation of surface runoff, results in lower net infiltration values.

Healthy vegetation is important for the proper functioning of the LID systems. Availability of enough water in the root zone to maintain healthy vegetation is an important concern for changing climatic conditions. Simulations of LID facilities with vegetation for the city of Toronto indicate that for historical climate conditions, the water availability in the root zone does not fall below the wilting point. A similar simulation for the future climate ensemble with the lowest expected moisture index indicates that, in general, the water availability in the root zone might decrease from historical levels but will still not breach the threshold of wilting point. However, it should be noted that irrigation may be required, depending on the plant species

The annual runoff was also estimated for the green roofs under Toronto's long-term climatic conditions. This was to determine whether the future climate ensembles are able to meet the water balance target suggested by the Wet Weather Flow Master Plan (WWFMP) for Toronto. The water balance target states that the annual runoff must be less than 50% of the annual precipitation from a particular site. After conducting the analysis, it can be concluded that there will be an expected increase in runoff for many future climate ensembles, leading to the water balance target might not being met in the future. The results also lead one to conclude that there is potential for an increased risk in flooding, erosion, and degraded water quality in receiving waters due to climate change.

Subsequently, the LID performance for ten locations in Ontario were compared and examined using future climate data that is expected to produce the wettest soil condition. Comparison of the annual net infiltration estimates indicate that cities further north (Timmins, Thunder Bay, and Kenora) are expected to lower values than the other seven locations examined. Other notable findings included North Bay having a large annual net infiltration as result of humid climatic

conditions in the future as indicated by large increase in moisture index. An increase in active days for the later part of the century is seen for many of the cities. Toronto has the greatest increase of 69 active days in the later part of the century. Niagara has the greatest decrease in active period of 30 days for the 2071-2100 period.

Although Toronto has the greatest number of active days, Kingston has the greatest annual net infiltration in the later part of the century. Still, the increase in the number of active days for Toronto resulted in Toronto having the greatest percent increase of 100% between the maximum annual net infiltration in the future compared to the base. With the increase in active period, an increase in the net infiltration is projected, even with the expected increase in actual evaporation due to rising temperatures.

For extreme precipitation analysis, the boundary fluxes for the green roof were examined initially. It was noted that the net infiltration and bottom flux (or runoff) were very similar other due to the small media depth. By increasing the thickness of the substrate, the peak flow can be delayed, assisting in reducing flooding near structures and erosion. Two key features that the green roofs assist with compared to the conventional roof are storm peak reduction and storm peak time delay. Ten locations in Ontario were examined for their performance in terms of peak reduction and peak time delay in the future. From the analyses it was concluded that in the future, there is a general projected decrease in peak reduction. This may result in overwhelming older stormwater management systems, flooding or erosion due to the sudden onset of high intensity rainfall. Toronto demonstrated an exception to the trend, where the historic had a smaller peak reduction than the future. It was determined that the storm distribution for Toronto differed, leading to unexpected results.

For the peak time delay, it is projected that in the future the time delay between the peak of the storm and peak of the runoff will be reduced. This would result in an increased risk of adverse effects of stormwater runoff during the storm. Kenora and North Bay are exceptions to this

projection. In the future, these two locations have a time delay that is projected to increase compared to the baseline. As the storm quantity in the future for Kenora is smaller than the historical data, the time delay is expected to increase. For North Bay, the storm distribution developed using Chicago method impacts the assessment of the LID hydrological performance as the future storm quantity is greater than the historic. Furthermore, it was also observed that the difference between the base and future time delay for 2-year storms was large in comparison to storms with greater return periods. For example, difference between base and future time delay for Timmins 48-hour 2-year and 100-year event is 26 minutes and 2.2 minutes, respectively. This implies that future small storms with a greater probability occurrence will have a smaller time delay between the storm peak and runoff peak.

Finally, the ponding depth and time were examined for the bioretention system using the base and future storm data of the ten locations in Ontario. Once again, with the exception of Kenora and North Bay, there is an expected increase in ponding and total time of ponding conditions in the future. In some cases, there is an increase in ponding depth of 50 cm, leading to large quantities of surface runoff for future climatic conditions. For the total ponding time, the largest increase is observed to be 13 hours greater than the base climactic conditions for a 100-year storm in Windsor. The future 100-year storm projection for the city of Windsor has the potential to result in ponding conditions up to 22 hours. The ponding time does not pass the maximum ponding time of 24 hours defined by CVC and TRCA (2010). However, such a large increase suggests that the design of the bioretention facilities may need to be modified to consider the changing climate.

All in all, the changing climate will impact the performance of LIDs in the future. There is an increase in the total quantity of water projected to enter these facilities. These LID systems will be required to be re-examined to perform to its full capacity. Otherwise, heavy risks to the environment, society, and economy can be expected due to flooding.

Chapter 5: Summary, Conclusions, and Recommendations for Future Research

5.1 Summary

Low Impact Developments (LIDs) are seen as an innovative solution to stormwater management. Considering it is a fairly new technique, there is some uncertainty in their performance, especially within the context of climate change. This study is divided into two parts, with the purpose of examining the performance of LID systems.

The first part of the study investigated the performance of pedotransfer functions in estimating the soil hydraulic properties of various LID substrates. Pedotransfer functions (PTFs) estimate soil hydraulic properties using routinely measured soil properties, such as soil texture, bulk density, particle size distribution, or porosity. Five LID substrates, three bioretention and two green roof, were sourced by local suppliers. The hydraulic properties of these substrates were measured using HYPROP (UMS, 2015) system and a modified permeameter. Other routine soil properties such as grain size distribution, organic content, and specific gravity, were measured to be used as inputs to the pedotransfer functions. The three different types of PTFs used to predict the hydraulic properties of the LID substrates were selected from the literature and are based on regression models, physicoempirical models, and artificial neural networks. Evaluation of the predicted soil hydraulic properties to the measured was completed through statistical analysis, visual inspection, and numerical modelling using the HYDRUS software (Šimůnek et al. 2008). Thirty years of daily historical climate data for the city of Toronto was used in the numerical model.

The second part of this research aimed to examine the effects of climate change on LID performance. Future long-term climate data (2011-2100) comparing of daily records of precipitation and potential evaporation and extreme precipitation events (48-hour) for ten locations in Ontario, Canada were used for the assessment of the green roof and bioretention

systems. Various hydrological benefits of the LID systems were examined in detail to observe the performance under changing climate using numerical modeling. Numerical modelling was also carried out using HYDRUS software. Design aspects for the green roofs included stormwater runoff reduction, peak intensity delay, peak time delay, and substrate thickness. For the bioretention system, design aspects included ponding and overflow, residence times and storage times.

5.2 Conclusions

5.2.1 Performance of Predicted Soil Hydraulic Properties

After completing the investigation of the predicted soil hydraulic properties to the measured, it was determined that there is a high level of uncertainty when using PTFs for LID media. There was no one particular PTF that would work best for all substrates examined. For example, the statistical performance of three bioretention media varied depending on the PTF chosen, even though they are all bioretention media. Similarly, two green roof substrates achieved a better statistical performance compared to the bioretention media examined. However, the predicted soil water characteristic curves (SWCC) of the bioretention media measured by DelVecchio (2017) performed statistically better when compared to the green roof media measured from Sandoval et al. (2017). Thus, there is a large variability in the statistical performance of the PTFs to the measured soil hydraulic properties of LID materials. The samples for the green roof and bioretention materials obtained from different suppliers also indicated that there is a wide variability in composition, geotechnical and hydraulic properties of these LID materials.

The difference in soil properties were examined to understand the possible reason as to why the performance of each LID varies. It was determined that LID substrates with a large organic content (greater than 25%) overestimated the saturated water content and air entry value. This was particularly shown for the PTFs that use regression equations. In addition, some substrates from DelVecchio (2017) exhibited bimodal characteristics. A bimodal SWCC has two peaks, whereas

a unimodal SWCC has one. The CalcPTF and Rosetta PTFs provide a unimodal SWCC prediction as they provide parameters for the Brooks and Corey (1964) and van Genuchten (1980) analytical functions. The AP model is not limited to the Brooks and Corey (1964) or van Genuchten (1980) analytical functions as it is derived from the particle size distribution which can exhibit bimodal behaviour. In general, there is limited capability in accurately estimating the SWCC of engineered media that vary from supplier and location.

5.2.2 Significance of Measured Soil Hydraulic Properties

Numerical modelling was completed using HYDRUS (Šimůnek et al. 2008) to assess the performance of LID systems using measured and estimated soil hydraulic properties. Based on the review of the modeling results it can be concluded that the measured soil hydraulic properties are more relevant for green roof systems compared to the bioretention. For LID systems that manage smaller quantities of water, use of measured soil hydraulic properties is highly recommended.

5.2.3 Long-Term Performance of LIDs under Changing Climate

Long-term analysis of the LID performance for the city Toronto demonstrated that an increase in the total quantity of water entering the LID system is projected. In particular, higher estimates of net infiltration are projected using the general circulation model Had GEM2ES. Therefore, it can be concluded that future climate projections should be considered for a number of different GCMs. The results also indicated that for the later part of the century (2071-2100) and greater emission pathway (RCP 8.5) projected greater estimates of the annual net infiltration for Toronto. This leads to two conclusions. First, assessments of this sort should consider separate assessments for various time periods as done in this research so that progressive design changes in the LID systems can be considered. Second, comparison of performance for different emission scenarios will enable the planners and designers to make changes to design considering the risk associated with various climate change scenarios.

Review of the climate data and numerical modelling results suggest that for many climate change scenarios, there will be an increase in the active period which could potentially lead to an increase in the amount of net infiltration. Therefore, it can be concluded that in the future the LID facilities might be operational over longer period during a calendar year and would have to manage larger quantities of water. This is attributed to not only the expected precipitation increase in the future, but also due to rising temperatures.

The results also indicate that the percent change in maximum infiltration values for the green roofs can be as much as 100%, while for bioretention it can be in the order of 50%. Lower increase in net infiltration values for bioretention facilities is shown to be related to the increase in actual evaporation as a result of increased potential evaporation in the future, hydraulic properties of the materials, and quantity of water that bioretention facilities have to handle. These observations lead one to conclude that green roofs are more prone to increase in precipitation in the future, while the effect of increase precipitation on bioretention will be offset by the expected increase in the potential evaporation.

The water target balance defined in the Wet Weather Flow Management Plan for Toronto was examined to demonstrate the performance of the LIDs in the future under changing climate. The water balance target states that the annual run-off from a development site must be less than 50% of the total annual rainfall. Based on the results it can be concluded that this water target will become more difficult to reach in the future without implementing design changes. It can also be concluded that in absence of design changes there will be an increased risk in flooding, erosion, and degraded water quality in the receiving waters.

For long-term analysis in Ontario, cities further north (Timmins, Thunder Bay, and Kenora) have a smaller annual net infiltration compared to the other seven cities examined. Moreover, it was noted that North Bay had the greatest annual net infiltration due to an increase in active period and water availability. After Toronto, North Bay had the greatest increase in active period of 31

days. For most locations, an increase in *AE* is expected due to rising temperatures. However, an increase in quantity of precipitation and active period will still result in increased *NI* values

5.2.4 Performance of LIDs under Extreme Precipitation Events

Green roof hydrological performance demonstrates that there could be a general decrease in the peak reduction in the future. In many instances, this can lead to a substantial increase in stormwater runoff intensity from the green roof substrate. Moreover, there could be a general decrease in peak time delay, between the peak of the storm and the peak of the runoff from the green roofs in the future. Future storms that have a smaller return period will have a smaller time delay between the storm peak and runoff peak compared to storms with a greater return period. Overall, this reduction in performance could potentially result in flooding and erosion due to greater storm intensities and quantities in Ontario.

In terms of bioretention hydrological performance in the future, a general increase in ponding depth and time is expected for most of the locations considered in Ontario. The surface ponding depth of 50 cm are expected for many locations across Ontario. Considering that the design requirements for the bioretention facilities for some locations is a mere 20 cm, this will result in large quantities of untreated stormwater runoff overflowing from bioretention facilities. For most of the locations considered in this research, the ponding times are expected to increase in the future. The largest increase was predicated for the city of Windsor, which is only two hours short of the one mosquito breeding cycle. Considering that the assessments presented in this research assumed average initial soil saturation, it can be concluded that there is a higher probability that for above average initial soil saturations ponding times in the future can be a major concern.

5.3 Contribution of This Research

This is the first study to measure and document various geotechnical and hydrological properties of LID materials that are available and are being used for green roofs and bioretention in southern

Ontario. This study highlights the importance of measured hydraulic properties and consequences of using estimated properties in the assessment of low impact development substrates. The study has developed a rational procedure to systematically quantify the various design aspects of LID systems within the context of climate change. This has been accomplished for both long term changes as well as extreme precipitation events.

5.3 Recommendations for Future Research

The following list is a recommendation for future research.

- Examine the performance of green roof and bioretention systems using either a live site or laboratory soil columns to better understand the system variabilities. This also will assist in providing model validation data.
- Contaminant removal capabilities of bioretention facilities were not considered in this research. Assessing these capabilities within the context of changing climate will be worthwhile.
- Examine heat transfer capabilities of green roofs under changing climate.
- Examine the survival of specific plant species that are used for green roofs.
- Increased net infiltration leads to risk in decreased system performance due to clogging resulting in additional maintenance requirements. Therefore, relationship between increased stormwater runoff and system clogging should be considered.
- Cost benefit analysis of LID design changes versus decreased performance within the context of changing climate.

References

Allen, R., Pereira, L., Raes, D., and Smith, M. 1998. Crop Evapotranspiration – Guidelines for computing crop water requirements. FAO Irrigation and drainage paper 56.

Arguedas-Rodriguez, F. 2009. Calibrating capacitance sensors to estimate water content, matric potential, and electrical conductivity in soilless substrates. Thesis, University of Maryland, College Park, Maryland. 137 pp.

Arya, L.M. and Paris, J.F. 1981. A physicoempirical model to predict the soil moisture characteristic from particle size distribution and bulk density data. *Soil Sci, Soc. Am. J.*, 45(6), 1023-1030.

Arya, L.M., Leij, F.J., van Genuchten, M. Th., and Shouse, P. J. 1998. Scaling Parameter to Predict the Soil Water Characteristic from Partice-Size Distribution Data. *Soil Sci. Soc. Am. J.* 63. 510-519.

Asaduzzaman, Md & Saifullah, Md & Mollick, AKM & Hossain, Md & Halim, GMA & Asao, Toshiki. 2015. Influence of Soilless Culture Substrate on Improvement of Yield and Produce Quality of Horticultural Crops. doi:10.5772/59708.

ASTM D2487. 2017. Standard Practice for Classification of Soils for Engineering Purposes (Unified Soil Classification System). ASTM International, West Conshohocken, PA.

ASTM D2974. 2014. Standard Test Methods Moisture, Ash, and Organic Material of Peat and Other Organic Soils. ASTM International, West Conshohocken, PA.

ASTM D5084. 2016. Standard Test Methods for Measurement of Hydraulic Conductivity of Saturated Porous Materials Using a Flexible Wall Permeameter. ASTM International, West Conshohocken, PA.

ASTM D5856. 2015. Standard Test Method for Measurement of Hydraulic Conductivity of Porous Material Using a Rigid-Wall, Compaction-Mold Permeameter. ASTM International, West Conshohocken, PA.

ASTM D6913. 2017. Standard Test Methods for Particle-Size Distribution (Gradation) of Soils Using Sieve Analysis. ASTM International, West Conshohocken, PA.

ASTM D7928. 2017. Standard Test Method for Particle-Size Distribution (Gradation) of Fine-Grained Soils Using the Sedimentation (Hydrometer) Analysis. ASTM International, West Conshohocken, PA.

ASTM D854. 2014. Standard Test Methods for Specific Gravity of Soil Solids by Water Pycnometer. ASTM International, West Conshohocken, PA.

Aubertin, M., Mbonimpa, M., Bussiere, B., and Chapuis, R. 2003. A physically-based model to predict the water retention curve from basic geotechnical properties. *Canadian Geotechnical Journal*, 40(6): 1104-1122. http://doi.org/10.1139/t03-054

Baninajarian, L. 2020. Effect of Future Extreme Precipitation Events on the Stability of Soil Embankments Across Ontario. York University. Canada.

Barbu, I. A. 2013. Development of Unsaturated Flow Functions for Low Impact Development Stormwater Management Systems Filter Media and Flow Routines for Hydrological Modelling of Permeable Pavement. *University of New Hampshire.*

Barbu, I. and Ballestero, T. 2014. Unsaturated Flow Functions for Filter Media Used in Low-Impact Development – Stormwater Management Systems. *Journal of Irrigation and Drainage Engineering*, 141(1): 1-11. doi: 10.1061/(ASCE)IR.1943-4774.0000766

Bashir, R., Ahmad, F., & Beddoe, R. 2020. Effect of Climate Change on a Monolithic Desulphurized Tailings Cover. *Water*, 12(9): 2645. https://doi.org/10.3390/w12092645

Bashir, R., Sharma, J., and Stefaniak, H. 2016. Effect of hysteresis of soil-water characteristic curves on infiltration under different climatic conditions. Canadian Geotechnical Journal, 53(2): 273–284. Canadian Science Publishing. doi:10.1139/cgj-2015-0004.

Berkompas, B., Marx, K., Wachter, H., Beyerlein, D., Spencer, B., 2008. A study of green roof hydrologic performance in the cascadia region. In: Proceedings of the Low Impact Development for Urban Ecosystem and Habitat Protection Conference, 2008. Seattle.

Berndtsson, J. C. 2010. Green roof performance towards management of runoff water quantity and quality: A review. *Ecological Engineering,* 39(3): 351-360.

Bezerra-Coelho, C., Zhuang, L., Barbosa, M., Soto, M., van Genuchten, M. 2018. Further tests of the HYPROP evaporation method for estimating the unsaturated soil hydraulic properties. *Journal of Hydrol. Hydromech*., 66(2). 161-169. doi: 10.1515/johh-2017-0046

Borris, M., Leonhardt, G., Marsalek, J., Österlund, H. 2016. Source-Based Modeling of Urban Stormwater Quality Response to the Selected Scenarios Combining Future Changes in Climate and Socio-Economic Factors. *Environment Management*, 58: 223-237. doi: 10.1007/s00267-016-0705-3

Brooks, R.H., and A.T. Corey. 1964. Hydraulic properties of porous media, Hydrology Papers, No.3, Colorado State University, Fort Collins, Colorado.

Brown, K. and Lemon, J. 2020. Cations and Cation Exchange Capacity. *Soil Quality Pty Ltd.*

Brunetti, G., Simunek, J., Piro, P. 2016. A Comprehensive Analysis of the Variably Saturated Hydraulic Behavior of a Green Roof in a Mediterranean Climate. *Vadose Zone Journal*, *15*(9). http://doi.org/10.2136/vzj2016.04.0032

Camargo, A.P., Marin, F.R., Sentelhas, P.C., Picini, A.G., 1999. Adjust of the Thornthwaite's method to estimate the potential evapotranspiration for arid and superhumid climates, based on daily temperature amplitude. Rev. Bras. *Agrometeorol*. 7 (2), 251–257

Cascone, S. 2019. Green Roof Design: State of the Art on Technology and Materials. *Sustainability*, 11. 1-28. http://doi.org/10.3390/su11113020

Castiglia Feitosa, R., Wilkinson, S. 2016. Modelling green roof stormwater response for different soil depths. *Landscape and Urban Planning,* 153. 170-179. http://doi.org/10.1016/j.landurbplan.2016.05.007

CCDP. 2018. CCDP - Ontario Climate Change Data Portal. Retrieved from http://www.ontarioccdp.ca/.

Choi, S., Xu, L., and Kim, H. 2019. Influence of physical properties of peat-based plotting mixes substituted with parboiled rice hulls on plant growth under two irrigation regimes. *Hortic. Environ. Biotechnol.,* 60: 895-911. doi:10.1007/s13580-019-00179-9

Credit Valley Conservation (CVC). 2015. Advancing Low Impact Development as a Smart Solution for Stormwater Management. Retrieved from https://cvc.ca/wp-content/uploads/2016/06/CVC_report_Final_Reduced.pdf

Credit Valley Conservation; Toronto and Region Conservation Authority (CVC and TRCA). 2010. Low Impact Development Stormwater Management Planning and Design Guide. Retrieved from https://cvc.ca/wp-content/uploads/2012/02/lid-swm-guide-chapter1.pdf

Davis, A., Shokouhian, M., Sharma, H., and Minami, C. 2006. Water Quality Improvement through Bioretention Media: Nitrogen and Phosphorus Removal. *Water Environ. Res.,* 78(3). 284-293. http://doi.org/10.2175/106143005X94376

De Boodt, M. and O. Verdonck. 1972. The physical properties of the substrates in horticulture. *Acta Hort*, 26:37-44.

DelVecchio, T. 2017. Evaluating soil type and flow path for the optimal balance of infiltration and evapotranspiration in vegetated stormwater control measures to achieve maximum volume and pollutant removal. Villanova University.

Dettmann, U., Bechtold, M., Frahm, E., and Tiemeyer, B. 2014. On the applicability of unimodal and bimodal van Genuchten-Mualem based models to peat and other organic soils under evaporation conditions. *Journal of Hydrology,* 515. 103-115. http://doi.org/10.1016/jhydrol.2014.04.047

Devlin, J.F. 2015. HydrogeoSieveXL: an Excel-based tool to estimate hydraulic conductivity from grain-size analysis. *Hydrogeology Journal*. http://doi.org/10.1007/s10040-015-1255-0

Durner, W. 1994. Hydraulic Conductivity Estimation for Soils with Heterogenous Pore Structure. *Water Resources Research*, 30(2). 211-223. http://doi.org/10.1029/93WR02676

Environment and Climate Change Canada. 2014. Engineering Climate Datasets - Climate - Environment and Climate Change Canada. Retrieved from https://climate.weather.gc.ca/prods_servs/engineering_e.html.

Environment and Climate Change Canada. 2018. Historical Climate Data - Environment and Climate Change Canada. Retrieved from https://climate.weather.gc.ca/historical_data/search_historic_data_e.html.

Environmental Protection Agency. 2018. *Urban Runoff: Low Impact Development*. United States. Retrieved from https://www.epa.gov/nps/urban-runoff-low-impact-development

Fassman-Beck, E., Voyde, E., Simcock, R., Hong, Y.S., 2013. 4 living roofs in 3 locations: does configuration affect runoff mitigation? *J. Hydrol*. 490: 11–20. doi: 10.1016/j.jhydrol.2013.03.004

Feddes, R. A., E. Bresler, and S. P. Neuman. 1974. Field test of a modified numerical model for water uptake by root systems, Water Resour. Res., 10(6), 1199-1206.

Feddes, R.A., P.J. Kowalik, and H. Zaradny. 1978. Simulation of field water use and crop yield. PUDOC, Wageningen, the Netherlands.

Flato, G., J. Marotzke, B. Abiodun, P. Braconnot, S.C. Chou, W. Collins, P. Cox, F. Driouech, S. Emori, V. Eyring, C. Forest, P. Gleckler, E. Guilyardi, C. Jakob, V. Kattsov, C. Reason and M. Rummukainen. 2013. Evaluation of Climate Models. In: Climate Change 2013: The Physical Science Basis. Contribution of Working Group I to the Fifth Assessment Report of the Intergovernmental Panel on Climate Change [Stocker, T.F., D. Qin, G.-K. Plattner, M. Tignor, S.K. Allen, J. Boschung, A. Nauels, Y. Xia, V. Bex and P.M. Midgley (eds.)]. Cambridge University Press, Cambridge, United Kingdom and New York, NY, USA.

Freeze, A. and Cherry, J. 1979. Groundwater. Prentice-Hall, Inc. Englewood Cliffs, New Jersey.

Fredlund, D.G., Rahardjo, H., and Fredlund, M.D. 2012. *Unsaturated Soil Mechanics in Engineering Practice*. John Wiley & Sons, Inc., Hoboken, New Jersey, USA.

Government of Canada. 2020. Growing Season. Retrieved from https://www.nrcan.gc.ca/climate-change/impacts-adaptations/climate-change-impacts-forests/forest-change-indicators/growing-season/18470

Griffin, W. 2014. Extensive green roof substrate composition: effects of physical properties on matric potential, hydraulic conductivity, plant growth, and stormwater retention in the mid-Atlantic. University of Maryland

Guber, A., and Pachepsky, Y. 2010. Multimodeling with Pedotransfer Functions. Documentation and User Manual for PTF Calculator. *Beltsville Agricultural Research Centre, USDA-ARS.*

Gupta, S.C., Larson, W.E. 1979, Estimating soil water characteristic from particle size distribution, organic matter percent, and bulk density. *Water Resour. Res.* 15, 1633-1635.

Handreck, K. and Black, N. 2002 Growing media for ornamental plants and turf. Second Edition. University of New South Wales Press, Sydney, Australia.

Hathaway, J.M., Brown, R.A., Fu, J.S., Hunt, W.F. 2014. Bioretention function under climate change scenarios in North Carolina, USA. *Journal of Hydrology.* 519: 503-511. https://doi.org/10.1016/j.jhydrol.2014.07.037

He, Z., and Davis, A. 2011. Process Modeling of Storm-Water Flow in a Bioretention Cell. *J. Irrig. Drain Eng,* 137(3). 121-131. http://doi.org/10.1061/(ASCE)IR.1943-4774.0000166

Herrera-Gomez, S., Quevedo-Nolasco, A., and Pérez-Urrestarazu, L. 2017. The role of green roofs in climate change mitigation. A case study in Seville (Spain). *Building and Environment*, 123: 575-584. https://doi.org/10.1016/j.buildenv.2017.07.036

Hess, A., Wadzuk, B., and Welker, A. 2015. Evapotranspiration and infiltration in rain garden system. *World Environmental and Water Resources Congress 2015.* 261-270. http://doi.org/10.1061/9780784479162.025

Hill, J., Drake, J., and Sleep, B. 2016. Comparisons od extensive green roof media in Southern Ontario. *Ecological Engineering.* 94, 418-426. http://doi.org/10.1016/j.ecoleng.2016.05.045

Hilten, R., Lawrence, T., Tollner, E. 2008. Modeling stormwater runoff from green roofs with HYDRUS-1D. *Journal of Hydrology, 358.* 288-293. http://doi.org/10.1016/j.jhydrol.2008.06.010

House, T., Bashir, R., Sharma, J., and Khan, U. 2017. Characterization of unsaturated hydraulic properties for soils used in Low Impact Development. *GeoOttawa 2017 Conference.*

IPCC. 2013. Climate Change 2013 The Physical Science Basis Working Group I Contribution to the Fifth Assessment Report of the Intergovernmental Panel on Climate Change.

IPCC, 2014. Climate Change 2014: Synthesis Report. Contribution of Working Groups I, II and III to the Fifth Assessment Report of the Intergovernmental Panel on Climate Change [Core Writing Team, R.K. Pachauri and L.A. Meyer (eds.)]. IPCC, Geneva, Switzerland, 151 pp.

Kelmendi, S. and Aliu, V. 2013. Flexible Use and Application of Energy Efficiency Measures in Existing Multi-Residential Buildings. 201-209. 10.33107/ubt-ic.2013.19.

Khan, U. 2010. Bioretention cell efficacy in cold climates. The University of Calgary.

Kumar, R., V. Shankar, and Jat, M. K. 2014. Evaluation of root water uptake models – a review. *ISH Journal of Hydraulic Engineering*, 1-10, http://doi.org/10.1080/09715010.2014.981955

LeFevre, G., Paus, K., Natarajan, P., Gulliver, J., Novak, P., and Hozalski, R. 2015. Review of Dissolved Pollutants in Urban Storm Water and Their Removal and Fate in Bioretention Cells. Journal of Environmental Engineering, 141(1), 1-23. doi:10.1061/ (ASCE)EE.1943-7870.0000876.

Li, Y. 2014. Hydrologic Performance Analyses, Modelling, and Design Tool Development for Green Roof Systems. University of Hawai'i.

Li, Y., and Babcock, R. 2015 Modeling Hydrologic Performance of a Green Roof System with HYDRUS-2D. *Journal of Environmental Engineering, 141*(11). 1-9. http://doi.org/10.1061/(ASCE)EE.1943-7870.0000976.

Liu, R. and Fassman-Beck, E. 2017. Hydrologic response of engineered media in living roofs and bioretention to large rainfalls: experiments and modeling. *Hydrological Processes*, *31*. 556–572. doi: 10.1002/hyp.11044

Liu, R. and Fassman-Beck, E. 2018. Pore Structure and Unsaturated Hydraulic Conductivity of Engineered Media for Living Roofs and Bioretention Based on Water Retention Data. *J. Hydrol. Eng.* doi: 10.1061/(ASCE)HE.1943-5584.0001621

Martin-Downs, D. 2013. *Flood Management for the July 8th Severe Weather Event.* Toronto: TRCA. Retrieved from http://archives.york.ca/councilcommitteearchives/pdf/sep%2019%20esc%20stranks%20flood.pdf

Massachusetts Department of Environmental Protection. n.d. Bioretention areas and rain gardens. Massachusetts Clean Water Toolkit. Retrieved from https://megamanual.geosyntec.com/npsmanual/bioretentionareasandraingardens.aspx

Meng, Y., Wang, H., Chen, J., Zhang, S. 2014. Modelling Hydrology of a Single Bioretention System with HYDRUS-1D. *The Scientific World Journal*. doi:10.1155/2014/521047

Merdun. H. 2006. Pedotransfer functions for point and parametric estimations of soil water retention curve. *Plant Soil Environ.* 52(7). 321-327.

Metselaar, K. 2012. Water retention and evapotranspiration of green roofs and possible natural vegetation types. *Resources, Conservation and Recycling,* 64. 49-55. doi:10.1016/j.resconrec.2011.12.009

National Association of City Transportation Officials (NACTO). 2013. Urban Street Stormwater Guide: Bioretention Swale.

National Atlas of Canada. 1974. Department of Energy, Mines and Resources Canada (ed. 4). 266 sheets. Retrieved from https://open.canada.ca/data/en/dataset/2cbe746a-0307-5328-908f-4fb7c19e45c3

Neuman, S.P., Feddes, R.A., and Bresler, E. 1974. Finite element simulation of flow in saturated-unsaturated soils considering water uptake by plants. Third Annual Report, Project No. A10-SWC-77. Hydraulic Engineering Lab., Technion, Haifa, Israel.

Nichols, W. 2018. Modeling Performance of an Operational Urban Rain Garden Using HYDRUS-1D. Villanova University.

O'Malley, I. 2019. *2X Faster: More flooding, rapid sea level rise in Canada*. Toronto: Weather Network. Retrieved from https://www.theweathernetwork.com/ca/news/article/2x-faster-lakes-oceans-climate-change-report-sea-level-rise-flooding-storm-surge-atlantic-pacific-snow-melt-rain

Palla, A., Gnecco, I., and Lanza, L.G. 2009. Unsaturated 2D modelling of subsurface water flow in coarse-grained porous matrix of a green roof. *Journal of Hydrology*, 379. 193-204. doi:10.1016/j.jhydrol.2009.10.008

Peng, Z., Smith, C., Stovin, V. 2019 Internal fluctuations in green roof substrate moisture content during storm T events: Monitored data and model simulations. *Journal of Hydrology, 573*. 872-884 doi:10.1016/j.jhydrol.2019.04.008

Penman, H.L. 1948. Natural evaporation from open water, bare soil and grass. In Proceedings of the Royal Society of London A: Mathematical, Physical and Engineering Sciences. *The Royal Society*. 120–145. Retrieved from http://rspa.royalsocietypublishing.org/content/royprsa/193/1032/120.full.pdf

Pereira, A.R., and Pruitt, W.O. 2004. Adaptation of the Thornthwaite scheme for estimating daily reference evapotranspiration. *Agricultural Water Management*, 66(3): 251–257. doi:10.1016/j.agwat.2003.11.003.

Perelli, G. 2014. Characterization of the green roof growth media. Western University.

Perkins, K. 2011. Measurement and Modeling of Unsaturated Hydraulic Conductivity. In *Hydraulic Conductivity – Issues, Determination and Applications* (p. 419 – 434). Retrieved from https://wwwrcamnl.wr.usgs.gov/uzf/abs_pubs/papers/KPerkins2011.Conductivity.pdf

Peters, A. and Durner, W. 2007. Simplified evaporation method for determining soil hydraulic properties. *Journal of Hydrology*, 356(1-2). 147-162. doi: 10.1016/j.jhydrol.2008.04.016

Piñeiro, G., Perelman, S., Guerschman, J., and Paruelo, J. 2008. How to evaluate models: Observed vs. predicted or predicted vs. observed? *Ecological Modelling*. 216, 316-322. doi: 10.1016/l=j.ecolmodel.2008.05.006

Pitt, R., Clark, S., and Field, R. 1999. Groundwater Contamination Potential from Stormwater Infiltration Practices. *Urban Water*, 1, 217-236.

Pk, S., Bashir, R., and Beddoe, R. 2020. Effect of climate change on earthen embankments in Southern Ontario, Canada. *Environmental Geotechnics.* https://doi.org/10.1680/jenge.18.00068

Qin, H., Peng, Y., Tang, Q., and Yu, S. 2016. A HYDRUS model for irrigation management of green roofs with a water storage layer. *Ecological Engineering*, 95: 399-408. doi: 10.1016/j.ecoleng.2016.06.077

Radcliffe, D. and Šimůnek, J. 2010. Soil Physics with HYDRUS. Modeling and Applications. CRC Press Taylor & Francis Group. Boca Raton, FL.

Rawls, W.J., Brakensiek, D.L., Saxton, K.E. 1982. Estimation of soil water properties. *Trans. ASAE* 25, 1316-1320.

Richards, L. 1931. Capillary conduction of liquids through porous mediums. *Physics*, 1 (5):318-333.

Ritchie, J.T. 1972. Model for predicting evaporation from a row crop with incomplete cover. *Water Resour. Res*. 8:1204–1213. doi:10.1029/WR008i005p01204

Sandoval, V., Suárez, F., Vera, S., Pinto, C., Victorero, F., Bonilla, C., Gironás, J., Bustamante, W., Rojas, V., Pastén, P. 2015 Porous Media Characterization to Simulate Water and Heat Transport through Green Roof Substrates. *Vadose Zone Journal, 16(4)*. doi:10.2136/vzj2016.10.0101

Schaap, M.G., Leij, F., and van Genuchten, M. Th. 2001. Rosetta: a computer program for estimating soil hydraulic parameters with hierarchical pedotransfer functions. *Journal of Hydrology*. 251:163-176.

Schindler, U., 1980. Ein Schnellverfahren zur Messung der Wasserleitfahigkeit im teilgesattigten Boden an Stechzylinderproben. *Arch. Acker Pflanzenbau Bodenkd*. 24:1–7.

Schultz, I., Sailor, D., and Starry, O. 2018. Effects of substrate depth and precipitation characteristics on stormwater retention by two green roofs in Portland OR. *Journal of Hydrology: Regional Studies*, 18: 110-118. doi: 10.1016/j.ejrh.2018.06.008

Schunn, C. D. and Wallach, D. 2005. Evaluating goodness-of-fit in comparison of models to data. In *W. Tack (Ed.)., Psychologie der Kognition: Reden and Vortr¨ageanl¨asslich der Emeritierung von Werner Tack*, pages 115–154, Saarbrueken, Germany. University of Saarland Press.

Simcock, R. and Dando, J. 2013. Mulch Specification for Stormwater Bioretention Devices. Prepared by Landcare Research New Zealand Ltd for Auckland Council. Auckland Council technical report, TR2013/056. Retrieved from https://knowledgeauckland.org.nz/media/1673/tr2013-056-mulch-specification-for-stormwater-bioretention-devices.pdf

Šimůnek, J., Šejna, M., Saito, H., and van Genuchten, M. Th. 2018a. The HYDRUS-1D Software Package for Simulating the One-Dimensional Movement of Water, Heat, and Multiple Solutes in Variably-Saturated Media. Version 4.17. Department of Environmental Sciences, University of California Riverside, Riverside, California.

Šimůnek, J., M. Šejna, and M. Th. van Genuchten. 2018b. New Features of the Version 3 of the HYDRUS (2D/3D) Computer Software Package. *Journal of Hydrology and Hydromechanics,* 66(2): 133-142. doi: 10.1515/johh-2017-0050.

Šimůnek, J., van Genuchten, M. Th., and Šejna, M. 2008. Development and applications of the HYDRUS and STANMOD software packages and related codes. *Vadose Zone Journal*. 7:587–600. doi:10.2136/vzj2007.0077

Singh, G., Panda, R. 2015. Bootstrap-based artificial neural network analysis for estimation of daily sediment yield from a small agricultural watershed. *Int. J. Hydrology Science and Technology*, 5(4). 333-348. doi: 10.1504/IJHST.2015.072634.

Soil Survey Staff. 1951. Soil survey manual. U.S. Department of Agriculture (USDA) Handbook No. 18. Soil Conservation Service.

Stevenson, D.S. 1982. Unreliabilities of pressure plate 1500 kilopascal data in predicting soil water contents at which plants become wilted in soil-peat mixes. *Can. J. Soil Sci*, 62: 415-419.

Stewart, R., Lee, J., Shuster, W., and Darner, R. 2017. Modelling hydrological response to a fully-monitored urban bioretention cell. *Hydrological Processes,* 31. 4626-4638. doi:10.1002/hyp.11386

Stovin, V., Poë, S., Berretta, C. 2013. A modelling study of long term green roof retention performance. *Journal of Environmental Management*, 131: 206-215. https://doi.org/10.1016/j.jenvman.2013.09.026

Susca, T., Gaffin, S. R., and Dell'Osso, G.R. 2011. Positive effects of vegetation: Urban heat island and green roofs. *Environmental Pollution*, 159(8-9). 2119-2126. doi: 10.1016/j.envpol.2011.03.007

Sutton, R., Rodie, S., Shelton, D. 2014. Stormwater management: Green roof basics. University of Nebraska. Retrieved from http://extensionpublications.unl.edu/assets/html/g2244/build/g2244.htm

Taylor, S.A., and G.L. Ashcroft. 1972. Physical edaphology: The physics of irrigated and nonirrigated soils. W.H. Freeman, San Francisco.

Thornthwaite, C.W. 1948. An Approach toward a Rational Classification of Climate. Geographical Review, 38(1): 55–94. doi:10.2307/210739.

Toronto Water. 2017. Wet Weather Flow Master Plant Implementation Status Update. Report for Action.

Tuller, M. and Or, D. 2003. Retention of water in soil and the soil water characteristic curve. *Encyclopedia of Soils in the Environment*. Elsevier Ltd. Oxford, U.K.

UMS. 2015. Manual HYPROP, Version 2015-01. UMS GmbH, Munich, Germany.

United States Environmental Protection Agency (U.S. EPA). 2007. Reducing Stormwater Costs through Low Impact Development (LID) Strategies and Practices. Report No. EPA 841-F-07-006. Washington, D.C.

United States Environmental Protection Agency (U.S. EPA). 2018. Urban Runoff: Low Impact Development. United States. https://www.epa.gov/nps/urban-runofflow-impact-development

van Genuchten, M.Th. 1980. A closed-form equation for predicting the hydraulic conductivity of unsaturated soils. *Soil Sci. Soc. Am. J*. 44. 892– 898. doi:10.2136/sssaj1980.03615995004400050002x

Vereecken H., Diels J., van Orshoven J., Feyen J., Bouma J. 1992: Functional evaluation of pedotransfer functions for the estimation of soil hydraulic properties. Soil Sci. Soc. Am. J., 56: 1371–1378

Vincent. L.A., Zhang, X., Mekis, É., Wan, H., and Bush, E.J. 2018. Changes in Canada's Climate: Trends in Indices Based on Daily Temperature and Precipitation Data. *Atmosphere-Ocean*, 56(5). 332-349. http://doi.org/10.1080/07055900.2018.1514579

Viola, F., Hellies, M., and Deidda, R. 2017. Retention performance of green roofs in representative climates worldwide. *Journal of Hydrology*, 553: 763-772. https://doi.org/10.1016/j.jhydrol.2017.08.033

Voyde, E., Fassman, E., Simcock, R., Wells, J., 2010. Quantifying evapotranspiration rates for New Zealand Green roofs*. J. Hydrol*. Eng. 15, 395–403

Wang, M., Zhang, D., Lou, S., Hou, Q., Liu, Y., Cheng, Y., Qi, J., and Tan, S.K. 2019. Assessing Hydrological Effects of Bioretention Cells for Urban Stormwater Runoff in Response to Climatic Changes. *Water*, 11. http://doi.org/10.3390/w11050997

Wesseling, J., J. Elbers, P. Kabat, and B. Van den Broek. 1991. SWATRE: Instructions for input. Winand Staring Ctr., Wageningen, the Netherlands.

Wösten J.H.M., Finke P.A., Jansen M.J.W. 1995: Comparison of class and continuous pedotransfer functions to generate soil hydraulic characteristics. *Geoderma*, 66: 227–237

Wösten J.H.M., Pachepsky, Ya. A., Rawls, W. J. 2001. Pedotransfer functions: bridging the gap between available basic soil data and missing soil hydraulic characteristics. *Journal of Hydrology*, 251. 123-150.

Weiss, P., and Gulliver, J. 2008. Contamination of Soil and Groundwater due to Stormwater Infiltration Practices. University of Minnesota. Retrieved from https://www.pca.state.mn.us/sites/default/files/stormwater-r-weiss0608.pdf

Yang, J., Yu, Q., and Gong, P. 2008. Quantifying air pollution removal by green roofs in Chicago. *Atmospheric Environment,* 42(31). 7266-7273. doi: 10.1016/j.atmosenv.2008.07.003

Zhang, X., Flato, G., Kirchmeier-Young, M., Vincent, L., Wan, H., Wang, X., Rong, R., Fyfe, J., Li, G., Kharin, V.V. 2019. Changes in Temperatures and Precipitation Across Canada; Chapter 4 *in* Bush, E. and Lemmens, D.S. (Eds.) Canada's Changing Climate Report. Government of Canada, Ottawa, Ontario, pp 112-193

Appendix A: Images of LID Substrates

Green Roof Substrate: GR1

Green Roof Substrate: GR2

Bioretention Substrate: BR1

Bioretention Substrate: BR2

Bioretention Substrate: BR3

Appendix B: Challenges Presented in the Laboratory

Saturated Hydraulic Conductivity

Initially, a constant head test was conducted following a procedure similar to ASTM D5856 (2015). However, challenges were discovered during the laboratory testing which led to a modified version of the constant head test. The methods followed, challenges presented, and solutions determined are discussed. Note that a constant head test was selected rather than a falling head test as the material is very coarse. Thus, the speed of the water level within the burette for the falling head test would be too quick to record.

Constant Head Test

Method

First, for sample preparation, two porous plates are de-aired using a dessicator to ensure that there is an uninterrupted flow within the permeameter. Once de-aired, the porous plate and filter paper were placed at the bottom of the permeameter. The height of the permeameter is 15.7 cm and the diameter is 7.5 cm. The distance between the side ports is 7.8 cm. Each LID media was then packed within the permeameter to the dry bulk density of 1g/cm^3. A dry bulk density of 1g/cm^3 was used as alternative studies have obtained sample cores from live sites and used a dry bulk density of approximately 1g/cm^3 (Griffin, 2014; Perelli, 2014; Liu and Fassman-Beck, 2017; Hill et al., 2016). Once packed, the filter paper and de-aired porous plate were placed at the top and the lid of the permeameter was screwed on (Figure B.1).

Figure B.1: Permeameter used in constant head test

The bottom port of the permeameter was attached to an inflow pipe, which was connected to an elevated reservoir filled with tap water. The two side ports were attached to two open manometer tubes (Figure B.2). The difference of the two manometer readings provided the difference in head required in the hydraulic conductivity measurement. The inflow port was opened, allowing the sample to saturate for at least 24 hours.

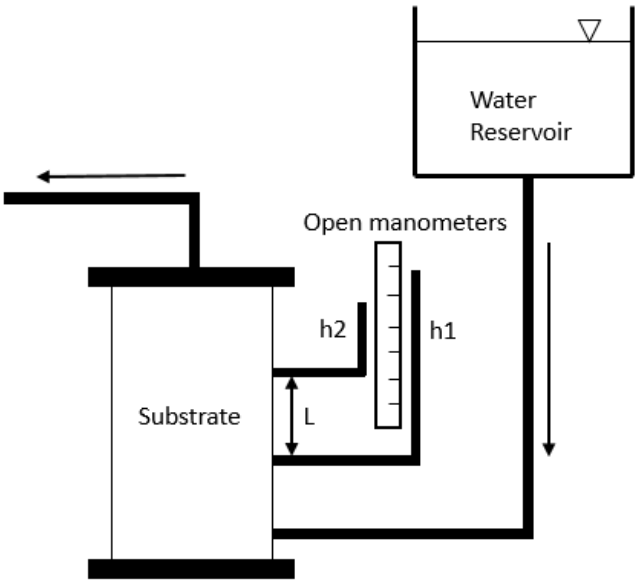

Figure B.2: Schematic of the constant head test

Before conducting the test, entrapped air was removed within the open manometer tubes by opening the air-bleed valve. In addition, water was flushed through the sample for a few minutes to ensure that any entrapped air was released. Moreover, the water level within the manometer tubes should be equal to the water reservoir level, otherwise there may be air bubbles blocking the ports.

A stopwatch, an empty beaker with a known mass, and thermometer were readily available before the start of the test. With the outlet port open, the discharge was captured with the empty beaker while simultaneously starting the stopwatch. When the beaker was removed, the stopwatch was immediately stopped and the amount of water that was discharged into the beaker was weighed. This is used to determine the volumetric flow rate. The temperature of the discharge was taken for temperature correction for the hydraulic conductivity. The height of the water reservoir was then decreased and the test was repeated.

Challenges and Solutions

While conducting the constant head test, the water level within the open manometer tubes were not stabilizing. Re-attempting the test led to a no-flow condition, thus demonstrating entrapped air within the sample. Packing the sample dry to get the desired dry bulk density and utilizing tap water rather than de-aired water may have both contributed to the air entrapment. In order to overcome this challenge, it was determined that passing CO_2 through the sample can assist in flushing out the air. However, the CO_2 would dissolve as it passes through the saturated porous plate used in the constant head test. Thus, rather than using porous plates, metal mesh and geotextile are used as a substitute (Figure B.3a). Subsequently, it was noted that packing the sample dry may lead to segregation. To deal with this problem, water was added to the sample to reach a gravimetric water content of 2%.

Modified Constant Head Test

Taking into account the challenges and solutions developed, the modified test was conducted. For this test, two side ports were installed into a compaction permeameter in order to attach the two open manometer tubes (Figure B.3b). The height of the compaction permeameter is 18.0 cm and the diameter is 15.2 cm. The distance between the two side ports is 7 cm. Before testing, it is a good practice to fill the permeameter with water to make sure that there is no leakage. Once it is confirmed that there are no visible signs of leakage, the permeameter was drained and dried, and a metal mesh and geotextile were placed at the bottom of the permeameter.

Similar to the previous constant head test, each LID sample was packed to a dry bulk density of 1 g/cm^3. The oven dried sample was split into four different bowls to help reduce the sample bias. To reduce segregation, water was added so that the sample reached a gravimetric water content of 2%. A packing procedure was adopted to avoid horizontal layering. When packing, the first lift was poured in and gently compacted. The top of the layer was then lightly scraped before pouring

in the next lift to avoid horizontal layering of the sample. Once the permeameter was filled, the geotextile and metal mesh were placed at the top and then were sealed with an appropriate cover (Figure B.3c).

Carbon dioxide was passed though the permeameter to assist in flushing out the air. Once the sample has been flushed with CO_2, the permeameter was attached to a water reservoir and two manometers. In order to reduce air entrapment in the system, de-aired water was used. The saturated hydraulic conductivity was determined by obtaining the volumetric flowrate by maintaining a constant head.

a) 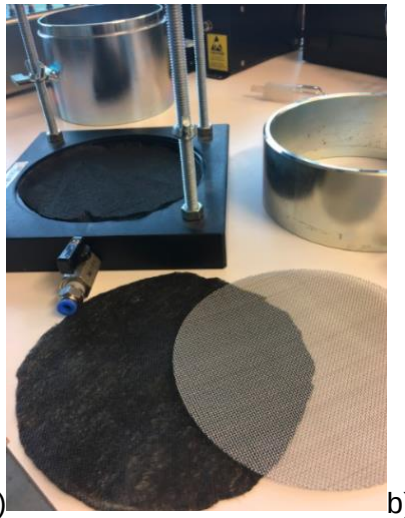 b) 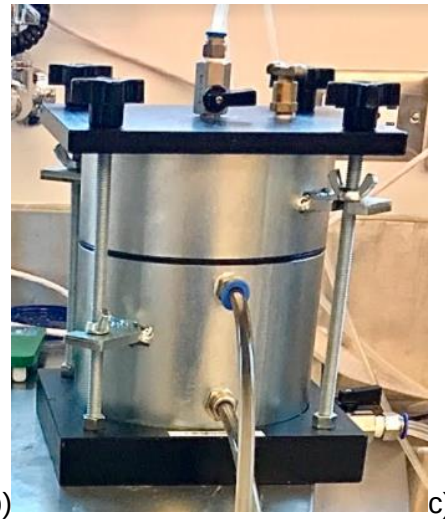 c) 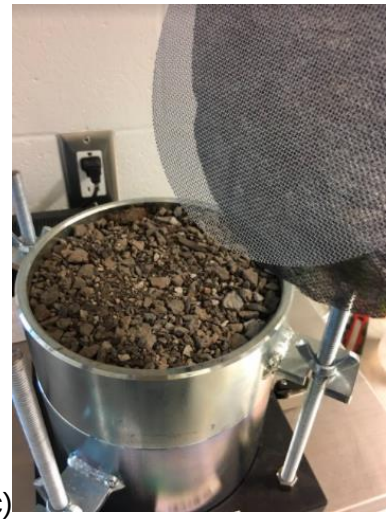

Figure B.3: Modified constant head test, (a) geotextile and metal sheet used, (b) two ports installed into compaction permeameter, (c) permeameter filled with green roof substrate

Soil Water Characteristic Curve

Figure B.4 demonstrates the challenges in measuring the SWCC for these coarse LID materials. Figure B.4 presents the two HYPROP tests completed for GR1 and BR1. The green roof substrate, GR1, was measured again as it was noted that the initial volumetric water content was 37% and the porosity was 57%. The porosity was calculated using the following equation:

$$\phi = 1 - \frac{\rho_d}{\rho_s} \quad [1]$$

where φ is porosity, ρ_d is the dry bulk density and ρ_s is the particle density. The dry bulk density for this first test was measured to be 0.87 g/cm^3. For GR1 test 2, the initial volumetric water content was measured to be 44% and a porosity of 47%, as the dry bulk density was 1.07 g/cm^3. BR1 was also measured as the SWCC slope is quite steep, resulting in a large *n* value for the van Genuchten (1980) equation. However, the second test resulted in an initial volumetric water content smaller than the first test, as shown in Figure B.4.

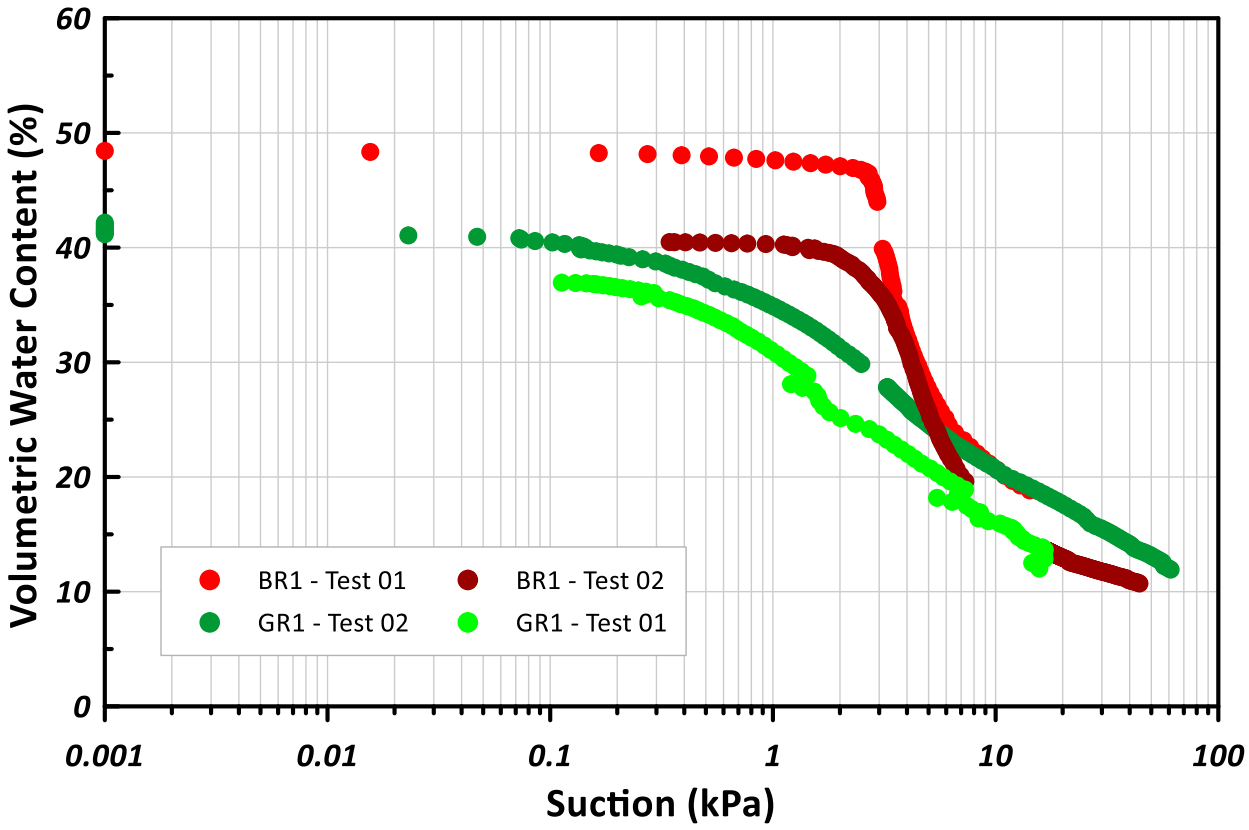

Figure B.4: Challenges in measuring the SWCC for LID substrates

Appendix C: Visual Examination of Measured and Predicted Soil Water Characteristic Curves

Green Roof Substrate: GR1

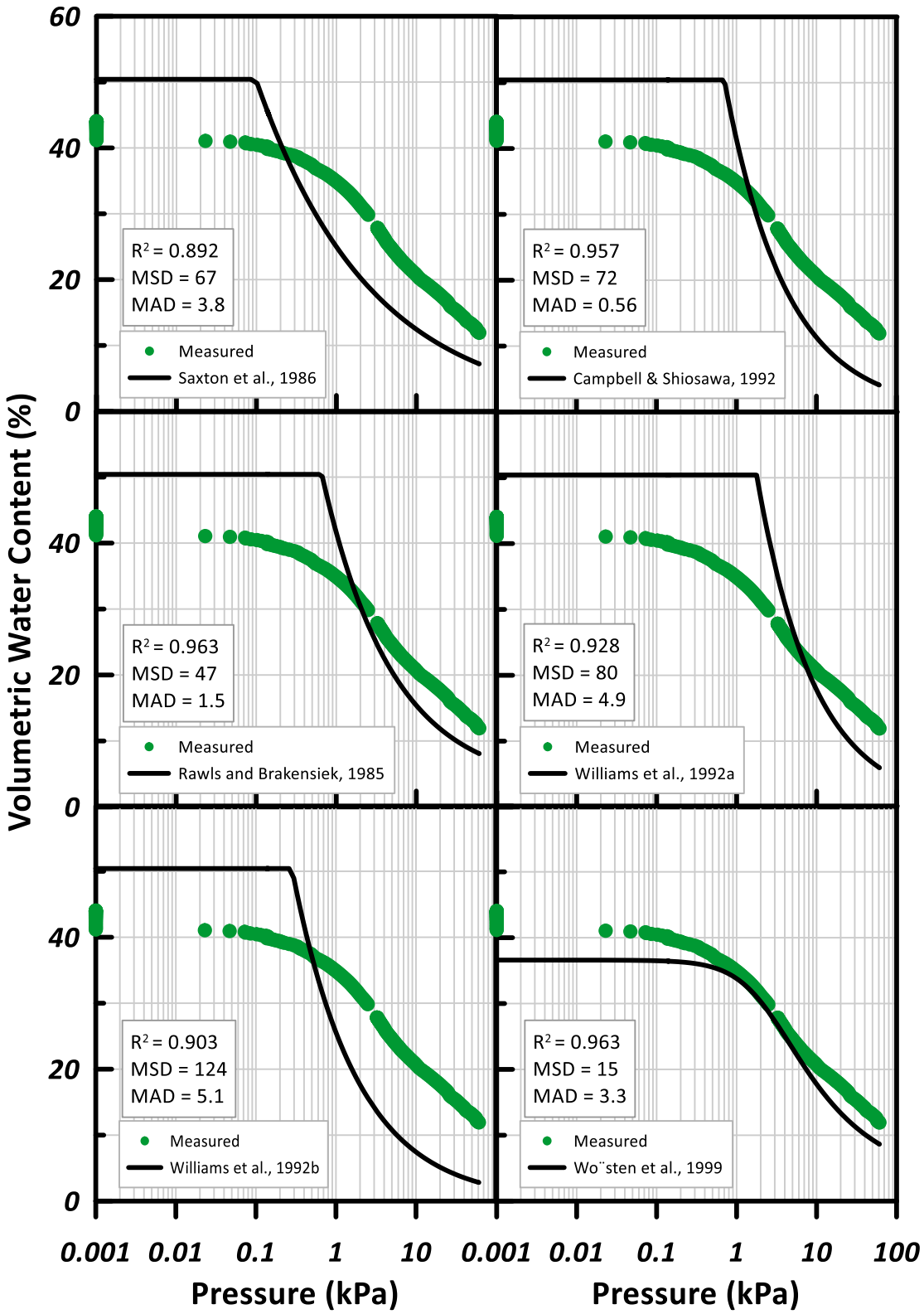

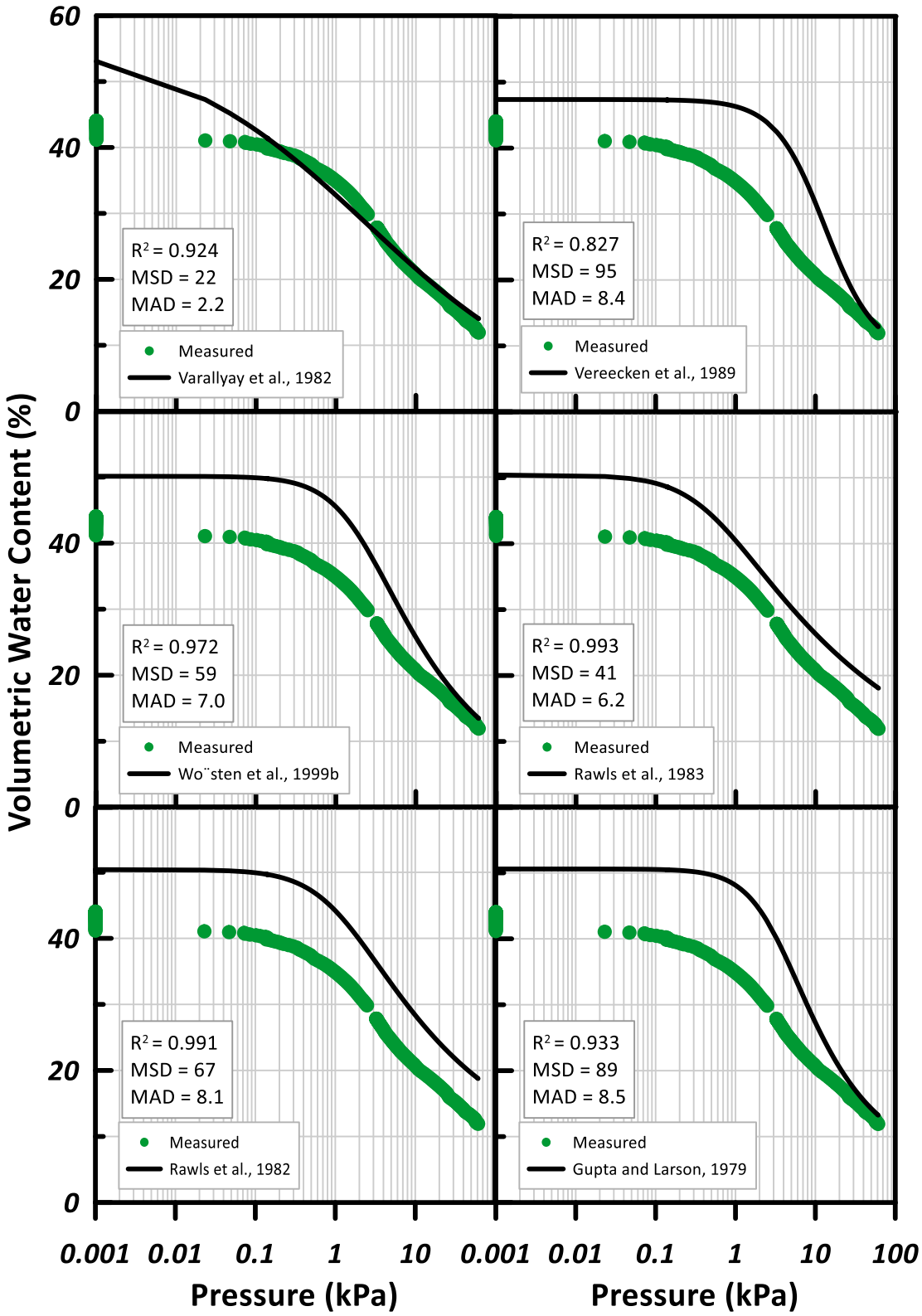
Volumetric Water Content (%)
60
40
20
0
R² = 0.924
MSD = 22
MAD = 2.2
Measured
Varallyay et al., 1982
R² = 0.827
MSD = 95
MAD = 8.4
Measured
Vereecken et al., 1989
R² = 0.972
MSD = 59
MAD = 7.0
Measured
Wo¨sten et al., 1999b
R² = 0.993
MSD = 41
MAD = 6.2
Measured
Rawls et al., 1983
R² = 0.991
MSD = 67
MAD = 8.1
Measured
Rawls et al., 1982
R² = 0.933
MSD = 89
MAD = 8.5
Measured
Gupta and Larson, 1979
0.001
0.01
0.1
1
10
100
Pressure (kPa)
Pressure (kPa)

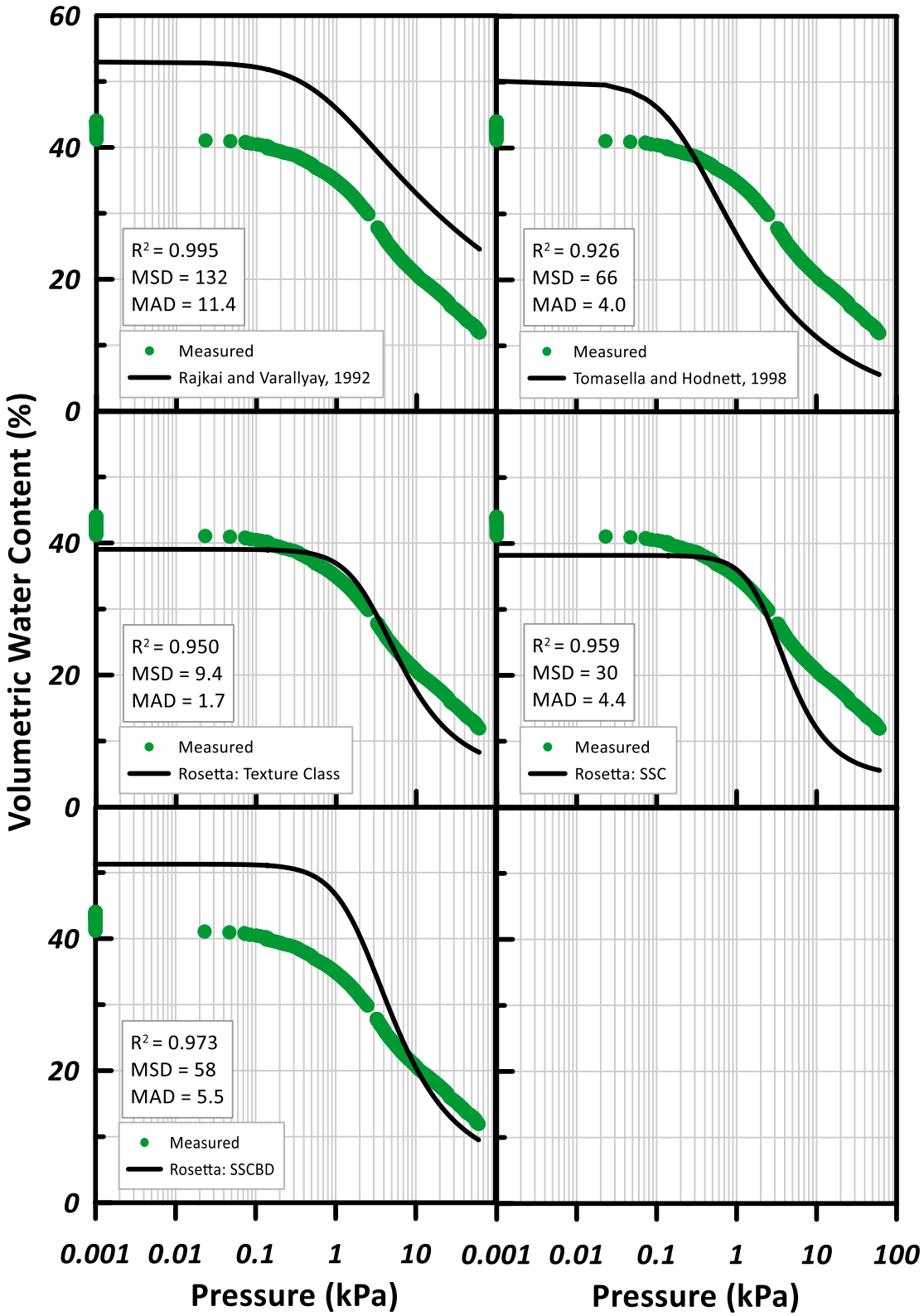
Volumetric Water Content (%)
60
40
20
0
R² = 0.995
MSD = 132
MAD = 11.4
Measured
Rajkai and Varallyay, 1992
R² = 0.926
MSD = 66
MAD = 4.0
Measured
Tomasella and Hodnett, 1998
R² = 0.950
MSD = 9.4
MAD = 1.7
Measured
Rosetta: Texture Class
R² = 0.959
MSD = 30
MAD = 4.4
Measured
Rosetta: SSC
R² = 0.973
MSD = 58
MAD = 5.5
Measured
Rosetta: SSCBD
0.001
0.01
0.1
1
10
100
Pressure (kPa)
Pressure (kPa)

Green Roof Substrate: GR2

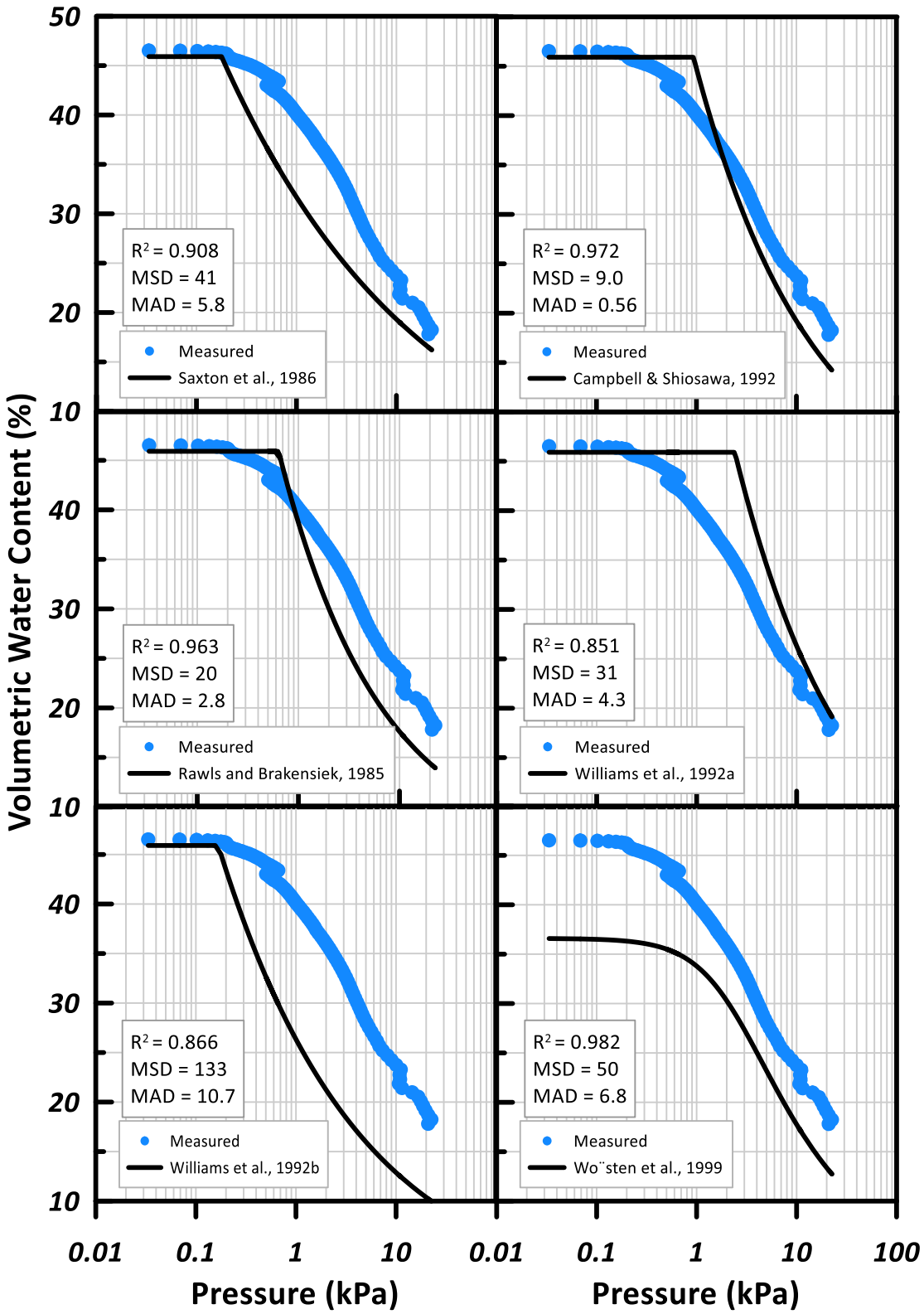

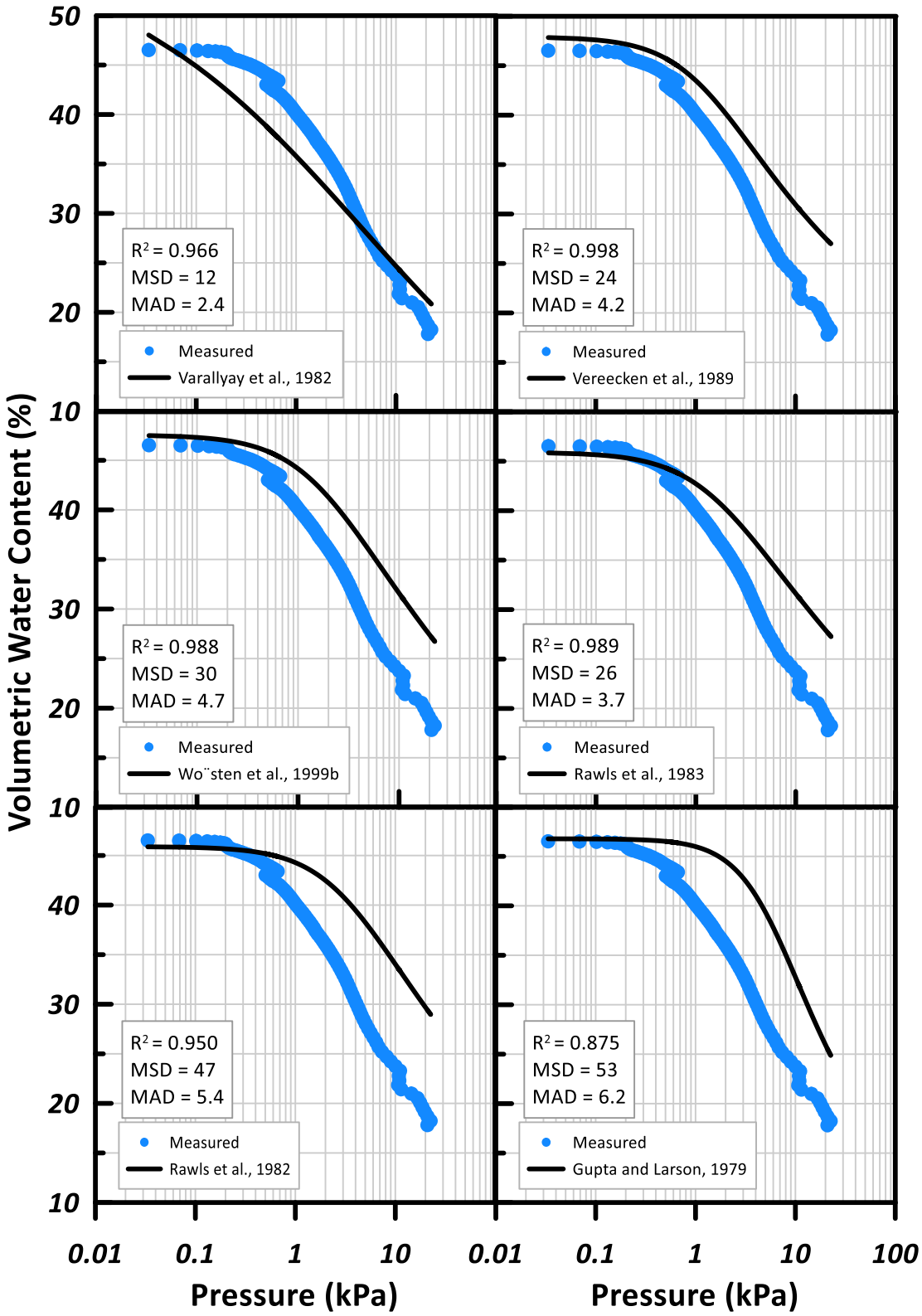
Volumetric Water Content (%)
50
40
30
20
10
R² = 0.966
MSD = 12
MAD = 2.4
Measured
Varallyay et al., 1982
R² = 0.998
MSD = 24
MAD = 4.2
Measured
Vereecken et al., 1989
R² = 0.988
MSD = 30
MAD = 4.7
Measured
Wo¨sten et al., 1999b
R² = 0.989
MSD = 26
MAD = 3.7
Measured
Rawls et al., 1983
R² = 0.950
MSD = 47
MAD = 5.4
Measured
Rawls et al., 1982
R² = 0.875
MSD = 53
MAD = 6.2
Measured
Gupta and Larson, 1979
0.01
0.1
1
10
100
Pressure (kPa)
Pressure (kPa)

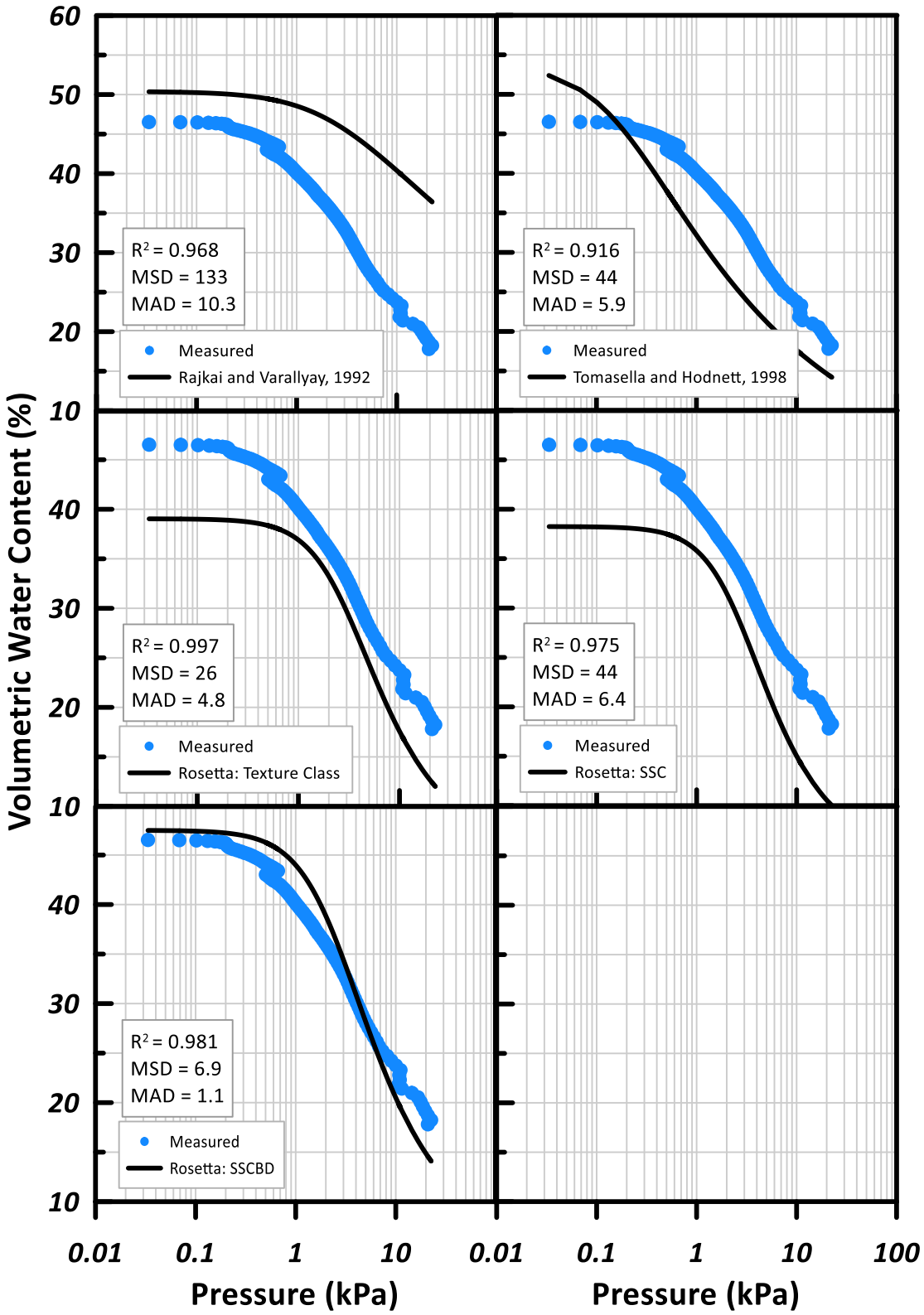
Volumetric Water Content (%)
60
50
40
30
20
10
R² = 0.968
MSD = 133
MAD = 10.3
Measured
Rajkai and Varallyay, 1992
R² = 0.916
MSD = 44
MAD = 5.9
Measured
Tomasella and Hodnett, 1998
R² = 0.997
MSD = 26
MAD = 4.8
Measured
Rosetta: Texture Class
R² = 0.975
MSD = 44
MAD = 6.4
Measured
Rosetta: SSC
R² = 0.981
MSD = 6.9
MAD = 1.1
Measured
Rosetta: SSCBD
0.01
0.1
1
10
100
Pressure (kPa)
Pressure (kPa)

Bioretention Substrate: BR1

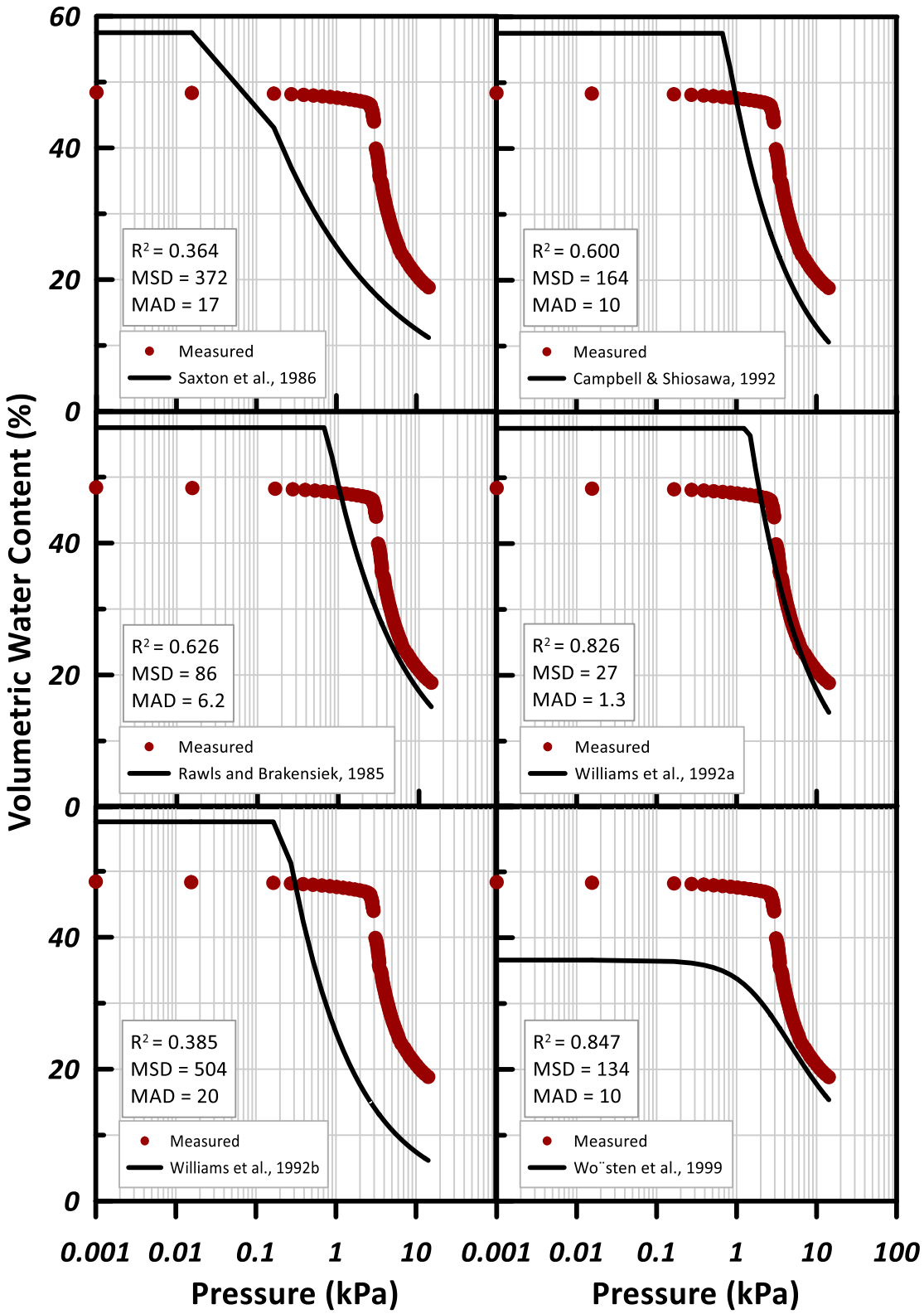

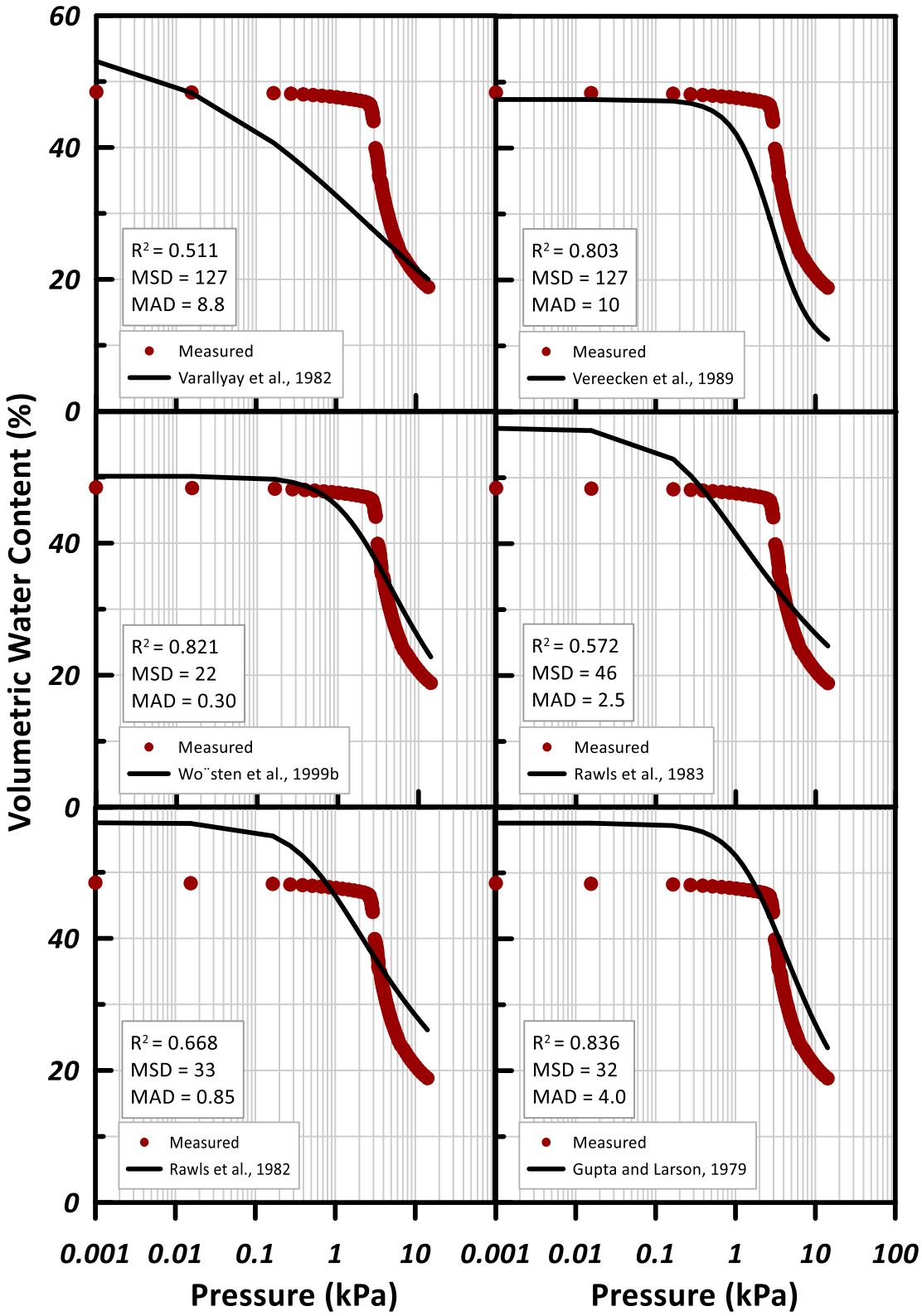
Volumetric Water Content (%)
60
40
20
0
R² = 0.511
MSD = 127
MAD = 8.8
Measured
Varallyay et al., 1982
R² = 0.803
MSD = 127
MAD = 10
Measured
Vereecken et al., 1989
R² = 0.821
MSD = 22
MAD = 0.30
Measured
Wo¨sten et al., 1999b
R² = 0.572
MSD = 46
MAD = 2.5
Measured
Rawls et al., 1983
R² = 0.668
MSD = 33
MAD = 0.85
Measured
Rawls et al., 1982
R² = 0.836
MSD = 32
MAD = 4.0
Measured
Gupta and Larson, 1979
0.001
0.01
0.1
1
10
100
Pressure (kPa)
Pressure (kPa)

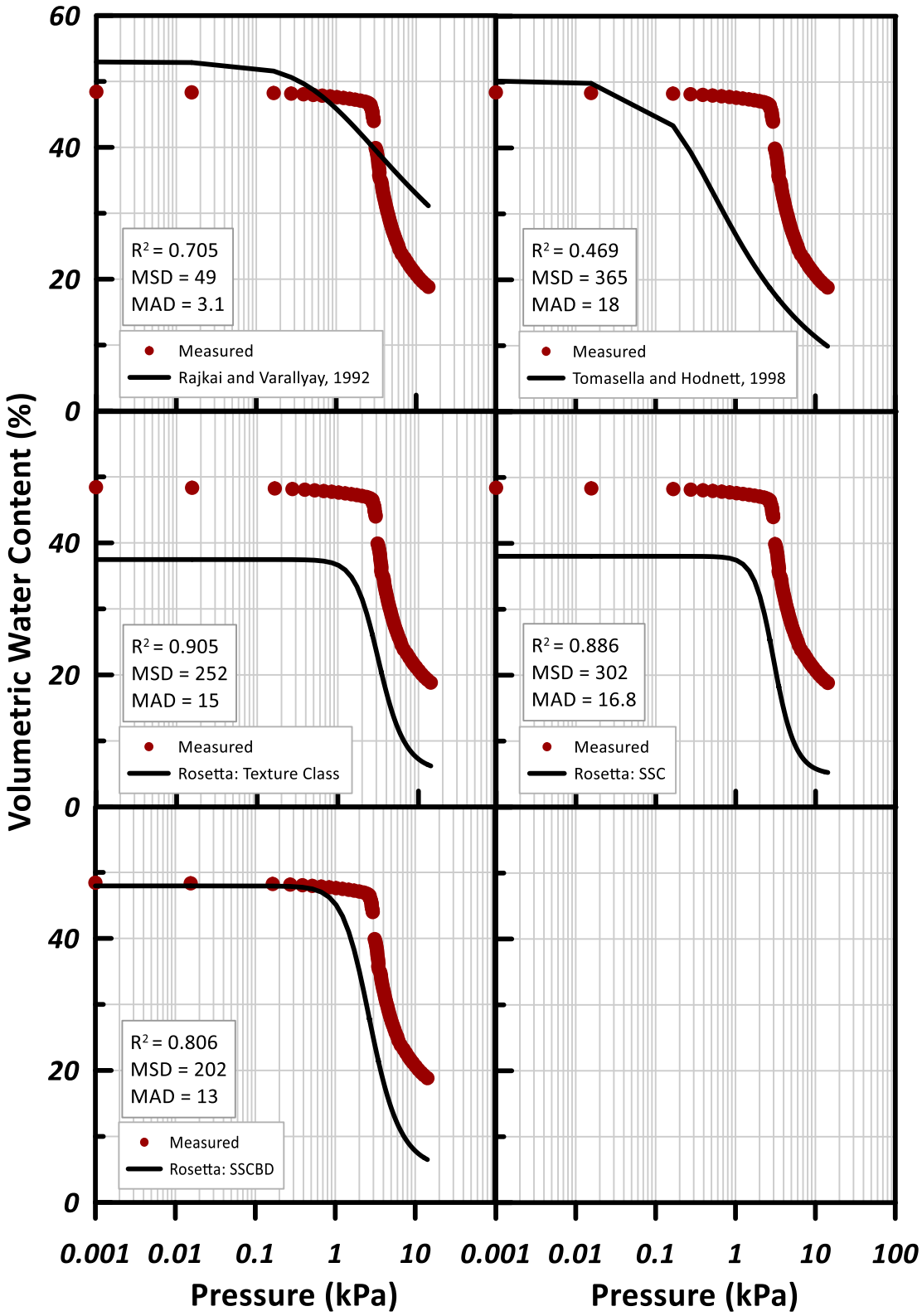
Volumetric Water Content (%)
60
40
20
0
R² = 0.705
MSD = 49
MAD = 3.1
Measured
Rajkai and Varallyay, 1992
R² = 0.469
MSD = 365
MAD = 18
Measured
Tomasella and Hodnett, 1998
R² = 0.905
MSD = 252
MAD = 15
Measured
Rosetta: Texture Class
R² = 0.886
MSD = 302
MAD = 16.8
Measured
Rosetta: SSC
R² = 0.806
MSD = 202
MAD = 13
Measured
Rosetta: SSCBD
0.001
0.01
0.1
1
10
100
Pressure (kPa)
Pressure (kPa)

Bioretention Substrate: BR2

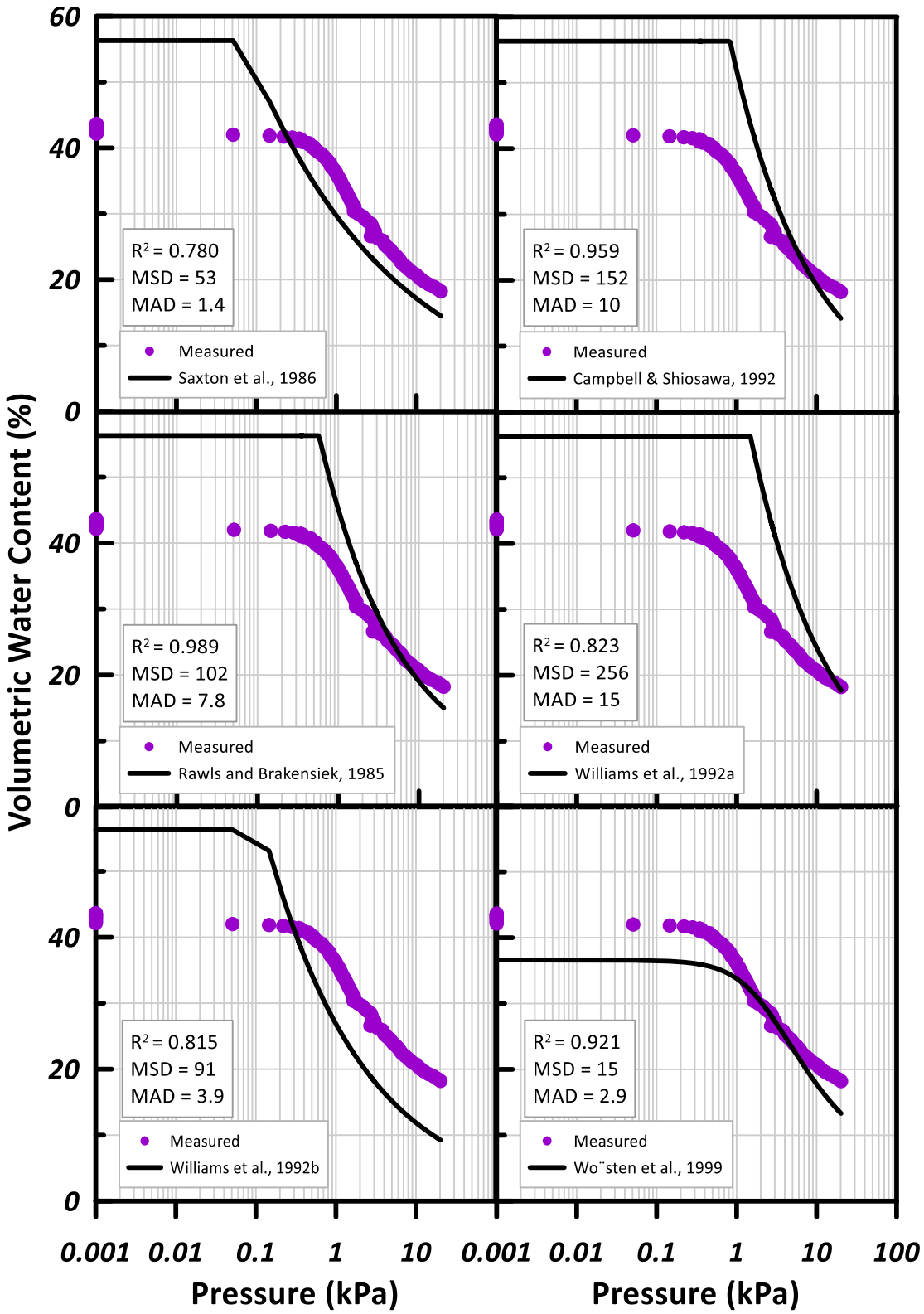

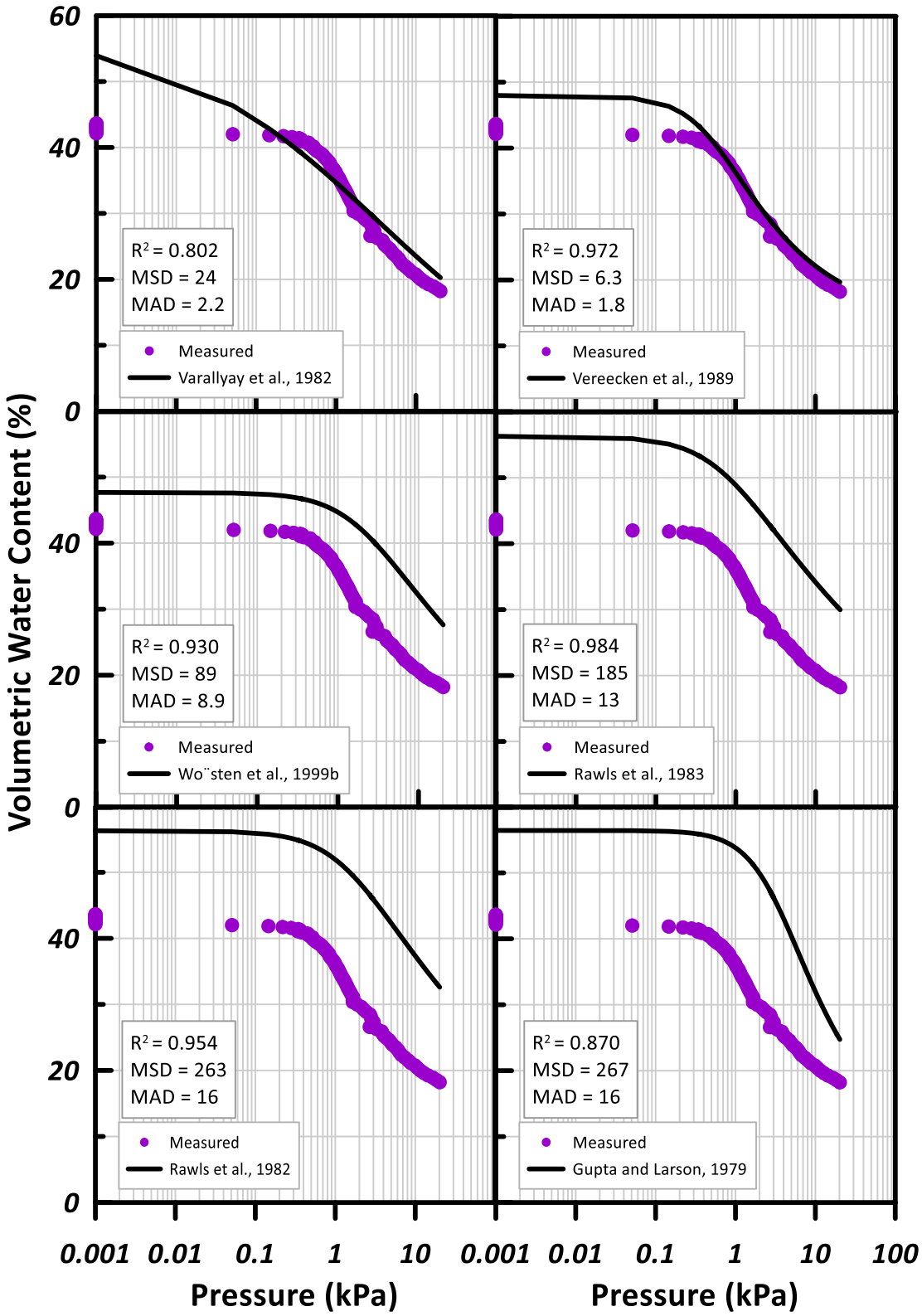
Volumetric Water Content (%)
60
40
20
0
R² = 0.802
MSD = 24
MAD = 2.2
Measured
Varallyay et al., 1982
R² = 0.972
MSD = 6.3
MAD = 1.8
Measured
Vereecken et al., 1989
R² = 0.930
MSD = 89
MAD = 8.9
Measured
Wo¨sten et al., 1999b
R² = 0.984
MSD = 185
MAD = 13
Measured
Rawls et al., 1983
R² = 0.954
MSD = 263
MAD = 16
Measured
Rawls et al., 1982
R² = 0.870
MSD = 267
MAD = 16
Measured
Gupta and Larson, 1979
0.001
0.01
0.1
1
10
100
Pressure (kPa)
Pressure (kPa)

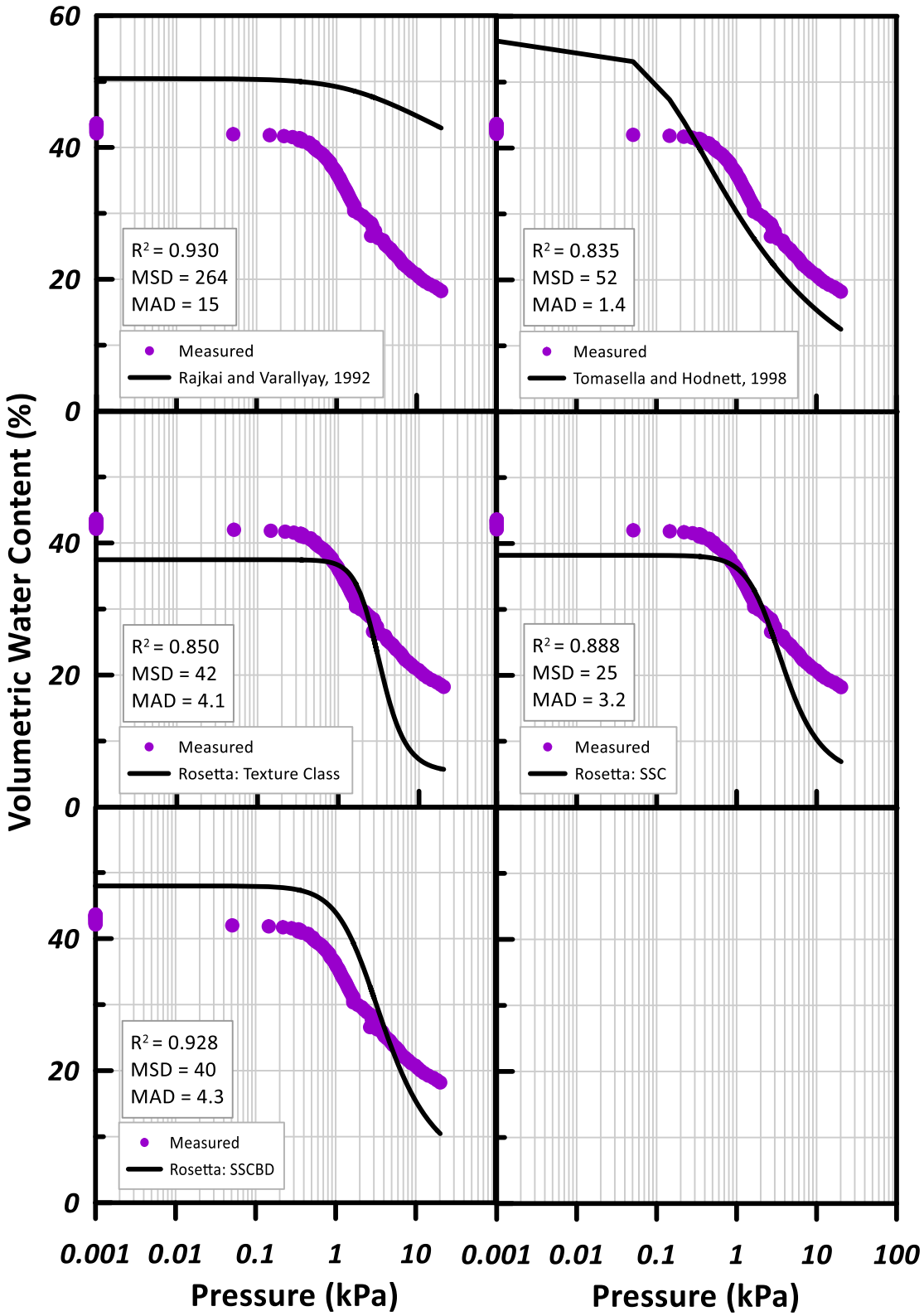
Volumetric Water Content (%)
60
40
20
0
R² = 0.930
MSD = 264
MAD = 15
Measured
Rajkai and Varallyay, 1992
R² = 0.835
MSD = 52
MAD = 1.4
Measured
Tomasella and Hodnett, 1998
R² = 0.850
MSD = 42
MAD = 4.1
Measured
Rosetta: Texture Class
R² = 0.888
MSD = 25
MAD = 3.2
Measured
Rosetta: SSC
R² = 0.928
MSD = 40
MAD = 4.3
Measured
Rosetta: SSCBD
0.001
0.01
0.1
1
10
100
Pressure (kPa)
Pressure (kPa)

Bioretention Substrate: BR3

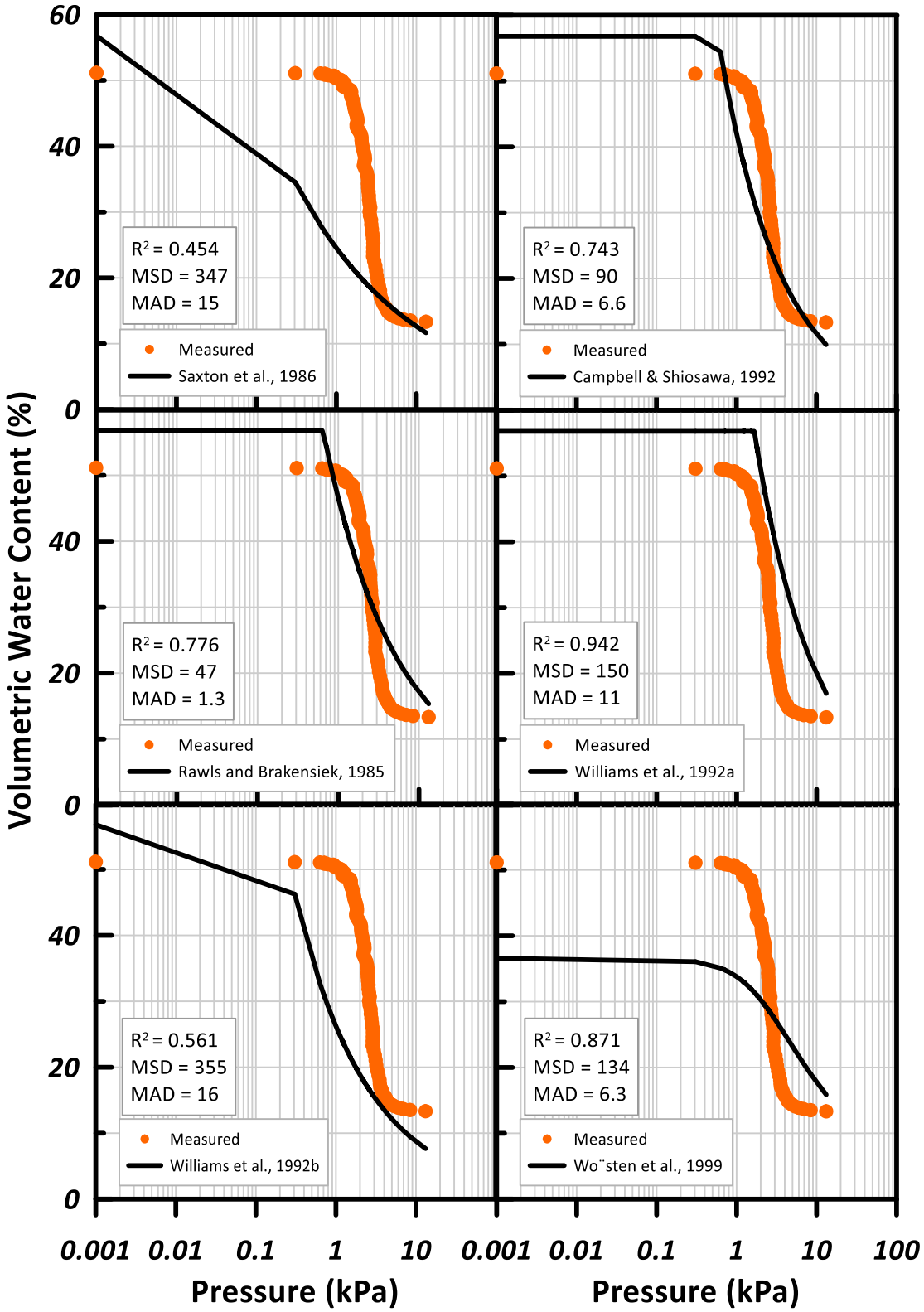

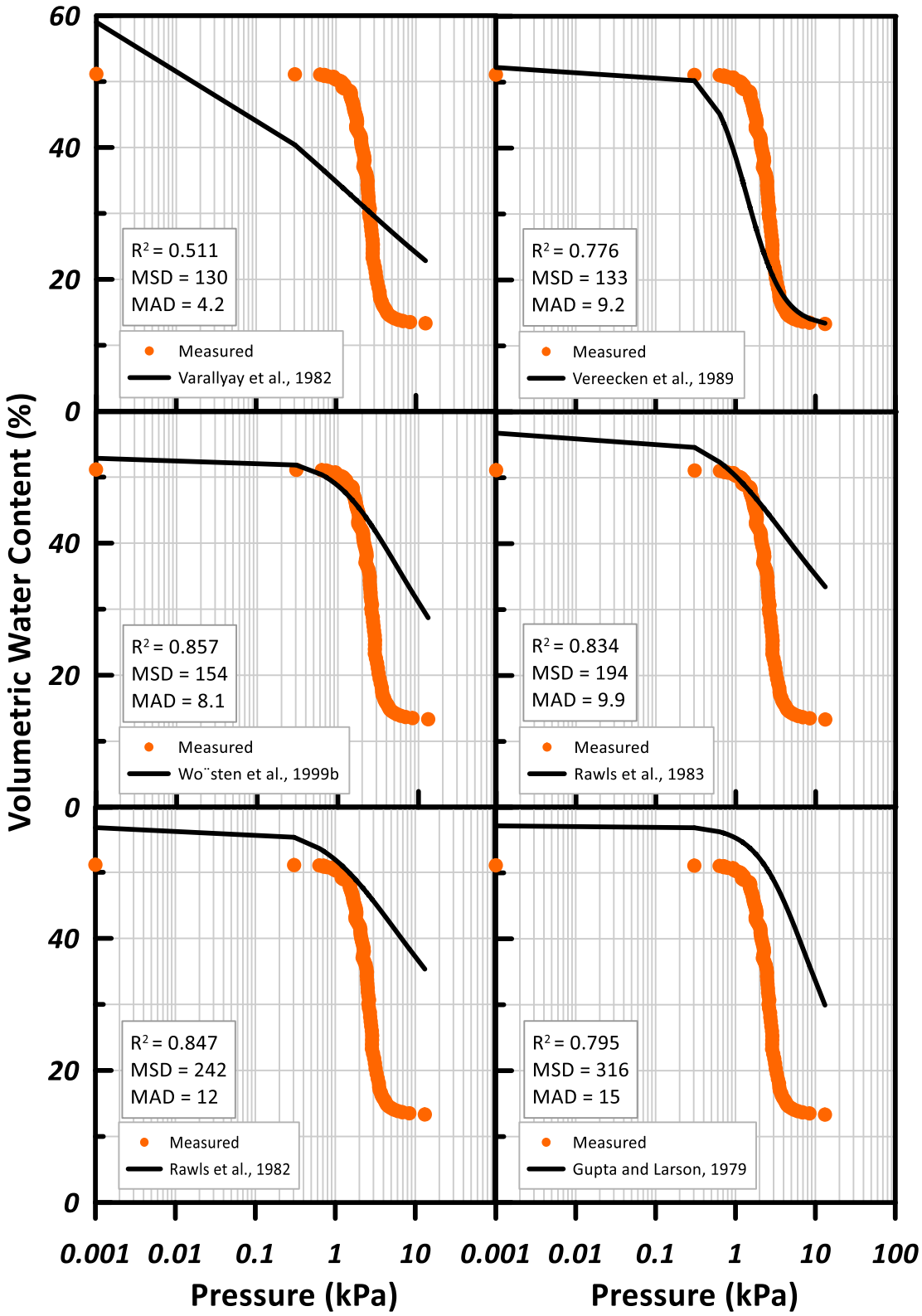
Volumetric Water Content (%)
60
40
20
0
R² = 0.511
MSD = 130
MAD = 4.2
Measured
Varallyay et al., 1982
R² = 0.776
MSD = 133
MAD = 9.2
Measured
Vereecken et al., 1989
R² = 0.857
MSD = 154
MAD = 8.1
Measured
Wo¨sten et al., 1999b
R² = 0.834
MSD = 194
MAD = 9.9
Measured
Rawls et al., 1983
R² = 0.847
MSD = 242
MAD = 12
Measured
Rawls et al., 1982
R² = 0.795
MSD = 316
MAD = 15
Measured
Gupta and Larson, 1979
0.001
0.01
0.1
1
10
100
Pressure (kPa)
Pressure (kPa)

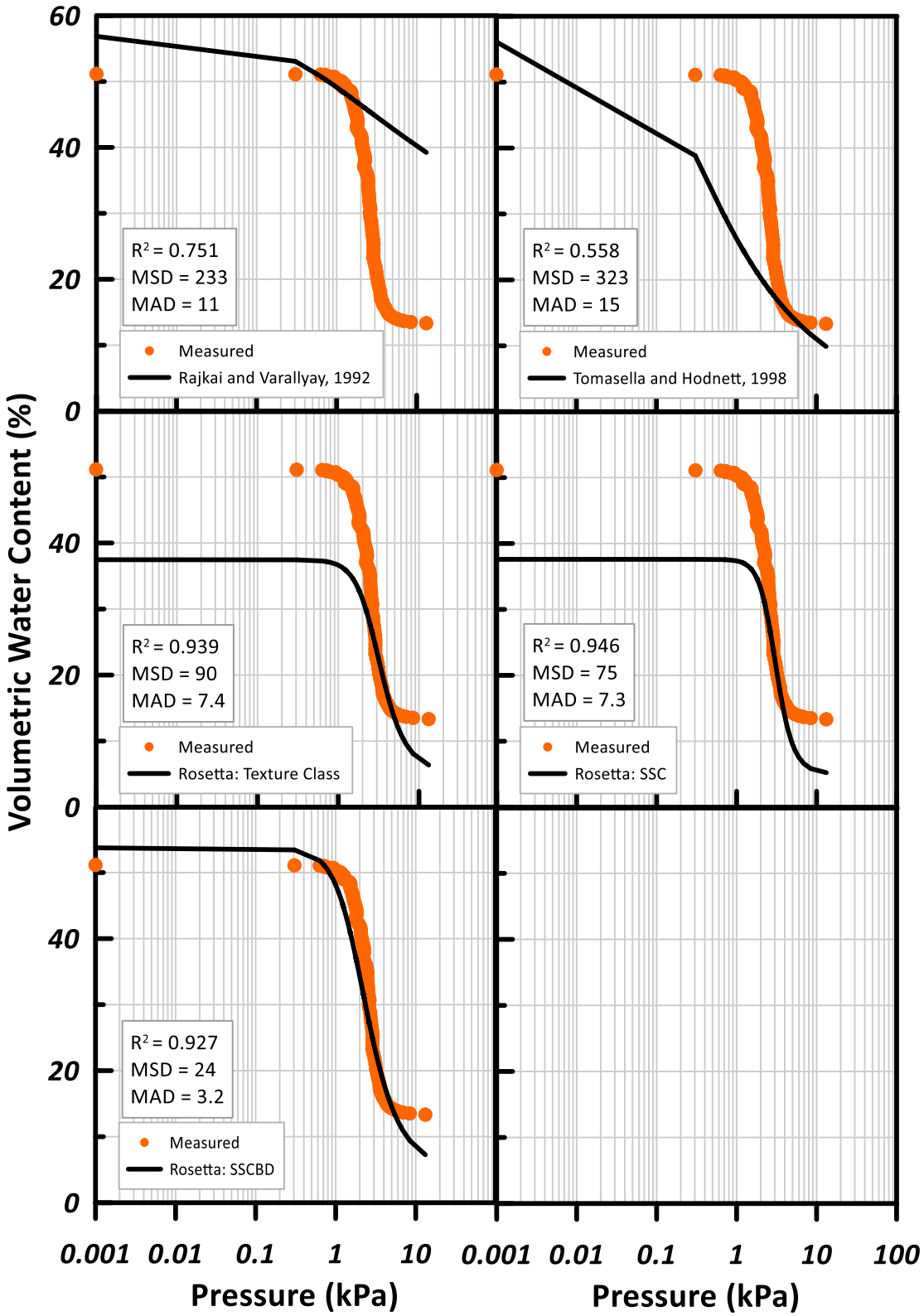
Volumetric Water Content (%)
60
40
20
0
R² = 0.751
MSD = 233
MAD = 11
Measured
Rajkai and Varallyay, 1992
R² = 0.558
MSD = 323
MAD = 15
Measured
Tomasella and Hodnett, 1998
R² = 0.939
MSD = 90
MAD = 7.4
Measured
Rosetta: Texture Class
R² = 0.946
MSD = 75
MAD = 7.3
Measured
Rosetta: SSC
R² = 0.927
MSD = 24
MAD = 3.2
Measured
Rosetta: SSCBD
0.001
0.01
0.1
1
10
100
Pressure (kPa)
Pressure (kPa)